High-Efficiency Organic Electroluminescent devices

Hiroshi Kanno

The University of Tokyo

November 2006

Abstract

High-Efficiency Red Emitting OLED

A red organic light-emitting device (OLED) with the widely-used red emitting layer (EML) has a shortcoming of low electroluminescent efficiency and high driving voltage primarily due to the inefficient energy transfer efficiency between a host material and a red emitter. we have developed the novel method to promote the energy transfer by introducing a dye sensitizer into an EML. The device performance has exhibited the improved luminance efficiency, lowered driving voltage and saturated red color purity over a wide range of currents. The energy transfer mechanism is studied considering using fluorescent and phosphorescent sensitizer dyes. The effects have been applied to a practical use in manufacturing OLED displays.

In another approach to high-efficiency red OLEDs, we have developed the new class of organic materials for a host and an emitter in an EML, an electron transporting material, and a hole transporting material. Carrier injection and transporting properties of each material and excited states of a host maetrial and the characteristics of energy transfer are studied to maximize the luminance efficiency of red OLEDs. For a host, a red emitter, an electron transporting material, and a hole transport material, we have successfully found the new class of materials for a high-efficiency red OLED. This research is a matter of importance in terms of the guideline for designing efficient devices.

High-Efficiency Red Emitting OLED

Aiming for the energy transfer where both triptets and singlets are efficiently radiatively deactivated, allowing for 100% internal quantum efficiency (IQE), white OLEDs ulitizing a blue fluorophore and green and red phosphors have been developed. The singlets generated in the blue fluorophore are consumed to blue fluorescence and remained triplets are diffused to the phosphors and green and red phosphorescence is emitted. In

the EML, the triplets and singlets are selectively transforred to the spacially separated fluorophore and the phosphors respectively. Furthermore, another white OLED wih 100% IQE is developed replacing the green emitter from a phosphor to a fluorophore, where the triplets generated in the blue fluorophore are transferred to the green fluorophore then to the red phosphor via Förste energy transfer mechanism. In the phosphor-sensitized WOLED triplet-triplet annihilation is reduced to achieve exceedingly high efficiencies even at high current region.

Additionally, the white OLED with a stacked structure with the novel charge generation layer has been fabricated. With the high-transmissino charge generation layer, the microcavity effect is designed to be minimal for excellent color stability over a wide viewing angle. Also, the carrier injection to the EML is studied in detail for achieving well-balanced white emission comprised of blue, green and red emission.

Application for Full-Color Displays

Top-emitting device strucrure and the RGBW pixel format and above-mentioned stacked strucrue have been proposed for the use in a full-color OLED display. Low-temperature polysilicone TFT backplane is used to demonstrate the effects of those technologies. The lifetime and power consumption are pronouncedly improved.

Finally, the future prospect of OLEDs is described.

Contents

Chapter 1.

Introduction

1.1 Organic Electronics

Organic electronic devices are the pathfinder for realizing the paradigm shift from the present electronics, which promises to be as easily manufactured as newspapers, magazines, and colorful posters. These common household products are produced using web-processing technologies where rolls of long paper are fed into machines to be cut, pressed, dyed and packaged. If brought to fruition, mass production of organic electronics will replace traditional semiconductor batch processes, and thereby allow electronics to compete with well-established very inexpensive devices such as the common incandescent bulb, and usher in new disposable products such as electronic identification tags by producing, for example, a roll-to-roll process (see Fig. 1-1).

Nowadays, a number of scientists, students and engineers have been questing organic electronics with huge enthusiasm to obtain the dominant position in electronics from long-lasting silicon-based devices. Especially, organic light emitting diodes (OLEDs), organic photovoltaics, organic TFTs, and organic semiconductor lasers have been aggressively studied for a practical use.

Organic electronics have a wide range of molecular weights and include small molecules such as pentacene and longer polymeric molecules. Organic semiconductors can be made with differing degrees of order, from single crystals to polycrystalline or amorphous films like silicon semiconductors. The properties depend on the order and chemical nature of the semiconductor. There are degrees of freedom in modifying the structure with the addition of side/end groups which impart added variety to the properties. Organic semiconductor based photoconductors are extensively used in xerography. Small molecule and conjugated polymer LEDs have been commercialized. Organic photovoltaics are now aggressively studied to achieve extremely cheap solar cells. Organic and polymer based TFTs have been proposed for applications such as displays and RF identification tags. It is significant matter of importance to promote the realization of the organic electronics and to open the door to a new era of new technology.

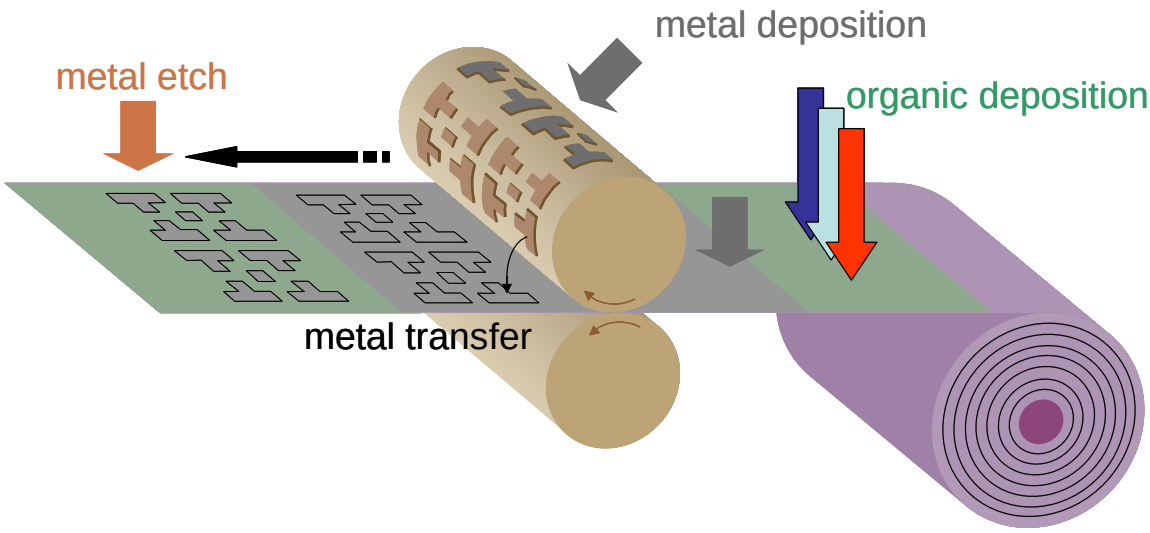

Figure 1-1 Schematic of a roll-to-roll process for a production of a organic device.

1.2 History of Organic Electronic

A significant step forward in organic technology came with the classical publication by Tang and VanSlyke of light-emitting devices [1] and solar cells [2] fabricated from thin amorphous layers deposited by thermal evaporation in vacuum. Although disordered films possess inferior electron transport characteristics, they can satisfy the requirement for extremely thin, low voltage, organic devices: electrically continuous films with smooth interfaces and no pinholes. Indeed, thermal evaporation is capable of growing continuous, molecularly-smooth, films as thin as 100Å, allowing vertical device feature sizes approaching molecular scales. As with the anthracene thin-film devices,[3] the reduction in organic thickness to ~1000Å in the solar cells and light-emitting devices enabled a dramatic reduction in operating voltage. A significant step was to use amorphous films to fabricate the first organic heterostructure light emitting device, increasing the quantum efficiency of luminescence by approximately two orders of magnitude to 1%, at an operating voltage of less than 10V; see Fig. 1-2. As described in Fig. 1-4, the heterostructure design was also used in a 1% power efficient solar cell. [4] With this work, organic materials first showed their potential as the basis for an efficient emissive technology applicable to all aspects of the display industry. An intense examination by chemists and electrical engineers followed.

In intensive effort of improving the efficiencies of OLEDs, several breakthrough-technologies are reported. The most innovative technology is what Forrest and Thompson had demonstrated high-efficiency electrophosphorescence. The use of a fluorescent dye leads to an upper limit of 25% on the internal quantum efficiency, due to the small fraction of singlet excitons created on hole-electron recombination. The use of phosphorescent dopants, however, allows the efficient utilization of both singlet and triplet excitons, removing the 25% upper limit on the internal efficiency. Utilizing phosphorescent dopants, the theoretical internal quantum efficiency of the OLED can be 100% harvesting both singlet and triplet energies. As shown in Fig. 1-3, The quantum efficiencies of these devices are as high as 20% (internal eff. » 90%) [4]. The phosphorescent dopants in these devices are heavy metal containing molecules (i.e. Pt, and Ir), prepared as both metalloporphyrins and organometallic complexes. The high level of spin orbit coupling in these metal complexes gives efficient emission from triplet states at room temperature.

In addition to the electroluminescence and photovoltaics applications described above, there is a growing interest in using organic materials in transistors. Such devices would compete with amorphous and polycrystalline silicon thin film transistors; but whereas these later materials typically require a glass substrate, organic materials may be deposited on a room temperature surface. Thus, organic materials are compatible with inexpensive, lightweight, flexible and mechanically rugged plastic substrates. For applications such as simple circuits on plastic cards, organic materials may therefore offer economic advantages. In their pristine state, organic materials have negligible amounts of free charge, and consequently, they have minimal dark conductivity. Although it is possible to increase the conductivity of organic materials by doping with ionic species such as iodine, transistors require that the conductivity be modulated by an external signal. A widely recognized solution to this problem is to employ a thin film transistor architecture Another organic material that has been successfully applied to thin film transistors is pentacene (see Fig. 1-5). In thin films, pentacene molecules stand vertically on the substrate and the π orbital intermolecular overlap is maximum in the horizontal direction, as required for the horizontal geometry of a thin film transistor.

Thus, the morphology of the pentacene is crucial to obtaining high field-effect mobilities. In the work [5] of Gundlach *et al.*, polycrystalline pentacene was deposited using thermal evaporation, but using single crystals has also proved highly successful. Arguably, using single crystals conflicts with the perceived advantages of organic materials in transistors, namely that they can be used with flexible plastic substrates.

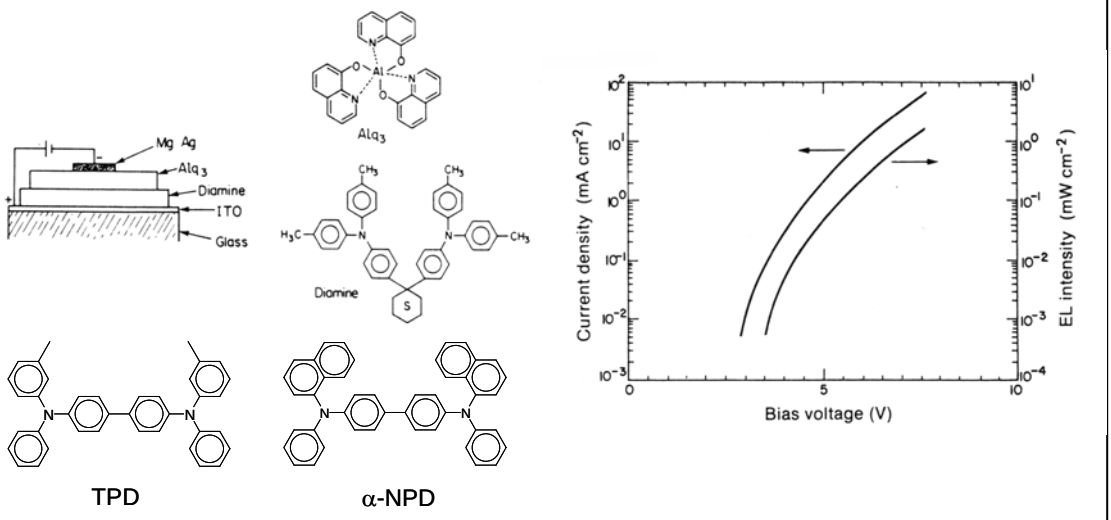

Figure 1-2. Tang and Van Slyke's OLED is built on a glass substrate coated with a transparent indium tin oxide layer acting as the anode. A diamine was used as the hole transporting material since this class of materials was found to have stable conductivity properties in earlier work on photoconductors. Many variations on the basic diamine structure were later investigated; for example, both TPD and α–NPD were found to make successful hole transport layers. The electron transporting and luminescent material employed was Alq_3. In these heterostructure devices electrons and holes combine at the diamine/Alq3 interface, but whereas there is minimal electron injection into the diamine layer, some holes penetrate into the first 100Å of Alq_3. Thus, excitons are formed in the Alq_3 and emission is observed from Alq_3 fluorescence. Electrons are injected into the organic layers from a Mg:Ag alloy cathode with an additional layer of Ag to protect the Mg from oxidation. After Tang and Van Slyke (1987).

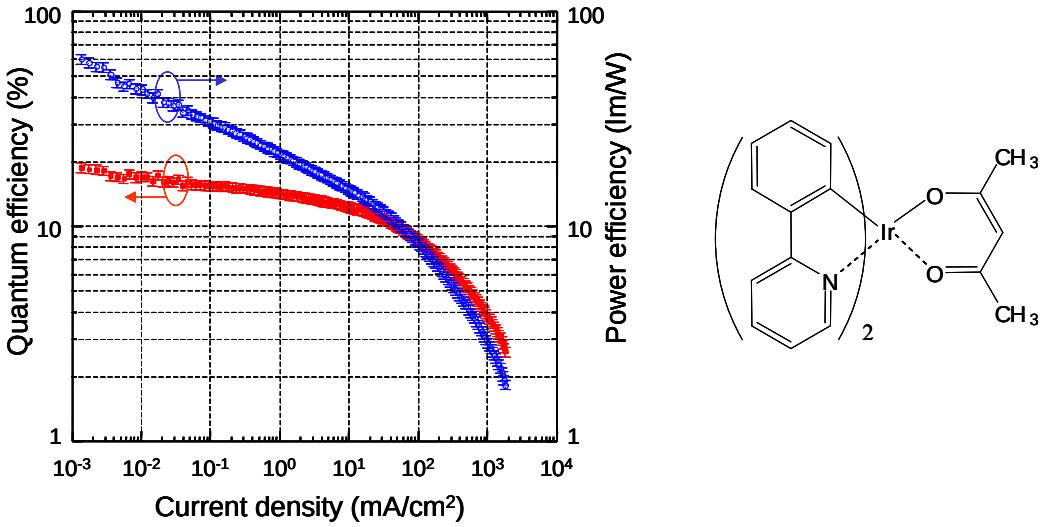

Figure 1-3. Baldo and Adachi's OLED is comprised of phosphorescent emitter, (ppy)2Ir (acac). For strong spin orbit coupling, the intersystem crossing and internal conversion rates are extremely fast. Thus, emission occurs predominantly from the lowest energy triplet state. Since the singlet / triplet forming ratio is 25%/ 75%, the OLED can theoretically harvest both singlet and triplet energies to show 100% internal quantum efficiency.

The device architecture for the green phosphor ppy2Ir(acac) employs the electron transport material 3-phenyl-4-(1'-naphthyl)-5-phenyl- 1,2,4-triazole as a host. The device exhibits an extremely high quantum efficiency of (19.0 ± 1.0)%. For a calculated output coupling efficiency of η_p=(22 ± 2)%, we obtain an internal efficiency of η_{int}=(87±1)%. The power efficiency peaks at (60±5) lm/W.

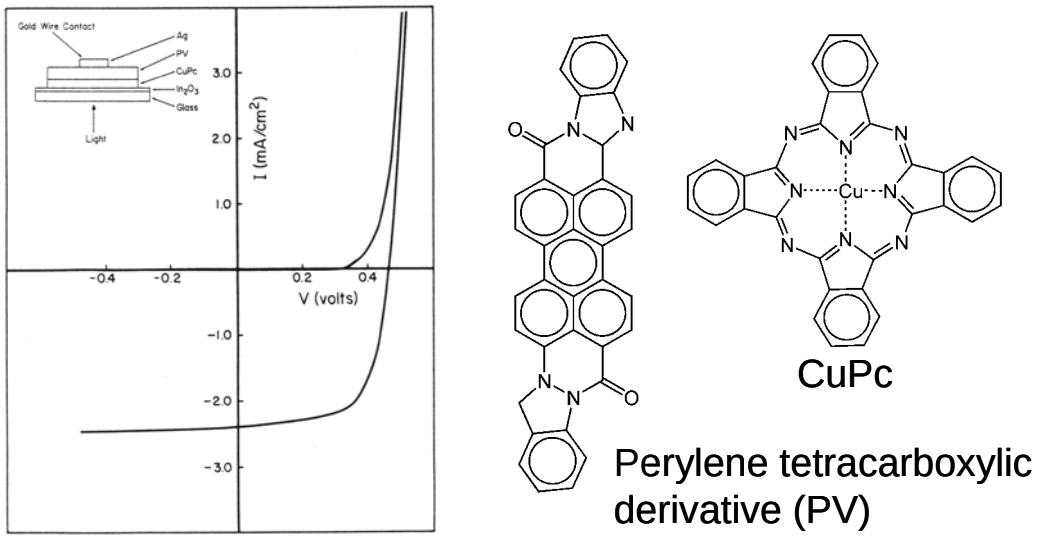

Figure 1-4. Tang's photovoltaic cell is built on a glass substrate coated with transparent indium tin oxide. Thermal evaporation in vacuum was used to deposit 250Å of copper phthalocyanine (CuPc) and then 450Å of a perylene tetracarboxylic derivative. A thin layer of Ag was used as the top contact. Light is absorbed in both the organic layers and the excitons diffuse to the organic/organic interface where they are dissociated. Holes extracted from the CuPc and electrons from the perylene tetracarboxylic derivative. Relative to photovoltaic devices made using conventional semiconductors, the very high absorption of the organic layers allows the fabrication of an extremely thin photovoltaic cell. This minimizes losses from non-radiative exciton recombination and reduces the ohmic losses, maximizing the fill-factor. Tang's CuPc/perylene tetracarboxylic solar cell remained the benchmark in the organic solar cell community for over ten years. After Tang (1986).

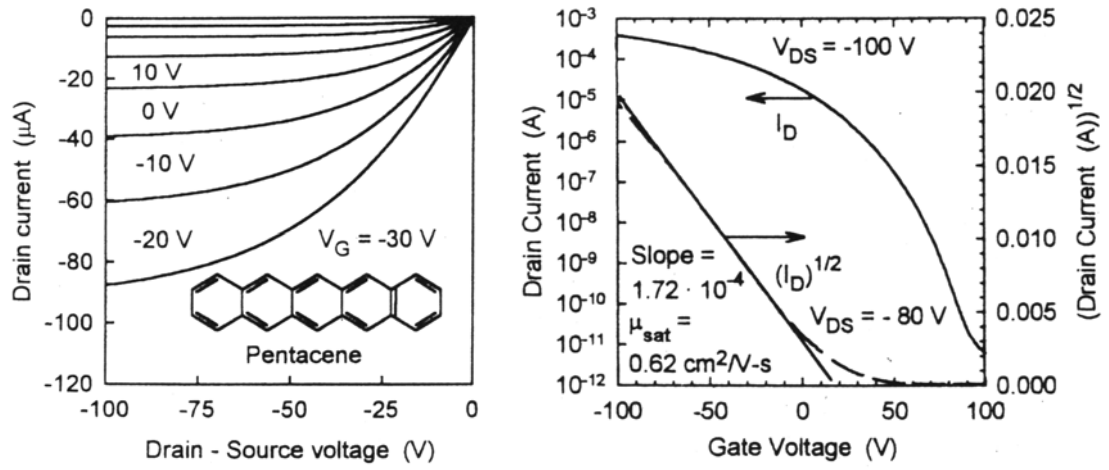

Figure1-5. On the left is the drain current (I_D) versus the drain to source voltage in a pentacene thin film transistor with a gate length and width of 20 μm and 220 μm, respectively, and a 400 nm gate dielectric thickness. The pentacene layer has an average thickness of 50 nm. Shown on the right are the $I_D^{1/2}$ versus gate voltage and log(I_D) versus gate voltage characteristics for the pentacene thin film transistor on the left. The field-effect mobility in the saturation region is greater than 0.62 cm^2/Vs with V_{DS} biased at –80 V. The thin film transistor on/off current ratio is greater than 10^8 and the subthreshold slope is 1.72 x 10^{-4}. From Gundlach *et al.* (1997).

1.3 Structure of OLEDs

An OLED directs electrical energy to the excitation of organic molecules; electrons are injected from a cathode, holes from an anode, and under the influence of an electric field the carriers hop toward one another. If both charges arrive on a single molecule, a molecular excited state may be formed. The binding energy of the state is significant (~ 1 eV) due to Coulomb interactions between such closely spaced carriers. Consequently, a molecular excited state is not readily dissociated and its properties are conserved as it diffuses between molecules, allowing it to be treated as a particle. These states are known as ‘excitons’.

The quantum efficiency of an OLED may be reduced if electrons or holes can leak all the way through the organic layers without combining with an opposite carrier and forming an exciton. But organic materials frequently possess different charge carrier

mobilities for electrons and holes; thus, as shown by Tang and VanSlyke,[1] an effective means to prevent carrier leakage is to use multiple layers with different transport characteristics in an organic heterostructure. For example, the structure in Fig. 1-6, uses an electron transport material to block the leakage of holes to the cathode, and a hole transport layer to block the leakage of electrons to the anode. Excitons are formed where the charges pile up at the organic interface. This structure has the additional advantage of forming the excitons away from the conductive contacts, which can accelerate the non-radiative decay of neighboring excitons, increasing losses. A variety of host materials are shown in Fig. 1-7.

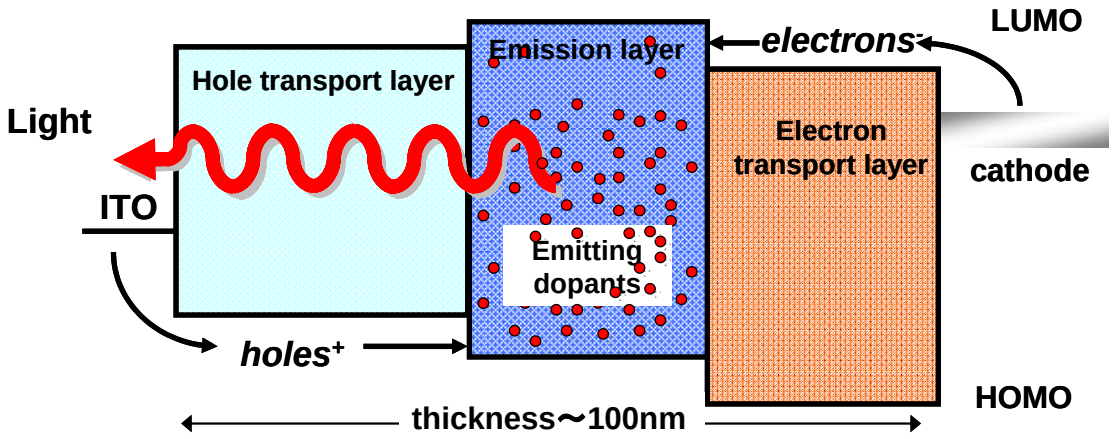

Figuer 1-6. A typical heterostructure OLED: carriers are confined at the organic interface by the applied electric field, and poor transport of the opposite carrier in the electron and hole transport layers. Guest molecules are added to the transport layers to capture excitons formed at the interface. These molecules may be chosen for their color and efficient luminescent properties, allowing flexibility in the emission characteristics of the OLED.

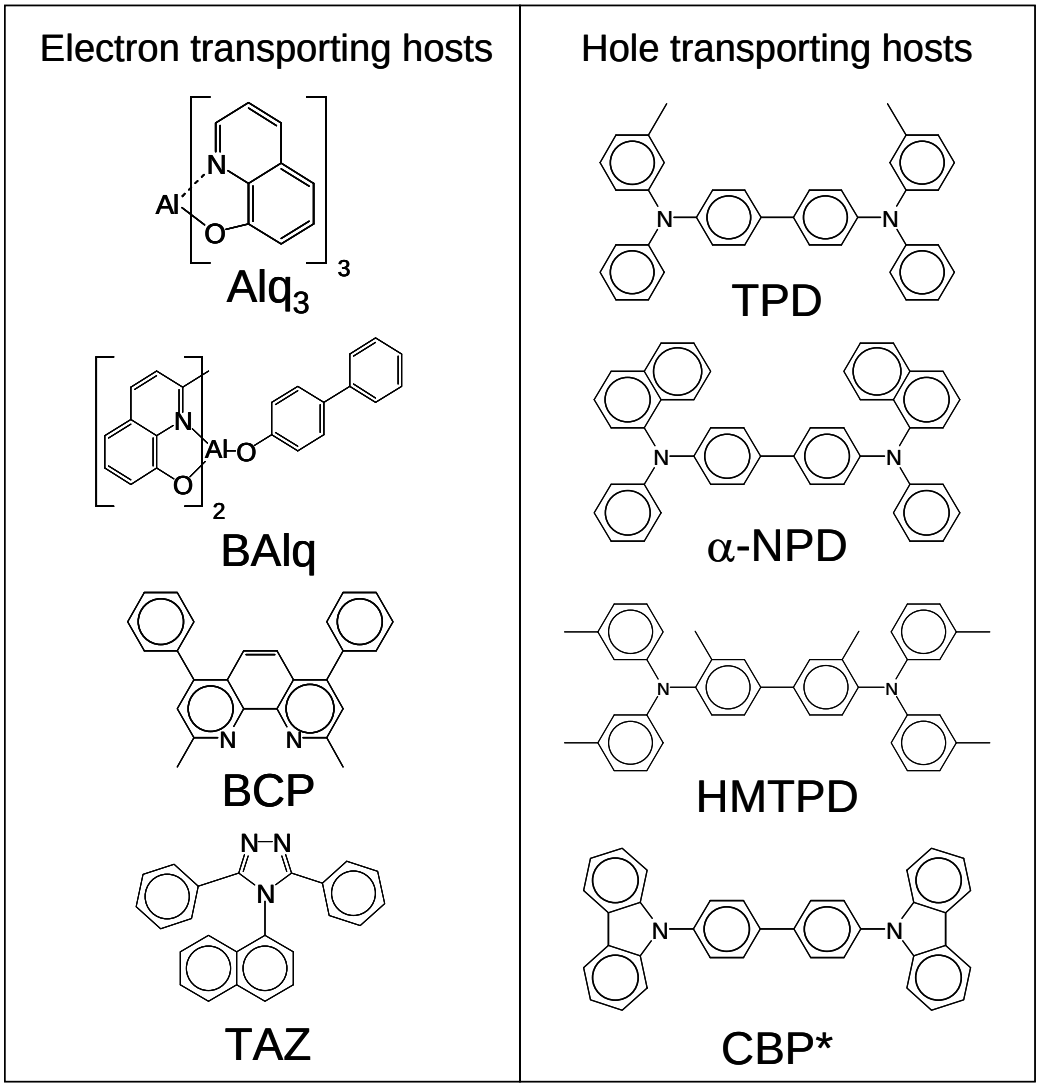

Figure 1-7. A selection of the host materials used in conjunction with phosphorescent dyes. CBP is highlighted because it may also transport electrons.

Additional flexibility in the emissive properties of the OLED may be gained by adding a small quantity of a guest molecule to the transport layers in the exciton formation region.[6] Highly luminescent materials can be chosen to capture excitons formed at the interface.[7] However, not all excitons can efficiently decay and emit light. The ground state of most molecules has a total spin, S = 0, and because the emission of a photon conserves spin, typically only S = 0 excited states can emit light in a fast and efficient process known as fluorescence. The probability of luminescence from the

remaining S = 1 excited states is generally so low that almost all their energy is lost to non-radiative processes. Because the ratio of S = 0 to S = 1 states is 1:3, they are known as singlet and triplet excitons, respectively. We define the fraction of emissive excitons as χ; in a fluorescent OLED the restriction to singlet excited states gives $\chi = 25\%$.

The other major limitations to the quantum efficiency of OLEDs are the probability of carrier recombination γ,and the output coupling fraction η_X, and the photoluminescent efficiency of the emissive material, ϕ_{PL}. The photoluminescent efficiency of a molecule under optical excitation is defined as the number of emitted photons per absorbed photon. Since the absorption of triplet excitons is typically very weak, ϕ_{PL} is generally a measurement of the efficiency of the re-radiation of absorbed singlet excitons. It can be optimized by chemical design of the emissive material, and is frequently close to 100%. For example, the addition of non-π-conjugated spacer groups to luminescent molecules can reduce intermolecular overlap, restraining dimer formation and the transport of excitons to defect sites. The output coupling fraction is limited by absorption losses and guiding of electroluminescence within the device and its substrate. A variety of techniques have been employed to increase the output coupling fraction, notably: roughening the substrate to increase scattering, and reduce guiding [7]; etching trenches in the substrate to reflect guided light in the viewing direction; [8] use of a low index substrate; and the use of transparent contacts to reduce absorption losses.[9]

In summary, the quantum efficiency of an OLED is may be expressed as:

$$\eta_Q = \chi \eta_X \phi_{PL} \gamma$$

where χ is the fraction of emissive excitons, η_X is the output coupling fraction, and ϕPL is the photoluminescent efficiency of the emissive molecule; see Fig. 1-8.

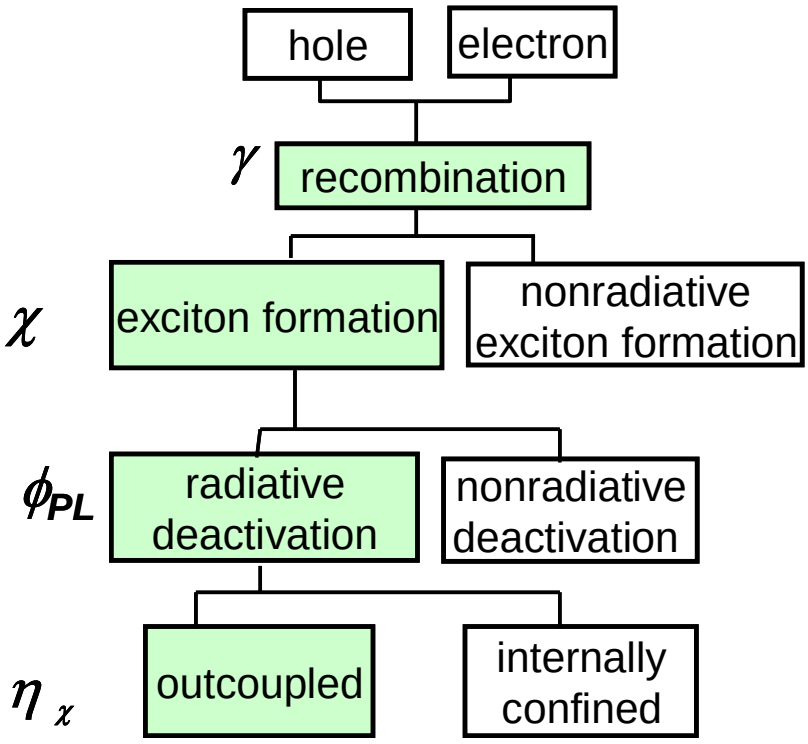

Figure 1-8. The basic mechanism of the OLED emission

1.4 Characteristics of OLEDs

OLED is the device that is on the cusp of widespread use. Research over the last two decades has paved the way for the implementation of efficient blue, green and red OLEDs in passive and active matrix displays. Low-information-content OLED displays first fabricated by Pioneer, followed by TDK, Philips, Nippon Seiki, RiTdisplay, LG electronics, Univision Technology, and Samsung SDI have already been commercialized. In October 1999, Sanyo and Eastman Kodak Co. prototyped a full-color higher-resolution OLED display with a TFT backplane, and they have since begun manufacturing higher-resolution OLED display products. The author has been involved in the development of OLEDs ranging from research from production as a member of Sanyo. The market size of OLEDs is rapidly expanding at a growth rate of 45 % in 2006, amounting to $ 9 million dollars.

There are several outstanding features for the interest in OLEDs for displays: emissive pixels, flexibility, weight, thickness, microsecond response times, and efficiency. A display with emissive pixels has a large (~180°) viewing angle along the horizontal axis, which is a figure of merit for liquid crystal displays (LCDs) as shown Fig. 1-9. However, the viewing angle of an emissive display is better described by a solid angle of 2π, since emissive pixels have lambertian patterns (constant luminance over all viewing angles in the forward direction).

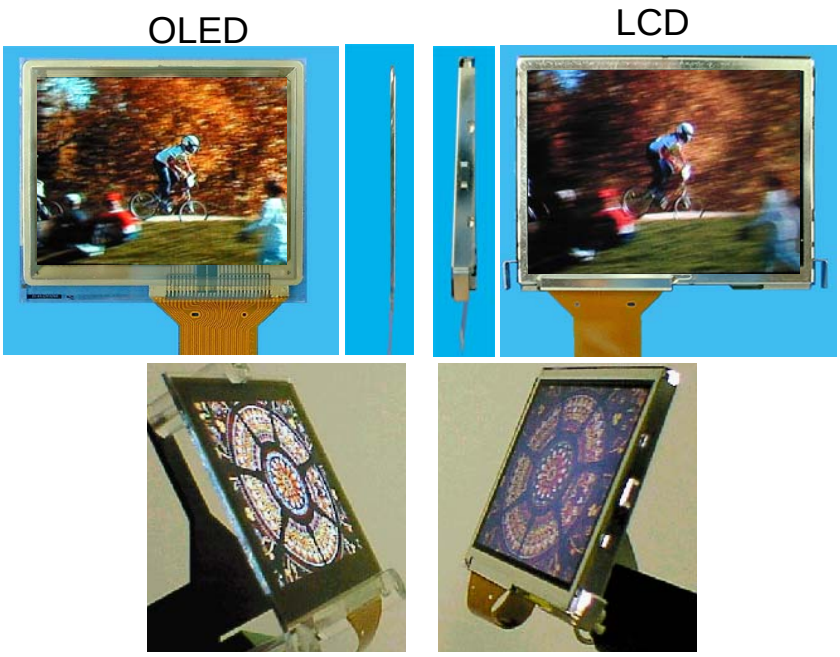

Figure 1-9. Top: The motion image in an OLED (Left) and an LED (Right). Comparison of thickness (middle). Bottom: Comparison of viewing angle.

Since OLEDs are comprised of organic thin films, they consequently have advantageous thickness, weight, and flexibility properties. The average OLED thickness is about 100 nm, so display thickness and weight are limited by the substrates. Paper thin, flexible displays grown on plastic substrates have been demonstrated by Universal Display Corporation, and these displays can only be a fraction of a millimeter thick. Another benefit of using these materials in displays is the short response times of OLEDs. The radiative lifetimes of OLED materials are in the range of a couple nanoseconds for fluorescent materials to ~500 ns for electrophosphorescent materials; both are well within the range required for video applications [10].

Finally, the most significant advantage of OLED technology is its high internal quantum efficiency, which approaches 100% [4] when electrophosphorescent dopants are employed. In contrast, the efficiency of an LCD is severely limited by the use of color filters, and one can estimate that two thirds of the available optical power is lost

since white light from fluorescent backlights must be filtered to provide the blue, green and red pixels required for color displays. Figure 1-10 shows the timeline of the increases in power efficiency that have been made in both organic and an inorganic LEDs. We note that WOLED efficiencies have improved by over an order of magnitude within a decade. The fact pronouncedly indicates that the potential of organic electronics.

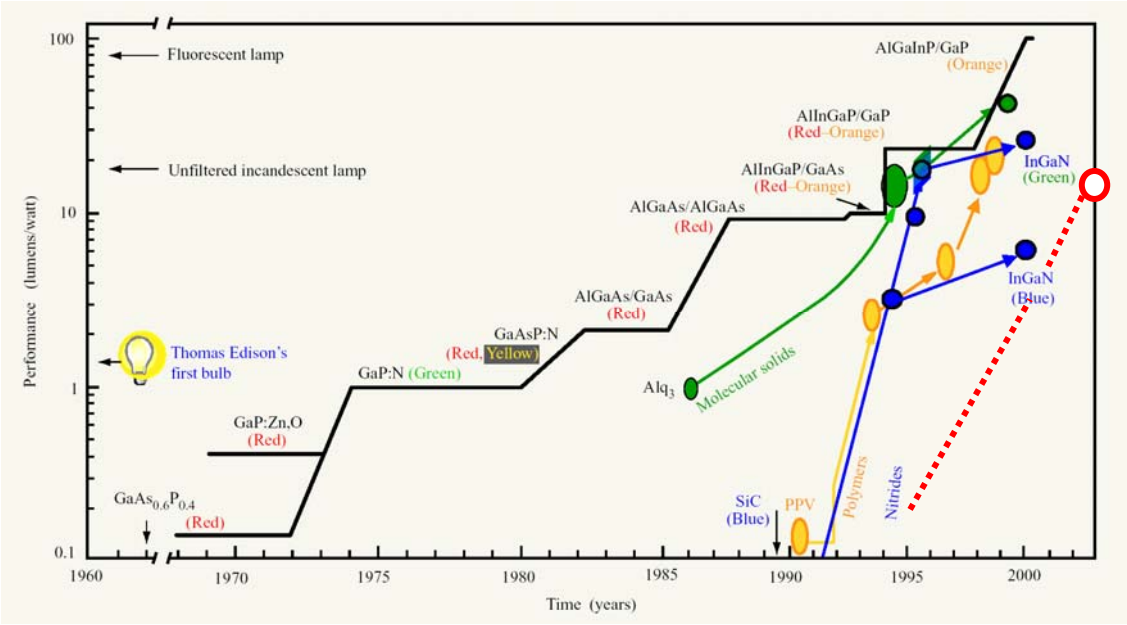

Figure 1-10 Timeline of the increase in light emitting diode efficiency adapted from Sheats *et al.* [11]. The red line and circle shows the increase for WOLEDs.

1.5 Application to displays

OLEDs have emerged as one of the most promising technologies for inclusion in flat-panel displays since they have various advantageous features for high display quality such as light-weight, wide-viewing angle, bright self-emission and rapid response. In early 2003, active-matrix full color OLED displays using small molecule materials have reached mass-production. However the performance needs to be improved in power efficiency, lifetime and high color purity, which is indispensable in order to replace LCDs. If the remained challenges are solved, OLEDs will gain a significant portion of the display market in the next two decades given the state of the art in displays shown in Fig. 1-11. While research continues to satisfy the needs of display manufacturers, interest in the application of white OLED (WOLED) technology for full-color diaplay applications is increasing.

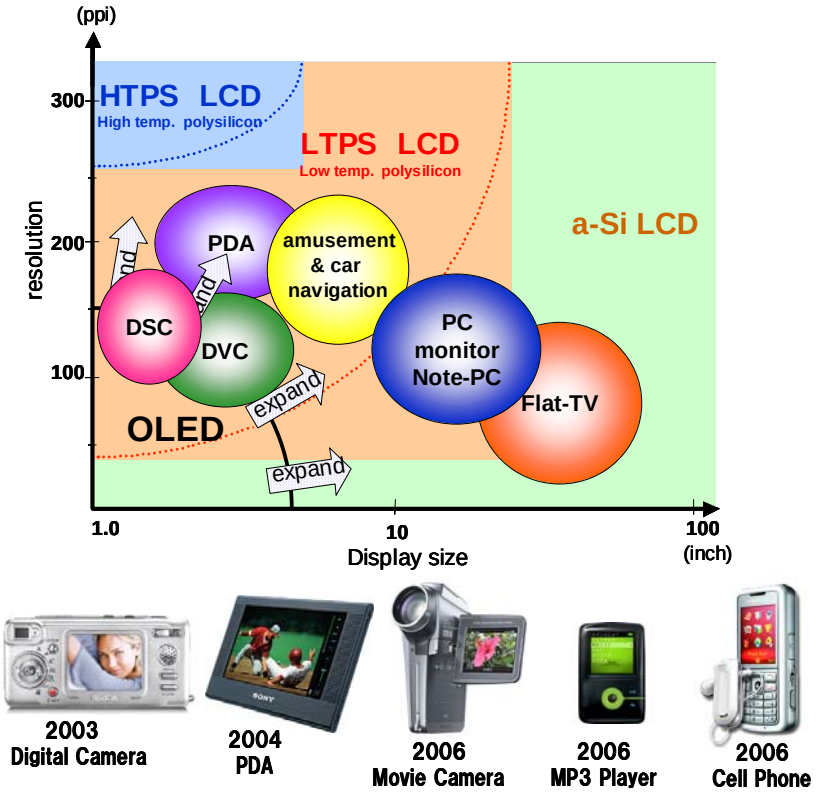

Figure 1-11. Top: Position of OLEDs in terms of display size and resolution. Bottom: Electronic appliances with full-color OLEDs.

From a practical viewpoint, the most attracting target of applications for OLEDs is small-sized full-color displays, which enjoys a huge market size over 30 billion dollars. At present, full-color OLEDs are in the middle of penetration in the market of small-size (<3 inch) displays, which are mounted in battery-powered portable electronic devices, such as a cell phone, a video recorder, a digital camera, and an MP3 player. The full-color OLED displays, however, have not been able to get a dominating position in the display industry. The most significant problem for full-color OLEDs is the high power consumption compared to the same-sized LCDs. For instance, the power consumptions of 2-inch-sized OLED and LCD are 350 mW and 250 mW excluding those of driver circuits, respectively. Thus, reduction in power consumption is as a matter of first priority. As shown in Fig. 1-12, there are two major full-color methods.

The one is pixelation of RGB EMLs, which can take advantage of the OLEDs' self-emissive feature. Among a red, green and blue OLEDs, a red OLED is the least efficient. When the widely-used efficient fluorescent emitters for RGB EMLs such as DCJTB, Quinacridone [12], BCzVBi [13] are employed in a full-color display, approximately 60% of the power consumption is from the red OLED whereas the green or blue OLEDs accupy 20% of the total, respectively.

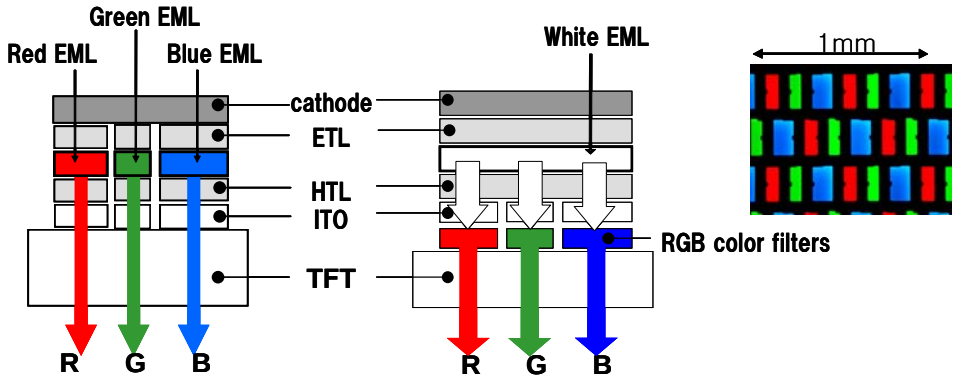

Figure 1-12. Cross-sectional structures of two different methods for full-color OLEDs.

The other full-color method, WOLED combined with color filters. In this method, the productivity can be significantly enhanced because an alignment of a presicion mask for RGB pixilation is not needed. The power consumption, however, is higher than that of a color-filter-free full-color display with pixelated RGB EMLs due to the absorption of white emission in color filters. The each color filter of red, green, and blue absorbs EL emission from a white OLED at a transmittance of roughly 30%. Consequently, a high-efficency white OLED is essential for this full-color method for compensating the energy loss by color filters.

The major challenges for promoting OLEDs to the dominating position in the full-color display market are, as mentioned above, lowering the power consumption. For that aim, the most important issues are to improve efficiencies for red OLEDs and white OLEDs.

1.6 Red OLED reviewed

Red light emitting materials are the key substance for red OLEDs since generated excion energy is transferred to an emiting material for generating red emission. The light-emitting materials can be in two possible forms, either as the emitter itself (host-emitter) or as the dopant incorporated into an appropiate host. The latter efficiently utilizes the Förster resonance energy transfer from the host. The most frequently used material is the green fluorescent material tris(8-hydroxyquinoline)aluminum (Alq). Numerous fluorescent materials, either as host-emitters or dopants, have been known (see Fig. 1-13) and developed since reports from Kodak on green OLED in 1987 and the dopant-based green and red OLEDs in 1989 [1, 6]. Whereas short wavelength light-emitting blue or green fluorescent materials are commonly used as either host-emitter or dopant, red fluorescent materials are less flexible and mostly limited to the dopant usage in the fabrication of red OLEDs. This is due to the nature of red fluorescent materials.

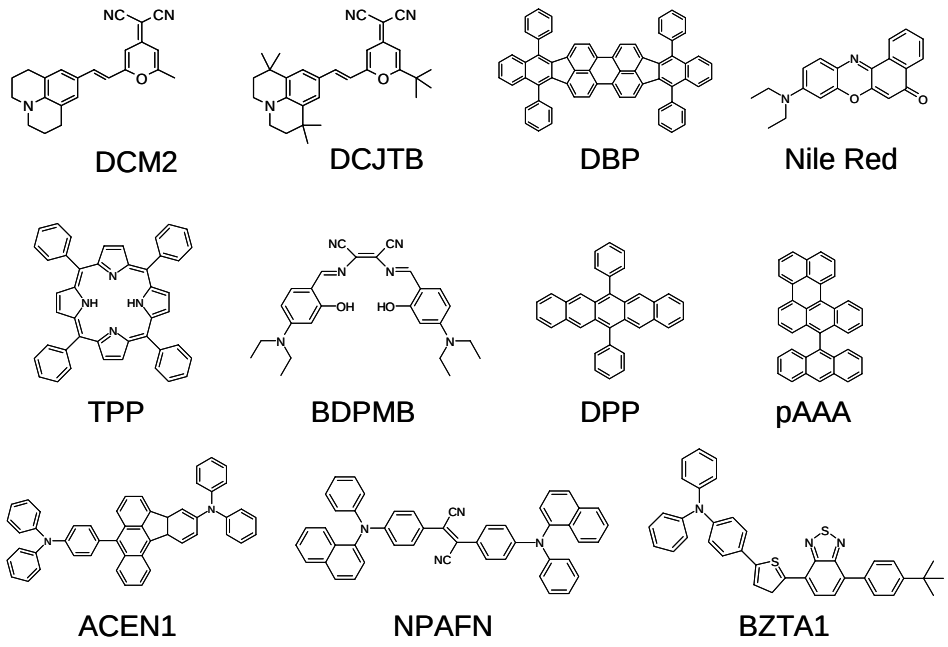

Figure 1-13. Chemical structures of typical red fluorescent emitters.

Fluorophores emitting long enough wavelength (emission maximum wavelength $_{max}$ > 610 nm) are usually polar, such as electron-donor-substituted pyran-containing compounds, or nonpolar but extensively -conjugated, such as polycyclic aromatic

hydrocarbon (PAH) or porphyrin-type macrocyclic compounds. Red emitters used in OLEDs include materials that are highly emissive in solution, such as Nile Red (9-diethylamino-5H-benzo[alpha]phenoxazine-5-one), DCM (4-(dicyanomethylene)-2-methyl-6-[4-(dimethylaminostyryl)-4*H*-pyran])[6], and those more weakly emissive, such as TPP (5,10,15,20-teraphenylporphyrin) [14, 15]. However, all these red fluorophores are prone to aggregation in solid state, due to either attractive dipole-dipole interactions or effective intermolecular π-stacking. Therefore, they are highly susceptible to concentration quenching and become either weakly emissive or even not emissive at all in solid state. Consequently, the guest-host doped emitter system becomes a common method for solving the problem of these red emissive materials when applied for OLEDs. Dopant molecules are dispersed and isolated in the host materials and thus concentration quenching can be avoided. However, the optimum dopant concentration is usually low, commonly no greater than 2%, and the effective doping range is extremely narrow and commonly no greater than ±0.5% of the optimum concentration. Realistically, OLEDs based on dopant are more difficult to adapt for mass production processes than those based on a nondoped host emitter, considering that reproducibility of the optimum doping level requires careful manufacturing control. From a practical standpoint, a solution to the red-light-emitting OLEDs, either in materials or devices perspective, is highly important.

Although quite a number of red fluorescent dyes have been synthesized and studied, DCM-type dyes, particularly DCJTB are still most efficient materials amoung them. Other types of red fluorescent dopants are also reported, though the efficiencies of them cannot reach those of DCM-type dyes. TPP, BDPMB [16], DPP [17, 18],and pAAA [19] exhibit fairly good performance amoung them. Various derivatives based on those dyes are reported as well [20-31]. Red OLEDs based on DPP and pAAA show unchanged EL efficiency over a wide range of current densities-as high as several hundred mA/cm^2 although the EL efficiency of most red OLEDs starts to decay at elevated current densities or driving voltages, regardless of whether EL originates from fluorescence or phosphorescence. As far as chemical structure, unlike most other red fluorophores containing heteroatoms, often nitrogen and oxygen, these two fluorophores are classical PAH-type compounds that have only carbon and hydrogen as the

composing elements. Unfortunately, even though they have impressive efficiency stability, red OLEDs containing PAH-type red dopant do not meet the requirement of EL intensity (either maximum or at low current density) and efficiency.

The first reported host-emitting nondoped red OLED was by Toguchi et al of NEC [32]. From a practical viewpoint, dopant-free OLEDs are very attractive since the presice control of dopant concentration is not needed. Several host-emitting materials, such as ACEN1[33], NPAFN[34], and BZTA1[35], are proposed. But the efficiencies are not high enough (see Table 1-1).

Phosphorescent red emitters were first proposed for OLEDs by M. E. Thompson. As shown in Fig. 1-14, PQIr(acac), BTPIr(acac), Ir_4F_5Mpiq, $Ir(piq)_3$[36-41] are widely used phosphorescent red emitters. The theoretical limit of IQE for the electrophosphorescence is 100%, harvesting both singlets and triplets, which is 4-fold increase compared to the conventional electroluminescence by fluorescence. Actually, the red electrophosphorescence from Ir_4F_5Mpiq has exhibited the peak external quantum efficiency (EQE) of 15% and power efficiency of 18 lm/W, which are the highest values for red OLEDs so far.

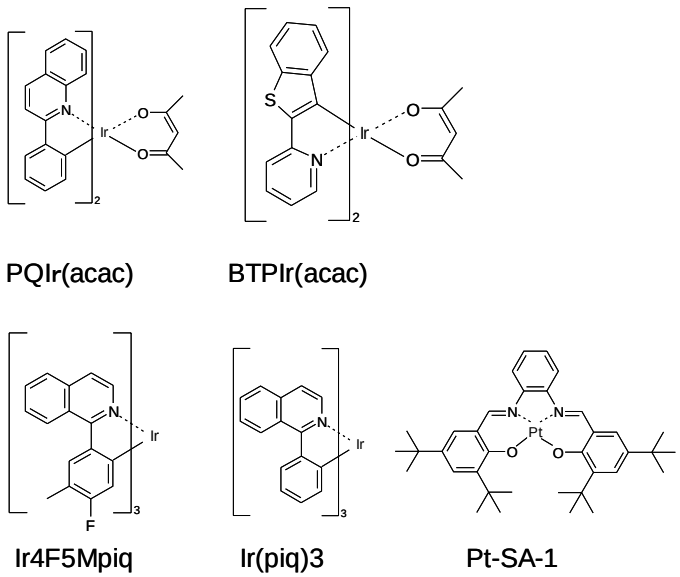

Figure 1-14. Chemical structures of typical phosphorescent emitters with a hevy metal.

One of the largest drawbacks, however, lays in the severe roll-off of the EQE at high currents due to triplet-triplet annihilation (ref. Chap.2). Comparison of the power efficiencies between electrophosphorescence and electrofluorescence reveals that at the operation currents for full-color displays, e.g. 20-100 mA/cm^2, the red OLEDs based on a fluorescent emitter still shows higher EQEs or power efficiencies. Moreover, CBP (see Fig. 1-17) and phosphorescence emitters are not robust enough to meet the requirement for the lifetime of displays primarily due to the unstabillity of a carbazole group and coordination bond to heavy atm such as Ir and Pt especially at an elevated temperature. Those challenges should be overcome to replace fluorescent materials in OLEDs products.

Table 1-1. Performance of the red OLEDs with a various fluorescent red emitter.

red emitter	λ_{max} (nm)	η_{ext} (%)[a]	η (cd/A)[b]	η_p (lm/W)[c]	CIE[d]	Refs.
DCJTB with rubrene	632	3.4	4.3	1.9	0.64, 0.36	chap.3
DBP	613	4.7	5.4	5.3	0.66, 0.34	chap.3
DCM2	650	-	-	0.011	0.64, 0.36	7
DCJTB	620	-	1.89	0.65	0.63, 0.37	42
TPP	655	0.07	-	-	0.70, 0.28	14
BDPMB	640	-	1.34	-	0.67, 0.33	16
DPP	625	-	1.2	0.33	0.63, 0.34	17
pAAA	616	-	0.6	-	0.63, 0.36	19
NPAFN : host-emitting:	636	2.4	2.5	1.7	0.64, 0.33	33
ACEN1 : host-emitting:	624	0.46	0.5	0.26	0.64, 0.34	34
BZTA1 : host-emitting:	626	0.99	0.91	0.58	0.63, 0.35	35

[a] Maximum reported external quantum efficiency.

[b] Maximum reported current efficiency.

[c] Maximum reported power efficiency.

[d] Commission Internationale de l'Eclairage coordinates at 100 cd/m^2.

1.7 White OLED reviewed

WOLEDs are of interest because they offer low-cost alternatives for backlights in flat-panel displays (see Fig. 1-15), and may also eventually provide tremendous cost savings for general lighting purposes. Lighting consumes ~765 TWh of electricity a year in the United States, or nearly 30% of all electricity produced for buildings, which corresponds to 18% of total building energy consumption. In terms of total primary energy consumption, lighting accounts for 8.3% of all the energy used in the United States, or about 22% of all the electricity produced. The cost for consumers to light their homes, offices, streets, and factories amounts to almost $58 billion a year [43].

Figure 1-15. Left: SANYO 15" active-matrix full-color display with white OLEDs and color filters demonstrated at CEATEC in October 2002. Right: OLED light demonstrated by Koizumi in 2003

Given these figures, it is easy to see that doubling the efficiency of lighting will bring tremendous savings. Also, if one considers that inefficient incandescent lamps, which were developed over 100 years ago, still accounts for 42% of the electrical energy consumed, one immediately realizes that emerging WOLED technology can satisfy a growing demand for high-quality efficient lighting.

The pace of research in the search for new white light sources has recently seen a marked increase (see Table 1-2) in response to the need for more efficient and

environmentally friendly solutions to the impending energy shortage. One particularly attractive means for producing energy efficient lighting is the use of OLEDs which operate at very low voltages (~5V) and with high luminance efficiency. If one compares the power efficiency of a typical incandescent light bulb at 12-17 lm/W to those of OLEDs made in the laboratory at 30-60 lm/W, one can quickly see that there is at least a factor of two to be gained by using OLEDs. This efficiency improvement can provide a significant savings if one considers the figures presented in Sec. 1.2.

Among methods for producing white light, electrophosphorescence stands out as the most effective mechanism for OLED emission due to its demonstrated potential for achieving 100% internal emission efficiency [4, Fig.1-3]. While electrophosphorescence, typically achieved by doping an organometallic phosphor into a conductive host, has been successfully used to generate the primary colors necessary for display applications, efficient generation of the broad spectral emission required of a white light source has remained elusive.

As Newton correctly discerned over 300 years ago, white light is comprised of several colors and spans the electromagnetic spectrum between 380 nm to 770 nm. The challenges facing WOLED technology is due, in large part, to the fact that fluorescence or phosphorescence emission from typical organic materials only spans about one-third of the visible range. Color tuning molecules to emit in the blue, green or red portion of the visible spectrum is easily achieved and can be accomplished with a variety of molecular structures and their derivatives [44, 45]; however, a single molecule has not been designed that efficiently emits over the entire visible spectrum. For white light illumination, a combination of three colors (blue, green and red) from at least two different dyes is therefore needed to produce white light; hence, WOLEDs have complex structures that incorporate more dopants than typical OLEDs.

One interesting approach which is discussed in Chapters 4, is to use the emission from fluorophore and phosphor, which can have 100% internal quantum efficiency and reduce triplet-triplet annihilation and energy loss from inter section crossing (ISC).

WOLED designers are probably the most creative group of researchers in the field of OLEDs. There are numerous solutions to the end product, which is an efficient high quality white light source with Commission Internationale de l'Eclairage (CIE)

coordinates similar to that of a blackbody radiator with a correlated color temperature between 2500 K and 6000 K, and a color rendering index (CRI, see Chapt. 2) above 80. Here, I highlight WOLEDs with noteworthy characteristics, over the last ten years.

One particularly sophisticated WOLED structure is shown in Fig. 1-16 [46]. Typically several emissive dyes are mixed in organic material sandwiched between two metal electrodes. The EML in the device in Fig. 1-16 has the three blue, green, and red dyes. This used to be possibly the most efficient WOLED before the WOLED reported.

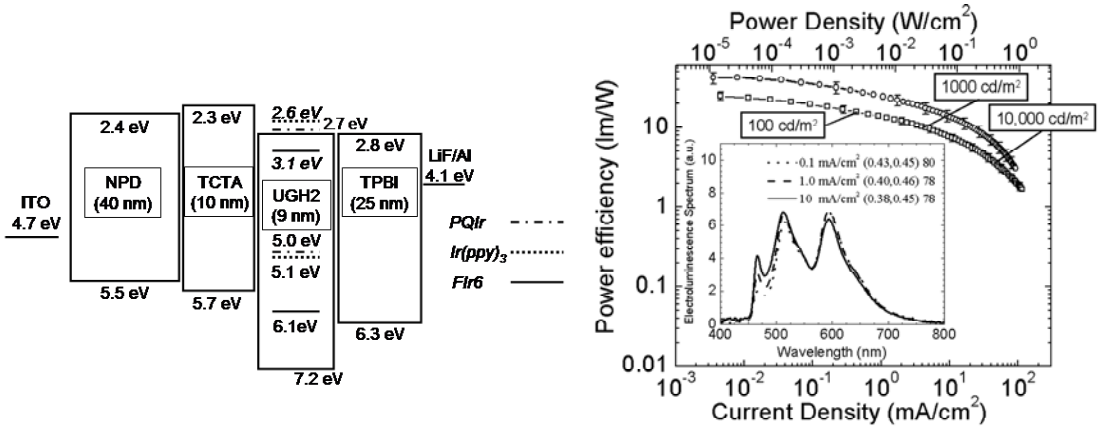

Figure 1-16. Left: Proposed energy level diagram of WOLED constituents showing their highest occupied and lowest unoccupied molecular orbital energies relative to vacuum. Right: Lighting (circle) and display relevant (square) power efficiencies versus current and power density. The WOLEDs have a maximum total power efficiency of η_t = 42 lm/W. Inset: Normalized electroluminescence spectra of WOLED emission at various current densities.[46].

The EQE and power efficiencies, CIE and CRI of noteworthy WOLEDs are listed in Table 1-2. A timeline of the increase in WOLED efficiency is given in Fig. 1-17.

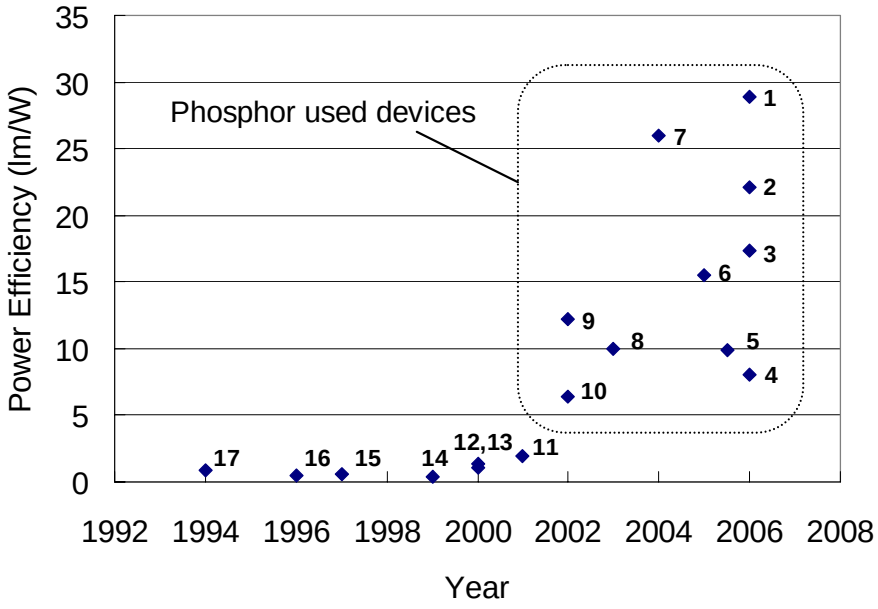

Figure 1-17. Improve in power efficiency of WOLEDs over the last ten years. Labeled points correspond to references in Table 1-2. There is a distinct improvement when electrophosphorescent dopants were introduced into WOLEDs.

Table 1-2. Selected WOLED architectures with their corresponding performance characteristics. Where the color rendering index (CRI) is not reported, a maximum value is estimated from spectral data.

No.	Architecture	η_{ext} (%)[a]	η_p (lm/W)[b]	CIE[c]	CRI	Refs.	year
1	Phosphor doped EMLs with double stacked structure	24.7	28.9	(0.39,0.45)	64	Chapt. 4	2006
2	Phosphor and fluorophore doped separate EMLs.	11	22.1	(0.38,0.40)	83	Chapt. 4	2006
3	Phosphor and fluorophore doped separate EMLs (after the work 2)	-	17.4	(0.47, 0.42)	85	47	2006
4	Phosphor sensitized EML	-	8	(0.33,0.35)	≤70	48	2006
5	Multi-emissive phosphor doped layers.	-	9.9	(0.43, 0.44)	82	49	2006
6	Double Phosphor-doped EMLs	13.5	15.5	(0.42,0.39)		Chapt. 5	2005
7	Triple doped phoshporescent emissive layer.	12	26	(0.43,0.45)	80	46	2004
8	Multilayer phosphorescent.	12	10	(0.35,0.36)	≤60	50	2003
9	Phosphorescent excimer.	6.4	12.2	(0.36,0.44)	67	51	2002
10	Multi-emissive phosphor doped layers.	5.2	6.4	(0.37,0.40)	83	52	2002
11	Two doped and one neat EMLs.	-	1.93	(0.35,0.34)	≤80	53	2001
12	Doped blocking layers.	-	1.39	-	-	54	2000
13	Multiple quantum wells.	-	1.1	(0.32,0.38)	≤80	55	2000
14	Interlayer sequential energy transfer.	0.5	0.35	(0.33,0.33)	≤70	56	1999
15	Hybrid polymer/inorganic.	1.9	0.63	(0.34,0.29)	≤70	57	1997
16	Three neat EMLs.	0.7	0.5	(0.31,0.41)	≤80	58	1996
17	Triple doped polymer with vacuum deposited transport	-	0.83	-	-	59	1994

[a] Maximum reported external quantum efficiency.

[b] Maximum reported external power efficiency.

[c] Commission Internationale de l'Eclairage coordinates at 100 cd/m^2.

1.8 Thesis Outline

The field of OLEDs branches into two divisions: polymer and small molecule. Each has advantages and disadvantages [60-62]; however, this thesis endeavors to enlighten its reader on the small molecule OLEDs. Chapter 2 will explain the relevant physics of organic electronic transitions and the terms used to characterize OLEDs. Chapter 3 will describe the high-efficiency red OLEDs. The high-efficiency white OLEDs are discussed in Chapter 4. Chapter 5 discusses the applications of the OLEDs described Chapter 3 and 4. This thesis concludes with an outlook for OLED technology in Chapter 6.

Chapter 1. References

[1] C. W. Tang and S. A VanSlyke, Appl. Phys. Lett. 51, 913 (1987).

[2] C. W. Tang, Appl. Phys. Lett. 48, 183 (1985).

[3] P. S.Vincett, W. A. Barlow, R. A. Hann, and G. G. Roberts, Thin Solid Films 94, 171 (1982).

[4] C. Adachi, M. A. Baldo, M. E. Thompson and S. R. Forrest, J. Appl. Phys. 90, 5048 (2001)

[5] D. J. Gundlach, Y. Y. Lin, T. N. Jackson, S. F. Nelson, and D. G. Schlom, IEEE Elect. Dev. Lett. 18, 87 (1997).

[6] C. W. Tang, S. A. VanSlyke, C. H. Chen, Appl. Phys. Lett. 65, 3610 (1989).

[7] V. Bulovic, A. Shoustikov, M. A. Baldo, E. Bose, V. G. Kozlov, M. E. Thompson, and S. R. Forrest, Chem. Phys. Lett. 287, 455 (1998).

[8] T.Yamasaki, K. Sumioka, and T. Tsutsui, Appl. Phys. Lett. 76, 1243 (2000).

[9] G. Parthasarathy, P. E. Burrows, V. Khalfin, V. G. Kozlov, and S. R. Forrest, Appl. Phys. Lett. 72, 2138 (1998).

[10] N. Karl, K.-H. Kraft, J. Marktanner, M. Muench, F. Schatz, R. Stehle, and H.-M. Uhde, J. Vac. Sci. and Tech. A 17, 2318 (1999).

[11] D. M. Burland, and U. Konzelmann, J. Chem. Phys. 67, 319 (1977).

[12] G. E. Jabbour, Y. Kawabe, S. E. Shaheen, J. F. Wang, M. M. Morrell, B. Kippelen, and N. Peyghambarian, Appl. Phys. Lett. 71, 1762 (1997)

[13] C. Hosokawa, H. Higashi, H. Nakamura, and T. Kusumoto, Appl. Phys. Lett. 67, 3853 (1995).

[14] P. E. Burrows, S. R. Forrest, S. P.Silbey, and M. E. Thompson, Appl. Phys. Lett. 69, 2959 (1996).

[15] Z. Shen, P. E. Burrows, V. Bulovic, S. R. Forrest, and M. E. Thompson, Science 276, 2009 (1997).

[16] P. Wang, Z. Hong, Z. Xie, S. Tong, O. Wong, C.-S. Lee, N. Wong, L. Hung, and S. Lee, Chem. Commun., 1664 (2003)

[17] L. C. Picciolo, H. Murata, and Z. H. Kafafi, Appl. Phys. Lett. 78, 2378 (2001).

[18] H. Murata, and Z. H. Kafafi, Proc. SPIE - Int. Soc. Opt. Eng., 4105, 474 (2001).

[19] B. X. Mi, Z. Q. Gao, M. W. Liu, K. Y. Chan, H. L. Kwong, N. B. Wong, C. S. Lee, L. S. Hung, and S. T. Lee, J. Mater. Chem. 12, 1307 (2002).

[20] B.Chen, X. Lin, L. Cheng, C.-S. Lee. W. A. Gambling, S.-T. Lee, J. Phys. D: Appl. Phys., 23, 30 (2001).

[21] M. Mitsuya, T. Suzuki, T. Koyama, H. Shirai, Y. Taniguchi, M. Satsuki, and S. Suga, Appl. Phys. Lett. 77, 3272 (2000).

[22] X. H. Zhang, B. J. Chen, X. Q. Lin, O. Y. Wong, C. S. Lee, H. L. Kwong, S. T. Lee, S. K. Wu, Chem. Mater. 13, 1565 (2001).

[23] B.-J. Jung, C.-B. Yoon, H.-K. Shim, L.-M. Do, and T. Zyung, Adv. Funct. Mater. 11, 430 (2001).

[24] C.-Q. Ma, Z. Liang, X.-S. Wang, B.-W. Zhang, Y. Cao, L.-D. Wang, and Y. Qiu, Synth. Met., 138, 537 (2003).

[25] X. T. Tao, S. Miyata, H. Sasabe, G. J. Zhang, T. Wada, and M. H. Jiang, Appl. Phys. Lett. 78, 279 (2001).

[26] J. Li, D. Liu, Z. Hong, S. Tong, P. Wang, C. Ma, O. Lengyel, C.-S. Lee, H.-L. Kwong, and S. Lee, Chem. Mater. 15, 1486 (2003).

[27] Y. Sakakibara, S. Okutsu, T. Enokida, and T. Tani, Thin Solid Films 363, 29 (2000).

[28] Y. Sakakibara, S. Okutsu, T. Enokida, and T. Tani, Appl. Phys. Lett. 1999, 74, 2587.

[29] X. H. Zhang, Z. Y. Xie, F. P. Wu, L. L. Zhou, O. Y. Wong, C. S. Lee, H. L. Kwong, S. T. Lee, and S. K. Wu, Chem. Phys. Lett. 382, 561 (2003).

[30] J. Yu, Y. Shirota, Chem. Lett., 984 (2002).

[31] P. Wang, Z.Hong, Z. Xie, S. Tong, O. Wong, C.-S. Lee, N. Wong, L. Hung, and S. Lee, Chem. Commun., 1664 (2003).

[32] S. Toguchi, Y. Morioka, H. Ishikawa, A. Oda, and E. Hasegawa, Synth. Met. 111, 57 (2000).

[33] T.-H. Huang, J. T. Lin, Y. T. Tao, C.-H. Chuen, Chem. Mater. 15, 4584 (2003).

[34] H.-C. Yeh, S.-J. Yeh, C.-T. Chen, Chem. Commun., 2632 (2003).

[35] K. R. J. Thomas, J. T. Lin, M. Velusamy, Y.-T. Tao, C.-H. Chuen, Adv. Funct. Mater. 14, 83 (2004).

[36] C. Adachi, M. A. Baldo, S. R. Forrest, S. Lamanky, M. E. Thompson, R. C. Kwong, Appl. Phys. Lett. 78, 1622 (2001).

[37] S. Lamansky, P. Djurovich, D. Murphy, F. Abdel-Razzaq, H.-E. Lee, C. Adachi, P. E. Burrows, S. R. Forrest, and M. E. Thompson, J. Am. Chem. Soc. 123, 4304 (2001).

[38] J.-P. Duan, P.-P. Sun, C.-H. Cheng, Adv. Mater., 15, 224 (2003).

[39] Y.-J. Su, H.-L. Huang, C.-L. Li, C.-H. Chien, Y.-T. Tao, P.-T. Chou, S. Datta, and R.-S. Liu, Adv. Mater. 15, 884 (2003).

[40] A. Tsuboyama, H. Iwawaki, M. Furugori, T. Mukaide, J. Kamatani, S. Igawa, T.Moriyama, S. Miura, T. Takiguchi, S. Okada, M. Hoshino, and K. Ueno, J. Am. Chem. Soc. 125, 12971 (2003).

[41] T. Tsuzuki, Y Nakayama, T. Iwata, S. Tokito, Appl. Phys. Lett. 88, 243511 (2006).

[42] C. H. Chen, C. W. Tang, J. Shi, and K. P. Klubek, Thin Solid Films 363, 327 (2000).

[43] U.S. Lighting Market Characterization, U.S. Department of Energy, Prepared by Navigant Consulting, Inc., Washington (September 2001).

[44] J. Brooks, Y. Babayan, S. Lamansky, P. Djurovich, I. Tsyba, R. Bau and M. Thompson, Inorg. Chem. 41, 3055 (2002).

[45] S. Lamansky, P. Djurovich, D. Murphy, F. Abdel-Razzaq, H.-E. Lee, C. Adachi, P. E. Burrows, S. R. Forrest and M. E. Thompson, J. Am. Chem. Soci. 123, 4303 (2001).

[46] B. W. D'Andrade, R. J. Holmes, and S. R. Forrest, Adv. Mater. 16, 624 (2004).

[47] G. Schwartz, K. Fehse. M. Pfeiffer, K. Walzer, and K. Leo, Appl. Phys. Lett. 89, 083509 (2006)

[48] G. Cheng, Y. Zhang, Y. Zhao, S. Liu, and Y. Ma, Appl. Phys. Lett. 88, 083512 (2006).

[49] G. Cheng, Y. Zhang, Y. Zhao, Y. Lin, C. Ruan, and S. Liu, Appl. Phys. Lett., 89, 043504 (2006).

[50] S. Tokito, T. Iijima, T. Tsuzuki and F. Sato, Appl. Phys. Lett. 83, 2459 (2003).

[51] V. Adamovich, J. Brooks, A. Tamayo, A. M. Alexander, P. I. Djurovich, M. E. Thompson, C. Adachi, B. W. D'Andrade and S. R. Forrest, New J. Chem. 26, 1171 (2002).

[52] B. D'Andrade, M. E. Thompson and S. R. Forrest, Adv. Mater.14, 147 (2002).

[53] C. W. Ko and Y. T. Tao, Appl. Phys. Lett. 79, 4234 (2001).

[54] X. Y. Jiang, Z. L. Zhang, W. M. Zhao, W. Q. Zhu, B. X. Zhang and S. H. Xu, J. Phys. D-Appl. Phys. 33, 473 (2000).

[55] S. Y. Liu, J. S. Huang, Z. Y. Xie, Y. Wang and B. J. Chen, Thin Solid Films 363, 294 (2000).

[56] R. S. Deshpande, V. Bulovic and S. R. Forrest, Appl. Phys. Lett. 75, 888 (1999).

[57] F. Hide, P. Kozodoy, S. P. DenBaars and A. J. Heeger, Appl. Phys. Lett. 70, 2664 (1997).

[58] R. H. Jordan, A. Dodabalapur, M. Strukelj and T. M. Miller, Appl. Phys. Lett. 68, 1192 (1996).

[59] J. Kido, K. Hongawa, K. Okuyama and K. Nagai, Appl. Phys. Lett. 64, 815 (1994).

[60] S. Forrest, P. Burrows, and M. Thompson, IEEE Spectrum, 37, 29 (2000).

[61] Y. Preezant, Y. Roichman and N. Tessler, J. Physics-Condensed Matter, 14, 9913 (2002).

[62] S. R. Forrest, Chemical Review 97, 1793 (1997).

Chapter 2.

Electronic Transitions in Organic Materials

2.1 Lighting standards and definitions

The understanding of terminology used to describe visible light and all its attributes — brightness, hue, and color — is important to grasp and apply in this field of research. This essential information enables a researcher to decipher the plethora of quantitative characterizations of emissive devices, and to gain insight into their design and fabrication. With this in mind, a basic set of the definitions of photometric quantities is given in Sec. 2.2.A, and a description of the human eye follows in Sec. 2.2.B. Properties of sunlight, and chromaticity coordinates are described in Secs. 2.2.C and 2.2.D, respectively.

2.1.A Basic concepts

There are numerous terms that are used throughout this field. Here, I mention some of them: luminance flux, candela, luminance, brightness and lambertian.

Luminance flux, Φ, is the time rate of flow of radiant energy, usually evaluated in terms of the eye's photopic or scotopic response (c.f. Sec. 2.3):

$$\Phi = K_m \int \phi V(\lambda) d\lambda \quad (1)$$

Here, Φ is in lumens (lm), ϕ is the radiant power in W/nm, λ is the wavelength in nm, $V(\lambda)$ is the photopic or scotopic response, and K_m is the maximum spectral luminous efficacy, which is 683 lm/W and 1754 lm/W for photopic and scotopic vision, respectively.

The candela (cd) [1] is defined as the *luminous intensity* (luminous flux per solid angle, $I = d\Phi / d\omega$), in a given direction, of a source that emits monochromatic radiation of frequency 540×10^{12} Hz (555 nm) and that has a radiant intensity in that direction of 1/683 W/sr. Further, the *luminance, L,* of a source is defined as the quotient of the luminous intensity in the given direction produced by a differential area element of the source divided by the orthogonal projection of the element of the source onto a plane perpendicular to that direction (i.e. $L = d^2\Phi / d\omega\, dA \cos\theta = dI / dA \cos\theta$), see Fig. 2.1. The units are therefore lm/sr.m^2 or cd/m^2. The *brightness* of a source is in part determined by the source luminance; however, brightness is a sensation that depends on the state of the eye and should not be confused with luminance.

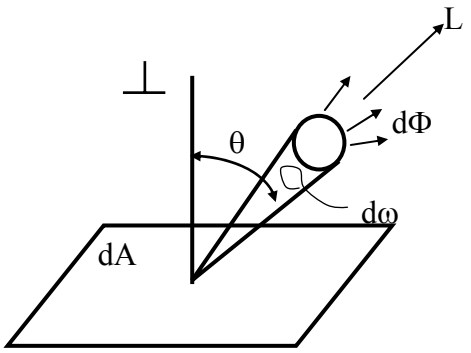

Figure 2-1. Diagram of luminous intensity definition.

With these definitions, a lambertian source is one whose luminous intensity in any direction varies as the cosine of the angle between that direction and the perpendicular to the surface element of the source ($I(\theta) = I_0 \cos\theta$). A lambertian source therefore has the same luminance regardless of viewing angle, and the total luminous flux per unit area is π times the luminance. All optical emissive devices are assumed to have a lambertian intensity profile in this thesis, since deviations are typically ~10% [2].

2.1.B The human eye

An understanding of the human eye is the basis for the science of color and lighting engineering. While light detection can be explained by an understanding of physics, chemistry and biology, the perception of light is a psychological phenomenon that is poorly understood, hence, standards for quantifying color, which are set by organizations such as the Commission Internationale de l'Éclairage (CIE), are mean valves for a representative group of tested people. This is very much in contrast to the scientific definition of a meter as the distance traveled by a ray of electromagnetic energy through a vacuum in 1/299,792,458 of a second.

The eye is designed to focus light onto the retina and for the conversion of light energy into electrical energy. As in any other optical device, the eye has a spectral response that is dependent on wavelength, and particular to the eye, on age [3]. The

cornea and crystalline lens filter out wavelengths below 380 nm. There is very little attenuation between 380 nm and 950 nm but beyond 950 nm, the attenuation by the infrared water bands is significant, and infrared radiation transmittance above 1400 nm is negligible.

With age comes many deleterious effects and the eye is not spared in this regard. Besides the well know decrease in the focusing ability of eye, absorbance of wavelengths increases across the visible range with a fourfold reduction in transmittance of shorter wavelengths over the reduction in the transmittance of longer wavelengths [4].

There are two main classes of photodetectors in the eye: rods and cones. Rods are extremely sensitive to light and are responsible for *scotopic* or night vision. The cones, which are divided into three classes, provide us with the ability to discriminate color and determine the *photopic* or day vision. Scotopic vision is active below 0.01 cd/m^2, and photopic vision requires luminance levels to be greater than 3 cd/m^2. In the *mesopic region* of luminance, between 0.01 and 3 cd/m^2, the eye has a mixture of scotopic and photopic responsivities. The peak spectral sensitivity of photopic vision is red-shifted by 40 nm from the peak spectral sensitivity of scotopic vision, and the photopic spectral responsivity is used in luminous intensity calculations. Figure 2-2 shows the photopic and scotopic responsivities normalized with respect to peak height.

The eye's ability to discriminate between wavelengths is dependent on photochemical and neurological processes. There are three peaks within the visible spectrum where discrimination of wavelengths is maximized and discrimination at the ends of the visible spectrum falls off rapidly [5]. Also, the differentiation of various hues from white is wavelength dependent. Colors at the end of the visible spectrum are more easily discerned from colors in the middle of the spectrum [6], hence, the very broad white region in the CIE chromaticity color chart (see Sec. 2.5).

The eye is a wonderful tool for humans to efficiently and effectively relate with our environment. Its form fits its function quite aptly but for the same function, a different organ may have developed had our planet not been exposed to radiation from our sun. All high quality light sources attempt to imitate the characteristics of visible light from

the solar spectrum, so some background information about this blackbody radiator is

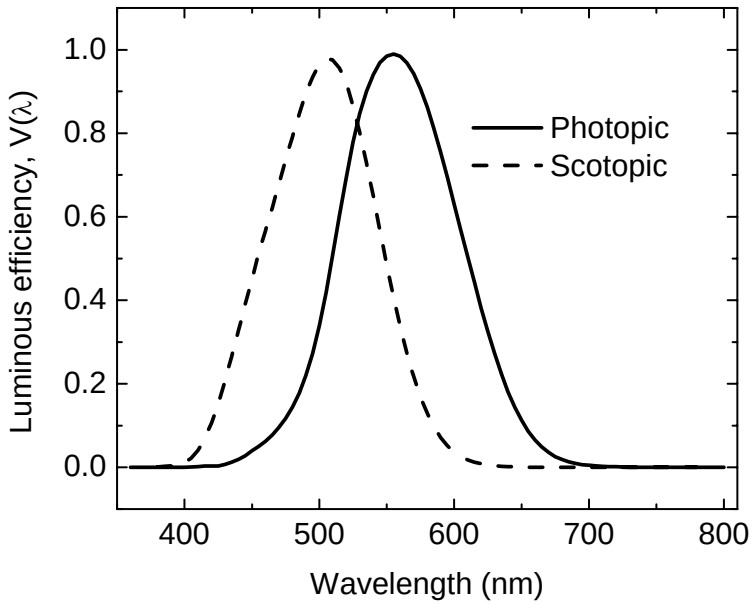

necessary.

Figure 2-2. Photopic and Scotopic luminous efficiency functions.

2.1.C Sunlight

The solar spectrum can be described by Planck's blackbody spectrum equation that relates the intensity and spectral properties of the body solely to its temperature:

$$\rho(\omega) = \frac{\hbar\omega^3}{\pi^2 c^3 \left(e^{\hbar\omega / k_B T} - 1 \right)}. \qquad (2)$$

Here, ρ is the energy density per unit frequency, h is Planck's constant, c is the velocity of light, k_B is the Boltzmann constant, ω is the angular frequency, and T is the Kelvin temperature.

Daylight differs significantly from Eq. (2) due to scattering and absorptive effects of the atmosphere. However, standards for lighting have developed based on the radiation from a blackbody, so the nature of the spectral output from the sun serves as a means to judge all other white light sources.

The *color temperature* of a blackbody is defined as its temperature for a particular perceived color. For example, a blackbody radiator with a color temperature of 10,000 K appears blue. For non-blackbody radiators i.e. sources of light for which Eq. (2) does not hold, the correlated color temperature (CCT) is the temperature of a blackbody radiator which has a color that most closely resembles that of the light source. The CCT, therefore, only specifies chromaticity and gives no information about the spectral power distribution.

Besides being used as a measure of chromaticity, the correlated color temperature is also used to specify the *color rendering index* of a light source. The color of two light sources may appear identical, *metameric*, when viewed directly and will therefore have the same color temperature; however, the color of the reflected light from an object illuminated by these two sources may be significantly different.

A method defined by CIE to distinguish between two metameric sources uses a color rendering inde*x* (CRI) [6]. The reflection from an object of a light source of a particular correlated color temperature is compared to the reflection from the same object under illumination from a blackbody radiator of the same color temperature. The similarity between the two sources is ranked on a scale of 0 to 100, where a rating of 100 is a perfect match. Sources with a CRI value above 80 are considered high quality lighting sources. A lower quality light source falls between 70 and 80, but this source is still considered good; whereas, a source with CRI below 70 is considered undesirable for natural lighting requirements.

The CRI and CCT reflect the chromaticity and spectral output of a light source compared to the sun and can represent very unsaturated colors between red and blue. A more comprehensive chromaticity measure is, however, needed for colors such as green. An intensity versus wavelength spectrum of a source describes the source in much more detail than chromaticity numbers and should always be referenced, since much information is lost converting spectral characteristics into chromaticity data.

2.1.D C.I.E. chromaticity coordinates

There are several methods to define the chromaticity of a light source: e.g. the DIN system [7], the Natural Color System [8], and the Munsell system [9]. The CIE chromaticity coordinate system [10] will be used throughout this thesis, since it is the preferred standard in the display and lighting industries. This method originally recommended in 1931 by the CIE defines all metameric pairs by giving the amounts *X, Y, Z* of three imaginary primary colors required by a standard observer to match the color being specified. These amounts are calculated as a summation of the spectral compositions of the radiant power of the source times the *spectral tristimulus values*, or *color matching functions* for an equal power source:

$$\begin{aligned} X &= \int S(\lambda)\bar{x}(\lambda)d\lambda \\ Y &= \int S(\lambda)\bar{y}(\lambda)d\lambda \\ Z &= \int S(\lambda)\bar{z}(\lambda)d\lambda \end{aligned} \quad (3)$$

Here, $S(\lambda)$ is the spectral irradiance of the source, and $\bar{x}(\lambda)$, $\bar{y}(\lambda)$, and $\bar{z}(\lambda)$ are the spectral tristimulus values plotted in Fig. 2-3. Chromaticity coordinates (*x, y, z*) are then calculated as follows:

$$\begin{aligned} x &= \frac{X}{X+Y+Z} \\ y &= \frac{Y}{X+Y+Z} \\ z &= \frac{Z}{X+Y+Z}. \end{aligned} \quad (4)$$

By convention, chromaticity is stated in terms of x and y, since 1 = x + y + z, and plotted in a rectangular coordinate system as shown in Fig. 2-4. In this chromaticity diagram, the points representing light of single wavelengths are plotted along a horseshoe-shaped curve called the spectrum locus. The line joining the extremities of the spectrum locus is known as the purple boundary and is the locus of the most

saturated purples obtainable. Chromaticity coordinates, CCT and CRI of common light sources are given in Table 2-1.

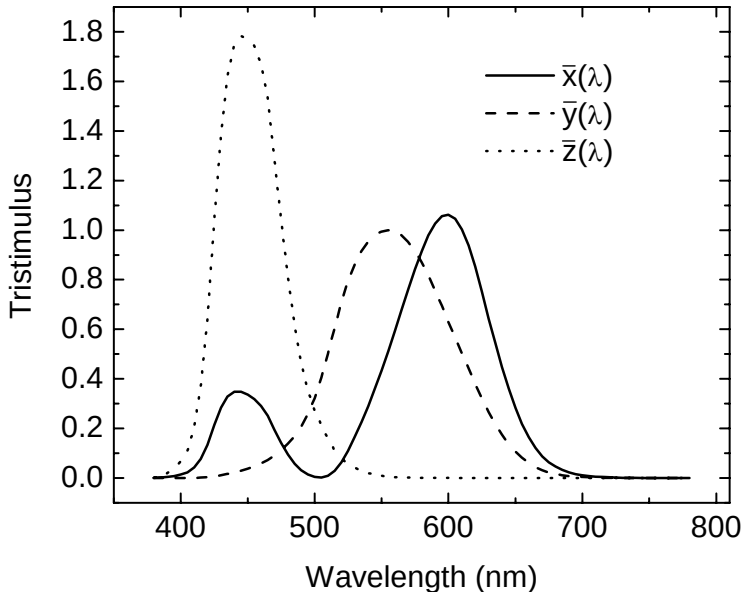

Figure 2-3. Spectral tristimulus values.

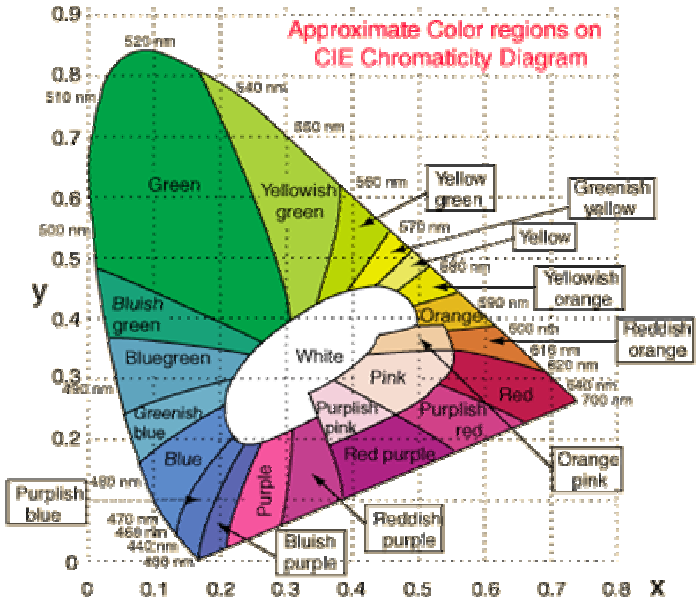

Figure 2-4. C.I.E. chromaticity diagram

Table 2-1 Chromaticity coordinates, color correlaed temperature (CCT) and color rendering indices (CRI) for common light sources.

Lamp	x	y	CCT	*CRI*
High pressure sodium	0.519	0.417	2100 K	24
Xenon	0.324	0.324	5920 K	94
Tungsten Halogen (CIE Standard Illuminant A) [11]	0.448	0.407	2856 K	100
Daylight (CIE Standard Illuminant D_{65}) [11]	0.313	0.329	6500K	90
Fluorescent, cool white	0.375	0.367	4080 K	89
Fluorescent, warm white	0.440	0.403	2940 K	72
Incandescent bulb	0.448	0.408	2854 K	100

.

2.2 Electronic transitions between energy states of a single molecule

Most of the theories used to elucidate photophysical and photochemical processes that are encountered in the field of organic light emitting devices were developed as early as in the 1920's, so there is a sufficient number of general texts that are useful reference tools [12-15]. Some selected topics that are required to understand and explain electronic transitions — fluorescence, phosphorescence, intersystem crossing, and internal conversion — in organic materials will be described in this chapter. The theory will initially focus on single molecules, and end with a discussion on transitions between molecules.

2.2.A Molecular electronic states

Using the Born-Oppenheimer approximation [16], the nuclear motion, electronic motion, and spin contributions to the molecular wave function are treated as independent functions. The approximation is considered valid since electronic motion (10^{-15} sec) is much more rapid than nuclear motion (10^{-12} sec). The approximation for considering spin independently is also valid, because magnetic and electronic interactions in organic molecules are typically weak. The 'true' molecular wave function, Ψ, is therefore approximated as follows:

$$\Psi \propto \psi_0 \chi \zeta \,. \tag{5}$$

Here, ψ_0, χ, ζ represent the approximate wave functions for the electronic wave function, for nuclear position, and for spin, respectively.

The specific nature of ψ_0 depends on the level of sophistication desired. For many qualitative analyses of molecular phenomena ψ_0 is approximated as the product of 'one-electron' molecular wave functions (orbitals):

$$\psi_0 = \prod_i \psi_i \,, \tag{6}$$

where ψ_i is a solution of the Schrödinger equation for a 'one-electron' molecule, i.e. a fictitious molecule where electron-electron repulsion is not consider. These

orbitals are commonly referred to as Hückel orbitals in introductory texts [17], and are built from linear combinations of atomic orbitals.

Using Eqs. (5) and (6), a (First Order) molecular electronic state is built by employing both the Pauli exclusion and the Aufbau principles such that two electrons are added to each of the lowest energy levels which correspond to ψ_i, using all the electrons available from the atoms comprising the molecule. As an example, consider the ground state configuration of formaldehyde.

$$\Psi(CH_2O) = |(1s_O)^2(1s_C)^2(2s_O)^2(\sigma_{CH})^2(\sigma'_{CH})^2(\sigma_{CO})^2(\pi_{CO})^2(n_O)^2(\pi^*_{CO})^0> . \qquad (7)$$

Here, $1s_o$, $2s_o$, $1s_c$ refer to ψ_i that are localized on oxygen and carbon, σ and π are sigma and pi bonding orbitals, σ' and π^* are sigma and pi anti-bonding orbitals, and n_o is the orbital containing a lone pair of electrons on oxygen. The number of electrons in each orbital is given by the superscript, and the π^*_{CO} is the lowest unoccupied molecular orbital (LUMO).

Physically, the total electronic distribution may be approximated as a superposition of each of the occupied ψ_i [see Eq. (6)], but only the highest occupied ψ_i needs to be explicitly considered for an electronic interpretation of ground state properties. We show in Chapter 5 that information about the higher energy orbitals can be obtained from ultraviolet photoemission spectroscopy.

2.2.B Singlet and triplet states

A singlet state is formed when a molecular configuration has no net spin (S=0) i.e. for every electron that has spin ½ (up), there is an electron that has spin -½ (down). Therefore, most molecules have a ground state singlet, since the electrons are placed in the lowest energy ψ_i according to the Pauli principle. However, in the excited state, a molecule may possess two electrons whose spins are parallel and hence has S = 1. A non-zero spin occurs because the electrons are unpaired and exist in two different orbitals, ensuring that the Pauli exclusion principle is obeyed.

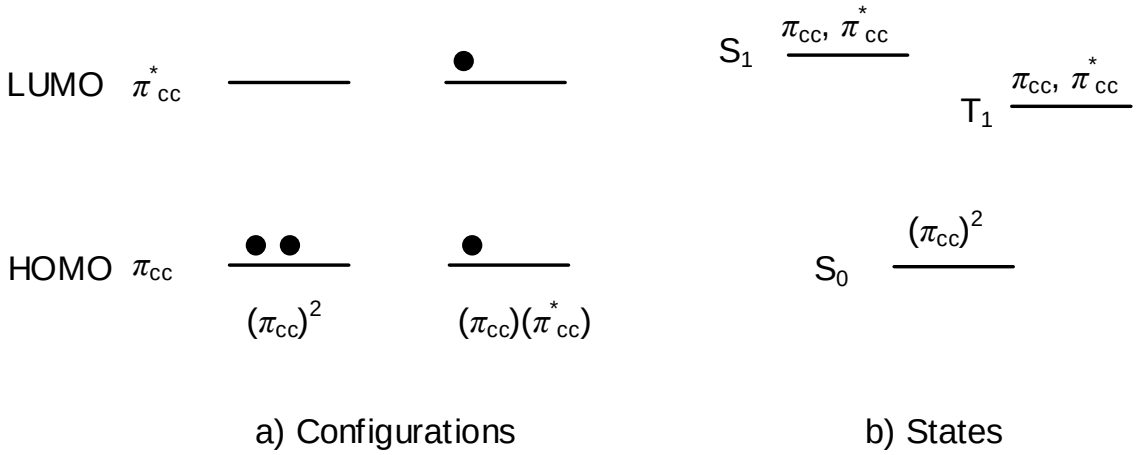

Figure 2-5 Schematic representation of a) electronic configurations and b) electronic states for the lowest excited states of ethylene (C=C).

Given a two-electron system derived from a particular electron orbital configuration, with each electron having spin ½, the total spin may be either S = 0 or 1. The S = 0 state or singlet state (*S*) is antisymmetric under particle exchange and is given by:

$$S = \frac{1}{\sqrt{2}}\left\{|\uparrow(1)\downarrow(2)> - |\downarrow(1)\uparrow(2)>\right\}, \tag{8}$$

where ↓ and ↑ represent the possible spin state of each electron. The S = 1 or triplet state (*T*) contains three states, all symmetric under particle exchange:

$$\begin{aligned} T &= \frac{1}{\sqrt{2}}\left\{|\uparrow(1)\downarrow(2)> + |\downarrow(1)\uparrow(2)>\right\} \\ T &= |\uparrow(1)\uparrow(2)> \\ T &= |\downarrow(1)\downarrow(2)> \end{aligned} \tag{9}$$

By convention, the ground electronic singlet state is represented by S_0, and electronically excited singlet states are labeled S_1, S_2 etc, where the subscript refers to the first and second singlet energy level manifolds above the ground singlet energy, respectively. Similarly T_1, T_2 are the first and second triplet energies above the ground energy state.

Given the symmetries of the singlet and triplet states, the spatial component (ψ_0) of a singlet state is symmetric, and ψ_0 of a triplet state is antisymmetric. These spatial symmetries are necessary because the total wave function of an electron (a fermion) must be antisymmetric. If we take $\psi_i(1)$ and $\psi_j(2)$ to be the individual electron wave functions that comprise the wave function of the excited state, the electronic repulsion between the two electrons is given by two terms: the *Coulomb integral*, *J*, and the *exchange integral*, *K*. These are defined as follows:

$$J = \frac{e^2}{4\pi\varepsilon_0} < \psi_i(1)\psi_j(2) | \frac{1}{r_{12}} | \psi_i(1)\psi_j(2) >, \tag{10}$$

$$K = \frac{e^2}{4\pi\varepsilon_0} < \psi_i(1)\psi_j(2) | \frac{1}{r_{12}} | \psi_i(2)\psi_j(1) >. \tag{11}$$

Here, *e* is the charge on an electron, and ε_0 the permittivity of free space. The energy of a spatially symmetric state is therefore:

$$\begin{aligned} E_+ &= \frac{e^2}{8\pi\varepsilon_0} < \psi_i(1)\psi_j(2) + \psi_j(1)\psi_i(2) | \frac{1}{r_{12}} | \psi_i(1)\psi_j(2) + \psi_j(1)\psi_i(2) > \\ &= J + K \end{aligned}, \tag{12}$$

and a spatially anti-symmetric state is:

$$\begin{aligned} E_- &= \frac{e^2}{8\pi\varepsilon_0} < \psi_i(1)\psi_j(2) - \psi_j(1)\psi_i(2) | \frac{1}{r_{12}} | \psi_i(1)\psi_j(2) - \psi_j(1)\psi_i(2) > \\ &= J - K \end{aligned}. \tag{13}$$

Since *J* and *K* are positive quantities, triplets are lower in energy that singlets.

2.2.C Potential energy surfaces and nuclear wave functions

A molecule in a particular electronic state may exist with various configurations of its nuclei, each configuration in space corresponding to a particular potential energy of the system. A map of the potential energy versus nuclear configuration for a given electronic state is called a potential energy surface [17]. For a polyatomic molecule, a polydimensional surface is required to describe the molecular motions; however, the group of nuclei in the molecule can be replaced by the molecular center of mass, and the

topological features of a simplified two dimensional potential energy curve may be generalized to include potential-energy surfaces.

The anharmonic potential energy curve is most frequently encountered in qualitative descriptions of bound physical states. Features of such a curve are shown in Fig. 2-6. If a molecule starts at point A, it experiences a restoring force, F, which moves the center of mass toward point C, the position of minimum potential energy (PE) at which F = dPE/dr = 0. Between the points A and B, the vibrational states are essentially continuous and the system behaves classically. Near point B, vibrations are quantized and energy from the environment is absorbed or emitted in quantized packets of vibrational energy called phonons. These wave functions are used to determine the Franck-Condon factors of radiative transitions. Additionally, the center of mass may also proceed from A to D in the absence of collisions, and this transition dissociates the molecule into fragments.

There are several very useful applications of potential energy curves. Firstly, excited states may also be represented by an anharmonic potential energy curve, so transitions between excited and ground states may be qualitatively understood. In general, the equilibrium position (r_0^*) in the excited state will be greater than the equilibrium position (r_0) in the ground state, and the shape of the excited-state curve will be flatter because the nuclei will be more loosely bound.

Secondly, potential energy curves can be used to describe states that are unbound, such as excimers and exciplexes. For these types of states, the potential energy curves describe the interactions of two molecules, and do not have an energy well in the ground state.

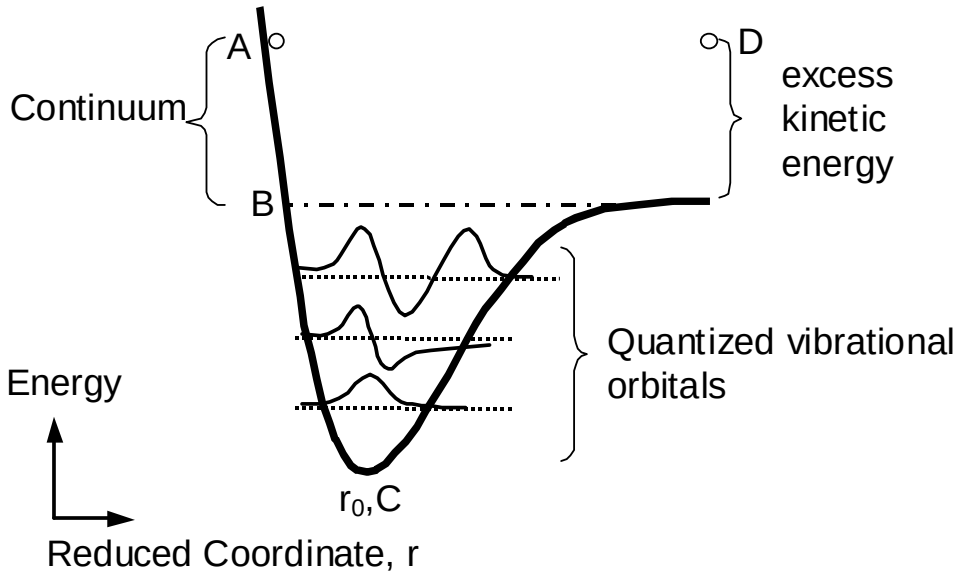

Figure 2-6. Anharmonic potential energy diagram of the center of mass of a molecule. Dashed lines indicate the vibrational energy level on top of which χ are drawn. The equilibrium distance r_0 of the center of mass is indicated.

2.2.D Fermi's 'Golden Rule' and transitions between states

In terms of quantum dynamics, Fermi's 'Golden Rule' is used to understand the rate of transitions that occur in chemical dynamics. It simply states that the rate of transition between two states is proportional to the square of the matrix element corresponding to the (weak) first order perturbation coupling the zero order states [18] and is given by:

$$rate(\sec^{-1}) = \frac{\rho}{\mathrm{h}} < H' >^2 . \qquad (14)$$

Here, ρ corresponds to the density of final states that can couple to the initial state, and $< H' >$ represents the matrix element for the (weak) perturbation coupling the initial and final states.

Given Eq. (5), there are three interactions that are prominent in chemical dynamics: electronic, spin and nuclear. For radiative transitions involving orbital interactions, the matrix element for the perturbation is the electronic dipole between the initial and final orbital states, and previous seminal works [19] have excellent derivations of *stimulated*, and *spontaneous emissions*, and *absorption*.

Transitions that involve the change of spin, such as the transition from a singlet to a triplet state (*intersystem crossing*), proceed via a spin-orbit coupling perturbation. This perturbation arises due the interaction between an electron's spin and the magnetic moment created by the electron oscillating in a closed orbit. The most salient feature of this interaction is that it increases with the mass of the atom. Via spin-orbit coupling, heavy atoms such as platinum and iridium can significantly mix triplet and singlet states, and thereby have extremely efficient triplet emission; whereas, the relaxation of an excited triplet state into a singlet ground state is strictly forbidden without spin-orbit interactions [20].

Thirdly, nuclear motion limits transitions according to the *Franck-Cordon principle*: Since electronic motions are much faster than nuclear motion, electronic transitions occur most favorably when the nuclear structure of the initial and final states are most similar [13]. The probability of any electronic transition is therefore directly related to the square of the vibrational overlap integral, i.e., $< \chi_i \mid \chi_f >^2$, which is called the Franck-Condon factor. This factor governs the relative intensities of vibrational bands in electronic absorption and emission spectra.

Figure 2-7. is a pictorial example of the absorption and emission of a photon using a reduced coordinate system. Absorption of a photon of energy E_a preferentially promotes an electron from $\mid a >$ to $\mid f >$, since $< a \mid f >^2$ is largest for this transition. The excited molecule relaxes via *internal conversions* to $\mid d >$, according to Kasha's rule [21], from where it preferentially radiatively relaxes to $\mid c >$, and emits a photon of energy E_b. The molecule then finally returns to $\mid a >$ by emitting phonons.

The energy of the emitted photon $E_b < E_a$, and this energy difference is called the Franck-Condon shift. In general, the energy red-shift is referred to as the Stoke's shift,

and it is due to the shift in the nuclear equilibrium positions of the excited and ground states, Δr.

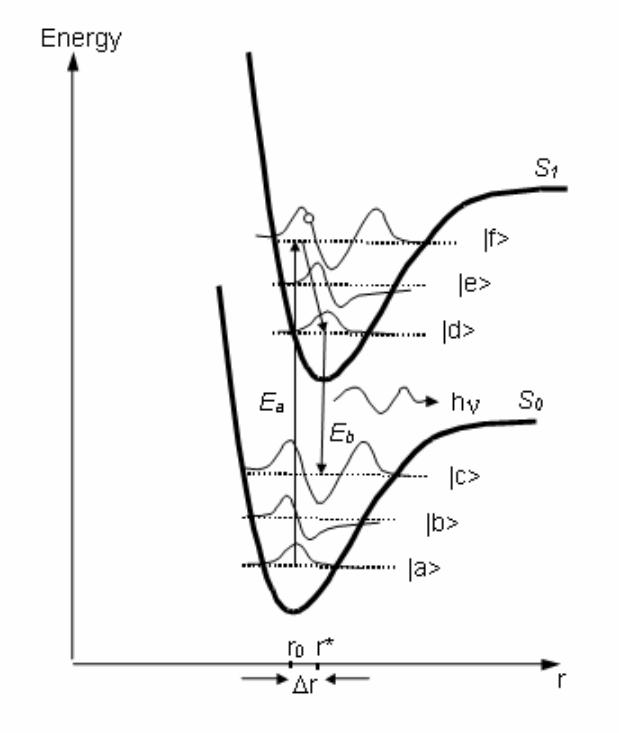

Figure 2-7. Potential energy curves showing the absorption and emission of a photon between the S_0 and S_1 states. Franck-Condon factors are maximized for the $|a>$ to $|f>$, and $|d>$ to $|c>$ transitions, and emission can only occur from $|d>$ according to Kasha's rule. The Stokes shift in the equilibrium positions of the excited and ground states is given by Δr.

2.3 Energy transfer between molecules

The previous section has thus far considered a single molecule, and this section will conclude the chapter with a discussion on energy transfer between molecules. There are three means by which energy is transferred from one molecule to another: radiative, Förster [22], and Dexter energy transfer mechanisms [23].

2.3.A Radiative energy transfer

The radiative mechanism of energy transfer is a trivial case, which consists of the emission of a quantum of light by one molecule and the subsequent absorption of the emitted photon by a second molecule [15]. This transfer is maximized when the quantum yield of emission by the first molecule is close to unity, when the second molecule has a high extinction coefficient, and when there is spectral overlap between the emission of the first molecule and the absorption of the second molecule.

2.3.B Förster dipole-dipole radiationless energy transfer

This is a resonant energy transfer mechanism where electronic dipoles of two molecules are coupled via a dipole-dipole interaction [14, 22, 24]. The Hamiltonian for this interaction is given by:

$$H'\left(\vec{R}\right)=\frac{1}{4\pi\varepsilon_r\varepsilon_0 R^3}\left(\vec{\mu}_D.\vec{\mu}_A-3\left(\vec{\mu}_D.\vec{R}\right)\left(\vec{\mu}_D.\vec{R}\right)\right), \tag{15}$$

where ε_r is the relative dielectric constant, $\vec{\mu}_D$ and $\vec{\mu}_A$ are the respective electric dipole moment operators on the donor and acceptor molecules, respectively, and $\vec{R}$ is the unit vector between the donor and acceptor molecules.

The transition rate of energy from the donor to the acceptor molecule, K_{DA}, is then found by substituting Eq. (15) into Eq. (16) and averaging over all possible orientations of $\vec{R}$. The final simplified result is given by:

$$K_{DA}(R)=\left(\frac{1}{\tau_D}\right)\left(\frac{R_0}{R}\right)^6. \tag{16}$$

Here, R_0 is the Förster radius, and τ_D is the average donor lifetime for recombination in the absence of energy transfer. The critical Förster radius is given by the following integral over all frequencies, ν:

$$R_0^6=1.25\times10^{17}\frac{\eta_D}{n^4}\int F_D(\upsilon)\alpha_A(\upsilon)\frac{d\upsilon}{\upsilon^4}, \tag{17}$$

where η_D is the donor quantum emission efficiency, n is the refractive index of the host, F_D is the area normalized emission spectrum of the donor, and α_A is the molar extinction coefficient of the acceptor. Typically values of R_0 for systems studied in the work are ~3.5 nm.

Förster energy transfer is discussed further in Chapter 4 in relation to phosphor sensitized fluorescence in organic light emitting devices. Spin is not conserved in this sensitization energy transfer, so triplets transfer energy to singlet states.

2.3.C Dexter energy transfer

Förster energy transfer is a long range Coulombic interaction that can exceed 10 nm, and is visualized as a transmitter-antenna mechanism. It is unlike Dexter energy transfer [14, 23], which is a short- range (~1 nm) exchange interaction that requires diffusive collisions between molecules. The rate constant of energy transfer in this case is given by:

$$K_{DA} = AJ \exp\left(-2R_{DA}/L\right), \tag{18}$$

where A is related to the orbital interactions, J is the spectral overlap integral normalized for the extinction coefficient of the acceptor, and R_{DA} is the donor-acceptor separation relative to their van der Waals radii, L [13]. It is immediately obvious that the exponential term limits the range of the interaction in this mechanism.

Dexter transfer can be envisaged as two electrons that are physically and coherently switched between two molecules i.e. an electron is removed from the donor molecule and inserted into the acceptor molecule, while simultaneously an electron is removed from the acceptor and inserted into the donor.

2.3.D The exciton

When a molecule is part of an extended solid, such as an organic crystal or solid film, there are important differences that exists between excited state properties of the single molecule and that of the extended system. Many, but not all, photophysical

processes of small aggregates of molecules and crystals are directly understood in terms of individual molecules due to their weak van der Waals interactions. However, the interaction energy between the molecules imposes a collective response embodied in a quasi-particle called an *exciton* [12]. Two types of excitons considered here are the Frenkel [25] and charge-transfer exciton [26]. The Frenkel exciton is a correlated electron-hole pair localized on a single molecule, with a radius comparable to the size of the molecule. A charge-transfer exciton is an un-relaxed polaron pair with the positive and negative polarons located on discrete, neighboring molecules.

2.3.E Fluorescence and Phosphorescence

In most stable molecules, the highest occupied molecular orbital (HOMO) is completely filled in the ground state. Consequently, the ground state wavefunctions of these molecules are spatially symmetric under electron exchange. There are important exceptions such as molecular oxygen, which has two unpaired electrons in different orbitals; but in general, molecules in the ground state have filled orbitals and this determines that they are singlets. Thus, the decay of excited singlet states is allowed, but the decay of triplet states to the ground state is disallowed. Singlet decay is rapid (with rate $k \sim 10^9\ s^{-1}$) and if a photon is emitted, the process is known as fluorescence; see Fig. 2-8. Although triplet-to-singlet transitions are forbidden under the processes described above, certain second order effects may mix singlet and triplet states, making the decay of a triplet weakly allowed. Under these circumstances, triplet decay is slow ($k < 10^6\ s^{-1}$) and if a photon is emitted, the process is known as phosphorescence.

Singlet-triplet mixing also encourages singlet-to-triplet energy transfer within a molecule, known as intersystem crossing (ISC). The energetic impetus for ISC are electron-electron interactions that break the degeneracy between singlet and triplet levels

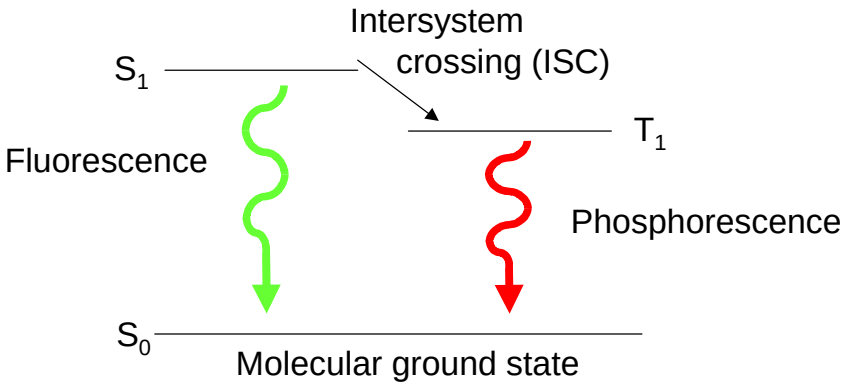

Figure 2-8 The relative positions of the first excited singlet and triplet levels in a typical molecule, showing the origins of fluorescence and phosphorescence.

2.4 Summary

This chapter described some of the microscopic physical mechanisms and states encountered throughout this thesis. The following chapters will provide examples of where these phenomena are utilized to design and develop red and white organic light emitting devices, and will build on these ideas to develop OLEDs for a practical use.

Chapter2. Reference

[1] The International System of Units (SI), U.S. Department of Commerce. National Bureau of Standards, Prepared by D.T. Goldman and D.T. Bell. Gaithersburg, MD, (1986).

[2] J. S. Kim, P. K. H. Ho, N. C. Greenham and R. H. Friend, J App. Phys. 88, 1073 (2000).

[3] W. D. Wright, Researches on normal and defective color vision. 1st ed. (London, 1946).

[4] S. Coren and J. S. Girgus, Vision Research, 12, 343 (1972).

[5] R. E. Bedford and G. W. Wyszecki, Journal of Opthamology, 48, 129 (1958).

[6] Method of measuring and specifying colour rendering properties of light sources, Commission Internationale de l'éclairage (CIE), Report no. 13.2, Paris (1974).

[7] M. Richter and K. Witt, Color Resolution Application, 11, 138 (1986).

[8] A. Hard and L. Sivik, Color Resolution Application, 6, 127 (1981).

[9] Standard test method for specifying color by the Munsell system, American Society for Testing and Materials, Report no. D 1535-80, Philadelphia (1980).

[10] Colorimety, Commission Internationale de l'éclairage (CIE), Report no. 15.2, Paris (1986).

[11] CIE Standard Illuminants for Colorimetry, Commission Internationale de L'éclairage (CIE), S005, Paris (1998).

[12] M. Pope and C. E. Swenberg, Electronic Processes in Organic Crystals and Polymers. 2nd ed. (Oxford University Press, New York, 1999).

[13] N. J. Turro, Modern Molecular Photochemistry. 1st ed. (University Science Books, Sausalito, 1991).

[14] J. A. Barltrop and J. D. Coyle, Principles of Photochemistry. 1st ed. (John Wiley & Sons, New York, 1978).

[15] J. B. Birks, Photophysics of Aromatic Molecules. 1st ed. (Wiley-Interscience, London, 1970).

[16] M. Born and J. R. Oppenheimer, Annals of Physics, 84, 457 (1927).

[17] M. J. Dewar and R. C. Dougherty, The PMO Theory of Organic Chemistry. 1st ed. (Prentice-Hall, Englewoods Cliffs, N.J., 1975).

[18] G. W. Robinson, Excited States. 1st ed. (Academic Press, New York, 1974).

[19] D. J. Griffiths, Introduction to Quantum Mechanics. 1st ed. (Prentice Hall, Upper Saddle River, N.J., 1995).

[20] M. A. Baldo, "The Electronic and Optical Properties of Amorphous Organic Semiconductors" (Ph.D. dissertation, Princeton University, 2001).

[21] M. Kasha, Spectroscopy of the excited state. 1st ed. (Plenum Press, New York, 1976).

[22] T. Förster, Discussion Faraday Society, 27, 7 (1959).

[23] D. L. Dexter, J. Chem. Phys.21, (1953).

[24] T. Förster, Modern Quantum Chemistry, Part 2. Action of Light on Organic Molecules (Academic Press, 1965).

[25] J. Frenkel, Phys. Rev. 37, 1276 (1931).

[26] E. A. Silinsh and V. Capek, Organic Molecular Crystals. 1st ed. (American Institute of Physics, New York, 1994).

Chapter 3.

High-efficiency Red Emitting OLEDs

3.1 Improvement in energy transfer between host and dopant

3.1.1 Fluorescent dye sensitization

Generally, an OLED has an EML with a host-dopant system where excitons are generated by recombination of carriers on host molecules. An efficient energy transfer from a host to a dopant results in a highly efficient emission from a dopant. Focusing on the energy transfer between a host material and an emissive dopant, I have improved current and power efficiencies and an operational stability. For enhancing the energy transfer between a host and an emissive dopant, the novel doping method has been proposed.

As mentioned in Chap.1, conventional red OLEDs have an EML which consists of a host material and a red emitting dopant. Tris(8-quinolinolato) aluminum (Alq) is widely used as a host material due to the excellent carrier transport characteristics, film morphology and thermal stability. For red emitting dopants, Nile red and phosphorescent $Eu(TTA)_3phen$ [1], porphyrin derivatives, such as TPP, ZnTPP, TPC, PtOEP [2], PtOx and PtDPP which give a saturated red emission, have been employed but the OLEDs with those dopants have low external quantum efficiencies of below 1%. 4-(dicyanomethylene)-2-methyl-6-(p-dimethylaminostyryl)-4H-pyran (DCM), whose emission peak is at 595nm, and the derivatives of 4-dicyanomethylene-2-methyl-6-[2-(2,3,6,7-tetrahydro-1H,5H-benzo[ij]quinolizin-8-yl)vinyl]-4H-pyran (DCM2) and 4-(dicyanomethylene)-2-*t*-butyl-6-(1,1,7,7-tetramethyljulolidyl-9-enyl) -4H-pyran (DCJTB) [3,6] are usually used for a fluorescent red emitter. Among them, DCJTB has an excellent chemical stability and color chromaticity and it, therefore, is one of the most promising red-emitting dopants out of few candidates that are utilized for a production. For a host material of DCJTB, Alq is used in an EML. However, red OLEDs doped with DCJTB at a concentration of approximately 2% exhibit low quantum efficiencies though the color purities are excellent (CIE coordinates: $x>0.63$), which is originated only from DCJTB emission. At the higher doping concentration of the emitter into the EML, the efficiency of the red OLED gets lower whereas the color purity gets more saturated. This is due to the concentration quenching controlled by dipole-dipole deactivating interactions as described by the Förster energy transfer model

[7,8]. However, at a lower concentration of DCJTB or a high current density, emission from Alq and DCJTB is observed, resulting in an orange emission rather than a pure red emission. The orange emission is due to an incomplete energy transfer from Alq to DCJTB, which results from the large difference in exiciton energy between Alq and DCJTB. Similarities are previously observed (e.g. Alq and DCM2) [9],

To obtain a high efficiency without lowering a color purity, a co-dopant, which is a fluorophore sensitizer, is introduced. The sensitizer works as an intermediary to transfer the excitation energy from Alq to DCJTB, leading to the emission only from DCJTB.

Fluorophore sensitization of an energy transfer allows for an improved efficiency without suffering a color change in the device performance. One of the best points of this technology is that we can use the same EML system of DCJTB-doped Alq though the sensitizing technique can be applied to other ELM systems.

As mentioned in Chap.2, the sensitization through the singlet energy of a sensitizer to that of an emitter is a theoretically forgiven process, following Förster energy mechanism (Fluorescence resonance energy transfer). The efficiency of Förster energy is determined by the following parameters.

(i) The distance between the donor and the acceptor.

(ii) The spectral overlap of the donor emission spectrum and the acceptor absorption spectrum.

(iii) The relative orientation of the donor emission dipole moment and the acceptor absorption dipole.

The efficiency of Förster energy *E* is defined as

$$E = \frac{1}{1 + (r/R_0)^6}$$

$$R_0{}^6 = 8.8 \times 10^{23}\ \kappa^2 n^{-4} Q_0 J$$

$$J = \int f_{\mathrm{D}}(\lambda)\, \epsilon_{\mathrm{A}}(\lambda)\, \lambda^4\, d\lambda$$

with R_0 being the Förster distance of this pair of donor and acceptor at which the FRET efficiency is 50%. The Förster distance depends on the overlap integral of the donor emission spectrum with the acceptor absorption spectrum and their mutual

molecular orientation. κ^2 is the dipole orientation factor, n is the refractive index of the medium, Q_0 is the fluorescence quantum yield of the donor in the absence of the acceptor, and J is the spectral overlap integral. f_D is the normalized donor emission spectrum, and ε_A is the acceptor extinction coefficient. κ^2 =2/3 is often assumed.

For a fluorophore sensitizer, rubrene has been chosen for the following reasons. Firstly, the energy levels well align with those of the adjusting HTL and ETL materials, which is energetically favorable to inject charge carriers directly in to the sensitizer as well as cascade energy transfer from a host material. As shown Fig. 3-1, rubrene as a sensitizer agrees with the above mentioned criteria (ii). The spectral overlap integral is expected to be maximized from Alq and rubrene to DCJTB. Also, the HOMO and the LUMO energies are between Alq and DCJTB. Given charge carriers are injected directly into the sensitizer doped in an EML, the HOMO and LUMO energies make lower carrier injection barriers compared to injecting into Alq. Secondly, rubrene is known to act as an excellent yellow emitter and a host material for fluorescent red emitter. [9]. The fact is favorable for a sensitizer to transfer via Förster mechanism in terms of the criteria (i).

The red OLEDs comprised of [ITO / NPD / DCJTB : rubrene : Alq / Alq / LiF / Al] are fabricated. The device doped with 4 % DCJTB has better color purity compared to 2 % DCJTB but lower efficiency. The devices with 2 % DCJTB had the same CIE coordinates regardless of the rubrene concentration (0 to 20 %). Devices doped with rubrene show the improved efficiencies with increasing concentration of rubrene while the chromaticity is unchanged. In contrast, the chromaticity of 2%-DCJTB and 0%-rubrene-doped device (corresponding to [2, 0] device) is shifted from (x=0.64, y=0.36) to (x=0.62, y=0.38) in a luminance range from 200 to 5000 cd/m^2.

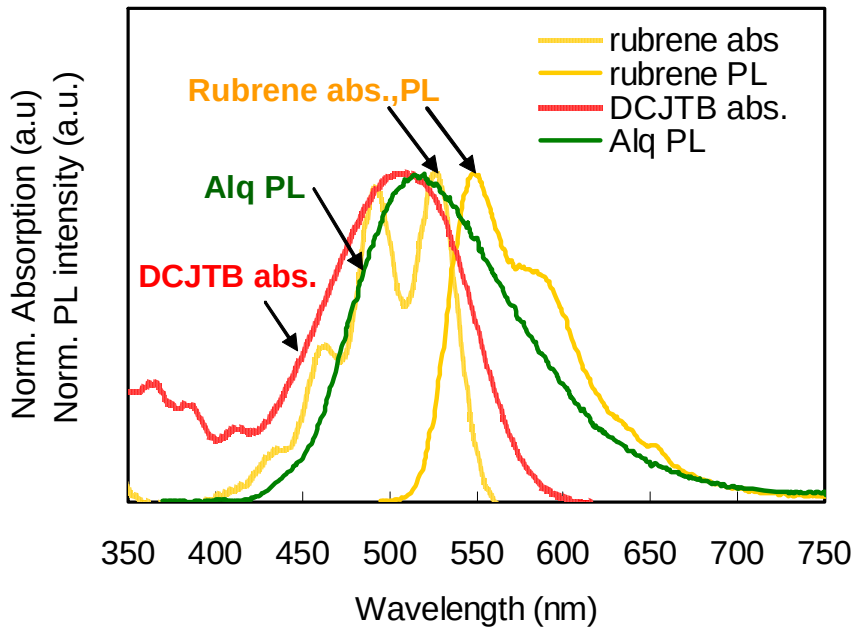

Figure 3-1. Absorption spectra of rubrene and DCJTB and photoluminescence spectra of Alq and rubrene in acetonitrile solution.

The luminance-voltage (L-V) characteristics and current efficiency-voltage characteristics of [2:0], [2:10] and [2:20] devices are shown in Fig. 3-2. As the concentration of rubrene increases, the driving voltage is lowered from 8.9 to 7.0 V at a current density of 20 mA/cm^2. By adding 10% or 20% of rubrene into the EML, a power efficiency of each device is more than doubled or tripled, respectively compared to that of the rubrene-undoped [2:0] device. This tendency is observed in a wide voltage range. In terms of operational stability, the lifetime is enhanced as a function of rubrene concentration (Fig. 3-2 Bottom).

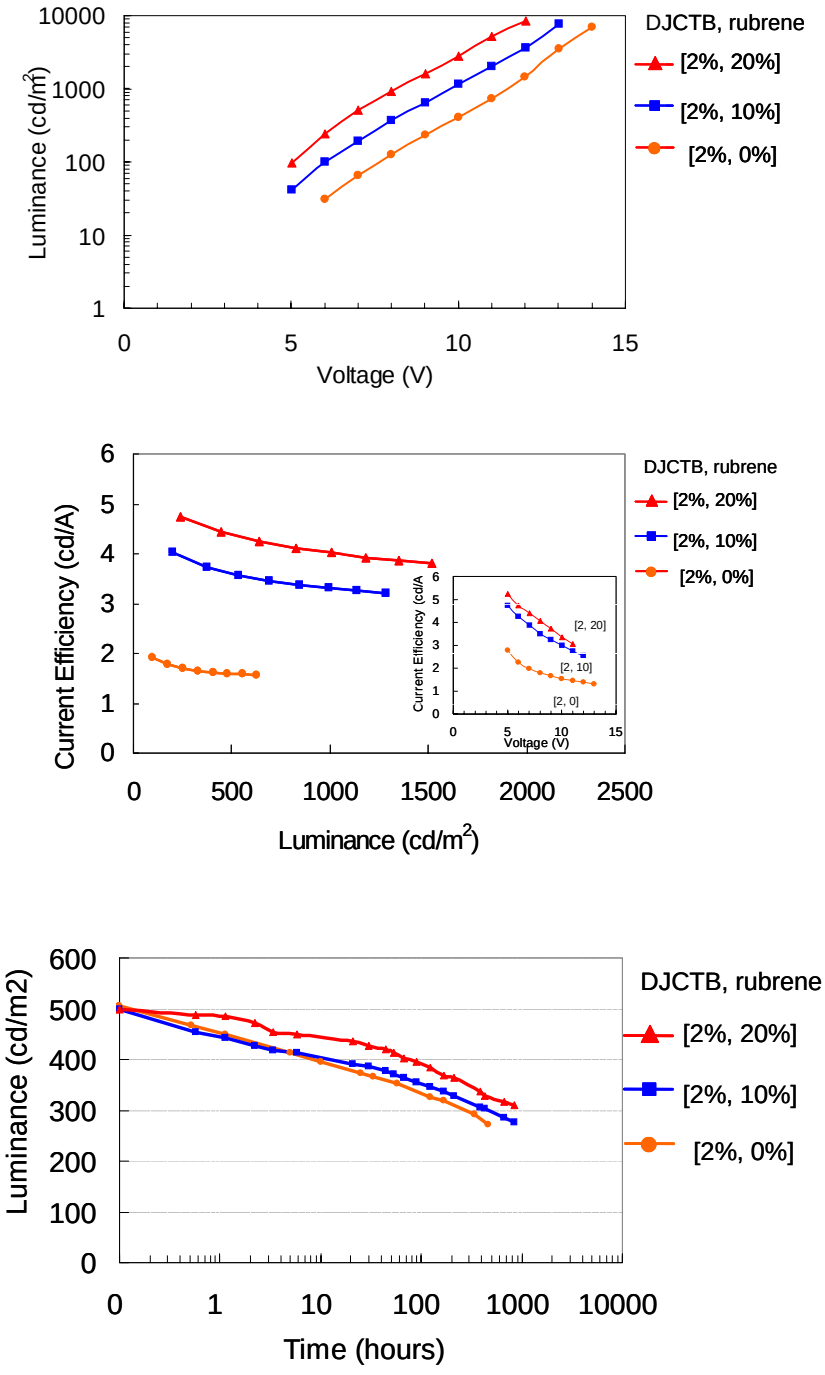

Figure 3-2. Top: Luminance-Voltage characteristics for the [2,0], [2,10], and [2,20] devices. Middle: Current-Luminance characteristics for the same devices as shown in the top figure. Bottom: The operational stability of the same device as shown in the top figure from an initial luminance of 500 cd/m^2.

The projected lifetimes of 600, 1,300 and 2,000 hours respectively for [2:0], [2:10] and [2:20] devices are obtained. The result is in agreement with the improved efficiency by rubrene doping as a fluorescent sensitizer. Moreover, the sensitizer is inferred to reduce the unstable cationic radical species of Alq formed as a result of an inefficient energy transfer to a dopant, which significantly shortens the lifetime.

To understand the effect of rubrene on color purity, efficiency, driving voltage and stability, the PL and EL spectra are studied (see Fig. 3-3). With [2:0], the PL spectrum shows two peaks from Alq and DCJTB. In contrast, the Alq peak greatly diminished in the spectra of [2:10] and [2:20], which leads to a single peak originated from DCJTB at 660nm. This is attributable to the improved energy transfer from Alq to DCJTB in the presence of rubrene. The EL spectra are the similarity to the PL spectra. As shown in the inset of Fig. 3-3 (bottom), the shoulder corresponding to Alq emission around 510 nm becomes smaller with an increasing concentration of rubrene while emission from rubrene at 560 is not observed at all. The main EL peak emission from DCJTB shifted to a longer wavelength. This result suggests that the rubrene successfully functions as an intermediary for energies to transfer.

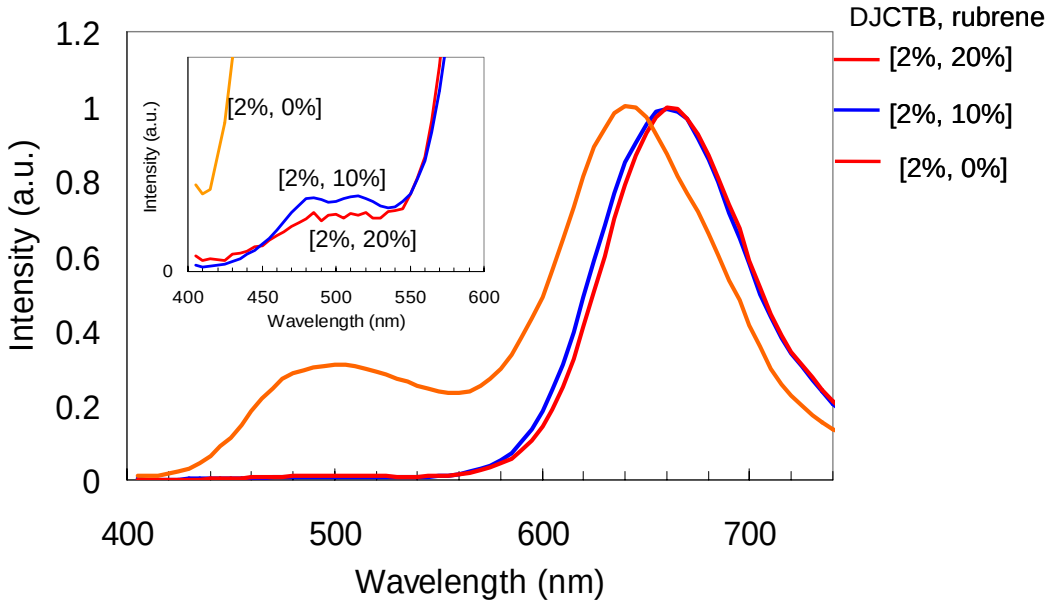

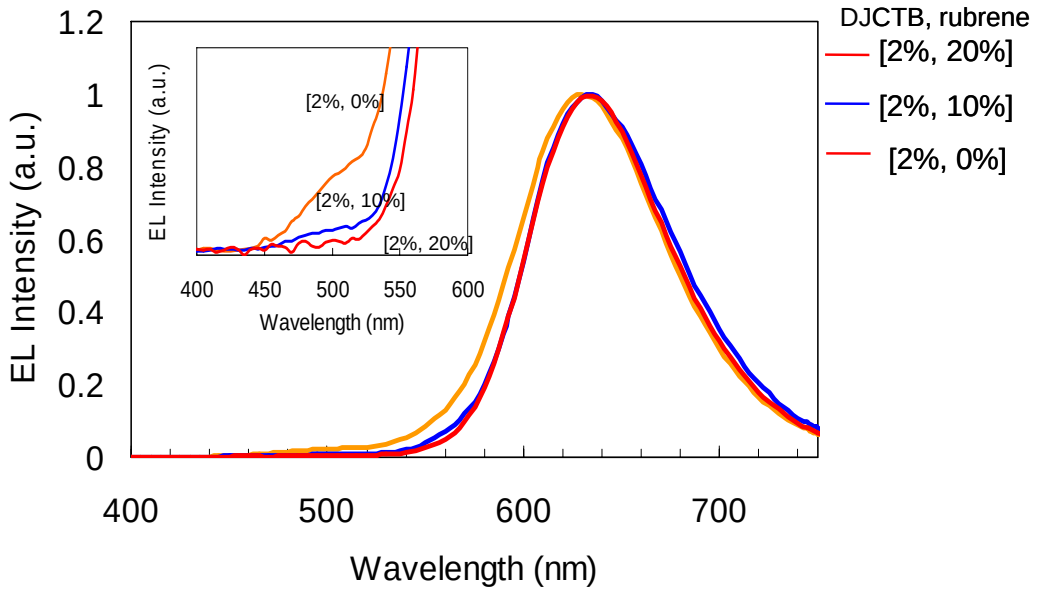

Figure 3-3. Top: Photoluminescence of the [2,0], [2,10], and [2,20] devices and the inset shows the magnified spectra. Bottom: Electroluminescence of the same device shown in the top fiture. The inset shows the magnified spectra.

As to the emission mechanism in the rubrene doped devices, the following process reasonably explains the mechanism. It is dominant with a low doping concentration of rubrene or without it, injected carriers recombine on the host molecules (Alq) and form Alq excitons. Energy is transferred from Alq to DCJTB via rubrene. In the case of [2:0] device, the emission from Alq occurs because of a relatively large difference of energy gaps between Alq and DCJTB.

Figure 3-4 shows the energy diagram of the device with rubrene. The HOMO and LUMO energies of rubrene are between those of Alq. Accordingly, injected carriers on the Alq molecules are transferred into the HOMO and LUMO levels of rubrene and recombination of carriers occurs on the rubrene molecules. However, as the concentration of rubrene increases, the carriers probably recombine more dominantly on rubrene and then energy is favorably transferred to DCJTB [9,10]. Because the HOMO and LUMO levels of DCJTB are nearly equal to those of rubrene, the energy transfer from rubrene to DCTJB occurs with a minimum energy barrier, resulting in enhanced an efficiency, lowered a driving voltage, suppression of an emission from Alq.

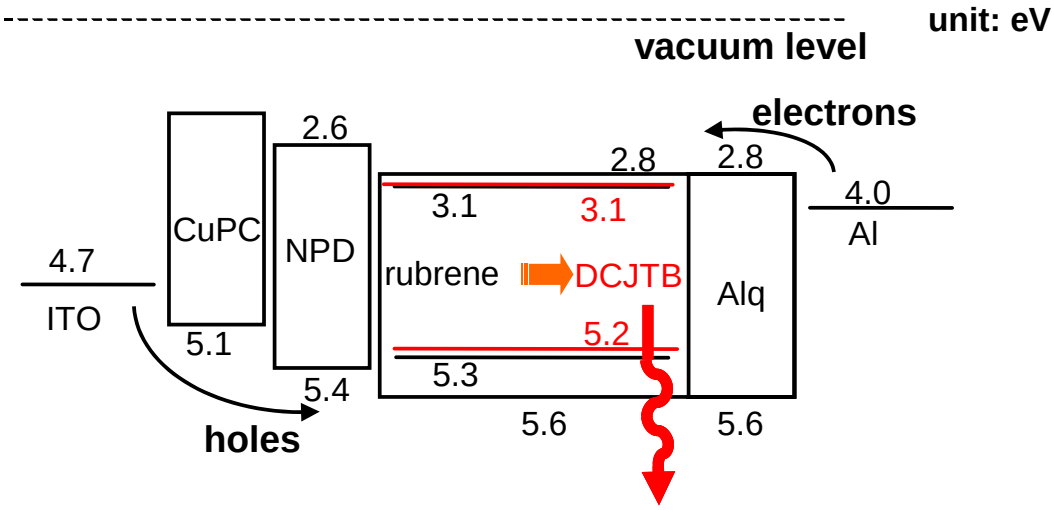

Fiure3-4. The proposed energy diagram of the fluorophore sensitized red OLEDs.

3.1.2 Phosphorescent dye sensitization

Recently, development of phosphorescent materials and devices has become a major focus since the reduction of power consumption is a big issue to be solved from a commercial point of view. There have been extensive studies directed to achieving high efficiency and stability with phosphorescent materials [11]-[14]. For example, an OLED employing phosphorescent organometallic Ir complex exhibited red emission with efficiency of 17.6 cd/A, CIE coordinates (x=0.61, y=0.38) and stability of 5,000 hours from Lo=300 cd/m^2 [13]. Hence, it is very important to find that how much the red phosphorescent OLEDs are advantageous compared to the best fluorescent red OLED, which is described in the previous section.

In this section, the sensitization employing phosphorescent material aiming at a high efficiency is studied (see Fig 3-5) in addition to the fluorophore-sensitization mentioned in the previous section. In the device, electron-hole recombination creates singlet (S) and triplet (T) excitons in the host material, although as indicated, charge trapping may be responsible for exciton formation in the other materials also. Ideally, all excitons are ultimately transferred to the triplet state of the phosphorescent emitter, as triplets in the sensitizer emit light which is not pure red. By increasing the concentration of the sensitizer relative to the phosphorescent emitter, we maximize the number of triplet excitons that participate in energy transfer to the singlet state of the fluorescent dye both via Dexter and Förster mechanism.

By the mechanism, we expect the improved lifetime as well as high efficiency since the stability of the phosphor-based OLED is significant problem.

Host material CBP is doped with $Ir(piq)_3$ [11] and $Ir(phq)_3$ [15] and the L-I-V characteristics and operational stabilities are examined. The structure of red device is [ITO (85nm) / CFx (1.0nm) / NPD (150nm) / CBP : $Ir(piq)_3$: $Ir(phq)_3$ (25nm) / BAlq (10nm) / Alq (40nm) / LiF (1nm) / Al (20nm)]. In the structure, $Ir(piq)_3$ and $Ir(phq)_3$ are Ir complexes. $Ir(piq)_3$ and $Ir(phq)_3$ have PL λmax at 637nm, 628nm respectively measured in a thin film of doped CBP. The device performance is summarized in Table 3-1.

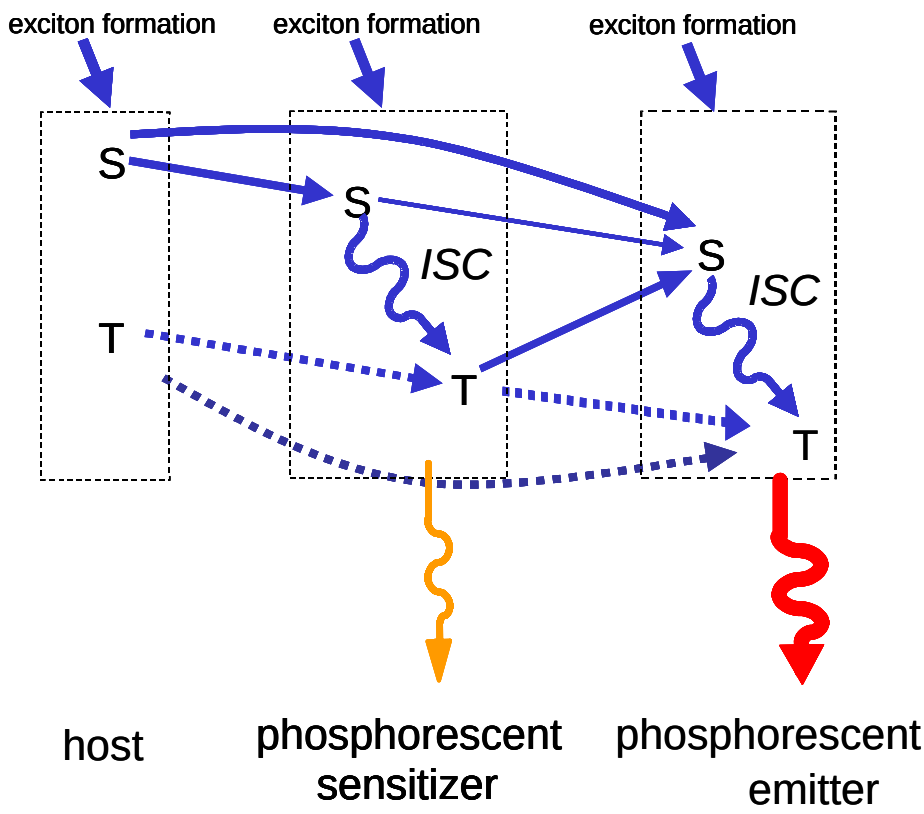

Figure 3-5. Proposed energy transfer mechanisms in the sensitized system. Dipole-dipole coupling (Förster) transfers are represented by solid lines and hopping (Dexter) transfers by dotted lines. Electron-hole recombination creates singlet (S) and triplet (T) excitons in the host material, although as indicated, charge trapping may be responsible for exciton formation in the other materials also. Ideally, all excitons are ultimately transferred to the triplet state of the phosphorescent emitter, as triplets in the sensitizer emit light which is not pure red. By increasing the concentration of the sensitizer relative to the phosphorescent emitter, we maximize the number of triplet excitons that participate in energy transfer to the singlet state of the fluorescent dye both via Dexter and Förster mechanism.

With increasing the doping concentration, the current efficiency increased to 17.1 cd/A and the peak EQE of 11.6%±1% is obtained with the 1.0 % - $Ir(piq)_3$ and 9.0 % - $Ir(phq)_3$ - doped device (corresponding to [1.0, 9.0]). Unlike with the fluorophore sensitizer described in the previous section, $Ir(phq)_3$ emits even at slight concentration as shown in Fig. 3-7 where a shoulder in short wavelength grows as an increasing doping concentration of $Ir(phq)_3$.

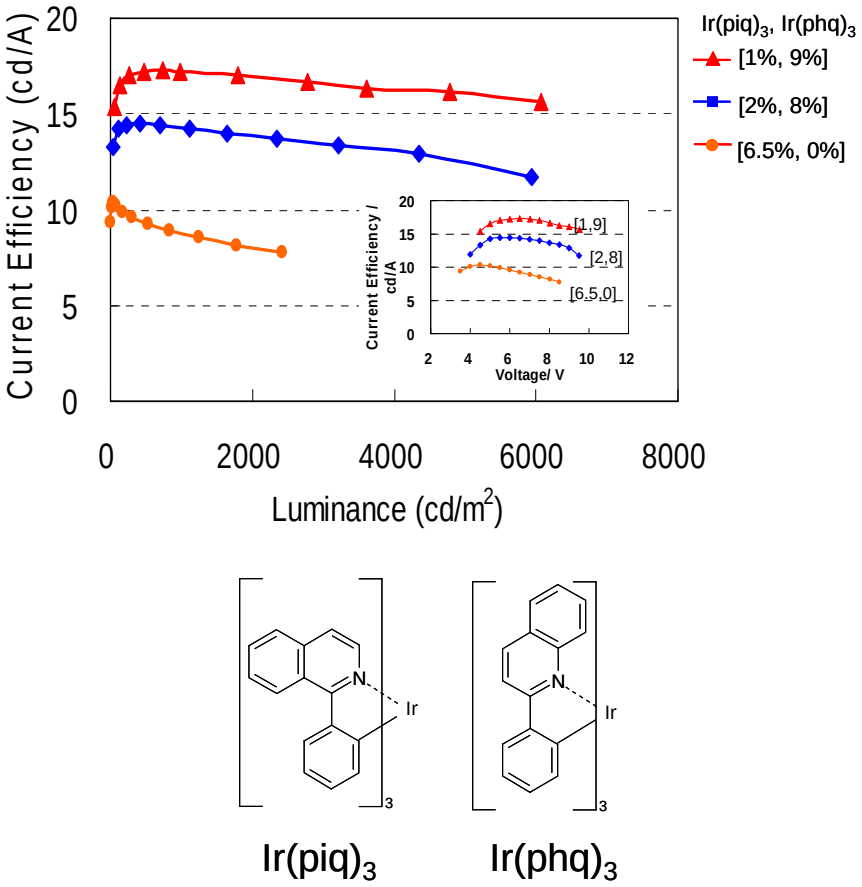

Figure 3-6. Top: Current efficiency – luminance of [1.0, 9.0], [2.0, 8.0], and [6.5, 0] devices. Bottom: Chemical structures of phosphorescent emitters.The device structure is The structure of red device is [ITO (85nm) / CFx (1.0nm) / NPD (150nm) / CBP : $Ir(piq)_3$: $Ir(phq)_3$ (25nm) / BAlq (10nm) / Alq (40nm) / LiF (1nm) / Al (20nm)].

Table 3-1. The device performances with various doping concentrations of a phosphor sensitizer and an emissive phosphorescent dopant at 20mA/cm^2.

			Device performance at the current density of 20mA/cm^2						
Device	$Ir(piq)_3$ (%)	$Ir(phq)_3$ (%)	Voltage (V)	Current Efficiency (cd/A)	Power Efficiency (lm/W)	CIE x	CIE y	$_{out}$	lumina (cd/m
[6.5: 0]	6.5	0	8.4	8.1	3.0	0.67	0.32	5.3%	162(
[6.5: 2.5]	6.5	2.5	7.6	8.6	3.6	0.66	0.34	5.7%	172(
[5.0: 5.0]	5.0	5.0	7.1	9.4	4.2	0.66	0.34	6.3%	188(
[8.0: 2.0]	2.0	8.0	6.9	14.1	6.2	0.64	0.35	9.6%	282(
[9.0: 1.0]	1.0	9.0	6.7	17.1	8.0	0.63	0.36	11.6%	342(

The Fig. 3-7 shows the EL spectra of device [6.5, 0], [2.0, 8.0] and [1.0, 9.0]. The emission from $Ir(piq)_3$ becomes more intense at higher doping in a range from 550 to 620nm. The current efficiency - luminance of these devices are shown in Fig. 3-6. Generally in the case of devices with a phosphorescent emitter, the efficiency at high current density becomes lowered due to triplet – triplet annihilation. A current efficiency over 15 cd/A is obtained over 6,000 cd/m^2 without large change of the efficiency in the device [1.0, 9.0]. Lifetime of the devices is over 2,200 hours from Lo=1,500 cd/m^2 at room temperature, which is equivalent to 5,700 hours from Lo=500 cd/m^2. That stability is found to be one of the best ever reported for phosphorescent red OLEDs. From a PL lifetime study of the EML film, the energy transfer from triplet state of $Ir(phq)_3$ to singlet state of $Ir(piq)_3$ via Förster mechanism (see Chap. 2).

This work shows that the overall characteristics of the phosphorescent red OLEDs are reaching the level of a production use.

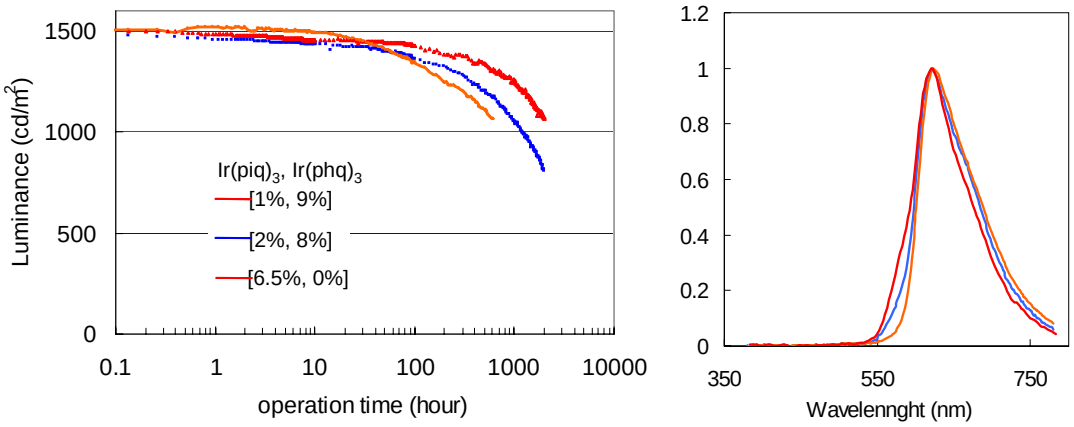

Figure 3-7. Left: The operational stability of the device [1.0, 9.0], [2.0, 8.0], and [6.5, 0]. Right: Electroluminescence of the same devices at 20 mA/cm^2.

3.2 Development of new materials

3.2.1 Emitting Layer

A: Fluorescent Emitting Layer

For achieving low power consumption or high power efficiency in an red OLED, the decreased driving voltage and increased electroluminescence (EL) current efficiency must be realized.[16-22] Red OLEDs comprising red-emitting host layer ordinarily suffer from a strong concentration quenching and have not reached high EL efficiencies over 5 cd/A retaining a high color purity. [16-19] The systems using a red-fluorescent emitter doped in a host material usually result in high driving voltages due to the strong charge trap.[16,19-21]

To obtain the maximum current efficiency from an organic material, it is necessary to harness both the spin-symmetric and anti-symmetric molecular excitations that result from electrical pumping. If the material is phosphorescent this is possible, and high efficiencies have been observed in phosphorescent [23,24] OLEDs. However, phosphorescence in organic molecules is rare at room temperature. The peak EL efficiencies of phosphorescent OLEDs are achievable only at low current densities ($\sim 10^{-1}$ mA/cm^2).[23-28] The EL efficiencies of phosphorescent OLEDs, however, decline drastically at a current range above 10 mA/cm^2 for practical use due to triplet-triplet exciton annihilation.[22-28] Even a high current efficiency was maintained at a high current density in phosphorescent OLEDs, their driving voltage tend to be high. Power efficiency of recently reported phosphorescent red OLED with over 10 % EQE at 20 mA/cm^2 remains at below 5 lm/W because of the high driving voltage.[26] Accordingly, it is important to develop a red OLED with an improved power efficiency at high currents. Red fluorescent emitter dispersed system is suitable for applications which require high brightness, such as large area displays although the alternative process of fluorescence is more common, it is approximately 75% less efficient due to its requirement for spin-symmetry conservation[29]. An efficiency of a red OLED with the most commonly used EML system, DCJTB-doped Alq, is successfully improved by introducing a fluorophore sensitizer as shown in the previous section. A new EML system, however, needs to be developed for drastic improvement of efficiency. In this

section, the red OLED with a high power efficiency and long lifetime using a novel fluorescent emitting layer is described.

Five OLEDs (A–E) including a control device, [ITO/CFx/4,4'-bis-(*N*-phenyl-1-naphthylamino)biphenyl (NPD) (60 nm)/emitting layer (40 nm)/electron-transporting layer (20 nm)/LiF (1 nm)/Al (200 nm)], were fabricated. Figure 1 (a), (b) and (c) show the red OLEDs architecture, chemical structures of tetra-phenyldibenzoperiflanthene (DBP) [30] and 9,10-bis[4-(6-methyl-benzothiazolyl-2-yl)phenyl]anthracene (DBzA) [31] and the energy levels of the highest occupied molecular orbital (HOMO) and lowest unoccupied molecular orbital (LUMO) for NPD, rubrene, DBP, Alq, and DBzA, respectively. The energy levels were determined by cyclic voltammetry and photoelectron spectrometer with Riken Keiki AC-1. Table I summarizes the materials and the performance characteristics for the fabricated OLEDs. Figure 3-9 shows the current density versus applied voltage characteristics for devices A – E together with the EL spectra for devices B and D shown in the inset figure. The classical device A consisting only of NPD and Alq double organic layers reproduces the EQE (~1%) of the ever reported diamine and Alq based devices.[19] The driving voltage of device A is decreased compared to that of the previously reported devices by the introduction of CFx film and LiF/aluminum cathode.[32-34] The device B with a DBP doped Alq emitting layer exhibits significantly high driving voltage compared to device A. In addition, its EL originates from both of Alq and DBP, resulting in very low efficiency. In contrast, device D with a DBP doped rubrene emitting layer shows comparable driving voltage to device C with DBP undoped rubrene emitting layer. The EL spectrum of device D is in good accordance with the photoluminescence spectrum of DBP in solution, exhibiting high color purity with Commission Internationale de I'Eclairage (CIE) coordinates of (0.66, 0.34).

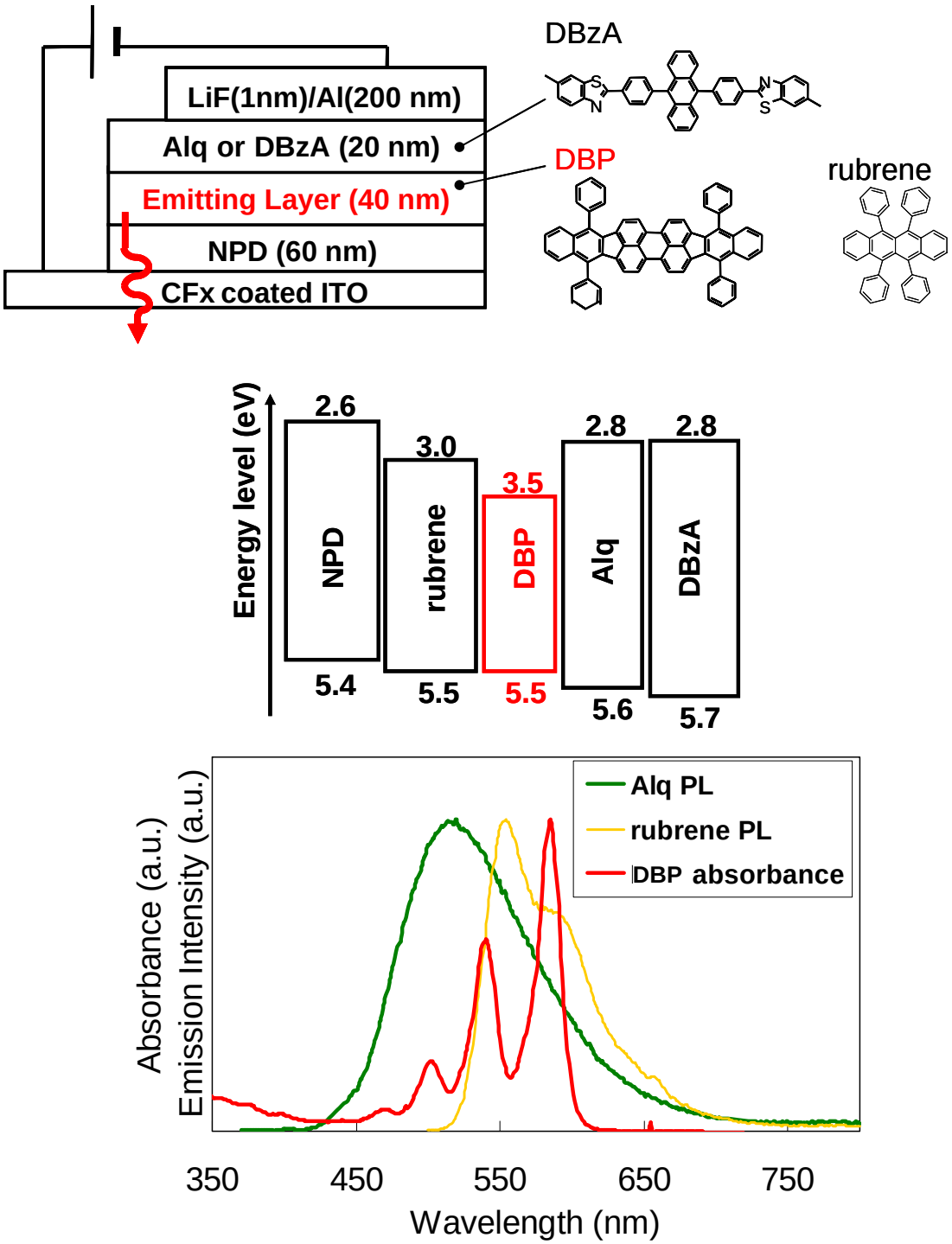

Figure 3-8. Top: The proposed device structure and chemical structures of a fluorescent red emitter, DBP, a host material, rubrene, and a electron transport material DBzA. Middle: The HOMO and LUMO energies of employed materials in the devices shown in this section. Bottom: Photoluminescence spectra of Alq and rubrene and absorption spectrum of DBP in THF solution.

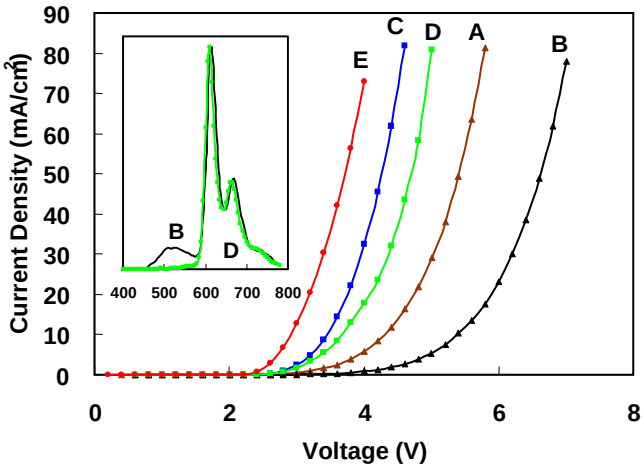

device	EML	ETL
A	Alq	Alq
B	Alq + 1%DBP	Alq
C	rubrene	Alq
D	rubrene + 1%DBP	Alq
E	rubrene + 1%DBP	DBzA

Figure 3-9. I-V characteristics of devices A-E. Inset figure depicts the electroluminescence of devices B and D.

The high driving voltage of device B is due to the charge trapping of DBP due to the large differences in energy levels of HOMO and LUMO between DBP and Alq. The low current efficiency of device B is also originated from the large energy difference because of low efficiency in energy transfer from Alq to DBP. In contrast, device D enjoys the trap-free low driving voltage and high current efficiency due to the energetically favorable host and dopant system with smaller differences in HOMO and LUMO energy levels between DBP and rubrene. We also observe the excellent overlap between the rubrene photoluminescence (PL) and the DBP absorption spectra in THF solution peaking at 554 nm and 585 nm respectively, compared to the case with the Alq (PL peak: 517nm) and DBP. The very low driving voltages of devices C and D are attributed to the excellent hole and electron transporting properties of rubrene.[35]

B: Phosphorescent Emitting Layer

Recently, red phosphorescent OLEDs have been widely investigated since they can achieve high current efficiency.[16,25-28,36] There have been, however, three major problems in a red phosphorescent OLED for practical use. Firstly, an external quantum efficiency or current efficiency of a phosphorescent OLED drastically

decreases at currents *e.g.* over 1 mA/cm^2, which limits the use of red phosphorescent OLED in applications which need high brightness. Picciolo et al. reported that current efficiency of red fluorescent OLED based on 6,13-diphenylpentacene is superior to that of red phosphorescent OLED based on platinum(II) porphine at high currents over 20 mA/cm^2.[22] Secondly, a driving voltage of a red OLED tends to be high, resulting in low power efficiency. Power efficiencies of recently reported phosphorescent red OLEDs with over 10 % external quantum efficiency at 20 mA/cm^2 remain at below 5 lm/W because of high driving voltages. Thirdly, operational stability of a red phosphorescent OLED is not sufficient enough though it has been pointed out that a phosphorescent OLED is potentially more stable than a fluorescent OLED since radiative phosphors shorten the lifetime of potentially reactive triplet exciton.[37]

A driving voltage, efficiency, and durability of an OLED much depend on the host material in an emitting layer (EML), which functions as a bipolar charge transporter, charge recombination site, and exciton energy transporter into emitter. Although many red phosphorescent emitters are reported including iridium and platinum complexes,[3-8] there have been few reports on novel host materials for the use in phosphorescent OLEDs. For improving the device performance by suppressing reverse energy transfer from emitter to host, 4,4'-bis(*N*-carbazolyl)biphenyl (CBP) has been widely used in a red OLED.[25-28,36] However, driving voltages of red OLEDs with CBP host are high because the poor energy matching between CBP and adjacent hole- and electron-transporting layers result in insufficient injection of hole and electron in the EML. Developing host materials other than CBP is important. Tsuji et al. reported that bis(2-methyl-8-quinolinolato)(biphenyl-4-olato)aluminum (BAlq) is successfully applied in a red phosphorescent OLED with an improved driving voltage, efficiency, and long lifetime.[38] And Tsuzuki et al employed an Ir complex for a phosphorescent red emitter.[39] Here we report the red phosphorescent OLED with further improved

efficiency and durability making use of bis[2-(2-benzothiazoyl)phenolato]zinc(II) ($Zn(BTP)_2$) [40] as a host material in an EML.

Figure 3-10 (Left) shows the simple architecture of the present red OLEDs consisting of three organic layers without an additional blocking layer, together with the chemical structures of the employed host materials and $Ir(piq)_3$. Table I summarizes the performance characteristics for the present OLEDs with various host materials. Devices F – I emit pure red EL originating from $Ir(piq)_3$ with CIE coordinates of (0.67, 0.33). Device J using a TBADN host, however, emits very weak blue light originated from TBADN. It is implied that a host material that serves efficiently in fluorescent OLED does not necessarily performs its function well in phosphorescent OLEDs.[41] It is found that device H using $Zn(BTP)_2$ host exhibited significantly lower driving voltage compared to devices F and G using previously reported CBP and BAlq, respectively. The low driving voltage of devices H and I is attributed to the better energy matching in HOMO energies of $Zn(BTP)_2$ and NPD and also in LUMO energies of $Zn(BTP)_2$ and DBzA. The low driving voltage is also attributed to the excellent electron injection properties of DBzA, which will be described in the next section. The current and external quantum efficiencies of device H are significantly higher than those of device F with CBP host overt a wide current range though they are slightly lower than those of device G with BAlq host. The efficiencies are improved in device I using 30% NPD-doped $Zn(BTP)_2$ host. Device I exhibited high current efficiency of 9.8 cd/A and low driving voltage of 3.2 V at a current density of 10 mA/cm^2, realizing a high power efficiency of 9.6 lm/W, which is among the highest values in the ever reported red OLEDs.

Figure 3-10 (Right) shows the PL spectra for the employed host materials and absorption spectrum of $Ir(piq)_3$. The high performance of $Zn(BTP)_2$ host and poor performance of TBADN are not explained by the spectra, since the PL spectra of

$Zn(BTP)_2$ and TBADN locate at the similar wavelength. This suggests that Forster energy transfer between the hosts and $Ir(piq)_3$ plays a minor role in the electroluminescence processes. The triplet exciton energy of $Zn(BTP)_2$ is estimated to be 2.5eV by phosphorescence at T=8 K (see Fig. 3-11). The triplets in $Zn(BTP)_2$ can be energetically transferred to the triplet excited states (λ_{max}=620nm) of $Ir(piq)_3$, leading to high PL efficiency from $Ir(piq)_3$. Also, since an NPD layer has an triplet energy at 2.3eV, the mixed layer of $Zn(BTP)_2$ and NPD (Device I) can also provide high efficiency PL from $Ir(piq)_3$. On the other hand, the phosphorescence from TBADN is not observed at T=8 K in the range from 400 to 650 nm, suggesting that the triplet energy of TBADN is lower than 1.9 eV, resulting in no EL emission in the $Ir(piq)_3$: TBADN film (Device J).

Here, we note that the EL efficiency with an $Ir(piq)_3$: CBP layer is half values of other devices, although the previously reported $Ir(piq)_3$ - based device exhibited a external qEQE of over 10%.[36] Therefore, unbalanced hole and electron injection into the emitter layer or energy transfer from $Ir(piq)_3$ into the adjacent electron transport layer of DBzA leads decrease in EL efficiency.

Figure 3-12 shows the luminance decay and voltage rise curves for devices F – J at a constant direct current of 80 mA/cm^2. The lifetime for devices F – H with single host is increased in the following order; device F with CBP host < device G with BAlq host < device H with $Zn(BTP)_2$. Moreover, device I with 30% NPD-doped $Zn(BTP)_2$ host exhibits approximately doubled lifetime of 250 hour compared to device H with

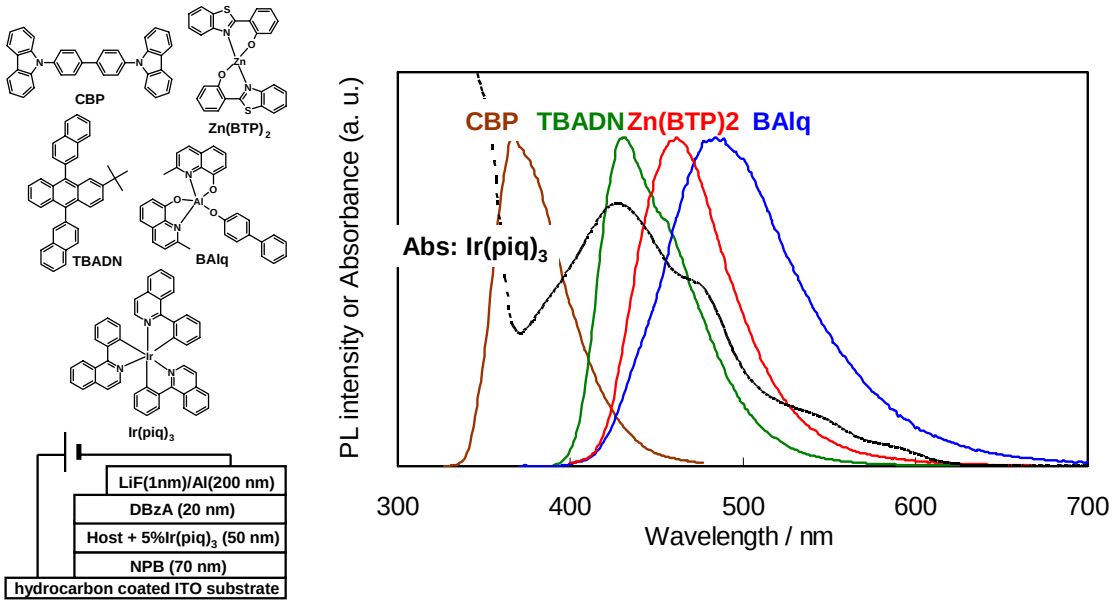

Figure 3-10. Left: Five OLEDs (F – J) with different host materials were fabricated, fluorocarbon coated ITO/NPD (70 nm)/Host : 5% $Ir(piq)_3$ (50 nm)/DBzA (20 nm)/LiF (1 nm)/Al (200 nm). The employed host materials for devices A, B, C, D, and E are CBP, BAlq, $Zn(BTP)_2$, Zn(BTP)2 : 30% NPD, and 2-*tert*-butyl-9,10-di(2-naphthyl)anthracene (TBADN), respectively. Right: PL Spectra for the employed host materials and absorption spectrum of $Ir(piq)_3$.

$Zn(BTP)_2$ single host. The voltage rise of device I is effectively suppressed compared to device F, G, and H. The improvements are attributed to the NPD in the EML which stably accepts hole, preventing degradation of n-type $Zn(BTP)_2$.[33]

In conclusion, we have revealed that $Zn(BTP)_2$ is successfully applied as a host in a red phosphorescent OLED. The red OLED making use of $Zn(BTP)_2$ host exhibits superior performance compared to the red OLED with ever reported CBP or BAlq host materials. The triplet state where the energy is transferred to that of phosphorescent emitter is found to be important for a phosphorescent EML to study the triplet energy transfer.

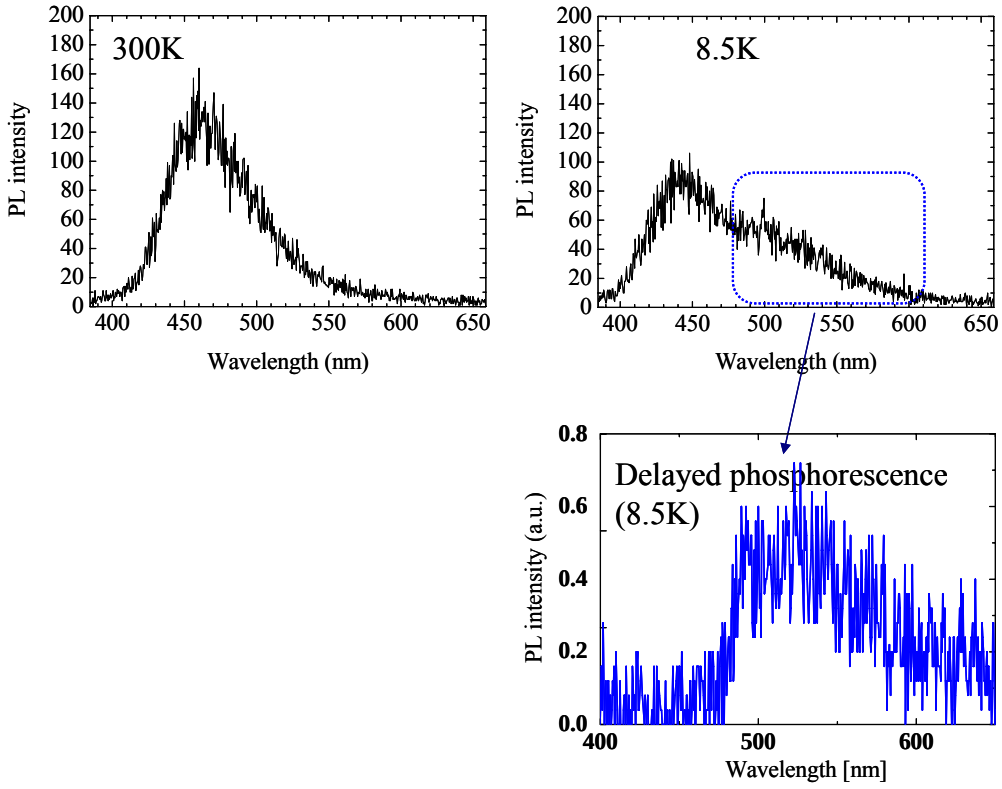

Figure 3-11. PL of Zn(BTP)2 at 300K and 8.5K. The delayed phosphorescent is shown in the bottom.

Table 3-2 The performance characteristics at a current density of 10 mA/cm^2 for the present organic light-emitting devices (hydrocarbon coated ITO /NPD (70 nm)/Host : 5% Ir(piq)$_3$ (50 nm)/DBzA(20 nm)/LiF (1 nm)/Al) depending on the host material.

device	Host	Voltage (V)	Chromaticity	Current Efficiency (cd/A)	Power Efficiency (lm/W)	External Quantum Efficiency
F	CBP	7.2	(0.67, 0.33)	2.3	5.2	6.1%
G	BAlq	5.2	(0.67, 0.33)	5.5	9.1	11.0%
H	Zn(BTP)$_2$	3.2	(0.67, 0.33)	8.6	8.8	10.3%
I	Zn(BTP)$_2$: 30%NPD	3.2	(0.67, 0.33)	9.6	9.8	11.7%
J	TBADN	4.6	(0.20, 0.15)	0.0	0.0	0.0%

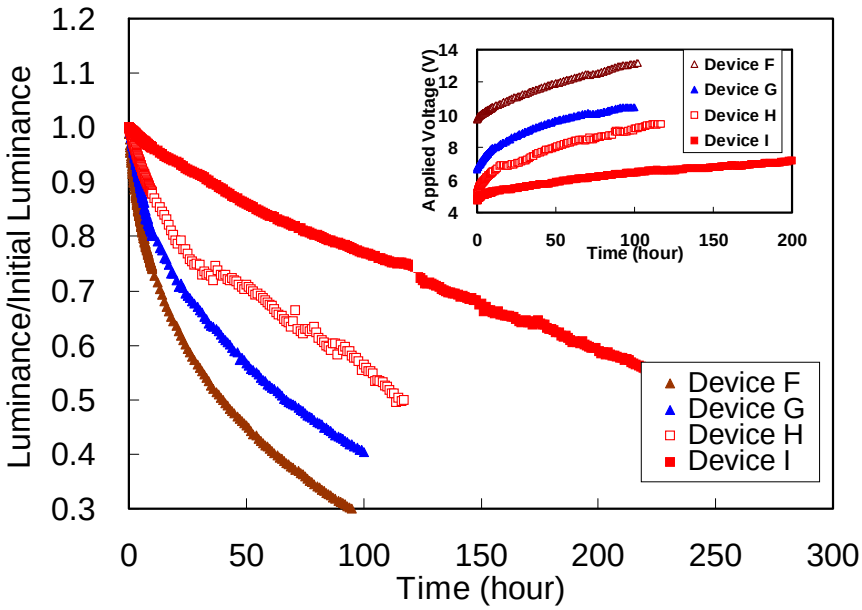

Figure 3-12. The operational stability of the devices shown in Fig3-10 at 80 mA/cm2. Inset: The voltage rise of the same devices

3.2.2 Electron Transport Layer

The remaining problems are to develop ETL materials for lowering drive voltage and long lifetime. The lowered drive voltage is attributable not only to the reduction in carrier injection barrier but also to the increase of charge carrier mobility. The electron mobility of an ETL in an OLEDs is know to be lower than that of the hole mobility of an HTL. Figure 3-13 shows the chemical structures of the typical electron transporting materials and the electron mobilities reported by Yasuda et al [42], using SCLC (Space Charge Limited Current) method. The electron mobility of Alq is much smaller as compared to that of the hole transporting material, NPD, which is about 10-3 cm2/Vs. On the other hand, the use of an ETL material such as BCP or OXD-7 is not encouraged since operational stabilities of devices with those materials are very poor. That is primarily due to recrystallization of the materials. Thus, it is very important to find a new class of electron transporting material and to achieve a high performance realizing the hole-electron carrier balance in an EML.

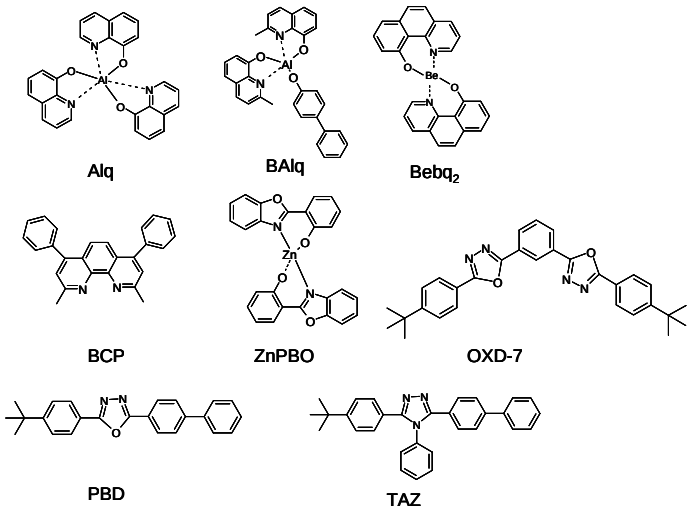

ETL material	(cm^2/Vs)
Alq	4.7×10^{-6}
ZnPBO	2.1×10^{-5}
BCP	1.1×10^{-3}
OXD-7	2.1×10^{-5}
PBD	1.9×10^{-5}

Figure 3-13. Chemical structures of electron transporting materials and their electron mobilites [Ref 42].

In this section, we propose the new class of electron transport material, which is DBzA (see Fig. 3-9). In the previously mentioned devices A-E shown in Fig. 3-9, DBzA electron-transporting layer in place of an Alq electron transporting layer exhibit a high efficiency (see table3-3). The current and power efficiencies of 5.4 cd/A and 5.3 lm/W at 20 mA/cm^2 for device E is ones of the highest value among the red fluorescent OLEDs which have ever been reported. [2-13] The current efficiency of 5.4 cd/A and the CIE coordinates of (0.66, 0.34) for device E remain almost unchanged to the high currents over 100 mA/m^2. Figure 3-14 shows current density versus applied voltage characteristics of the hole- and electron-only devices to study the carrier transport in 200-nm-thick Alq and rubrene. Both of hole- and electron-only devices of rubrene show much improved injected current compared to those of Alq based devices. These results indicate that DBP doped rubrene emitting layer is potentially the excellent host material for realizing high current efficiencies and low driving voltages. Moreover, it is inferred that injected hole flux exceed to electron flux in device D by the comparison of voltage

at current regions over 1 mA/cm^2 for rubrene-based hole- and electron-only devices. The electron only device using DBzA as an electron injection layer much improves electron injection compared to the countepar with Alq as an ETL.

Table 3-3. Device performances comparing various EMLs and ETLs. The values are measured at 20 mA/cm^2.

Device	EML	ETL	Voltage (V)	CIE(x、y)	Current Efficiency (cd/A)	Power Efficiency (lm/W)	External Quantum Efficiency
A	Alq	Alq	4.7	(0.31, 0.56)	3.4	2.2	1.10%
B	Alq + 1%DBP	Alq	6.1	(0.60, 0.37)	0.4	0.2	0.30%
C	rubrene	Alq	3.8	(0.49, 0.50)	0.5	0.4	0.20%
D	rubrene + 1%DBP	Alq	3.9	(0.66, 0.34)	2.1	1.7	1.70%
E	**rubrene + 1%DBP**	**DBzA**	**3.2**	**(0.66, 0.34)**	**5.4**	**5.3**	**4.70%**

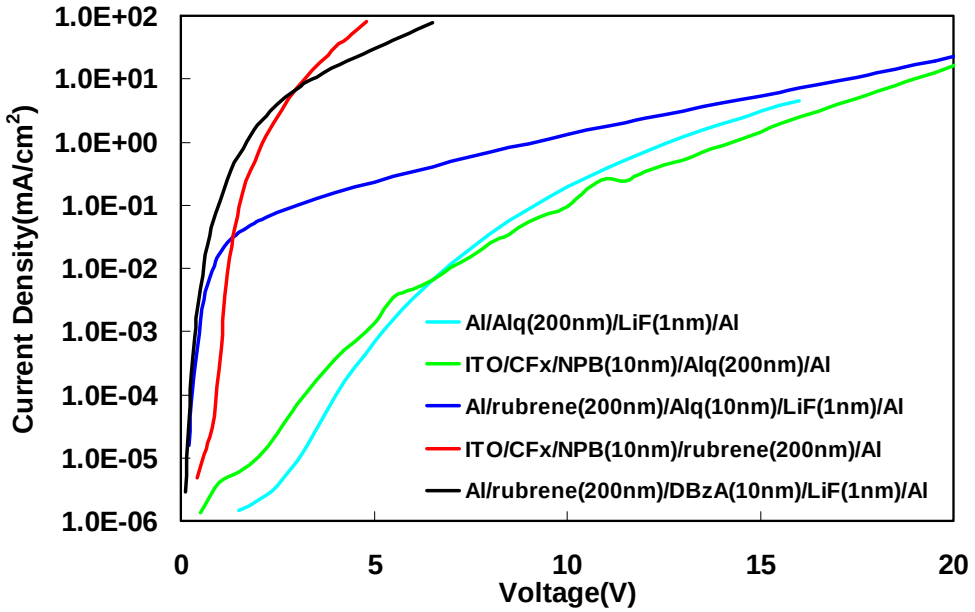

Figure 3-14. I-V characteristics of hole-only devices and electron-only devices. Hole-only devices ITO/CFx/NPD (10 nm)/rubrene or Alq(200 nm)/Al and electron -only devices Al / rubrene (0 or 200 nm)/Alq or DBzA (10 nm)/LiF (1 nm)/Al.

The better balance of injected hole and electron fluxes would be the reason for the enhanced current efficiency of device E (by a factor of 2.5) compared to device D.

Figure 3-15 shows the luminance decay curves together with the voltage rise curve at a current density of 80 mA/cm^2 for devices D and E, corresponding to the initial luminances of 1570 and 3570 cd/m^2, respectively. The half-luminance time for device D and E were estimated to be 1,000 hour and 223 hours, respectively. The driving voltage of the devices was very stable being less than 0.2 V rise per 100 hour. The relationship between lifetime and initial luminance is generally expressed by eq (1).

$$(L_1/L_2)^n = k(\tau_1/\tau_2) \quad (1)$$

where L_1 and L_2 are initial luminances, τ_1 and $\tau 2$ are corresponded lifetimes to L_1 and L_2, respectively, n is the acceleration coefficient, and k is a constant. We have obtained n = 1.5 ~ 1.7 for various fluorescent OLEDs in our previous study,[20] which is in good accordance with the studies by Féry et al.[21] When applied n = 1.6 to the present OLED, the half lifetimes of the devices D and E at an initial luminance of 100 cd/m^2 are 82,000 and 68,000 hours, respectively. It is implied that the present red

OLEDs are promising for practical application in view of low power consumption and long lifetime.

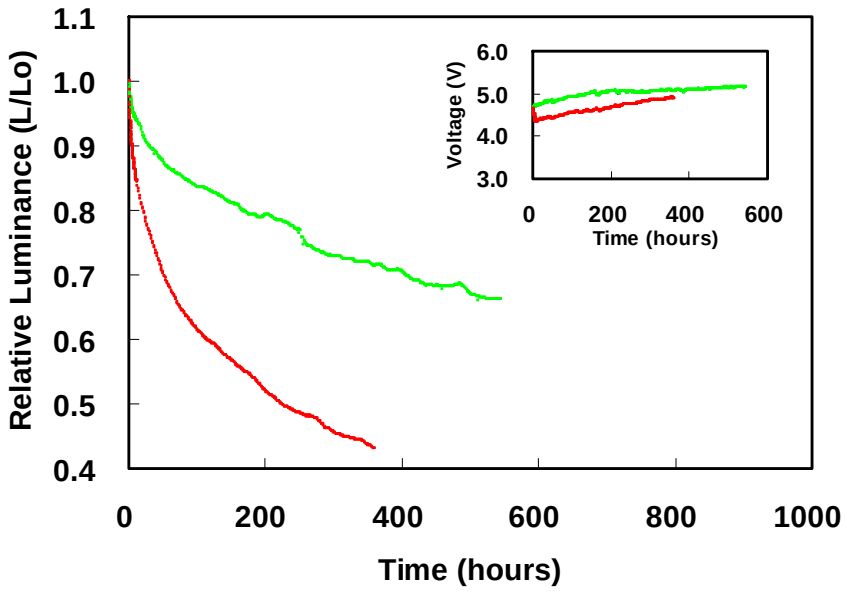

Figure 3-15. Luminance decay curves of device D (green solid line) and E (red solid line) with DBzA and Alq, respectively at a current density of 80 mA/cm^2. Inset shows the voltage rise of the same devices.

In this section, high efficiency fluorescent red OLEDs using DBP doped rubrene as a novel emitting layer is described. As shown in Fig. 3-16, hole injection barrier of rubrene is smaller than that of Alq and electron injection to rubrene is energetically more favorable. These fact well explain the lower driving voltage and higher power efficiency than those of the red OLED with an Alq host. Furthermore, the fluorescent energy transfer is efficient without a sensitizer with the smaller energy gap between DBP and rubrene.

The CIE coordinates are (0.66, 0.34) without color shift over a wide range of current densities. By introducing an electron transporter, DBzA, the current and power efficiencies of 5.4 cd/A and 5.3 lm/W are obtained. Moreover, the red OLEDs exhibit a long lifetime.

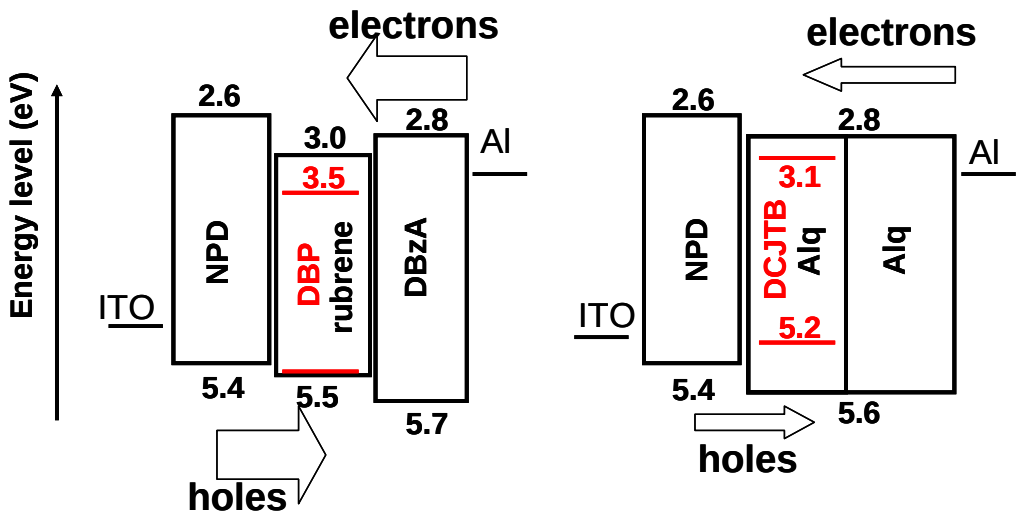

Figure 3-16. The proposed energy diagrams of the devices with the novel EML (Left) and the conventional EML (Right), respectively.

3.2.3 Hole Transport Layer

For OLEDs based on low molecular-weight organic compounds, many classes of organic compounds have been investigated as EMLs and ETLs although arylamine derivatives have been principally used as HTLs for the following reasons.[43-47]

(i) The hole mobility of a triarylamine derivative is high enough for achieving OLEDs with low driving voltages.

(ii) The energy level of the highest occupied molecular orbital (HOMO) of a triarylamine derivative is low enough for an efficient hole injection from an anode such as indium tin oxide (ITO).

(iii) The energy level of the lowest unoccupied molecular orbital (LUMO) of a triarylamine derivative can be high enough for blocking electron leaking from an EML, leading to a higher electroluminescence (EL) efficiency.

(iv) The energy gap between HOMO and LUMO of a triarylamine derivative is wide enough for blocking exciton leaking from an EML, leading to higher EL efficiency.

(v) The cation radicals of a triarylamine derivative are stable, which is one of the material requirements of HTL for long lifetimes.

It is a subject of significance to find a new class of materials for an HTL in OLEDs, in other words, to expand the material selectivity of an HTL in OLEDs for optimizing the device performance. There have been, however, very few reports of OLEDs using materials other than triarylamine derivatives as HTLs. [48,49] Sano et al. reported that pyrazoline derivatives function well as an HTL in contact with ITO anode in OLEDs.[48] Wu et al. investigated the hole-transporting properties of furan-containing oligoarylene and applied it as an HTL in contact with a hole injection layer comprising poly(3,4-ethylendioxythiophene)/poly(4-stylenesulphonate) in OLEDs.[49] However, it is not clearly discussed in the literatures that how much the device performance is improved by using the new class of the materials as an HTL in OLEDs instead of conventional arylamine derivatives.

Polyacene derivatives, including anthracene and naphthacene derivatives, have been successfully employed as host or guest materials of EMLs in OLEDs.[50,51.41] They allow for stable and durable OLED operations as well as superior EL efficiencies. They are also characterized by the excellent charge transporting properties. A naphthacene derivative, 5,6,11,12-tetraphenylnaphthacene (rubrene) has been reported to exhibit very high hole mobility of over 0.1 cm^2/V s in thin film transistors.[35] Charge transport properties of anthracene derivatives have not been investigated in detail. However, the low driving voltages of the OLEDs with an EML consisting of anthracene derivatives indicate that they are excellent charge transporter.[41] It is expected that OLEDs with higher operational stabilities and lower driving voltages can be achieved if such polyacene derivatives are successfully introduced as HTLs in OLEDs. Here, we report that polyacene derivatives are able to serve efficiently as HTLs in OLEDs. Three polyacene derivatives, 2-*tert*-butyl-9,10-di(2-naphthyl)anthracene (TBADN), 9,9',10,10'-tetraphenyl-2,2'-bianthracene (TPBA), and rubrene are investigated.

Figure 3-17 shows the cyclic voltammograms for TBADN, TPBA, and rubrene. All of the polyacene derivatives are found to undergo both of reversible anodic oxidation and cathodic reduction to form stable cation and anion radicals, respectively.[52] Thus, these compounds are able to generate stable cation and anion radicals. It is expected that the polyacene derivatives are stable when they accept holes and electrons in OLEDs.

Table I summarizes the oxidation and reduction potentials, HOMO and LUMO energy levels, and HOMO – LUMO energy gaps for NPD, TBADN, TPBA, and rubrene, based on the cyclic voltammetry. The HOMO and LUMO energy levels are important for facilitating a hole injection from anode and blocking electrons leaking from an EML, respectively, when they are applied as HTLs in OLEDs. The HOMO – LUMO energy gap of the materials are decreased in the order, NPD ~ TBADN > TPBA > rubrene, which reflects the length of π-electron conjugation in the molecules.

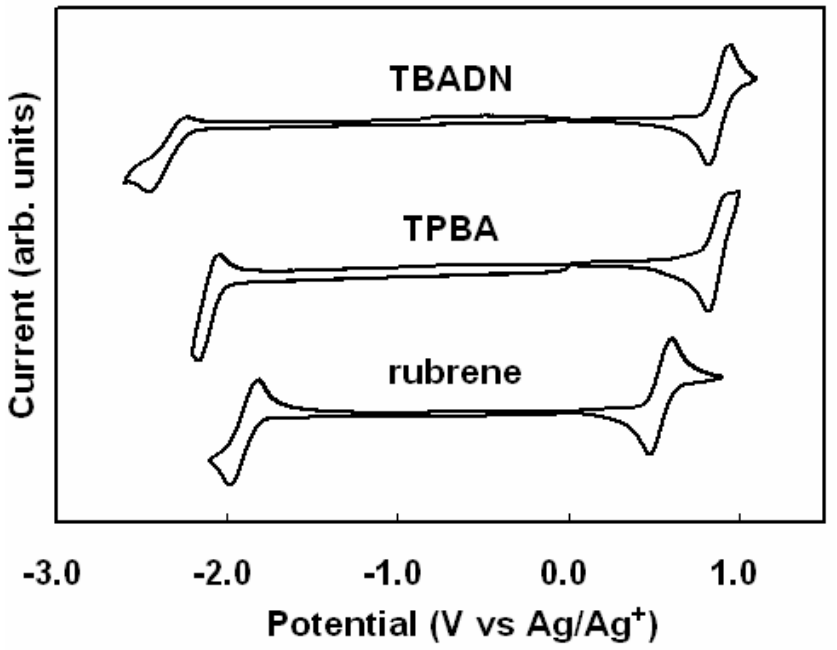

Figure. 3-17. Cyclic voltammograms of TBADN, TPBA, and rubrene. Measured in dichloromethane (for oxidation) and THF (for reduction). Scan rate: 100 mV/s.

Table3-4. Half-wave oxidation and reduction potentials ($E_{1/2}^{ox}$ and $E_{1/2}^{red}$), HOMO and LUMO energy levels, and HOMO – LUMO energy gaps for NPB, TBADN, TPBA, and rubrene.

compound	$E_{1/2}^{ox}$ (V *vs.* Ag/Ag^+)[a]	$E_{1/2}^{red}$ (V *vs.* Ag/Ag^+)[a]	HOMO energy level (eV)[b]	LUMO energy level (eV)[b]	HOMO – LUMO energy gap (eV)[c]
NPB	0.48	-2.66	5.40	2.26	3.24
TBADN	0.89	-2.35	5.81	2.57	3.24
TPBA	0.87	-2.11	5.79	2.81	2.99
rubrene	0.55	-1.91	5.47	3.01	2.46

[a]Determined by cyclic voltammetry in dichloromethane (for oxidation) and THF (for reduction) with $Ag/AgNO_3$ (0.01 M) as a reference electrode. Scan rate: 100 mV/s. [b]Determined as HOMO energy level of NPB is 5.40 referenced to vacuum, which was measured with a photoelectron spectrometer with a Riken Keiki AC-1 [c]Determined from the oxidation and reduction potentials.

Five OLEDs (A–E) including a control device have been fabricated, [ITO/CFx/HTL (60 nm)/1% tetraphenyldibenzoperiflanthene (DBP) doped rubrene (40 nm)/tris(8-quinolinolato)aluminum (Alq) (20 nm)/LiF (1 nm)/Al (200 nm)]. The HTLs of the devices A- D, and E are NPD, TBADN, TPBA, rubrene, and Alq, respectively. Figure 3-18 depicts the side view of the fabricated OLED and chemical structures of the employed materials. The red EML, 1% DBP doped-rubrene, is chosen in the following reasons. First, the deep-red EML with the very low exciton energy can eliminate the factor of exciton energy transfer from EML to HTL for focusing on hole injection ability of an HTL. The energy transfer from EML to HTL occurs if the rubrene HTL contacts with blue or green EML which generates excitons with larger energy than the HOMO – LUMO energy gap of rubrene. Secondly, the detailed discussion on the charge balance in the device is possible since we previously studied OLEDs with the EML. Thirdly, it is important to develop red OLEDs for a practical use since the EML has been found to exhibit both of high efficiency and operational stability in OLEDs (see the previous section).

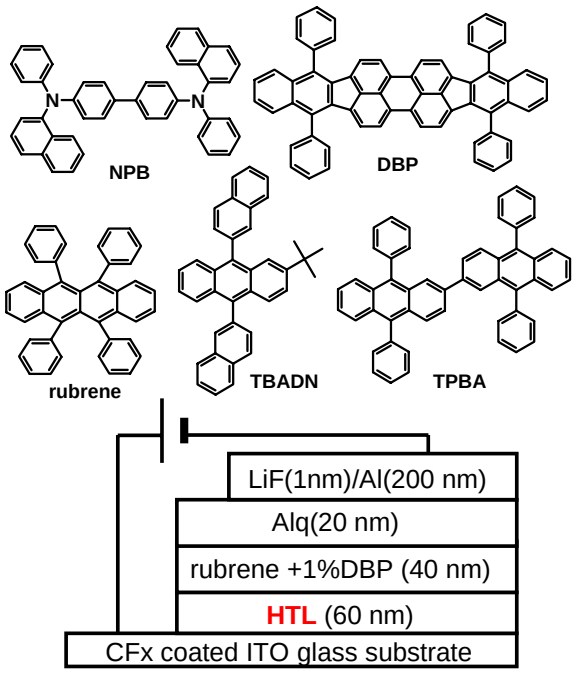

Figure 3-18. Side view of the fabricated OLEDs and chemical structures of the employed materials.

Figure 3-19 shows EL spectra for devices A and E and current density – applied voltage characteristics for devices A – E, and (c) current efficiency – current density characteristics for devices A – E. Table 3-5 summarizes performance characteristics for the devices. Devices A – D exhibit the red EL originated from DBP although device E with the Alq HTL exhibits orange EL from both of Alq and DBP. It is implied that electron easily leaks from the EML into the Alq HTL in device E. The current efficiency of each device is stably high in the wide range of current density of 1~100 mA/cm^2. The current efficiency and driving voltage of each device are much dependent on the employed HTL material. These results indicate that the employed polyacene derivatives, TBADN, TPBA and rubrene, function well in devices B, C, and D, respectively. In contrast, Alq is not able to serve as an efficient HTL in device E. The driving voltages of devices A – E are considered to predominantly reflect the hole injection abilities of the materials used for an HTL. From this viewpoint, hole injection ability is decreased in the order, rubrene > NPD ~ TPBA > TBADN > Alq. To study the order of hole injection ability, hole-only devices with the materials are studied.

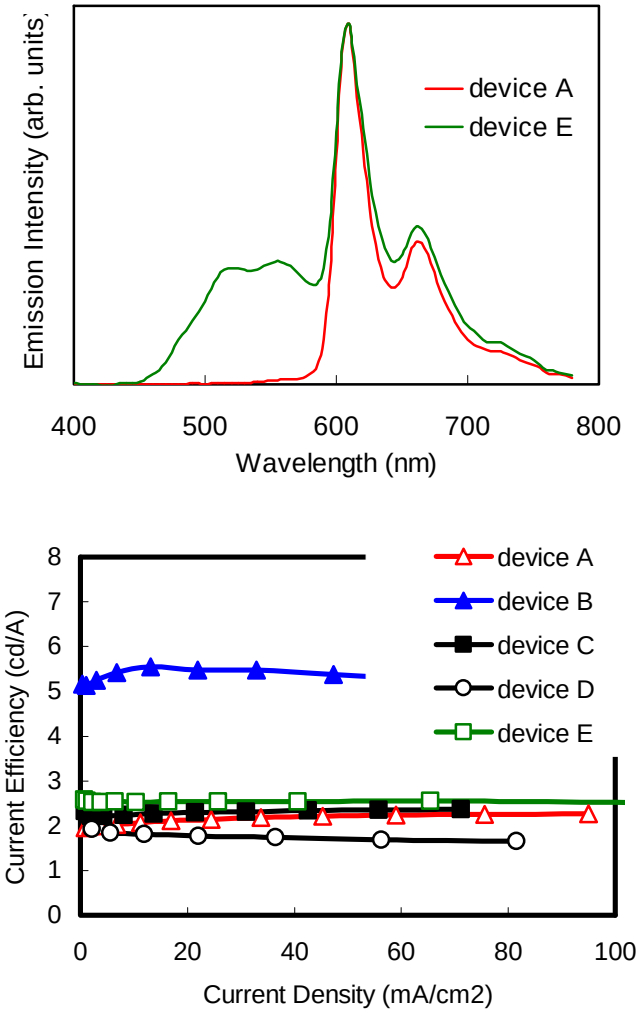

Figure. 3-19. Top: EL spectra for devices A and E. Bottom: Current efficiency – current density characteristics for devices A – E. The device structure is shown in Fig. 3-18
The HTL material, NPD, TBADN, TPBA, rubrene, and Alq, are used in A-E devices, respectively.

The order of hole injection ability of polyacene derivatives is also in accordance with the order of their oxidation potentials. This is attributed to the improved hole injection from ITO anode into a polyacene derivative with the lower oxidation potential since the better alignment of the work function of ITO (5.2 eV) and HOMO energy level of HTL is achieved.[53]

There is a pronounced tendency in Table II that an OLED with a higher driving voltage

exhibits a higher current efficiency in devices A-D. This is attributed to the improvement in the balance of injected flux of holes and electrons in the OLED with reduced hole injection. This explanation is based on the hypothesis that hole flux exceeds to electron flux in a conventional OLED with NPD and Alq, which is in good accordance with our previous study of OLEDs employing 1% DBP doped-rubrene EMLs.

TABLE 3-5. Performance characteristics at a current density of 20 mA/cm^2 for OLEDs A – E (ITO/CFx/HTL (60 nm)/rubrene + 1%DBP (40 nm)/Alq (20 nm)/LiF (1nm)/Al) depending on the employed HTL materials.

device	HTL	Voltage (V)	Chromaticity[a)]	Current Efficiency (cd/A)	Power Efficiency (lm/W)	External Quantum Efficiency
A	NPB	3.9	(0.66, 0.34)	2.1	1.7	1.7%
B	TBADN	6.2	(0.66, 0.34)	5.5	2.8	4.5%
C	TPBA	4.0	(0.66, 0.34)	2.3	1.8	1.8%
D	rubrene	3.4	(0.66, 0.34)	1.8	1.7	1.5%
E	Alq	9.7	(0.49, 0.45)	2.6	0.9	1.3%

[a)]presented in 1931 Commission Internationale de l'Eclairage coordinate.

Figure 3-20 shows the luminance decay and voltage rise curves for devices A and D driven under a current density of 80 mA/cm^2. The initial luminances are 1583 cd/m^2 and 1208 cd/m^2 for devices A and D, respectively. Device D with a rubrene HTL exhibits much improved luminance lifetime compared to device A with an NPD HTL.

OLEDs employing HTLs consisting of polyacene derivatives have been investigated for the first time. The red OLEDs with DBP doped rubrene EMLs in combination with polyacene derivatives, TBADN, TPBA, and rubrene have been found to emit efficient red EL. Their device performances have been compared to the reference OLED using most widely used arylamine, NPD, as a HTL. The OLED with the TBADN HTL has been found to exhibit much higher current efficiency than the

OLED with the NPD HTL. The TPBA HTL has functioned comparably with NPD HTL in the OLEDs. The OLED using rubrene as an HTL is advantageous in driving voltage and luminance lifetime compared to the reference device with the NPD HTL. The results indicate that the polyacene derivatives are promising for use in OLEDs as a novel class of HTLs, expanding the variety of HTL materials for optimizing the performance of OLEDs.

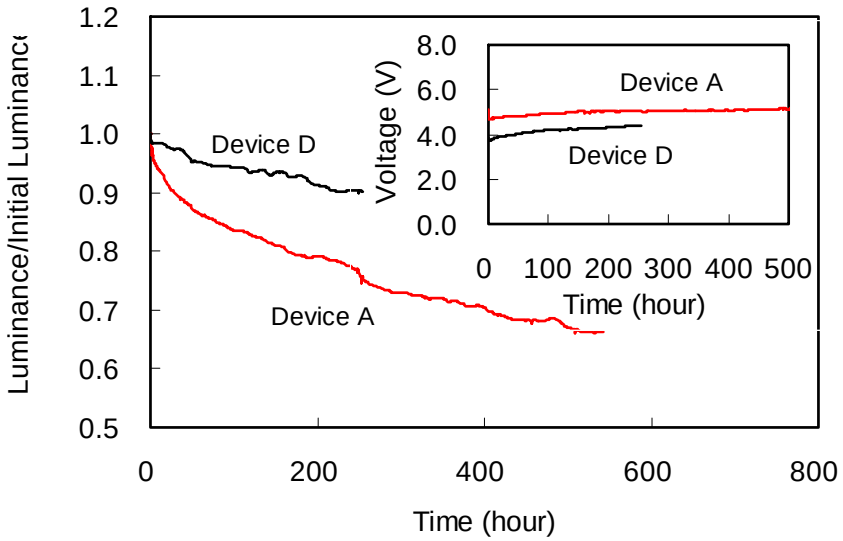

Figure. 3-20. Luminance decay curves for devices A and D at a current density of 80 mA/cm^2. Initial luminances are 1583 cd/m^2 and 1208 cd/m^2 for devices A and D, respectively. Inset: Voltage rise curves for devices A and D.

3.3 Summary

I have shown primarily two pathways for achieving high efficiency red OLEDs. Firstly, we have improved the energy transfer efficiency by introducing a dye sensitizer into the conventional EML system comprised of DCJTB doped Alq. Especially, the original idea that rubrene intermediates fluorescent energy transfer has proved to be very promising method in terms of high efficiency, color stability, low voltage, and long lifetime. Furthermore, I have applied the same concept to phosphor-based red OLEDs successfully. This method has been widely used in the industries already. Though there are few robust emitting materials which shows high stability, the sensitization can totally enhance the device performance without suffering anything.

Secondly, we have developed new classes of materials for red OLEDs. Focusing on materials for a red EML, an ETL, and an HTL, the high-efficiency red fluorescent OLEDs have been obtained. Especially, the EML comprised of rubrene as a host material and DBP as a red emitter has been proposed for the first time. Furthermore, DBzA as a new electron transporting material can be successfully applied with combination of NPD as a hole transporter, which gives an excellent balance of carriers injected into the EML.

Chapter 3. References

[1] C. Adachi, M. A. Baldo and S. R. Forrest, J. Appl. Phys. Lett. 87, 8049 (2000).

[2] P. E. Burrows, S. R. Forrest, T. X. Zhou and L. Michalski, Appl. Phys. Lett. 76, 2493 (2000).

[3] C. W. Tang, in proc. SID International Symposium Digest of Technical Papers, San Diego 181 (1996).

[4] Z. Y. Xie, L. S. Hung and S. T. Lee, Appl. Phys. Lett. 79, 1048 (2001).

[5] C. H. Chen, C. W. Tang, J. Shi, and K. P. Klubek, Thin Solid Films 363, 327 (2000).

[6] B. Chen, X. Lin, L. Cheng, C. S. Lee, W. A. Gambling and S. T. Lee, J. Phys D: Appl Phys. 34, 30 (2001).

[7] W. M. Su, W. L. Li, Z. R. Hong, M. T. Li, T. Z. Yu, B. Chu, B. Li, Z. Q. Zhang, and Z. Z. Hu, Appl. Phys. Lett. **87**, 213501 (2005).

[8] Y. Kawamura, J. Brooks, J. J. Brown, H. Sasabe, C. Adachi, Physical Review Letters 96, 017404.

[9] T. K. Hatwar, G. Rajeswaran, J. Shi, Y. Hamada, H. Kanno and H. Takahashi, in proc. 10th Int. Workshop on Inorg. And Organic Electroluminescence, Hamamatsu 31 (2000).

[10] H. Murata, C. D. Merritt, and Z. H. Kafafi, IEEE J. Select. Topics in Quantum Elect. 4, 119 (1998).

[11] S. Okada, H. Iwawaki, M. Furugori, J. Kamatani, S. Igawa, T. Moriyama, S. Miura, A. Tsuboyama, T. Takiguchi, and H. Mizutani, SID Digest 1360 (2002).

[12] M. Pfeiffer, S. R. Forrest, K. Leo, and M. E. Thompson, Adv. Mater. 14, 1633 (2002).

[13] R. C. Kwong, M. R. Nugent, L. Michalski, T. Ngo, K. Rajan, Y. J. Tung, M. S. Weaver, T. X. Zhou, M. Hack, M. E. Thompson, S. R. Forrest, and J. J. Brown, Appl. Phys. Lett. 81, 162 (2002).

[14] J. J. Lih, C. F. Sung, M. S. Weaver, M. Hack, and J. J. Brown, SID Digest 14 (2002).

[15] K. Saito, N. Matsusue, H. Kanno, Y. Hamada, H. Takahashi, and T. Matumura, Jpn. J. of App. Phys. 43, 2733 (2004).

[16] C. H. Chen, Chem. Mater. 16, 4389 (2004).

[17] W. Wu, H. Yeh, L. Chan, and C. H. Chen, Adv. Mater. 14, 1072 (2002).

[18] S. Chen, X. Su, Y. Liu, G. Yu, X. Sun, W. Qiu, Y. Ma, D. Zhu, Adv. Funct. Mater. 15, 1541 (2005).

[19] C. W. Tang, S. A. VanSlyke, and C. H. Chen, J. Appl. Phys. 65, 3610 (1989).

[20] K. Cheon and J. Shinar, Appl. Phys. Lett. 81, 1738 (2002).

[21] Nuesch, F. et al. Adv. Funct. Mater. 15, 323-330 (2005).

[22] L. C. Picciolo, H. Murata, and Z. H. Kafafi, Appl. Phys. Lett. 78, 2378 (2001).

[23] M. A. Baldo, D. F. O'Brien, Y. You, A. Shoustikov, S. Sibley, M. E. Thompson, and S. R. Forrest, Nature 395, 151 (1998).

[24] M. A. Baldo, S. Lamansky, P. E. Burrows, M. E. Thompson, & S. R. Forrest, *Applied Physics Letters* 75, 4-6 (1999).

[25] C. Adachi, M. A. Baldo, S. R. Forrest, S. Lamansky, M. E. Thompson, R. C. Kwong, Appl. Phys. Lett. 78, 1622 (2001).

[26] C.-L. Li, Y.-J. Su, Y.-T. Tao, P.-T. Chou, C.-H. Chien, C.-C. Cheng, and R.-S. Liu, Adv. Funct. Mater. 15, 387 (2005).

[27] Y.-H. Song, S.-J. Yeh, C.-T. Chen, Y. Chen, Y. Chi, C.-S. Liu, J.-K. Yu, Y.-H. Hu, P.-T. Chou, S.-M. Peng, and G.-H. Lee, Adv. Funct. Mater. 14, 1221 (2004)

[28] C.-H. Yang, C.-C. Tai, and I.-W. Sun, J. Mater. Chem. 14, 947 (2004).

[29] M. A. Baldo, D. F. O'Brien, M. E. Thompson, & S. R. Forrest, Physical Review B 60, 14422-14428 (1999).

[30] J. D. Debad, J. C. Morris, V. Lynch, P. Magnus, and A. J. Bard, J. Am. Chem. Soc. 118, 2374 (1995).

[31] Y. Hamada, N. Saito, K. Nishimura, and H. Kanno, JP Patent, No. 3,728,309 (Sep. 30, 2003)

[32] S. A. VanSlyke, C. H. Chen, and C. W. Tang, Appl. Phys. Lett. 69, 2160 (1996).

[33] L. S. Hung, L. R. Zheng, and M. G. Mason, Appl. Phys. Lett. 78, 673 (2001).

[34] C. C. Hsiao, C. H. Chang, T. H. Jen, M. C. Hung, S. A. Chen, Appl. Phys. Lett. 88, 033512 (2006).

[35] V. Podzorov, S. E. Sysoev, E. Loginova, V. M. Pudalov, M. E. Gershenson, Appl. Phys. Lett. 83, 3504 (2003).

[36] A. Tsuboyama, H. Iwawaki, M. Furugori, T. Mukaida, J. Kamatani, S. Igawa, T. Moriyama, S. Miura, T. Takiguchi, S. Okada, M. Hoshino, and K. Ueno, J. Am. Chem. Soc. 125, 12971 (2003).

[37] P. E. Burrows, S. R. Forrest, T. X. Zhou, and L. Michalski, Appl. Phys. Lett. 76, 2493 (2000).

[38] T. Tsuji, S. Kawami, S. Miyaguchi, T. Naijo, T. Yuki, S. Matsuo, H. Miyazaki, Soc. Inf. Display Int. Symp. 35, 900 (2004).

[39] T. Tsuzuki, Y. Nakayama, J. Nakamura, T. Iwata, and S. Tokito, Appl. Phys. Lett. 88, 243511 (2006).

[40] T. Sano, Y. Nishio, Y. Hamada, H. Takahashi, T. Usuki, and K. Shibata, J. Mater. Chem. 10, 157 (2000).

[41] S. W. Wen, M. T. Lee, C. H. Chen, IEEE/OSA J. Display Technology 1, 90, (2005).

[42] T. Yasuda, Y. Yamaguchi1, D. Zou, and T. Tsutsui, Jpn. J. Appl. Phys. 41, 5626 (2002), and references cited therin.

[43] C. Adachi, S. Tokito, T. Tsutsui, and S. Saito, Appl. Phys. Lett. 55, 1489 (1989).

[44] C. H. Chen, J. Shi, and C. W. Tang, Macromol. Symp. 125, 1 (1997), and references cited therin.

[45] U. Mitscke and P. Bäuerle, J. Mater. Chem. 10, 1471 (2000)

[46] Y. Shirota, J. Mater. Chem. 15, 75 (2005), and references cited therin..

[47] P. Strohriegl, J. V. Grazulevicius, Adv. Mater. 14, 1439 (2002).

[48] T. Sano, T. Fujii, Y. Nishio, Y. Hamada, K. Shibata, K. Kuroki, Jpn. J. Appl. Phys. 34, 3124 (1995).

[49] C. Wu, W. Hung, T. Liu, L. Zhang, T. Luh, J. Appl. Phys. 93, 5465 (2003).

[50] Y. Hamada, T. Sano, K. Shibata, K. Kuroki, Jpn. J. Appl. Phys. Part2 34, L824 (1995).

[51] J. Shi, C. W. Tang, and C. H. Chen, U.S. Patent, No. 5,935,721 (August 10, 1999).

[52] J. Bard, L. R. Faulkner, Electrochemical Methods Fundamentals and Applications, John Wiley & Sons, Inc. New York, 240 (2001).

[53] X. M. Ding, L. M. Hung, L. F. Cheng, Z. B. Deng, X. Y. Hou, C. S. Lee, and S. T. Lee, Appl. Phys. Lett. 76, 2704 (2000).

Chapter 4.

High-efficiency White Emitting OLEDs

4.1 WOLED with Selective Energy Transfer

4.1.1 Singlet and Tripletl exciton transfer system

As mentioned in Chap. 2, the main target of WOLEDs is a full-color display market. It is needless to say that much higher power efficiency is required for WOLEDs to prevail in the market.

Lighting accounts for approximately 22% of the electricity consumed in buildings in the United States, with fully 40% of that amount consumed by inefficient (~15 lm/W) incandescent lamps[1, 2]. This has generated increased interest in the use of WOLEDs due to their potential for significantly improved efficiency over incandescents in combination with low-cost, high-throughput manufacturability. Though developments in new organic materials and the device structure have been major approaches, it is always important to find the efficient energy transfer in each device. One of the most impressive WOLED characteristics reported thus far have been achieved in all-phosphor-doped devices with a potential for 100% internal quantum efficiency[2] (IQE). In this section, it is described that a new concept that exploits a blue fluorescent dopant in exchange for a phosphor, in combination with green and red phosphor dopants to yield high power efficiency, and stable color balance, while maintaining the potential for unity IQE. Two distinct modes of energy transfer channel nearly all of the triplet energy to the phosphorescent dopants, retaining the singlet energy exclusively on the blue fluorescent dopant. Additionally, eliminating the exchange energy loss to the blue fluorophore allows for roughly 20% increased power efficiency compared to a fully phosphorescent device.

Table 4-1: Selected electrophosphorescent WOLED architectures with their corresponding performance characteristics.

Architecture	η_{ext} [%]	η_p [lm/W]	CRI	Refs
Exciton managed fluorescent/ phosphorescent	11.0, 11.0†, 7.8‡	22.1, 16.1†, 5.8 ‡	85	This Work (Chap.4.1)
Phosphorescent triple-doped	12*, 8.0†, 3.2‡	26*, 13.3†, 1.8 ‡	80	3
Two phosphor doped layers	12*, 9.3†, 4.1‡	10*, 4.6†, 1.3 ‡	<60	4
Single dopant phosphorescent	6.4	12	67	5
Multiple phosphor doped layers	5.2	6.4	83	6
Phosphorescent triplet excimers	4	4.4	78	7
Blue-fluorescent/ Red-phosphorescent	1.4	0.92	<60	8
Phosphorescent sensitizer	1.8	4.1	<60	9

Here, η_{ext} and η_p are the forward viewing external quantum and power efficiencies, respectively. Where η_{ext} or CRI is not reported, a value is calculated from the luminous efficiency and spectral data provided in the reference.

*Values at 10-3 mA/cm^2;

†Values at 1mA/cm^2;

‡Values at 102 mA/cm^2; Values without specific notation are the maximum reported.

Electrophosphorescent OLEDs have been demonstrated to harvest 100% of the excitons generated by electrical injection, corresponding to a 4-fold increase in efficiency compared to that achievable in singlet-harvesting fluorescent OLEDs [10]. In this context, electrophosphorescent WOLEDs have been reported to exhibit [3-5,11] high quantum (5% to 12%) and luminous power efficiencies (6 to 20 lm/W) at

brightnesses <100 cd/m^2. However, blue electrophosphorescent devices have exhibited short operational lifetimes[12] that limits the color stability of all-phosphor-doped WOLEDs. Also, compared with their fluorescent counterparts, WOLEDs employing phosphorescent blue dopants excited via the conductive host introduce an approximately 0.8eV exchange energy loss in power efficiency. This results from the energetic relaxation following intersystem crossing (ISC) into the emissive triplet state. This loss can be avoided by resonant injection from the hole (HTL) and electron transport layers (ETL) into the phosphor triplet state[3,13], but the subsequent transfer to green and red dopants required to generate white light can reintroduce these parasitic energy losses. In this section, it is described that a new WOLED architecture that employs a fluorescent emitting dopant to harness all electrically generated high energy singlet excitons for blue emission, and phosphorescent dopants to harvest the remainder of lower-energy triplet excitons for green and red emission (see Fig. 4-1).

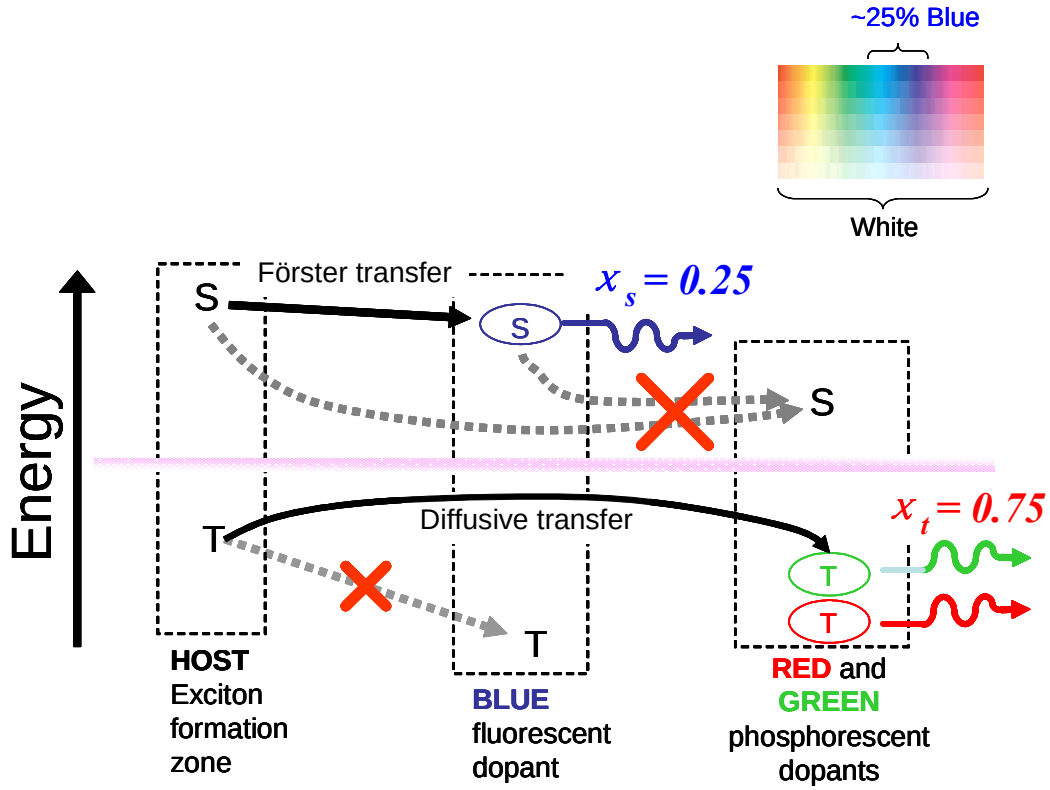

Figure 4-1. Proposed energy transfer mechanisms in the fluorescent/phosphorescent WOLED. This clearly illustrates the separate channels for triplet and singlet formation and transfer directly onto their corresponding emissive dopants. The majority of excitons are formed in the host material with a singlet-to-triplet formation ratio of χs/χt. The singlet excitons in the two formation regions at each side of the light emitting layer (EML) are rapidly, and near-resonantly transferred to the blue fluorescent dye located in these regions. The phosphor-doped region is located in the center of the EML and separated from the exciton formation zones by spacers of undoped host material. The triplets then diffuse efficiently to the central region, where they transfer to the lower energy green or red phosphor dopants, again by a nearly resonant process to the green dopant triplet manifold, and with some energy loss to the red triplet. Diffusion of singlet excitons to the phosphor dopants is negligible due to their intrinsically short diffusion lengths [14]. Parasitic effects of charge trapping onto the phosphorescent dopants are discussed in the text.

This structure takes advantage of the fortuitous connection between the proportion of singlets dictated by spin statistics (i.e., one singlet vs. three triplets are produced by

electrical excitation[15]) and the roughly 25% contribution of blue to the perceived white light spectrum. This allows for resonant energy transfer from both the host singlet and triplet energy levels that minimizes exchange energy losses, thereby maximizing device power efficiency while maintaining the potential for unity IQE. This approach has the further advantages of a stable white balance with current, a high efficiency at high brightness due to reduced geminate exciton recombination[16], and an enhanced lifetime due to the combined use of a stable fluorescent blue, and long lived phosphorescent green and red dopants in a single emissive region.

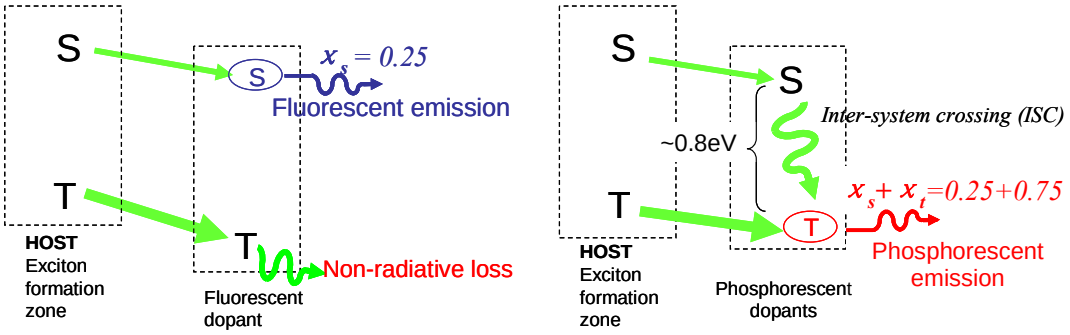

Figure 4-2. The comparison between energy transfer of singlets and triplets to fluorescent and phosphorescent dopants.

4.1.2 WOLED with 100% internal quantum efficiency

The WOLED consists of a blue fluorophore, 4,4'-*bis*(9-ethyl-3-carbazovinylene)-1,1'-biphenyl (BCzVBi)[17] doped in a region spatially separate from the highly efficient green and red phosphorescent dopants *fac*-tris(2-phenylpyridine) iridium ($Ir(ppy)_3$) and iridium(III) bis(2-phenyl quinolyl-N,$C^{2'}$) acetylacetonate (PQIr), respectively. All lumophores are doped into a single, common conductive host, 4,4'-bis(N-carbazolyl)biphenyl (CBP), to form the extended emissive layer (EML) which is sandwiched between the electron transporting/hole blocking layer of 2,9-dimethyl-4,7-diphenyl-1,10-phenanthroline (BCP), and the 4,4'-bis[N-(1-naphthyl)- N-phenyl-amino]-biphenyl (NPD) HTL.

The principle of device operation is illustrated in Fig. 4-1. Excitons are formed on the host with a singlet-to-triplet formation ratio of χ_s/χ_t. Singlet excitons are transferred following a resonant Förster process onto the lightly doped (5%) blue fluorophore as opposed to direct trap formation[17]. The non-radiative host triplets, however, cannot efficiently transfer to the fluorophore by the Förster mechanism, nor by Dexter transfer due to the low doping concentration. On the other hand, triplets typically have long diffusion lengths[15] (~100nm), and hence can migrate into the center of the EML where they transfer onto the phosphors. Resonant transfer of the host triplet onto the green phosphor avoids exchange energy losses at this stage, although there are some unavoidable losses in transferring into the lowest energy red phosphor. Finally, placing an undoped host spacer with a thickness larger than the Förster radius (~3nm) between the blue flourophore and the phosphors prevents direct energy transfer from the blue dopant to the green and red phosphors. This device architecture is unique in that the singlet and triplet excitons are harvested along completely independent channels, and hence the transfer from host to dopant for both species can be separately optimized to be nearly resonant, thereby minimizing energy losses while maintaining a unity IQE. Figure 4-3 provides evidence for this transfer mechanism by comparing the unnormalized electroluminescent spectra of three devices. The result indicates that exciton diffusion from the point of origin at the edges of the EML, rather than direct charge trapping and exciton formation on the phosphor, dominates since carriers trapped by $Ir(ppy)_3$ would result in a noticable decrease in the BCzVBi emission. Triplet

diffusion from the edges of the EML to the phosphorescent doped region is consistent with previous observations in red fluorescent/phosphorescent OLEDs, where the fluorophore “filters” out the singlet excitons, leaving only triplets to diffuse to a spatially separated phosphor doped region[10].

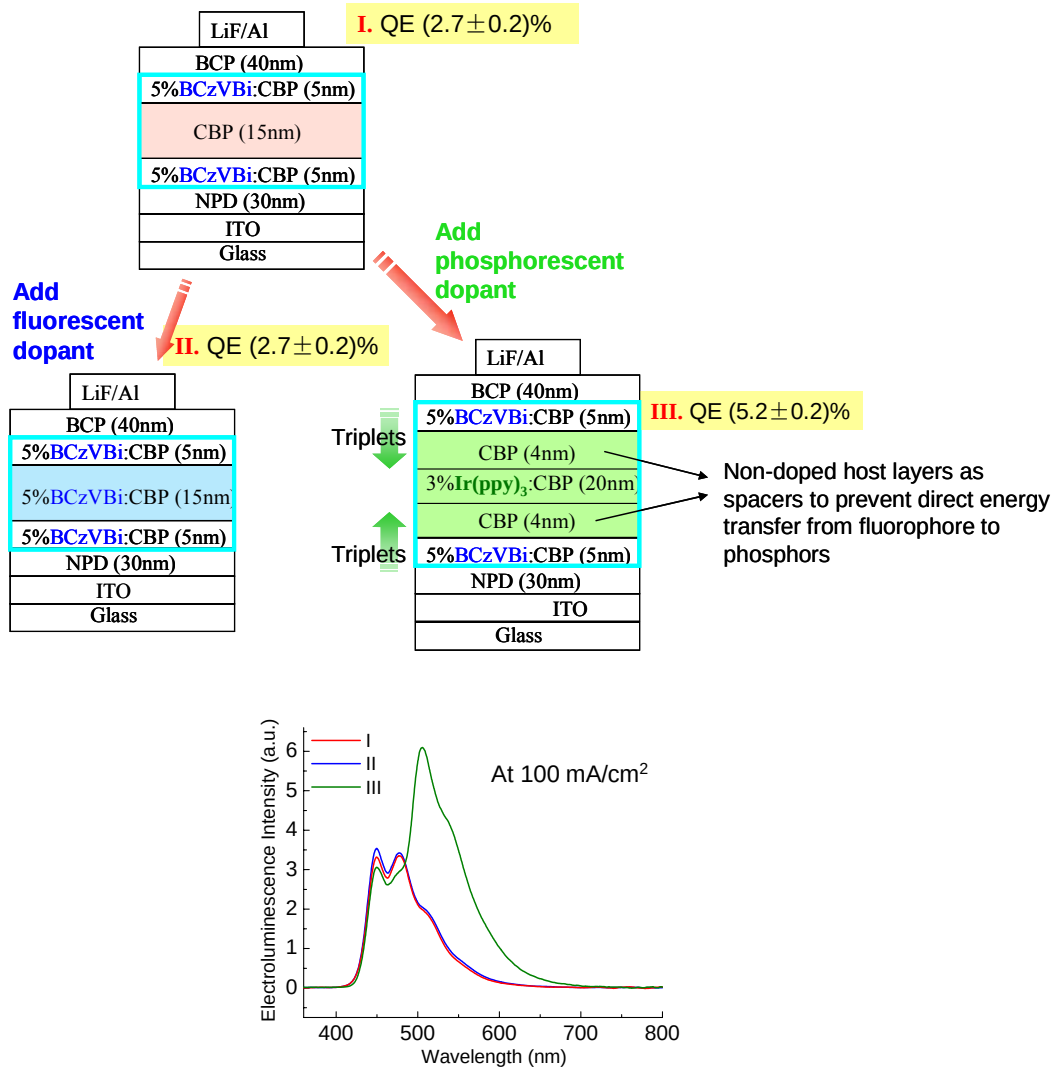

Figure 4-3. Top*:* Device structures I-III. Bottom: Unnormalized electroluminescence spectra of three device structures shown in the top. The three spectra suggests that excitons are primarily formed at the two interfaces, and that fluorescent doping across the entire emission layer does not increase the blue luminescence intensity (compare Devices I and II). However, doping the middle of the EML with the phosphor, $Ir(ppy)_3$, results in additional green emission without a corresponding decrease in blue, BCzVBi emission (Devices I and III), indicating that triplets formed on CBP are efficiently transferred to $Ir(ppy)_3$, whereas the BCzVBi acts to harvest, or "filter" out all of the singlets.

These observations shown in Fig. 4-3 and 4-4 suggest that excitons are generated at both the HTL/EML and EML/ETL interfaces, consistent with the ambipolar conductivity of CBP[18,19]. Exciton formation at the edges, with correspondingly low generation in the bulk of the EML can be undestood as follows: large densities of holes (p) electrons (n) pile up at the energy barriers at two EML interfaces. The exciton formation probability, which is ~nxp, is thus also significantly higher at these locations as compared with the EML bulk.

Based on these results, WOLEDs are fabricated by doping the middle region of the EML with both the green and red phosphorescent dopants (Fig. 4-4, inset). Since the high HOMO energy of PQIr suggests that it can trap holes in the CBP host, a slight decrease of the blue emission intensity is observed in the WOLED. Fitting of the WOLED spectrum in Fig. 4-4 with the individual dopant spectra, suggests that the ratio of emission from fluorescent to phosphorescent dopants approaches the ratio of 1/3, consistent with the singlet-to-triplet exciton formation ratio in emissive organic materials[15,20,21] Furthermore, given the performance characteristics of the purely fluorescent BCzVBi device (Device II in Fig. 4-3), we can also find that the fraction of excitons trapped by, and formed directly on the phosphorescent dopants in the EML is χ_{trap} =(18 ±5)%. To interpret the emission spectrum, the WOLED EQE is expressed as:

$$\eta_{ext} = \left(1-\chi_{trap}\right)\cdot\eta_B + \left[(1-\chi_{trap})\cdot\chi_t + \chi_{trap}\right]\cdot\eta_{GR} \qquad (1)$$

where η_B and η_{GR} are the external quantum efficienices (EQEs) of a singly doped blue fluorescent device, and the comparable singly doped green and red phosphorescent devices, and χ_{trap} is the fraction of excitons trapped and formed directly on the phosphorescent dopants in the EML. By fitting the WOLED spectrum in Fig. 4-4 at J = 100 mA/cm^2 with the electroluminescence spectra of the three individual dopant materials, and accounting for photon energy in these power spectra, it is find that (20 ±2)% of the total quantum efficiency is due to emission from the blue fluorescent dopant, and (80 ±2)% is from green and red phosphorescent dopants. Given the performance characteristics (η_B) of the purely BCzVBi device (Device II in Fig. 4-3), we calculate χ_{trap} = (18±5)% from the first term in Eq. (1).

That is, approximately 30% of the excitons are formed by direct trapping on the phosphor dopants, whereas the remaining 70% are formed at the edges of the EML, at which point the triplets subsequently diffuse into the center where they are transferred from host to phosphor dopant prior to emission.

A maximum forward viewing EQE of η_{ext} = (11.0 ± 0.3)% is achieved at a current density J=(1.0 ±0.6) mA/cm^2, and decreases only slightly to η_{ext} = (10.8 ± 0.3)% at a high forward viewing luminance of 500 cd/m^2, as shown in Fig. 4-4. This device gives a maximum forward viewing power efficiency of η_p = (22.1 ±0.3) lm/W. Since illumination sources are generally characterized by their total emitted power, this device therefore has maximum total efficiencies[3] of $\eta_{p,t}$ = (37.6 ±0.6) lm/W, and $\eta_{ext,t}$ = (18.7 ± 0.5)%. At a practical surface luminance of 500cd/m^2, ηp,t=(23.8±0.5) lm/W, or approximately 50% greater than for common incandescent lighting. Although the commercially available blue fluorophore has a low η_{ext}=2.7% (compared with a maximum expected 5% achieved in the literature), the WOLED performance, nevertheless, represents a considerable improvement over the best all-phosphorescent devices previously reported [3,4,8].

The intrinsic singlet-to-triplet ratio and the separation of the channels in harvesting the two excitonic species gives a well-balanced and largely current independent color rendition, resulting in CRI = 85 at all current densities studied, which is the highest CRI among the reported values for a WOLED. CIE) coordinates have a negligible shift from (0.40, 0.41) at 1 mA/ cm^2 to (0.38, 0.40) at 100 mA/cm^2. This differs from observations of an all-phosphor-doped WOLED, where blue emission becomes stronger with increasing driving voltage[3] due to the requirement for high energy excitation of the blue phosphor. In the inset of Fig. 4-4 are images of three devices, each driven at 4 times higher drive current than the device above it in the array to show the color stability of the emission.

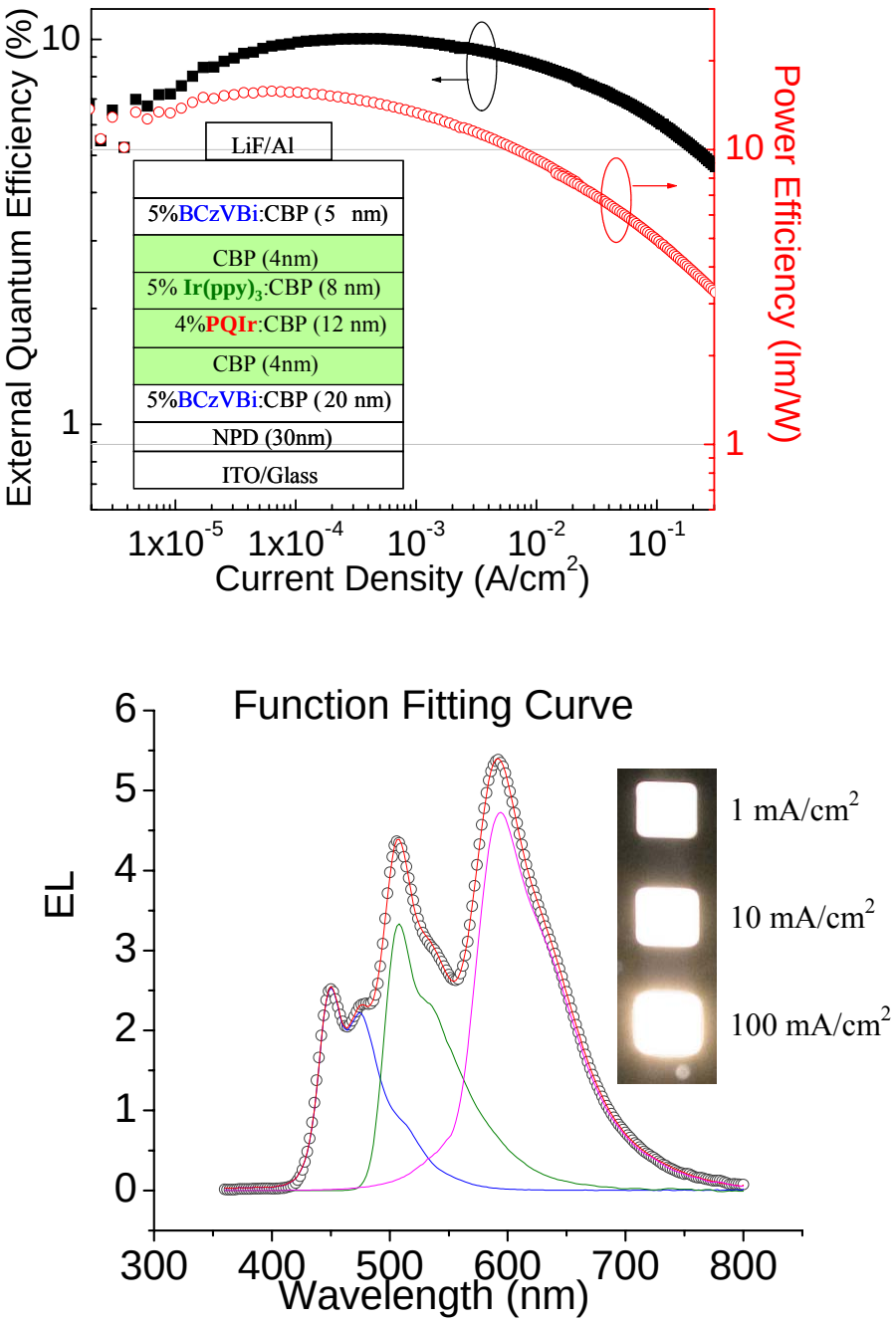

Figure 4-4.

To further understand exciton diffusion, in Fig. 4-5 we plot (open circles) η_{ext} due

to $Ir(ppy)_3$ emission versus the position of a thin (5nm) slab of 5 wt% $Ir(ppy)_3$:CBP located at various distances from the HTL/EML interface within a 200nm thick CBP EML (see inset, Fig. 4-5). Exciton diffusion through the EML is modeled as shown in Fig. 4-5 (solid line) as follows: In steady state, and assuming that all singlet formation occurs at the HTL/EML (x=0), and EML/ETL interfaces (x=200nm) (in Fig. 4-5), a solution to the triplet diffusion equation gives:

$$n(x) = \frac{1}{\sinh\left(\frac{L}{L_D}\right)}\left[\chi_t \cdot n_R \cdot \sinh\left(\frac{x}{L_D}\right) + \chi_t \cdot n_L \cdot \sinh\left(\frac{L-x}{L_D}\right)\right] + \chi_s \cdot n_L \cdot \delta(x) + \chi_s \cdot n_R \cdot \delta(x-L) \quad (2)$$

where n is the total exciton density: $n(x=0) = n_L$ and $n(x=L=200nm) = n_R$, L_D is the triplet diffusion length, and the delta function terms account for the presence of contributing singlets at the interfaces. Since the EQE from $Ir(ppy)_3$ emission is proportional to the exciton density in the $Ir(ppy)_3$-doped slab Fig. 4-5 (solid curve) shows the fit of the efficiency at J = 10mA/cm^2 versus x using Eq. (2) and $\chi_t=3\chi_s$, from which we infer L_D = (460±30) Å (error bars account for the spread in fits at additional current densities). With this calculated diffusion length, integration of the total exciton density in the phosphorescent doped region in the WOLED predicts that (75 ±5)% of the phosphorescent emission results from triplet exciton diffusion from the adjacent EML interfaces, in agreement with the value calculated from analysis of the spectral content of the emission (Eq. (1)).

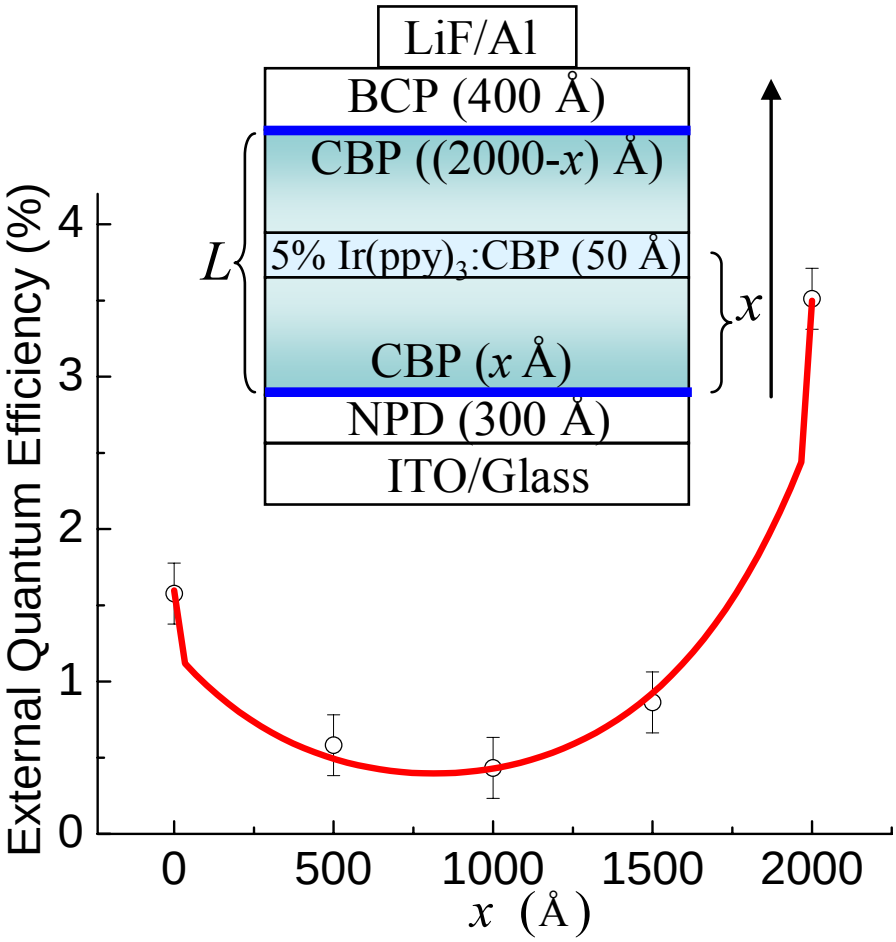

Figure 4-5. EQE (open circles) from $Ir(ppy)_3$ emission at 10mA/cm^2 versus distance between the 50-Å slab of 5 wt.-% $Ir(ppy)_3$:CBP and the NPD/CBP interface in the structure shown in inset. A fit following Eq. (2) for triplet diffusion gives the solid curve and a triplet diffusion length of L_D=(460 ±30) Å. The error bars indicate the deviations in measurement. Inset: Schematic cross-section of the test structures: NPD (30nm)/CBP (x nm)/ 5 wt.-% $Ir(ppy)_3$:CBP (5nm)/CBP ((200-x) nm)/ BCP (40nm), with x= 0, 50, 100, 150, 200.

4.1.3 Analysis of Exciton Forming

For a further examination of the exciton forming mechanism of the above-mentioned device, we quantitatively analyze the operation of this device in steady-state based on the values of a diffusion coefficient D and a triplet–triplet bimolecular quenching rate constant K_{TT}, which are $D = (1.4 \pm 0.3) \times 10^{-8}$ cm^2/s, and $K_{TT} = (1.6 \pm 0.4) \times 10^{-14}$ cm^3/s, reported by Giebink, et al. [22]. With the method, it is assumed that negligible diffusion of singlets away from their fluorescent zones at both EML edges due to their comparatively shorter diffusion lengths [23]. All quenching processes are neglected except T–T annihilation since it is expected to be the dominant source of loss for the diffusing triplets. In addition, we assume that triplets do not transfer to the blue fluorescent dopant due to the poor guest–host orbital overlap that results from their different molecular conformations [24]. Finally, the exciton distribution is assumed to exponentially decrease with distance from each edge of the EML [29] with characteristic length, d_{EX} (see Fig. 4-5). In this structure, nearly every injected charge results in an exciton since the transport layers (NPD and BPhen) confine charge within the emissive layer, thereby providing balanced electron and hole injection [30].

The component of the EQE due to blue emission from BCzVBi is directly proportional to the number of singlets present in the two fluorescent zones. Using the fluorescent quantum yield of BCzVBi (FL) and the optical out-coupling efficiency through the glass substrate [3] and [25] (OC = 0.2), we can estimate the singlet density, S, as a function of injection current density, J. By equating S to the integral of the singlet exciton formation profile (see Fig. 4-5) over the two distinct fluorescent zones, we can determine the total exciton density distribution, since three triplets are formed for every singlet [26]. In addition, we allow for a fraction, α_T, of the total exciton population to form by trapping directly on the phosphors. Using this profile, the rate equations for the singlet and triplet densities in the emissive layer are

$$\frac{\partial T}{\partial t} = D_T \frac{\partial^2 T}{\partial x^2} - \frac{T}{\tau_T} - k_{TT} T^2 + \frac{3J(1-\alpha_T)}{q d_{EX}(1-\exp[-x_0/d_{EX}])}\left[\frac{\eta_{Blue}}{\phi_{FL}\phi_{OC}}\right] + \left(\delta_{Left}\exp\left[\frac{-x}{d_{EX}}\right]\right) + \delta_{Right}\exp\left[\frac{x-x_0}{d_{EX}}\right] + \left[\frac{3J(\eta_{Blue})\alpha_T}{q\phi_{FL}\phi_{OC}W_{PH}} - TK_{TG}\right]_{PH\ region} \quad (3)$$

and

$$\frac{\partial S}{\partial t} = -\frac{S}{\tau_S} + \frac{J(1-\alpha_T)}{q d_{EX}(1-\exp[-x_0/d_{EX}])}\left[\frac{\eta_{Blue}}{\phi_{FL}\phi_{OC}}\right] + \left(\delta_{Left}\exp\left[\frac{-x}{d_{EX}}\right]\right) + \delta_{Right}\exp\left[\frac{x-x_0}{d_{EX}}\right] + \left[\frac{J(\eta_{Blue})\alpha_T}{q\phi_{FL}\phi_{OC}W_{PH}}\right] \quad (4)$$

Here, $\delta_{Left/Right}$ are the weighting fractions for exciton formation at the left/right side of the emissive layer (see Fig. 4-5), and τ_G and τ_S are the phosphor and BCzVBi lifetimes, respectively. We find that FL 0.6 for BCzVBi in toluene solution, using standard procedures [32]. Also, ηBlue is the forward-emitted EQE for an optimized, purely fluorescent device using a 5 wt.% BCzVBi:CBP emissive layer, and ranges from 2.7% at J = 1 mA/cm^2 to 2.3% at 100 mA/cm2. Any deviation in the blue component of the F/P WOLED efficiency from ηBlue is a result of the fraction, α_T, of excitons formed by direct charge trapping on the phosphor molecules outside of the fluorescent zones, as described by the last term on the right-hand side of Eqs. (3) and (4).

Solving Eqs. (3) and (4) in steady-state for S(x) and T(x), we can express the fluorescent (η_{FL}) and phosphorescent (η_{PH}) components of the total WOLED efficiency as

$$\frac{J}{q\phi_{oc}\phi_{FL}}(\eta_{FL}) = \frac{1}{\tau_s}\int_{\text{FL region}} S(x)dx \qquad (5)$$

and

$$\frac{J}{q\phi_{oc}}(\eta_{PH}) = \frac{1}{\tau_G}\int_{\text{PH region}} [\,T(x)+S(x)\,]dx \qquad (6)$$

where the phosphor quantum yield is taken to be unity [33]. Figure 4-6 summarizes the results by Giebink, showing lines of constant component efficiency (solid = fluorescent; dashed-dotted = phosphorescent) at a current density of 10 mA/cm^2 for the device in Fig. 4-4, as determined from the weighted contributions of the dopant photoluminescent spectra to the device emission. These are overlaid on contours that indicate the percentage of total excitons formed by trapping on the phosphors (dotted line). Note that the total exciton fraction formed in the phosphor-doped region, indicated by the contours, is slightly greater than the trapping fraction, α_T, since the exponential tails of the edge form Fitting results: CBP triplet dynamics Parameter CBP cation distributions also extend into the phosphor-doped region.

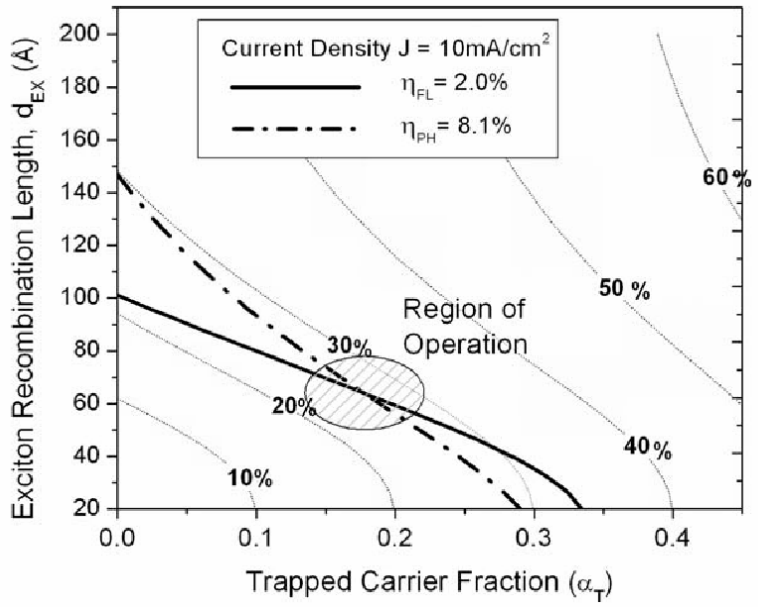

Figure 4-6. Model results for the fluorescent/phosphorescent WOLED calculated using Eqs. (3), (4), (5) and (6) in text. The dotted contours indicate the percentage of excitons that are formed by direct charge trapping on the phosphor dopants. Superimposed on this contour plane are lines of constant component dopant efficiency at a current density of J = 10 mA/cm^2 for the fluorophore (solid line) and phosphor (dashed-dotted line) that are obtained by fits to the WOLED.

Although neither d_{EX} nor α_T are known, the device operating point must correspond to the crossing of the fluorescent and phosphorescent efficiency lines. The crossings at all current densities (1 and 100 mA/cm^2, not shown) lie within the shaded region of Fig. 4-6, indicating a characteristic exciton formation length of d_{EX} 75 Å, and a total exciton trapping fraction of 20–30%.

In Fig. 4-7 we simulate the EQE at this operating point. For the fluorescent component, we find good agreement at all current densities. At low current densities, however, the model overestimates the phosphorescent emission component of the EQE. This discrepancy is attributed to losses, such as exciton–polaron and singlet–triplet quenching, not accounted for in the model. However, at higher current densities where T–T annihilation becomes the dominant source of loss, the model prediction falls close to the device data.

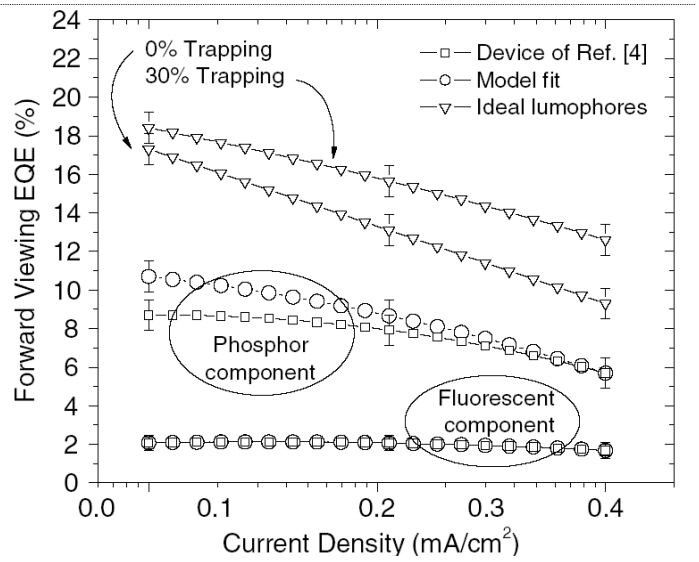

Figure 4-7. Forward-emitted external quantum efficiency (EQE) vs. current density obtained from the data of the WOLED (squares) and the fit (circles) given by the model in the text. The separation of the device EQE data into individual fluorescent and phosphorescent contributions is obtained by weighting to the photoluminescent spectra of each lumophore in the fit to the WOLED emission spectrum as shown in Fig. 8, making sure to account for the intensity to quantum yield conversion. Inverted triangles indicate predictions for the structure in Fig. 4-4 using "ideal" emitters having unity quantum yield for the cases of 0% and 30% direct exciton formation on the phosphors.

Balanced white emission with a high color rendering index [26] (CRI) can be achieved with a smaller blue emissive component than the singlet spin fraction (χ_S = 1/4) affords. Charges that form excitons by trapping increase the phosphor emission at the expense of blue fluorescence, since they are prevented from otherwise forming BCzVBi singlets. Trap formation is thus beneficial to device performance since the trapped exciton fraction is not subject to diffusive transport losses, and the reduced triplet density at the EML edges decreases T–T quenching. From the photoluminescent spectrum of each dopant (see Fig. 4-4), we calculate that CRI > 80 can be maintained for up to 35% exciton formation via direct trapping. Thus, the device operates close to the optimum point, representing a tradeoff between high efficiency and white color balance.

We can extend this model to predict the performance for this same structure using

an "ideal" fluorescent dopant with unity luminescent quantum yield. As shown in Fig. 4-7, the maximum forward-emitted efficiency increases from 17% (CRI = 86) in the absence of trapping to 18.5% (CRI = 81) for an optimum trapping fraction of 30%. Accounting for all white light emitted [27] the total (integrated) EQE for this optimized device is 31%. In addition, the roll-off in EQE with increasing current density is lessened (as compared to the device without trapping) since T–T annihilation is reduced, as discussed above.

4.1.4 Conclusion

Compared with previous all-phosphor, high efficiency WOLEDs, the device also has a less pronounced efficiency roll-off at high current densities. For example, in Fig. 4-8 we show a comparison of η_{ext} vs. J for an all-phosphor white device[3], the device of this work, and a fluorescent BCzVBi Device II. The high-current decline in η_{ext} of the all-phosphor white is due to triplet-triplet annihilation[19,28] where the EQE decreases following the equation shown below. In contrast, there is a striking resemblance between the efficiency roll-off of the current device, and that of Device II. Modeling of the roll-offs in these two structures is complicated by recombination processes such as exciton-polaron quenching[16], singlet-triplet annihilation, and field-induced exciton dissociation. Nevertheless, for both of these latter devices, the current density at the point that η_{ext} has declined by half from its peak, is > 7 times that of the conventional phosphor device, while the peak EQE occurs at a value of J nearly 1000 times larger. The apparent absence of triplet-triplet annihilation suggests that the highest density of triplet excitons is at the interfaces in the fluorescent doped regions, where they subsequently diffuse towards the center, thereby lowering the local density (Fig. 4-5) in the region of the guest phosphors. The reduced sensitivity of η_{ext} to current density is another clear difference between the WOLED of this study and previous, high efficiency all-phosphor devices.

$$\frac{\eta}{\eta_0} = \frac{J_0}{4J}\left(\sqrt{1+8\frac{J}{J_0}}-1\right) \qquad (7)$$

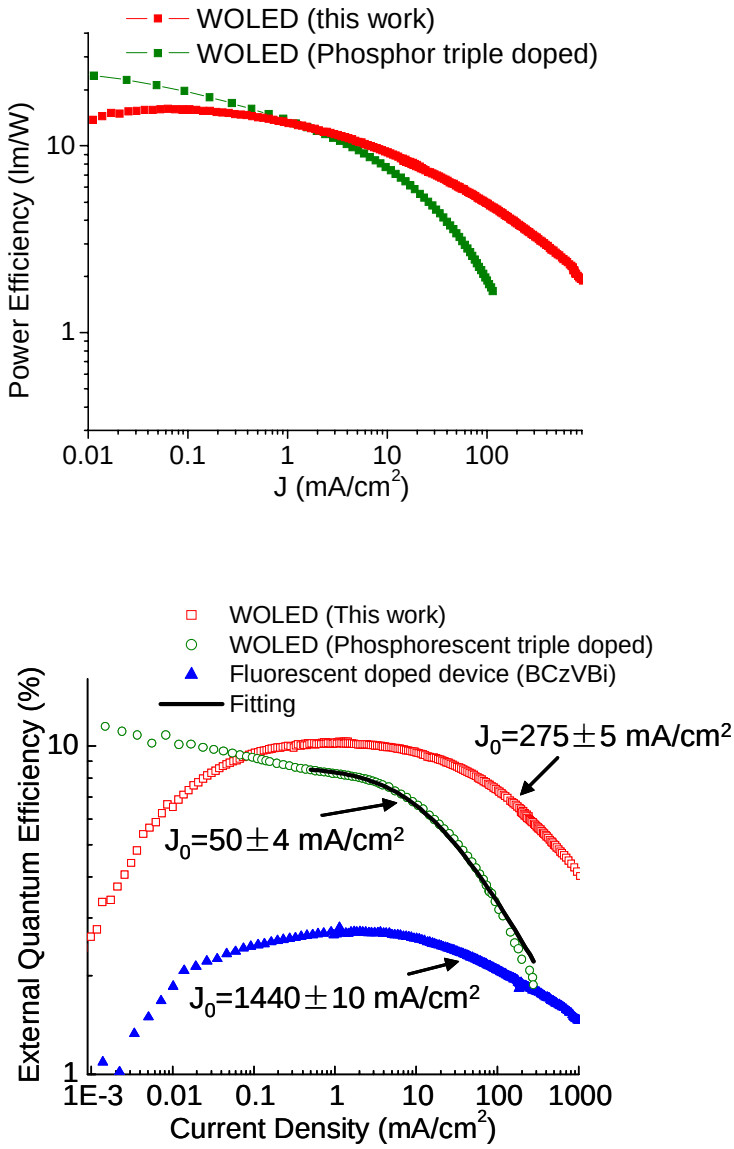

Figure 4-8. Top: Comparison of power efficiency between the phosphor triple doped device (Ref 3) and the proposed device. Bottom: Comparison of EQE roll-off among the proposed device and the phosphor triple doped white device and a blue fluorescent BCzVBi device**.** The high current roll-off of the phosphor device is described by triplet-triplet annihilation (fit shown as solid line), yielding an onset current density J_0 = (50±4)mA/cm^2.

Note that the efficiency of the present device can be further improved by using fluorescent dopants [29] with IQE=25% and phosphors[30,31] with IQE=100%, resulting in a total WOLED internal quantum efficiency of 100%. Using such "ideal" chromophores whose spectra are the same as the current dopants used, an approximately 34% total EQE and 60 lm/W power efficiency can in principle be achieved using this structure, corresponding to a four-fold increase over incandescent power efficiency, and even competing with high efficiency, high CRI fluorescent lighting sources. As noted above, the exchange energy difference between the host singlet and dopant triplet states can lead to a loss of luminance efficiency in all-phosphor doped WOLEDs. By applying this design concept to systems where the host singlet is resonant with the blue flourophore singlet state, and the host triplet is resonant with the green phosphor triplet level, this structure can have a power efficiency improvement of ~20% compared to similarly ideal all-phosphor devices. ,

4.2 WOLED with Phosphore Sensitized Emitting Layer

4.2.1 Energy transfer with a phosphor sensitizer

A novel WOLED consisting of an EML with a blue fluorophore doped layer and a spatially separated red and green phosphor doped layer is demonstrated to have very high luminance and quantum efficiencies in the previous section. This device, operating on the principle of distribution of all excitons formed in the host to their respective dopants, has the potential for achieving 100% internal quantum efficiency (IQE), while achieving a higher power efficiency than all-phosphor doped WOLEDs. An alternative approach reported here simplifies the fluorescent/phosphorescent (F/P) WOLED by replacing all but one of the three primary color emitting dopants with a fluorophore while still retaining its ability to achieve 100% IQE. In this device, the red phosphor is exchanged for a red fluorescent dopant whose emission is sensitized by the presence of a co-doped phosphor in a common conductive host [32,33]. By lightly doping the sensitized layer with the fluorophore, less than complete transfer of triplets from the green phosphor results in a mixture of red and green emission. Combined with the emission from the spatially distinct singlet-harvesting blue fluorophore, the desired white color balance is achieved. With this method, a wide variety of fluorescent dyes can be used for WOLEDs. Moreover, this device can maintain the high luminance and quantum efficiencies of the all-phosphor and F/P architectures, whereas previously reported phosphor sensitized WOLEDs [9,34,35] have relatively low efficiencies due to the poor energy transfer dopants.

To obtain the maximum current efficiency from an organic material, it is necessary to harness both the spin-symmetric and anti-symmetric molecular excitations that result from electrical pumping. If the material is phosphorescent this is possible, and high efficiencies have been observed in phosphorescent [10,36] OLEDs [37]. However, phosphorescence in organic molecules is rare at room temperature, and although the alternative process of fluorescence is more common, it is approximately 75% less efficient due to its requirement for spin-symmetry conservation [15]. We demonstrate that this deficiency can be overcome by using a phosphorescent sensitizer to excite a fluorescent dye. The mechanism for energetic coupling between phosphorescent and

fluorescent molecular species is a long-range, non-radiative energy transfer (see Chapter 2). Using this technique, the internal efficiency of fluorescence can be as high as 100%, a result previously only possible with phosphorescence. As an example, we employ it to nearly quadruple the efficiency of a fluorescent red OLED.

Very few organic materials have been found to be capable of efficient room temperature phosphorescence from triplets [10,36,15]. In contrast, many organic molecules exhibit fluorescence,[40] and fluorescence is also unaffected by triplet-triplet annihilation which degrades phosphorescent emission efficiency at high excitation densities[10]. Consequently, fluorescent materials are suited to many electroluminescent applications, particularly those such as passive matrix displays that require high excitation densities.

It is desirable therefore to find a process whereby triplets formed after electrical excitation are not wasted, but instead are transferred to the singlet excited state of a fluorescent dye. There are two mechanisms for triplet-singlet energy transfer from a donor molecule (*D*) to an acceptor (*A*). In hopping transport [41], exciton transfer is a short-range process dependent on the overlap of molecular orbitals of neighboring molecules. It also preserves the symmetry of the donor and acceptor pair [41]. Thus, a triplet-singlet energy transfer is not possible via a hopping mechanism. A change in spin-symmetry is possible if the donor exciton breaks up and reforms on the acceptor via incoherent electron exchange [41]. However, this process is considered to be relatively unlikely as it requires the dissociation of the donor exciton, which in most molecular systems has a binding energy of ~1eV.

As discussed in Chapter 2, the alternative mechanism is Förster energy transfer[41]. Here, molecular transition dipoles couple and exchange energy. The efficiency of energy transfer (η_{ET}) is:

$$\eta_{ET} = \frac{k_{ET}}{k_{ET} + k_R + k_{NR}}, \tag{8}$$

where k_{ET} is the rate of Förster energy transfer from *D* to *A* and k_R and k_{NR} are the radiative and non-radiative rates on the donor, respectively. From Eq. (8), energy transfer is efficient if $k_{ET} > k_R + k_{NR}$, however, in Förster's theory k_{ET} is proportional to the oscillator strength of the donor transition [41], as is k_R. Thus, η_{ET} is approximately

independent of oscillator strength if $k_R >> k_{NR}$, i.e. if the donor is efficiently phosphorescent then it is possible to obtain triplet-singlet energy transfer via the Förster mechanism. Note that a 'pure' triplet has an infinite lifetime and no probability of Förster energy transfer since the oscillator strength of its decay is zero. However, the slightest perturbation (i.e. some overlap between the triplet and ground state on the donor) can counteract the presence of non-radiative modes and yield efficient energy transfer. Such triplet-singlet energy transfers were predicted by Förster [42] and confirmed by Ermolaev and Sveshnikova [43], who detected the energy transfer using a range of phosphorescent donors and fluorescent acceptors in rigid media at 77K or 90K. Large transfer distances were observed; for example with triphenylamine as the donor and chrysoidine as the acceptor, the interaction range is 52Å.

Unfortunately, when a fluorescent acceptor is doped directly into a phosphorescent donor material, the close proximity of the donor and acceptor increases the likelihood of hopping transfer between the donor and the acceptor triplets. Once excitons reach the acceptor triplet state, they are effectively lost since these fluorescent dyes typically exhibit extremely inefficient phosphorescence (i.e. $k_{NR} >> k_R$).

Another technique is to dope both the phosphorescent material and the fluorescent acceptor into a conductive organic host. Ideally, the phosphor then sensitizes the energy transfer from the host, now acting as the donor, to the fluorescent acceptor. Cascade Förster energy transfer of singlets has been demonstrated for fluorescent materials[44], however in this work, all energy is ideally transferred into the triplet state of the sensitizer, where it is then transferred to the singlet state of the fluorescent dye, i.e.

$$\begin{aligned} {}^1D^* + {}^1X &\rightarrow {}^1D + {}^1X^* \\ {}^1X^* &\rightarrow {}^3X^* \\ {}^3X^* + {}^1A &\rightarrow {}^1X + {}^1A^* \\ {}^1A^* &\rightarrow {}^1A + h\nu \end{aligned} \tag{9}$$

and,

$$\begin{aligned} {}^3D^* + {}^1X &\rightarrow {}^1D + {}^3X^* \\ {}^3X^* + {}^1A &\rightarrow {}^1X + {}^1A^* \\ {}^1A^* &\rightarrow {}^1A + h\nu \end{aligned} \tag{10}$$

Here, the photon energy is *hv,* and the donor, sensitizer and fluorescent acceptor are represented by *D*, *X* and *A,* respectively. Triplet and singlet states are signified by a superscript 3 or 1, respectively, and excited states are marked by asterisks. The multiple-stage energy transfer is described schematically in Fig. 4-9. Hopping transfers are indicated by dotted arrows, Förster transfers by solid arrows. Processes resulting in a loss in efficiency are marked with a cross. In addition to the energy transfer paths shown in the figure, direct electron-hole recombination is possible on the phosphorescent and fluorescent dopants as well as the host. Triplet exciton formation after charge recombination on the fluorescent dye is another potential loss mechanism.

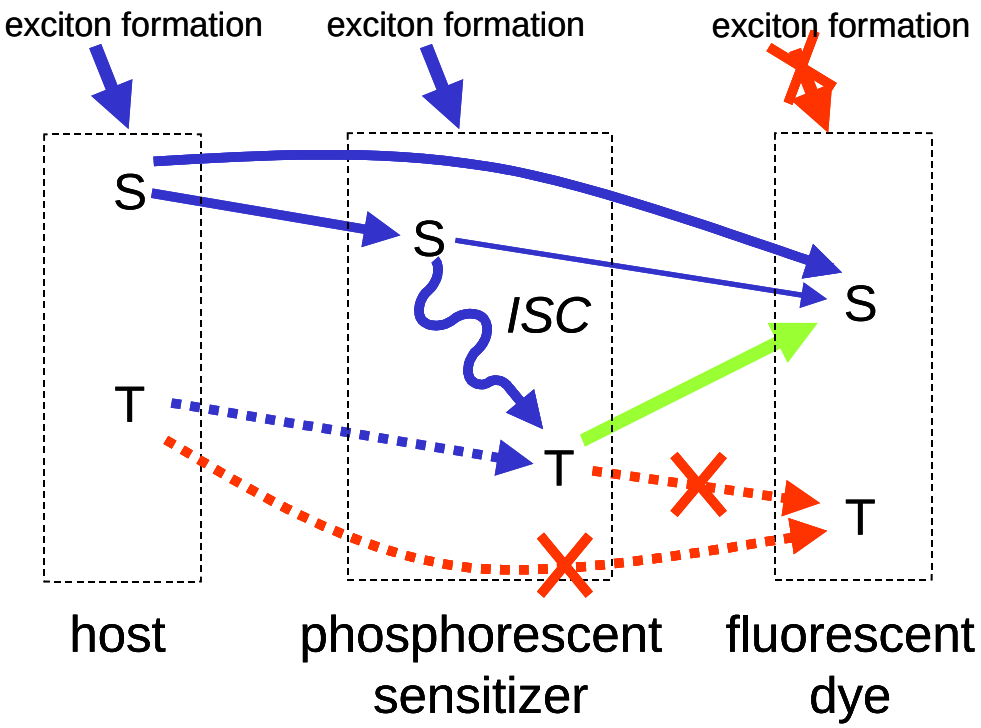

Figure 4-9. Proposed energy transfer mechanisms in the sensitized system, which corresponds to $Ir(ppy)_3$ and DCJTB doped CBP shown in Fig. 4-10. Förster transfers are represented by solid lines and hopping transfers by dotted lines. Electron-hole recombination creates singlet (S) and triplet (T) excitons in the host material, although as indicated, charge trapping may be responsible for exciton formation in the other materials also. Ideally, all excitons are ultimately transferred to the singlet state of the fluorescent dye, as triplets in the dye non-radiatively recombine. Thus, direct energy transfer to the triplet state of the fluorescent dye is a source of loss and it is indicated by a cross. By increasing the concentration of the sensitizer relative to the fluorescent dye, we maximize the number of triplet excitons that participate in energy transfer to the singlet state of the fluorescent dye via dipole-dipole coupling.

4.2.2 High efficiency at high currents

The fluorescent/phosphor sensitized fluorescent (F/P/F) WOLED structure is shown in Fig. 4-10. The conductive host for both fluorescent and phosphorescent dopants is CBP. Two separate blue fluorescent emitting regions are doped with BCzVBi[45,46], while the phosphor sensitized zone contains $Ir(ppy)_3$ and DCJTB co-doped in CBP to generate green and red emission, respectively. Exciton formation

occurs at the interface between the blue doped regions in the EML, and the 4,7-diphenyl-1,10-phenanthroline (Bphen) electron transport and exciton blocking layer (ETL), as well as at the opposite blue fluorophore doped EML interface with the hole transport layer (HTL) consisting of NPD. An undoped CBP region forms a spacer between the fluorescent region and a phosphor doped CBP zone in the center of the EML. The spacer prevents singlet excitons formed on the blue fluorophore to transfer to the lower energy green phosphor and red fluorophore. However, CBP triplets, with their characteristically long diffusion lengths (>100nm), migrate into the spatially separated phosphor-doped region.[28]

Generally, red emitting dopants act as carrier trapping sites, and consequently the operating voltages of red OLEDs are increased due to the resulting reduced carrier mobility. In the phosphor sensitized F/P WOLED, the red dopant is only lightly doped at ~0.1%, thereby preventing significant carrier trapping on the fluorophore. Moreover, the power efficiency is increased over that expected for an all-phosphor doped EML by eliminating exchange energy losses incurred by the very high energy required to excite the blue phosphor from both the singlet and triplet states of the fluorescent host.

The phosphor-sensitized green+red EML lacking the blue dopants was used to investigate energy transfer as a function of DCJTB concentration. As shown in Fig. 4-10, the red emission increases with DCJTB concentration. The devices with 0.05% and 0.1% DCJTB have nearly equal green and red intensities. The peak EQEs of these devices are comparable to that of the $Ir(ppy)_3$-only, green phosphorescent device, indicating that the sensitization process is almost lossless, as reported previously.[33] At 0.15 % doping of DCJTB, however, the efficiency decreases and the drive voltage at a fixed current is increased. This suggests that at DCJTB concentrations >0.1%, charge trapping becomes a significant channel for exciton formation, as is typical in purely red-fluorophor-doped OLEDs.

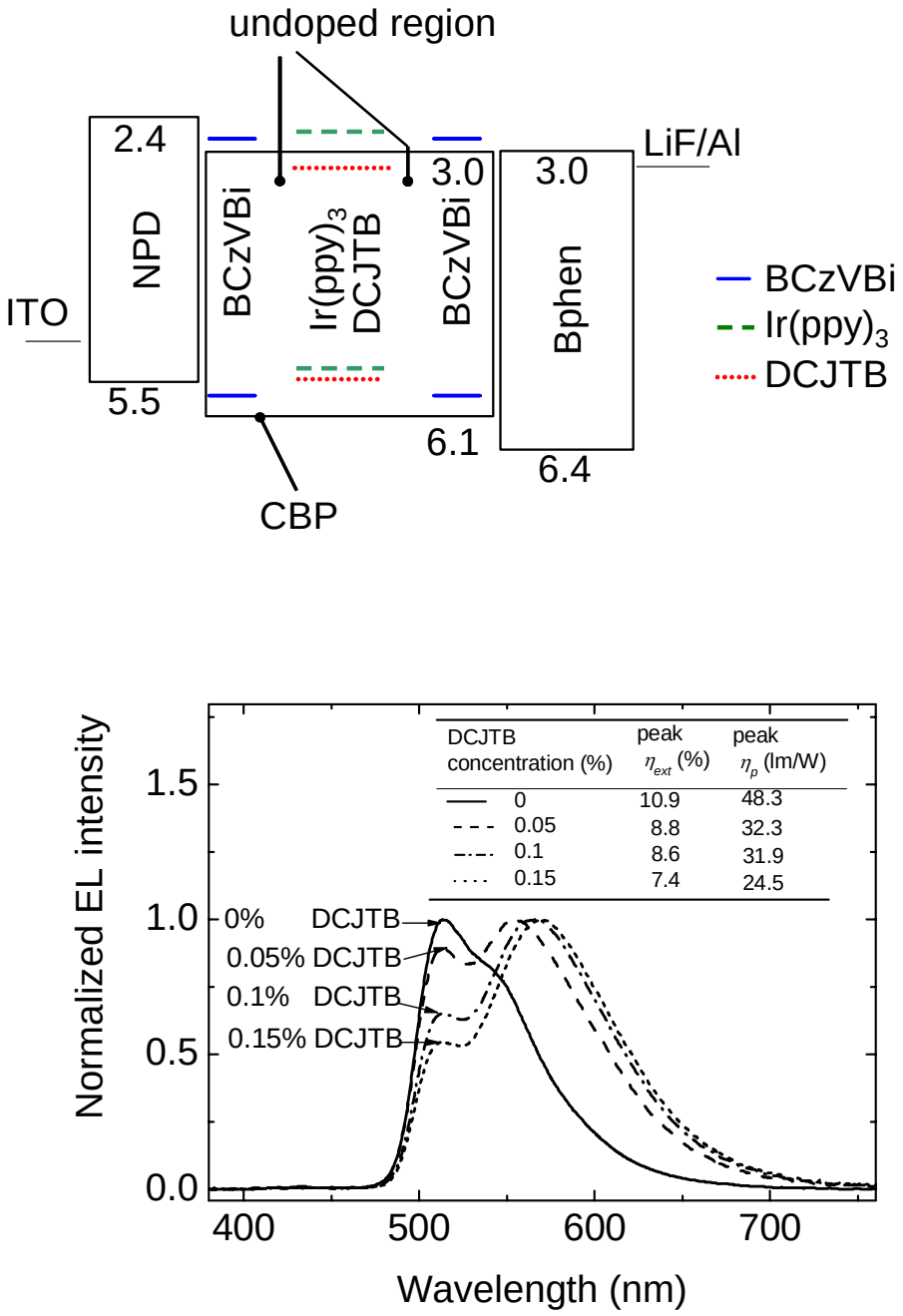

Figure 4-10. Top: The proposed device structure of the phosphor-sensitized WOLED. $Ir(ppy)_3$ is used as a phosphor sensitizer and DCJTB is a fluorescent red emitter. BCzVBi-doped CBP is the exciton formation zone from which the triplets diffuse to the phosphor. Bottom: Electroluminescent spectra of the $Ir(ppy)_3$- doped EML comprising of CBP: DCJTB. Inset table shows the peak external quantum and power efficiencies.

Based on these results, phosphor-sensitized F/P/F WOLEDs were grown with 0.08 % DCJTB, with the $Ir(ppy)_3$ concentration varied from 0 % to 8 % in CBP, also including the blue fluorescent doped zones and accompanying spacers at the edges of the EML. The F/P/F WOLED efficiencies and electroluminescence spectra are shown in Fig. 4-11, respectively. With increased $Ir(ppy)_3$ concentration from 2% to 8%, the EQE and power efficiency pronouncedly increase. The total EQE and power efficiency measured at a surface luminance of 800 cd/m^2 in a 4π solid angle for the 8% $Ir(ppy)_3$ sensitized device are $\eta_{ext,tot}$=13.1±0.5% and $\eta_{p,tot}$=20.2±0.7 lm/W, respectively. These values are approximately 20% lower than obtained for the above-described F/P WOLED.

In the absence of the $Ir(ppy)_3$ sensitizer, the efficiencies drop sharply to 3.2±0.2 % and 3.9±0.2 lm/W, as expected for a purely fluorescent device. We also find that the red emission from DCJTB increases with increased $Ir(ppy)_3$, concentration (see Fig. 4-11). Indeed, at 8 % $Ir(ppy)_3$ in CBP, triplet excitons originating in the blue doped zones at the EML edges are effectively transported via diffusion through the CBP spacers, and transferred to the red fluorescent dye by phosphorescent sensitization. The likelihood of direct triplet transfer from the blue dopant to DCJTB, or to $Ir(ppy)_3$, or excitation of these low energy dopants by charge trapping has not been quantified. In comparison with the F/P device (see Chap. 4.1) whose trapping fraction was approximately 25%, that of the F/P/F device is considered to be smaller due to the extremely low doping concentration of the red dopant. Trapping can reduce the overall device efficiency somewhat, although it has been shown by Giebink, et al.[22] that this process can be used to optimally tune the white emission spectrum.

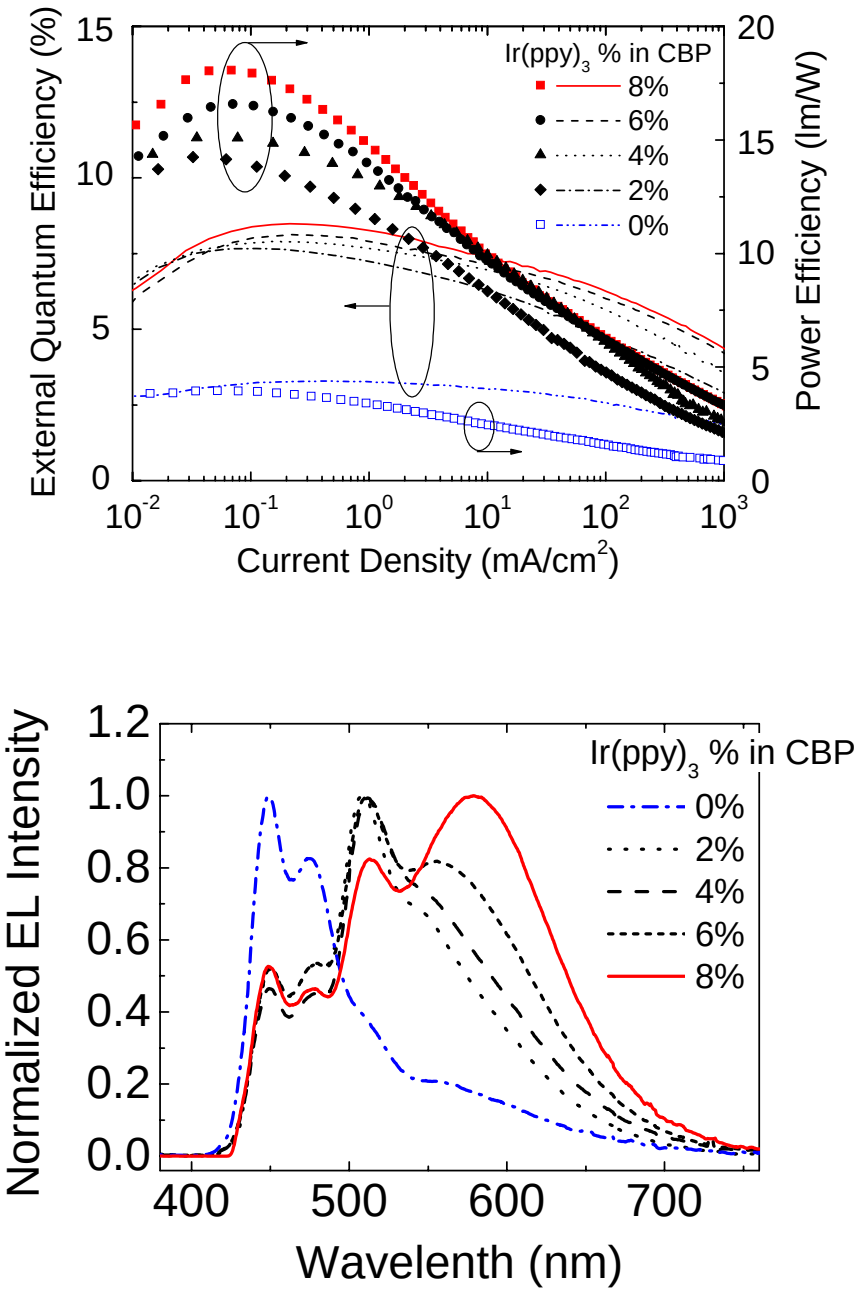

Figure 4-11.Top: EQE and power efficiency of phosphor-sensitized WOLED where the phosphor doping concentration is varied from 0-8%. Bottom: Electroluminescent spectra of the same devices.

Figure 4-12 shows the EL transient decay of the WOLED with 8 % $Ir(ppy)_3$. The response of DCJTB in $Ir(ppy)_3$ as shown in Fig. 4-12 is identical to that of $Ir(ppy)_3$, much slower than the intrinsic transient lifetime of DCJTB of ~1 ns.[32] This suggests that the radiative states of the phosphor can be readily transferred via the dipole-dipole Förster process to the radiative singlet state of the fluorophore co-doped with both the host and phosphor molecules as shown Fig. 4-9, which can lead to 100% IQE of OLEDs.

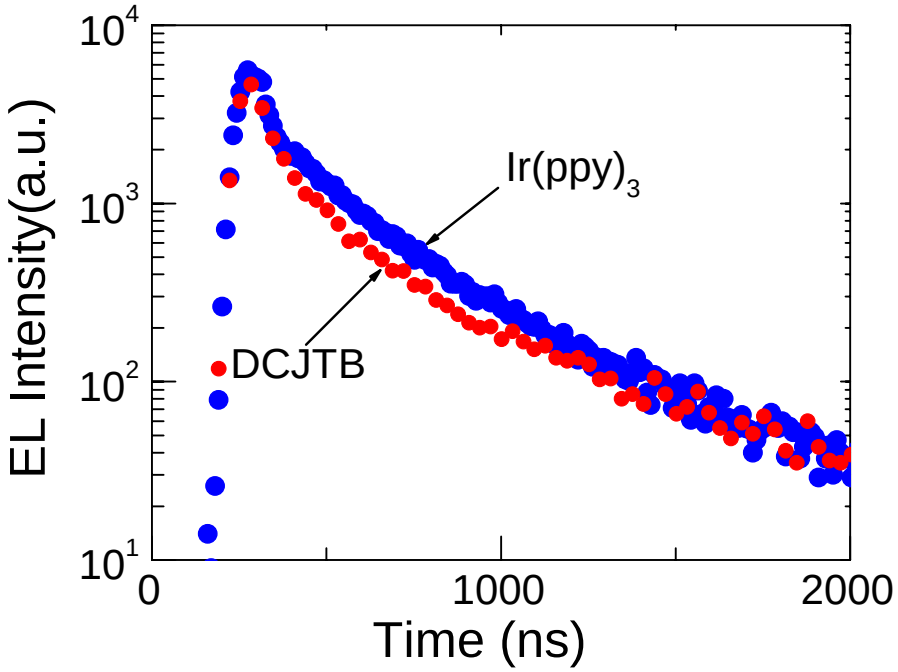

Figure 4-12. Transient electroluminescence response of the DCJTB (red) and $Ir(ppy)_3$ (green) spectral components of the device.

4.2.3 Conclusion

In summary, we have demonstrated high efficiency WOLEDs employing a phosphor sensitizer combined with blue and red fluorescent dopants. By changing the relative concentrations of the red fluorophore to the green phosphorescent emitter/sensitizer, we obtain efficient triplet transfer from the blue-doped zones at the edges of the EML to the red-emitting DCJTB via the phosphorescent sensitizer, $Ir(ppy)_3$,

while at the same time harvesting nearly all the singlets originating in the CBP host by the blue dopant itself. These results demonstrate that phosphor-sensitized WOLEDs constitute a simple and efficient (100% IQE) route to achieving high brightness sources for indoor lighting using only a single phosphorescent dopant.

4.3 Stacked WOLED with the Novel Charge Generation Layer

4.3.1 MoO_3 as the Charge Generation Layer

High efficiency white organic light emitting devices (OLEDs) [3,4,47] other than above mentioned onesare of interest due to their potential uses in full-color active-matrix displays coupled with color filters, and also as solid state lighting sources. For full-color display backlights, high brightness is required due to loss of light in optical films and the small aperture ratio (~40 %) in the thin film transistor backplane.[48] Similarly, high brightness (>800 cd/m^2) is required for solid state lighting sources. To achieve both high brightness and efficiency, the stacked OLED (SOLED) [49-51] consisting of multiple electroluminescent elements connected in series has been introduced. More recently, high efficiency green-emissive SOLEDs have been demonstrated that use a transparent charge generating interlayer such as indium tin oxide (ITO),[52] V_2O_5,[52] or an organic p-n junction[53] where the HTL and ETL layers are doped with $FeCl_3$ and Li, respectively. In the SOLED structure as shown in Fig. 4-13, the luminance at a fixed current density increases linearly with the number of stacked and independent OLED elements. This can lead to a significant improvement in lifetime (see Chap.5.1) as well as external efficiency by reducing degradation that accompanies high drive currents required to achieve similarly high brightness in a single element OLED.

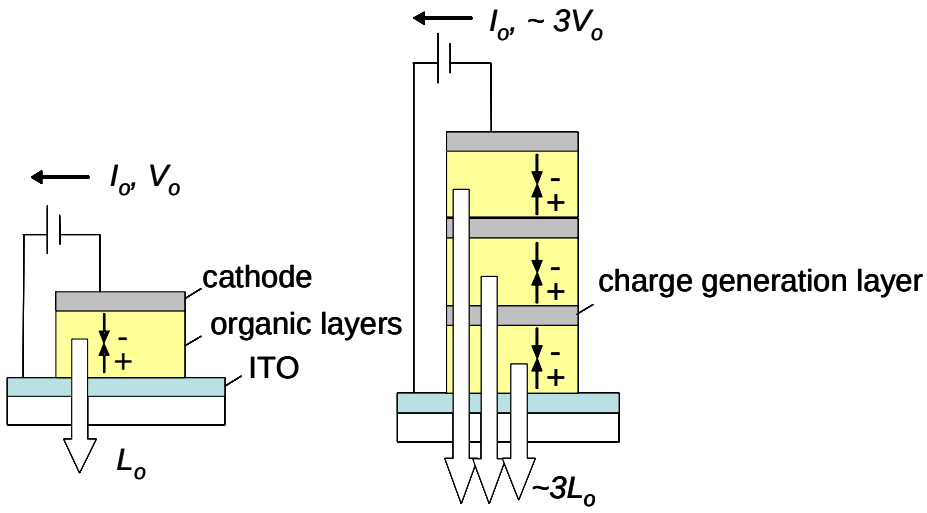

Figure 4-13. Schematics of a stacked OLED structure.

Table 4-2. The charge generation layer and the device

Charge generation layer	Device Architecture	η_{ext} (1) [%]	η_p (1) [lm/W]	η_c (1) [cd/A]	Color	Refs	Year
Bhen:Li/MoO_3		15.1	9.0	42	White	This Work Chap.4.1	2006
BCP:Cs/V_2O_5	NPB/Alq_3: C545T	-	8.2 (-)	32 (7.8)	Green, (White)	52	2003
Mg:Alq/WO_3	NPB/C545T:Alq/Alq				Green	68	2004
Alq:Li/NPB:$FeCl_3$	NPB/C545T:Alq	-	~6.5	21	Green	53	2004
LiF/Ca/Ag	NPB/Alq_3: C545T/BCP		7.6	20	Green	69	2005
Alq:Mg/m-MTDATA:F4-TCNQ	NPB/Alq	-	-	-	Green	70	2006
E314/Li_2O/LG-101	TMM-004:$Ir(ppy)_3$	25	40	92	Green	This Work Chap.5.1	2006

(1)Values are measured with 2-unit-stack OLEDs.

Here, we demonstrate high-efficiency white-emissive SOLEDs based on phosphorescent emitters with a Li-doped ETL. To the best of our knowledge, it is the first report using a vacuum-thermally-deposited MoO_3 film interposed between stacked elements.

The MoO_3 film is measured by X-rad diffraction (XRD) and atomic force microscope (AFM) and the surface is found to be amorphous and very flat with Ra=0.5 nm (see Fig. 4-14) Figure 4-15 shows the transmittance of MoO_3. The film is more transparent over the wavelength range from 400 nm to 500 nm compared with previously reported V_2O_5 interlayers, [54,55] which is essential to achieve an efficient white SOLED. Furtheremore, it is easier to handle than the corrosive and optically absorbing $FeCl_3$ To our knowledge, this also is the first device that utilizes the phosphor with pyrazolyl-based ligands that provides a blue - green emission in a white emitting OLED.

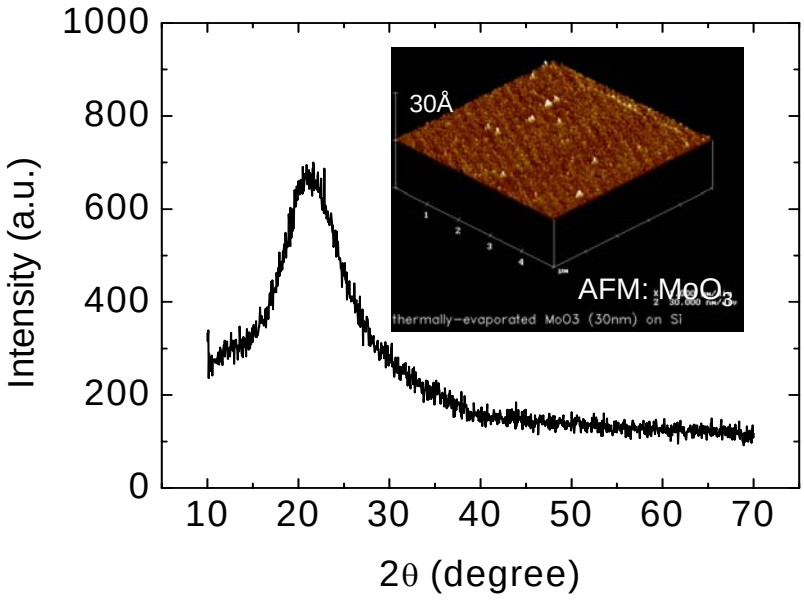

Figure 4-14. XRD spectrum of MoO_3, AFM image of MoO_3.

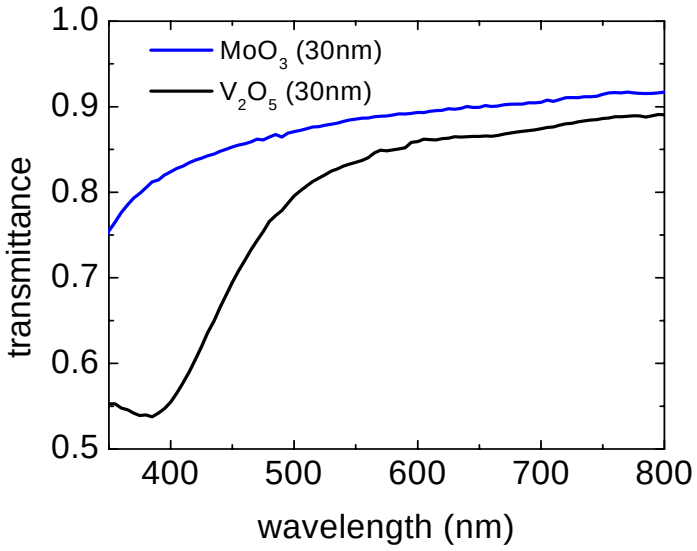

Figure 4-15. Transmittance spectrum of 30-nm-thick MoO_3 compared to 30-nm-thick V_2O_5. Both films are thermally evaporated.

4.3.2 Carrier Balance and Optical Structure

Figures 4-16 and 4-17 show the chemical strucures of employed materials and the proposed energy diagram of the white electrophosphorescent SOLED consisting of multiple, nearly identical white emitting OLED elements, or subpixels. HOMO energies for each material are measured using ultraviolet photoemission spectroscopy, and the position of LUMO energies are estimated by adding the energy corresponding to the onset of optical absorption to the HOMO energy. This proceedure generally leads to a systematic underestimation of the HOMO-LUMO energy gap by 0.5 to 1.0 eV.

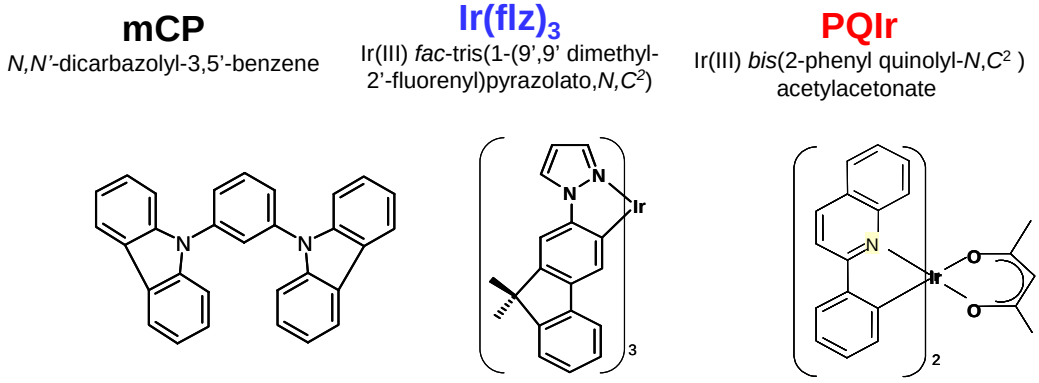

Figure 4-16. The molecular structures of mCP, FlzIr and PQIr.

The Li-doped Bphen region, in which strong charge transfer among Li atoms and Bphen molecules occur, behaves as the source for bipolar charge-carrier supply. Assuming the activation energy for electron transfer from Li to Bphen to be less than 0.2 eV, for example, the number of bounded electron-hole pairs in the form of Bphen:Li^+ produced by thermal activation energy of k_T (0.026 eV at room temperature) is estimated to be the order of 10^{17} cm^{-3}. [56] A strong electric field originated from an external applied voltage may help to increase the number of bounded electron-hole pairs. For the picture of no-bounded free carrier generation from the bounded electron-hole pairs, one may refer a scheme for free charge carrier production from "thermalized or relaxed bound charge-pair" proposed by Noolandi and Hong based on the Onsager theory. [57] The produced mobile electrons on Bphen molecules are assumed to move within the Li-doped Bphen layer with the assist of applied field and are transferred to the Bphen layer. On the other hand, the produced holes, which are assumed to be bounded on Li atoms or Li clusters, are assumed to be directly injected to the adjacent MoO_3 layer, possibly via field-assisted tunneling and are transferred to the NPD layer.

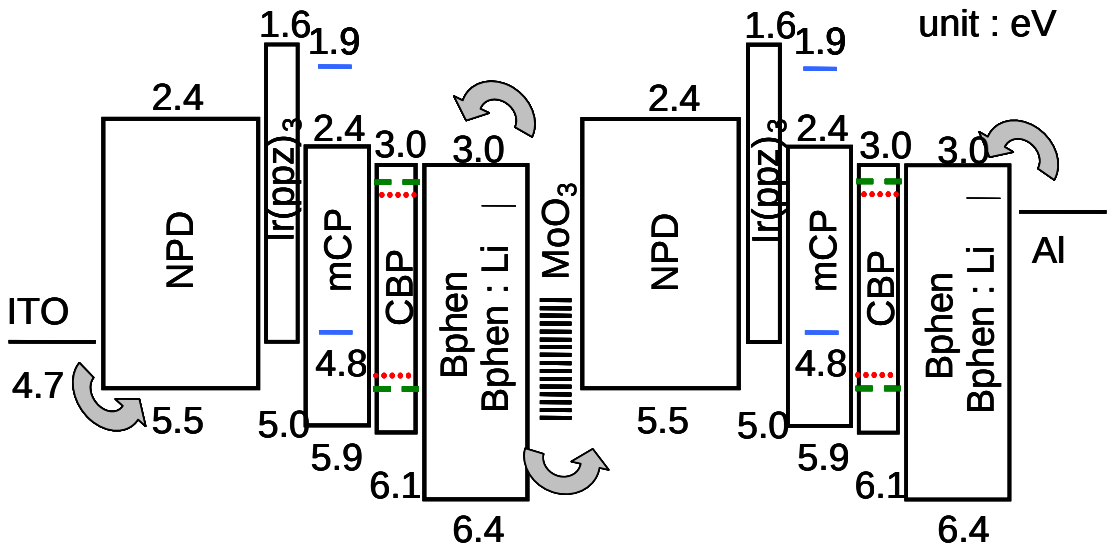

Figure 4-17. Proposed energy level diagram of a white stacked organic light emitting device (SOLED) with two electrophosphorescent elements. Numbers indicate the respective highest occupied and lowest unoccupied molecular orbital (HOMO and LUMO, respectively) energies relative to vacuum. The HOMO and LUMO energies of $Ir(ppy)_3$ and PQIr are (5.1 eV, 2.6 eV) and (5.0 eV, 2.7 eV), respectively. The arrows indicate the carrier injection from electrodes and the MoO_3 charge generation layer.

In the white SOLED, two or three electrophosphorescent (EP) sub-pixels are stacked (corresponding to a 2- or 3-SOLED, respectively), with the thickness of the NPD HTL varied in each element. To achieve both high efficiency and balanced emission intensity from each phosphor to achieve the desired white color temperature (5500 K), it is crucial to

(i) effectively confine the carriers and excitons within the emission layers (EMLs) of each sub-pixel in the stack

(ii) ensure that all exciton formation occurs within each EML

(iii) control optical interference and weak microcavity effects.[58-63]

In our devices, varying the NPD thickness determines the total optical path length through the stack. Given that the charge mobility of NPD is roughly 100 times higher than in the other organic materials used, its thickness variation (<100 nm) does not

significantly affect the drive voltage nor the carrier balance, and hence the position of the recombination zone.[64]

We employ *fac*-tris(1-(9, 9 dimethyl-2-fluorenyl)pyrazolyl-*N*, $C^{2'}$) Ir(III) ($Ir(flz)_3$) as a blue-green phosphor[65] doped at 10 wt% into a N,N'-dicarbazolyl-3,5-benzene (mCP) host.[66] Here, the $Ir(flz)_3$ LUMO is at 1.9 eV, and HOMO at 4.8 eV, referenced to vacuum. The low HOMO energy of $Ir(flz)_3$ relative to that of mCP suggests that $Ir(flz)_3$ is a hole trap. Electron injection into $Ir(flz)_3$ directly from the secondary host, CBP is energetically unfavorable. The exciton formation, therefore, occurs by direct excitation of the triplet, either by injection from the CBP LUMO, or by electron transfer from the mCP LUMO. Also, the shallow LUMO level is at least 0.5 eV above those of mCP and CBP, as well as the other dopants, thus preventing electron leakage from the EML into the adjacent layers. Furhermore, *fac*-tris(1-phenypyrazolyl-*N*,$C^{2'}$)iridium(III) ($Ir(ppz)_3$) and BPhen with wider energy gaps than those of the phosphors and host materials act as barriers to exciton and charge diffusion across the EML/HTL and EML/ETL interfaces, respectively. The use of blockers maintains charge balance within each EML, since the Li-doped Bphen/MoO_3 more efficiently generates electrons than holes. In the EML adjacent to the layer comprised of $Ir(flz)_3$:mCP, the green-emitting phosphor, $Ir(ppy)_3$ is co-doped with the red phosphor, PQIr in CBP to enhance the energy transfer from the host to PQIr.[3] Here the concentrations of $Ir(ppy)_3$ and PQIr are 3 wt% and 10 wt%, respectively. The majority of excitons in this region are generated by direct trapping on both PQIr and $Ir(flz)_3$.

Figure 4-18 shows the EL and PL transient in the device. Longer and shorter lifetimes in biexponential EL decays range between (t = 16.8 ± 2ms) and (19.4 ± 2ms), and between (t = 1.2 ± 0.1ms) and (t = 1.5 ± 0.1ms) as the pulse bias is increased from 20 to 28V. With the pulse amplitude increased, more electrons can be transferred from the mCP/CBP LUMO levels into $Ir(flz)_3$, resulting in rapid decay is diminished at higher pulse voltages. With -5V reverse bias between 20 V pulses, the shorter lifetime is reduced to (810 ± 80ns), and the rapid decay becomes less dominant and the luminance is reduced, signifying that the charges accumulated on $Ir(flz)_3$ are being swept out more quickly than charge diffusion or internal electric fields. Based on a monoexponential decay (t = 31.2 ± 0.5ms) of PL (inset), T-T annihilation

is ruled as the source of the biexponential EL decay. At higher voltage pulses, the initial rapid decay is reduced. These transient studies also indicate that the electron injection from mCP and CBP into $Ir(flz)_3$ is unfavorably due to the high LUMO level of $Ir(flz)_3$. The direct excitation of the $Ir(flz)_3$ triplet is therefore most likely to happen via electron injection from the LUMO of CBP and / or mCP. Unlike FIr6 and FIrpic with low LUMO levels (3.1 eV, 3.2 eV), an EML doped with $Ir(flz)_3$ (LUMO:1.9eV) remarkably reduces NPD emission, leading a high efficiency. The high LUMO level of $Ir(flz)_3$ effectively blocks the electron leakage into the HTL and the triplet level is excited and directly form excitons on the molecules. Thus, $Ir(flz)_3$ with the unusually high LUMO energy effectively blocks leakage of electrons and make the excellent carrier balance for achieving white light. And it also emits greenish blue light. This is the key material in the device which makes it possible to obtain the high-efficiency WOLED.

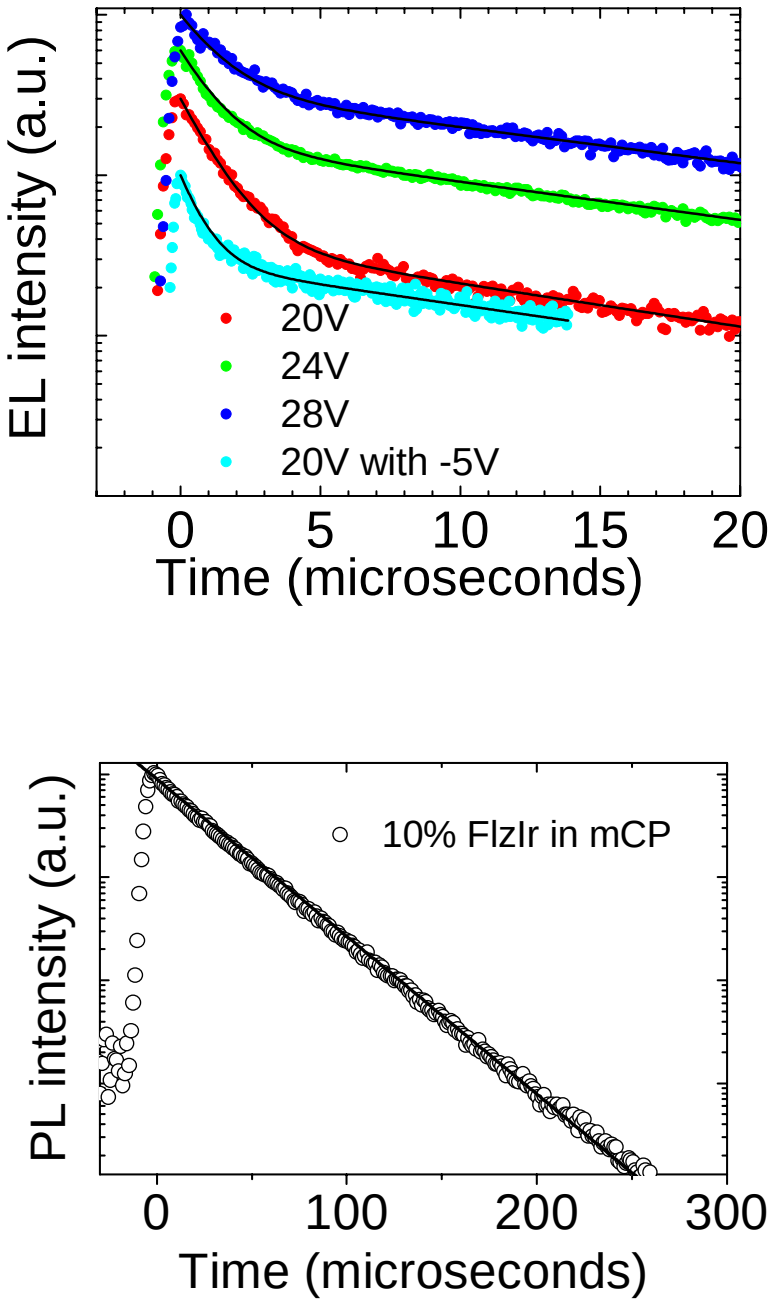

Figure 4-18. Top: Transient EL decay of $Ir(flz)_3$ in the 3-unit SOLED device at 300K under 300 ns pulse excitation at 20 V (red) and pulses with reverse bias at -5V (light blue), 24 (green) and 28V (blue), approximately corresponding to J = 1.0, 10, 100 mA/cm^2, respectively. Bottom: Transient PL decay of $Ir(flz)_3$ doped-mCP film excited at λ = 337 nm under 1 ns pulse at 300K.

Figure 4-19 shows the EP spectra of a 2- SOLED with the NPD thickness varied from 40 to 100 nm in 20–nm steps in the top element between the MoO_3 interlayer and the Al cathode. The $Ir(flz)_3$ emission becomes more intense with thicker NPD while the operational voltage and external efficiencies are not significantly changed (see inset, Fig. 4-19). Here, "external efficiency" (as distinct from quantum efficiency), is defined as the ratio of the total number of photons emitted by the OLED into the forward viewing direction, to the number of electrons injected from the cathode.

Figure 4-19 (Bottom) shows the results of optical simulations of the EP spectra for 2-SOLEDs. The refractive indices (n) of ITO and MoO_3 in the visible region employed in the simulation were measured by ellipsometry to be n = 1.9 and n = 2.2, respectively. Due to the index difference with the organic films (n = 1.7), weak microcavity effects are expected. In the simulation, we consider the SOLED as a stratified structure consisting of isotropic and homogeneous layers with plane-parallel interfaces.

Based on the fact that the equations governing the propagation of the optical electric field are linear and that the tangential component of the electric field is continuous, [62, 63] it can be described by 2×2 matrices, including interface matrices describing each interface between adjacent layers, and phase matrices describing the propagation through each layer, following a previous report [59]. For simplicity, only normal angle emission is considered. Using the product of these matrices, we can calculate the propagation of source fields in the emission layer to the outside, including all interference effects [60]. The optically-simulated spectra are in reasonable agreement with the experimental results. In the case where the NPD thickness in a bottom-unit between ITO and MoO_3 is similarly varied, the optical simulation also fits in with the observed spectra. These facts indicate the changes in spectra with varied thickness of NPD are dominantly attributed to the optical interference and weak microcavity effects rather than electrical characteristics such as carrier transport and exciton diffusion. Based on this, a strict control of layer thickness, especially of NPD, is essential in the proposed SOLED architecture.

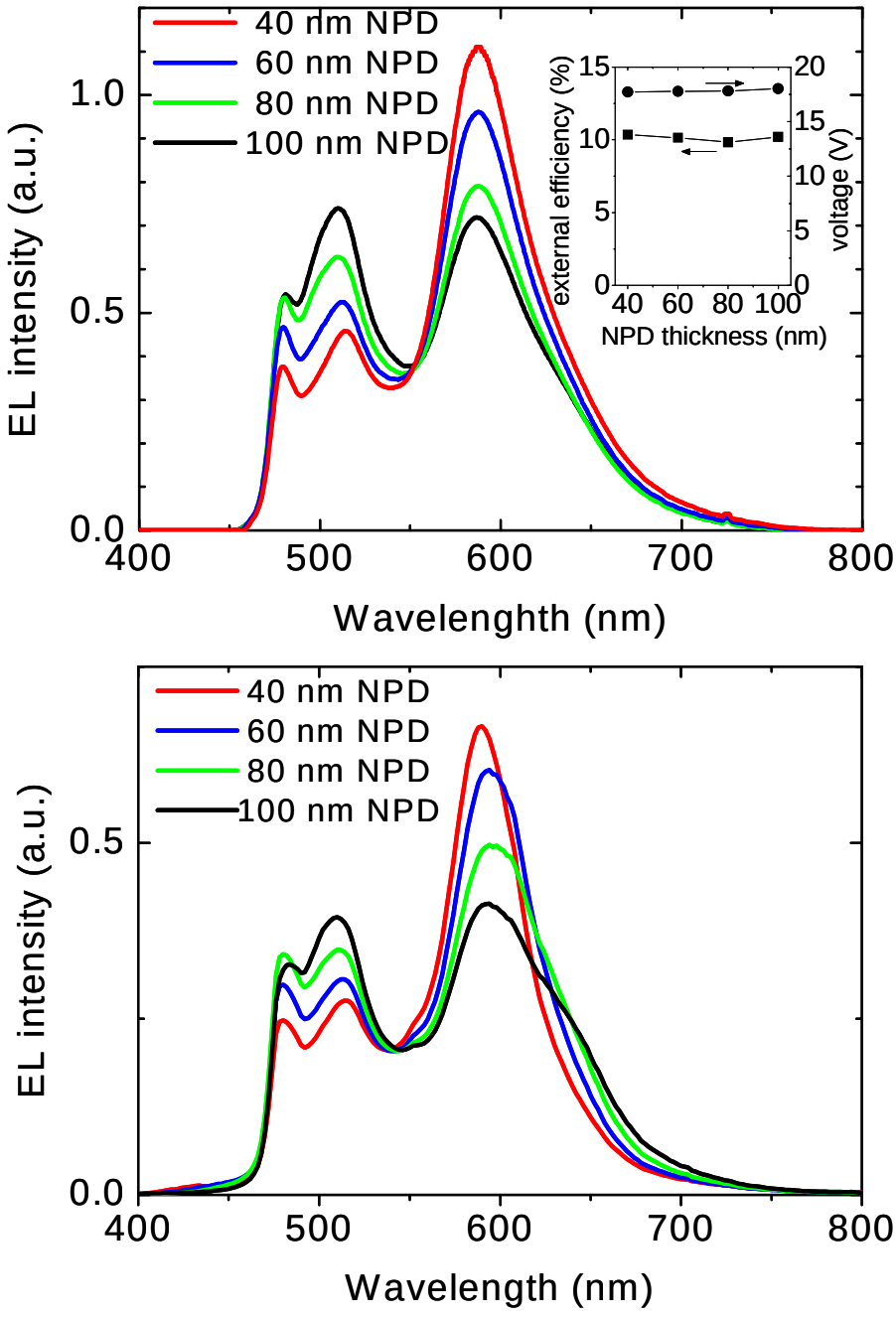

Figure 4-19. Top: Electrophosphorescent spectra at current density J=10 mA/cm2 of white SOLEDs with varied NPD thickness. Inset: External efficiency (squares) and operation voltage (circles) at J = 10 mA/cm2 as a function of NPD thickness. Bottom: Calculated electrophosphorescent spectra for devices with the same structure as in Top.

The external and luminous power efficiencies of 1-, 2- and 3- SOLEDs are shown in Fig. 4-20. The corresponding device structures and their performances are summarized in Table 4-3. The maximum forward viewing external efficiency for 3- SOLED is η_{ext} = 34.9±2.2 % at J = 0.035 mA/cm^2 (η_p = 22.7±1.4 lm/W at J = 0.0032 mA/cm^2). Since illumination sources are typically characterized by their *total* emitted power when placed in suitable illumination fixtures,[67] the 3- SOLED therefore has total external and power efficiencies at an approximate forward surface luminance of 500 cd/m^2 of $\eta_{ext,tot}$ = 51.0±3.2 %, $\eta_{p,tot}$ = 20.7±1.4 lm/W.

We find that the maximum external efficiencies of 1-, 2- and 3-SOLEDs are approximately proportional to the number of sub-pixels over a wide range of current densities.[51] For example, the maximum η_{ext} of the 2- and 3- SOLEDs are 1.8 and 2.6 times higher than that of a conventional OLED with a similar structure, indicating that the internal floating electrode efficiently generates both electrons and holes. The maximum external efficiency shifts toward increasing current density as the number of sub-pixels increases. Note that the luminous power efficiency of the 3-SOLED is lower than that of comparable 1- and 2-SOLEDs at low current densities due to a drop in intensity at a wavelength of 550 nm for the 3-SOLED.

The drive voltage at a fixed J increases with the number of sub-pixels. Note that Li-doping of Bphen allows for efficient electron injection, and hence a high external efficiency. When undoped-Bphen is placed adjacent MoO_3, the external and power efficiencies are lowered and the drive voltage is raised dramatically compared with its Li-doped counterpart (see Table 4-3). These results suggest inefficient charge generation resulting from the absence of the combination of the insulating MoO_3 and the Li-doped Bphen.

Figure 4-21 shows the EP spectra of 1-, 2- and 3-SOLEDs at a J=10 mA/cm^2. We infer that the pronounced change in the spectrum of the 3-SOLED (and its resulting decrease in luminous efficiency, see Fig. 4-20) is a consequence of optical effects as discussed above. The dependence of the spectrum on J of the 3-SOLED is shown in the inset of Fig. 4-21, indicating a shift to the blue at high J due to a weak induced charge imbalance in the three sub-pixels. Commission Internationale de L'Eclairage

chromaticity coordinates for 1-, 2- and 3-SOLEDs are (x=0.37, y=0.46), (x=0.39, y=0.45) and (x=0.35, y=0.44), respectively as shown Table 4-3 The color shift at high current densities is found to be very small as shown in Fig. 4-21 inset.

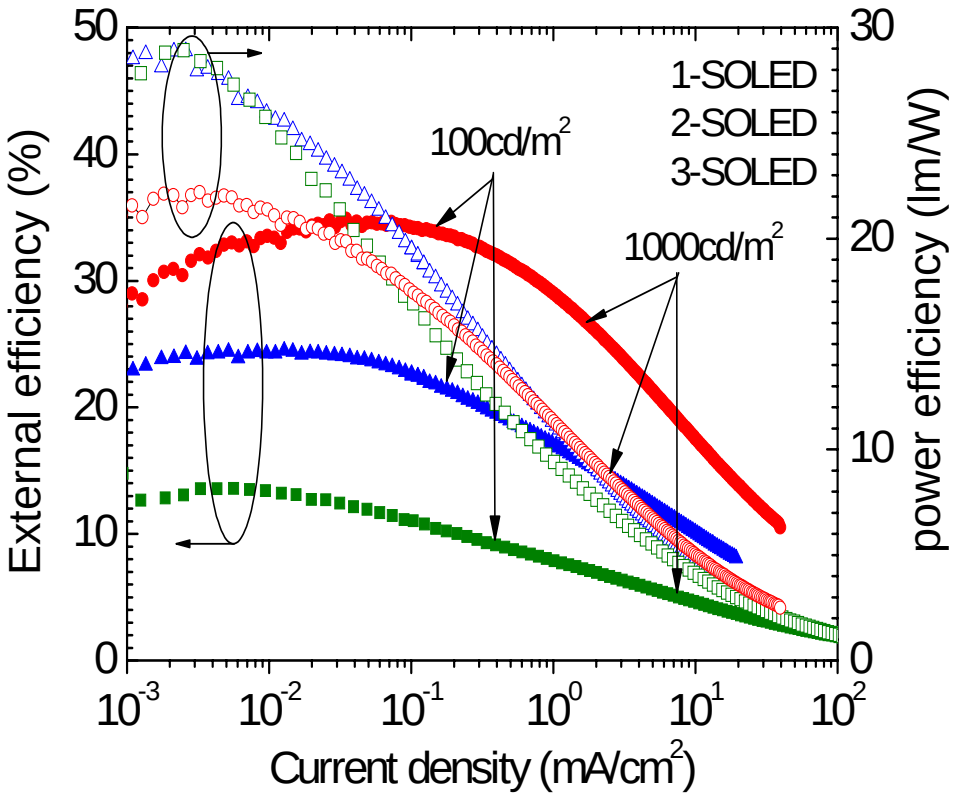

Figure 4-20. Forward viewing external and luminous power efficiencies of 1- (squares), 2- (triangles) and 3- (circles) SOLEDs as functions of current density. The arrows indicate values at brightnesses of 100 and 1000 cd/m^2 as measured in the forward viewing direction.

Table 4-3. Device characteristics of 1-, 2-, 3-SOLED.

Device: Structure [a]	max η_{ext} (η_{ext}) [1] (%)	max η_p (η_p) [1] (lm/W)	max efficiency (cd/A)	voltage at J=10	CIE (x,y) at J=10	Color rendering index
1-SOLED : EP_a	13.6±1.2 (6.4±0.6)	28.9±2.5 (6.6±0.6)	34.9±3.1	9.2	(0.37, 0.46)	62
2-SOLED : $EP_a/MoO_3/EP_b$	24.7±1.9 (16.8±1.3)	28.9±2.2 (10.9±0.8)	66.6±5.0	18.0	(0.39, 0.45)	64
3-SOLED : $EP_a/MoO_3/EP_c/MoO_3/EP_c$	34.9±2.2 (30.0±3.7)	22.7±1.4 (12.2±0.8)	77.0±5.0	24.1	(0.35, 0.44)	66

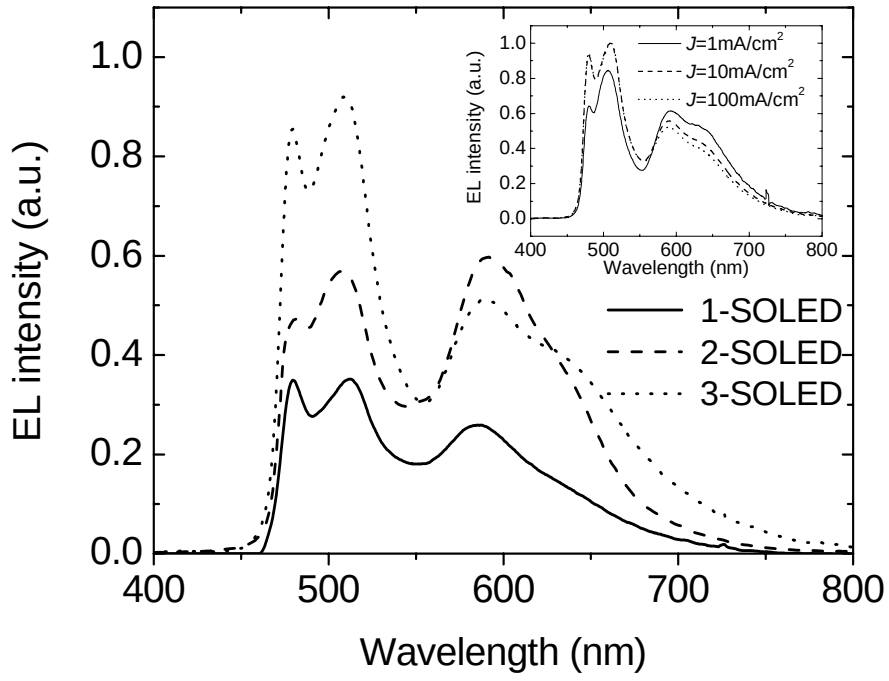

Figure 4-21. Electrophosphorescent spectra of 1-, 2- and 3-SOLEDs at a current density of J = 10 mA/cm2. Inset: Electroluminescent spectra of a 3-SOLED at J = 1, 10 and 100 mA/cm2.

4.3.3 Stacked Fluorescent/Phosphorescent WOLED

Since electrophosphorescence has been demonstrated to lead to nearly 100% harvesting of the electronically generated excitons[10], the efficiency of white OLEDs employing metallorganic phosphors has consequently also improved, resulting in EQE and power efficiency as high as 13.5 % and 16.7 lm/W, respectively (see Chap. 5.). However, drawbacks remain to the current approaches to solid state lighting based on OLEDs. For example, the peak efficiency is often achieved at low current density (~10^{-2} mA/cm^2), and hence low brightness, due to exciton quenching by triplet-triplet annihilation at high current.[28] For lighting, it is essential to obtain high-efficiency at high luminance (>800cd/m^2).

In the previous sections, distinguished approaches to high-efficiency white OLEDs have been demonstrated, foremost among them introduces a blue emissive fluorescent dopant together with red and green emissive phosphorescent dopants in the emission layer (EML) (see Chap. 4.1). In that device, the blue fluorescent dopant harvests a majority of singlet excitons, with the remainder of lower energy triplets diffusing through the conductive host to directly excite the green and red phosphors. This architecture allows for increased power efficiency by resonant energy transfer from the conductive host into both the singlet and triplet energy levels. Indeed, this architecture eliminates exchange energy losses of 0.5 to 1.0 eV resulting from ISC from the host singlet into a blue phosphor triplet state. Moreover, the device is expected to have an extended operational lifetime by employing a high stability blue flurophore. Another approach for achieving high efficiency at high brightness is via a SOLED[49-53]. With an exciton-confined architecture combined with stacked electrophosphorescent elements separated by transparent charge generation layers, total external ($\eta_{ext,\ tot}$) and power efficiencies ($\eta_{p,\ tot}$) of 51% and 20.7 lm/W at a luminosity of 500 cd/m^2 have recently been achieved (see Chap. 4.3).

In this section, we demonstrate a white emitting SOLED (WSOLED) employing the fluorescent/phosphorescent (F/P) dopant concept within a stacked architecture, with each F/P element in the stack separated by a transparent MoO_x charge generation layer. Here, CBP is used as the conductive host for both fluorescent and phosphorescent dopants. The blue fluorescent emitting zone is doped with BCzVBi[45,46], while the

green and red phosphorescent regions contain $Ir(ppy)_3$ and PQIr[6,19].

The device structure is shown in Fig. 4-22. An undoped CBP region is inserted in each element, forming a spacer between the fluorescent region and a phosphor doped CBP zone in the center of the EML. This undoped spacer prevents singlet excitons formed on the blue fluorophore to transfer to the lower energy green and red phosphors. However, CBP triplets, with their characteristically long diffusion lengths (>100nm), migrate into the spatially remote phosphor doped region as described in Chap. 4.1.

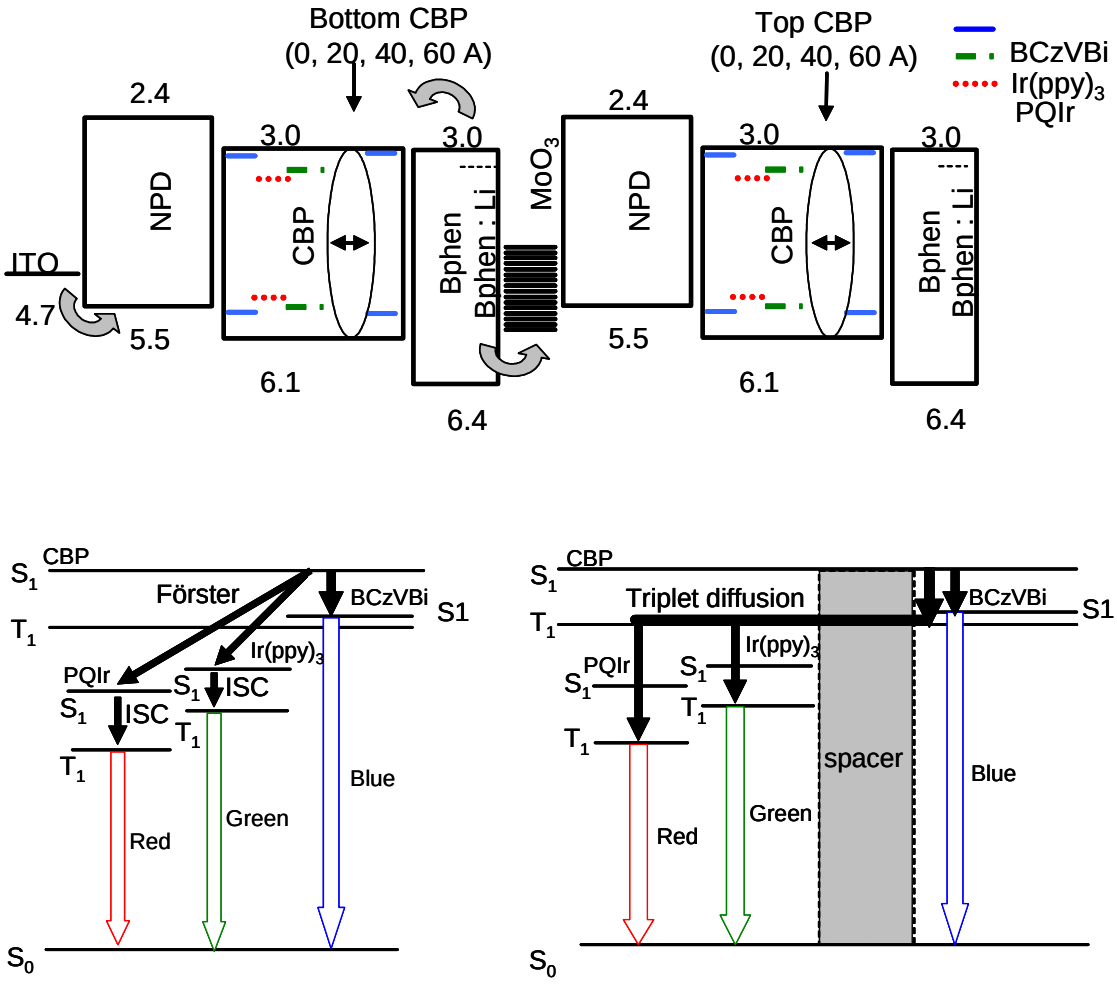

Figure 4-22. Top: The proposed energy diagram of the stacked F/P WOLED.
Bottom: The energy transfer with (Right) or without (Left) a spacer layer.

In these investigations, the NPD thickness in each separate emitting element in the stack is optimized to produce the desired white balance in the presence of weak optical interference that is characteristic of these multilayer structures.[58] Figure 4-23 shows the external and power efficiencies for various thicknesses of the CBP spacer in 2-element-white SOLEDs (2-WSOLEDs).

Note that increasing the CBP spacer thickness also increases the total EQE despite a corresponding relative decrease in the intensity of the blue emission, as shown in Fig. 4-24. This shift in the balance between phosphorescent and fluorescent emission is attributed to a change in the position where exciton recombination occurs. Assuming significant hole transport on the highest occupied molecular orbital (HOMO) of the phosphor dopants within the CBP transport gap, the insertion of an undoped CBP layer (HOMO = 6.1eV) at the EML/ETL interface introduces an energy barrier to transport into the BCzBVi HOMO at 5.5eV from the vacuum level [46]. Thus, the spacer impedes hole transport, resulting in a larger hole density leading to hole trapping in the phosphor doped region. This suggests that the phosphorescent emission is increased at the expense of fluorescence. The extended recombination zone also results in an increase in total quantum efficiency, since excitons formed directly on the phosphors are not subject to geminate recombination that occurs on diffusion through this region.

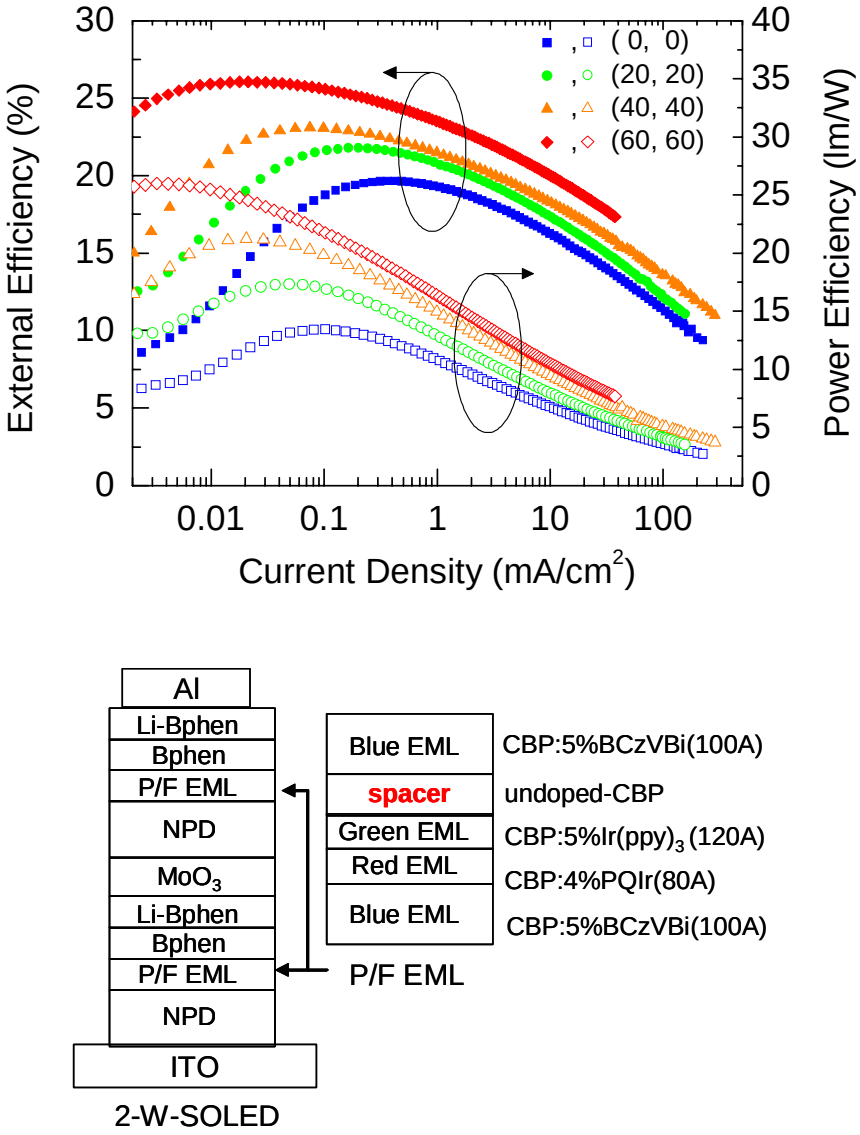

Figure 4-23. The external and power efficiencies for various thicknesses of the CBP spacer in 2-element-white SOLEDs (2-WSOLEDs). The peak external and power efficiencies, CIE coordinates, and CRI change from η_{ext} = 20±2 %, η_p = 13±1 lm/W, (x=0.36, y=0.41), and CRI=83; to η_{ext} = 26±3 %, η_p = 26±3 lm/W, (x=0.40, y=0.50) and CRI=66 as the spacer thickness is varied from 0 nm to 6 nm in both the top and bottom EMLs. Moreover, the operating voltage at a current density of J= 10 mA/cm^2 is lowered from 18.4 V to 16.7 V with increasing spacer thickness.

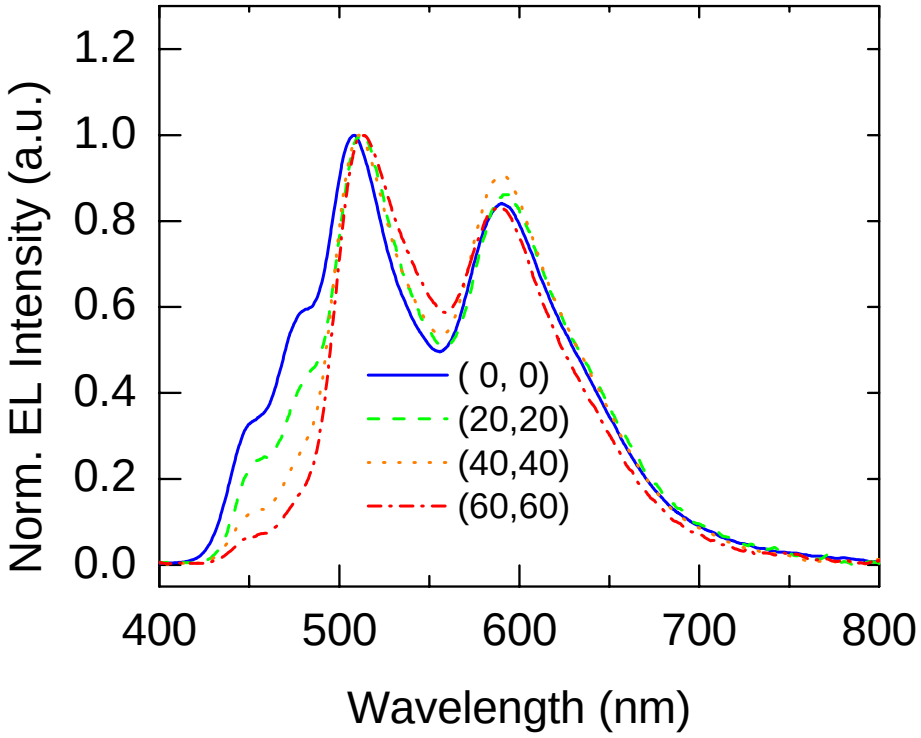

Figure 4-24. Electroluminescent spectra of 2-W-SOLEDs with spacer thickness varied

The corresponding device structures and their performances are summarized in Table 4-4. Only slight changes in the emission spectra are observed over a wide range of current for each device. The external efficiencies are approximately proportional to the number of stacked elements. For the 3-WSOLED, maxima of forward viewing external and power efficiencies of η_{ext} = 33 ±3 % at J = 1.1 mA/cm^2 and η_p = 14±1 lm/W at J = 0.22 mA/cm^2 are obtained, respectively. The total external and power efficiencies are estimated to be $\eta_{ext,tot}$ = 57±6 % and $\eta_{p,tot}$ = 22±2 lm/W at a luminance of 1000 cd/m^2 when placed in suitable illumination fixtures.[6,67] The WSOLEDs in this work exhibit significant improvement, having higher external efficiencies at increased currents compared to previously demonstrated all-phosphor doped WSOLEDs with a peak forward viewing external efficiency of η_{ext} = 34.9±2.2 %, measured at a relatively low current density of 0.01 mA/cm; see Fig. 4-25.

The power efficiency of the 1-WSOLED differs from the 2- and 3-WSOLEDs at low currents (< 10^{-1} mA/cm^2), but is otherwise increased in the order of 1-, to 2- to 3-elements, since the voltage at a given current increases sublinearly with the number of stacked elements. This results from the very small hole injection barrier between MoO_x and NPD due to the nearly perfect alignment of their HOMO levels (corresponding 5.6 eV for MoO_x, and 5.5eV for NPD).

The peak efficiencies shift towards higher current densities by approximately two orders of magnitude compared to previous reports[6] and the less pronounced efficiency roll-off at the highest currents is possibly due to reduced localization of triplet excitons in the extended EML, reducing triplet-triplet annihilation.[28]

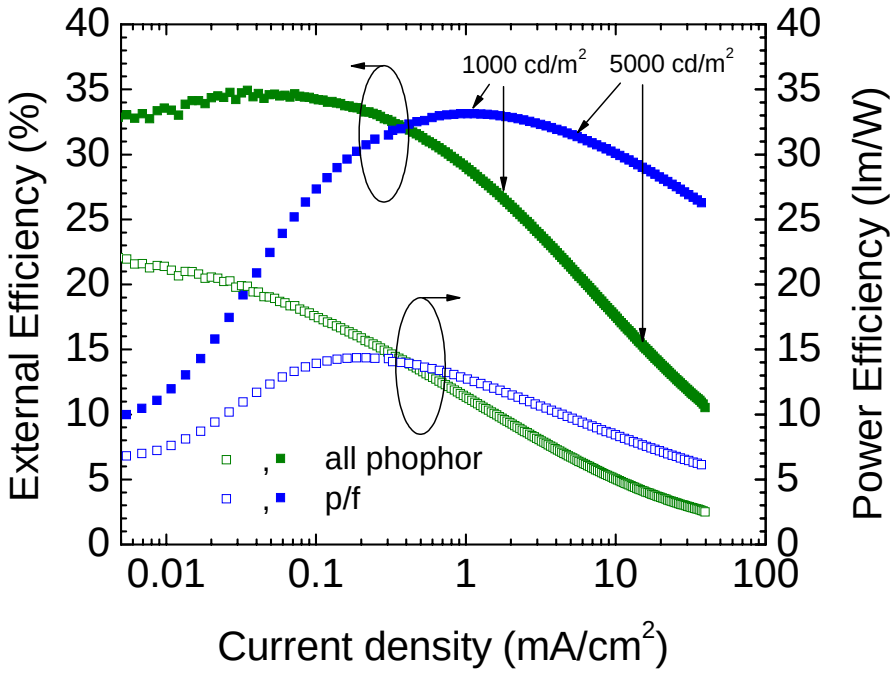

Figure 4-25. The comparison with the previously reported all-phosphor WOLED.

Table 4-4. Device characteristics of 1-, 2-, 3-SOLED.

Device:	Structure [a)]	max η_{ext} (%) (at J mA/cm^2)	max η_p (lm/W) (at J mA/cm^2)	voltage at J=10	CIE (x,y) at J=10	Color rendering index
1-W-SOLED :	EL_a	11.9±1.2 (J=0.779)	16.5±1.7 (J=0.028)	11.4	(0.37, 0.42)	83
2-W-SOLED :	$EL_b/MoO_3/EL_c$	22.5±2.3 (J=1.00)	13.8±1.4 (J=0.174)	22.1	(0.38, 0.44)	81
3-W-SOLED :	$EL_a/MoO_3/EL_b/MoO_3/EL_b$	33.2±3.3 (J=1.14)	14.4±1.4 (J=0.215)	30.3	(0.38, 0.44)	82

a) EL=electroluminescent subpixel element consisting of NPD (variable thickness) / 5 % BCzVBi : CBP (10 nm) / 4 % PQIr : CBP (8 nm) / 5 % $Ir(ppy)_3$: CBP (12 nm) / CBP (2 nm) / 5 % BCzVBi : CBP (10 nm) / Bphen (25 nm) / Bphen : Li (1: 1 molar ratio) (25 nm). The NPD thickness in each EL element is ELa: 60nm, ELb: 100nm, and ELc: 40nm.

4.3.4 Conclusion

It has been demonstrated that high efficiency white electrophoshporescent devices consisting of stacked white EP-OLEDs with a blue-green phosphor separated by thin and transparent MoO_3 charge injecting interlayers. The external efficiencies approximately scale with the number of white emissive sub-pixels. The white SOLEDs reach a maximum forward viewing η_{ext} = 34.9±2.2 % for a 3-SOLED and total $\eta_{ext,tot}$ = 51.0±3.2 % at a luminance of 500 cd/m^2. The forward viewing and total power efficiencies are relatively independent of the number of elements in the stack, peaking at η_p = 28.9±2.2 lm/W ($\eta_{p,tot}$ = 18.5±1.4 lm/W) and 22.7±1.4 lm/W ($\eta_{p,tot}$ = 20.7±1.4 lm/W) for 2- and 3-SOLEDs, respectively. The use of both electron and hole blocking layers, combined with a MoO_3/Li-doped BPhen charge generation layer ensures a uniform white color balance for each sub-pixel in the stack, along with very high efficiency for charge injection. These results demonstrate that white electrophosphorescent SOLEDs are a promising means for achieving high brightness and efficient sources for indoor lighting and display backlights.

It has also been demonstrated that high efficiency white stacked OLEDs based on a blue fluorescent, and green and red phosphorescent emitters combined with transparent MoO_x charge injecting interlayers. By changing the spacer thickness between the fluorescent and phosphorescent emitting zones within the EML, we obtain balanced exciton formation resulting in white emission without sacrificing the efficiency of the individual F/P OLED emitting elements. These results demonstrate that white electrophosphorescent SOLEDs constitute a promising route to achieving high brightness and efficient sources for indoor lighting.

4.4 Summary

In this chapter, high-efficiency WOLEDs based primarily on phosphorescent emitter are presented, which allows for 100% IQE. The sections cover the most promising technologies for achieving the high efficiencies. Approaches for high efficiency WOLEDs are proposed in terms of improving the efficiency of energy transfer and the device architecture and the necessary conditions are also discussed. Especially, the formation process of excitons is carefully examined in each devices

considering the energy diagrams. The results can be widely applied for application of full-color displays and lighting sources.

In Chap.4-1, high-efficiency WOLED without ISC energy loss is proposed. The highly efficient WOLED, with a color rendition that is unusually independent of current density, has potential for use in the next generation of sources for solid-state indoor lighting. The total exciton trapping fraction and the exciton diffusion length are analyzed based on the experimental results.

In Chap. 4-2, the WOLEDs have an extended carrier recombination zone, which leads to high external efficiencies at high brightness. The devices reach a maximum forward viewing external efficiency of η_{ext} = 8.5±0.3 % for the WSOLED with 8% $Ir(ppy)_3$, and a total efficiency of $\eta_{ext,tot}$ = 13.1±0.5 % at a luminance of 800 cd/m^2. This corresponds to a total power efficiency of $\eta_{p,tot}$ = 20.2±0.7 lm/W with a CRI of 79.

In Chap. 4-3, the WSOLEDs have an extended carrier recombination zone, which leads to high external efficiencies at high brightness. The devices reach a maximum forward viewing external efficiency of η_{ext} = 33±3 % for a 3-WSOLED, and a total efficiency of $\eta_{ext,tot}$ = 57±6 % at a luminance of 1000 cd/m^2, representing a 25% increase relative previously reported all-phosphor doped WSOLEDs. The result thus far is one of the highest among what have been ever reported. The stacked structure of F/P WOLED is also demonstrated and high efficiencies at high currents have been achieved.

Chapter 4. References

[1] (ed. Energy, U. S. D. o.) xii (U.S. Governmment Printing Office, Washington DC, 2001).

[2] B. W. D'Andrade, and Forrest, S. R. Adv. Mater. 16, 1585 (2004).

[3] B. W. D'Andrade, R. J. Holmes, and S. R. Forrest, Adv. Mater.16, 624 (2004).

[4] S. Tokito, T. Iijima, T. Tsuzuki, and F. Sato, Appl. Phys. Lett. 83, 2459 (2003).

[5] V. Adamovich, J. Brooks, A. Tamayo, A. M. Alexander, P. I. Djurovich, B. W. D'Andrade, C. Adachi, S. R. Forrest and M. E. Thompson,. New J. Chem. 26, 1171 (2002).

[6] B. W. D'Andrade, M. E. Thompson, and S. R. Forrest, Adv. Mater. 14, 147 (2002).

[7] B. W. D'Andrade, J. Brooks, V. Adamovich, M. E. Thompson, and S. R. Forrest, Adv. Mater. 14, 1032 (2002).

[8] D. S. Qin, and Y. Tao, Appl. Phys. Lett. 86, 113507 (2005).

[9] G.. Cheng, F. Li, Y. Duan, J. Feng, S. Liu, S. Qiu, D. Lin, Y. Ma, and S. T. Lee,. Appl. Phys. Lett. 82, 4224 (2003).

[10] M. A. Baldo, D.F. O'Brien, A. Shoustikov, S. Sibley, M. E. Thompson, and S. R. Forrest, Nature 395, 151 (1998).

[11] G. Schwartz, K. Fehse, M. Pfeiffer, K. Walzer, and K. Leo, Appl. Phys. Lett. 89, 083509 (2006)

[12] Y. J. Tung, et al. Society for Information Display 35, 1, 48 (2004).

[13] R. J. Holmes, B. W. D'Andrade, X. Ren, J. Li, M. E. Thompson, Appl. Phys. Lett. 83, 3818 (2003).

[14] I. Sokolik, R. Priestley, A. D. Walser. R. Dorsinville, and C. W. Tang, Appl. Phys.Lett. 69, 4168 (1996).

[15] M. A. Baldo, D. F. O'Brien, M. E. Thompson, Phys. Rev. B 66, 14422 (1999).

[16] J. Kalinowski, et al, Chem. Phys.297, 39 (2004).

[17] C. Hosokawa, H. Higashi, H. Nakamura, and T. Kusumoto, Appl. Phys. Lett. 67, 3853 (1995).

[18] C. Adachi, M. E. Thompson, and S. R. Forrest, IEEE J. Sel. Top. Quant. Elec. 8, 372 (2002).

[19] M. A. Baldo, and S. R. Forrest, Phys. Rev. B 62, 10958 (2000).

[20] M. Reufer, M. J. Walter, P. G. Lagoudakis, A. B. Hummel, J. S. Kolb, H. G. Roskos, U. Scherf, and J. M. Lupton. Nature Materials 4, 340 (2005).

[21] M. Segal, M. A. Baldo, R. J. Holmes, S. R. Forrest, and Z. G. Soos, Phys. Rev. B 68, 075211 (2003).

[22] N. C. Giebink, Y. Sun, and S. R. Forrest, submitted for publication (2006).

[23] C. W. Tang, S. A. Vanslyke and C. H. Chen, J. Appl. Phys. 65, 3610 (1989).

[24] C. Hosokawa, H. Higashi, H. Nakamura and T. Kusumoto, Appl. Phys. Lett. 67, 3853 (1995).

[25] G.. Gu, D. Z. Garbuzov, P. E. Burrows, S. Venkatesh, S.R. Forrest and M.E. Thompson, Opt. Lett. 22, 396 (1997).

[26] In Method of measuring and specifying colour rendering properties of light sources, Commission Internationale de L'êclairage (CIE), 1974.

[27] B. W. D'Andrade and S. R. Forrest, Adv. Mater. 16, 1585 (2004).

[28] M. A. Baldo, C. Adachi, and S. R. Forrest, Phys. Rev. B 62, 10967 (2000).

[29] H. Murata, Z. H. Kafafi, and M. Uchida, Appl. Phys. Lett. 80, 189 (2002).

[30] Y. Kawamura, K. Goushi, J. Brooks, J. J. Brown, H. Sasabe, and C. Adachi, Appl. Phys. Lett. 86, 071104 (2005).

[31] C. Adachi, M. A. Baldo, M. E. Thompson, S. R. Forrest, J. Appl. Phys. J. Appl. Phys. 90, 5048 (2001).

[32] M. A. Baldo, M. E. Thompson, and S. R. Forrest, Nature 403, 750 (2000).

[33] B. W. D'Andrade, M. A. Baldo, C. Adachi, J. Brooks, M. E. Thompson, and S. R. Forrest, Appl. Phys. Lett. 79, 1045 (2001).

[34] G. Lei, L. Wang, and Y. Qiu, Appl. Phys. Lett. 85, 5403 (2004).

[35] Y. Zhang, G. Cheng, Y. Zhao, J. Hou, and S. Liu, Appl. Phys. Lett. 86, 011112 (2005).

[36] M. A. Baldo, S. Lamansky, P. E. Burrows, M. E. Thompson, and S. R. Forrest, Appl. Phys. Lett. 75, 4 (1999).

[37] S. A. VanSlyke, and C. W. Tang, (Eastman Kodak Company, Rochester NY, US, 1985).

[38] V. Cleave, G..Yahioglu, P. Le Barny, R. Friend, and N. Tessler, Adv. Mater. 11,

285 (1999).

[39] C. H. Chen, J. Shi, and C. W. Tang, Macromolecular Symposia 125, 1 (1997).

[40] U. Brackmann, Lambdachrome Laser Dyes (Lambda Physik, Gottingen, 1997).

[41] M. Klessinger and J. Michl, Excited states and photochemistry of organic molecules (VCH Publishers, New York, 1995).

[42] T. Forster, Discussions of the Faraday Society 27, 7 (1959).

[43] V. L. Ermolaev and E. B. Sveshnikova, Doklady Akademii Nauk SSSR 149, 1295 (1963).

[44] M. Berggren, A. Dodabalapur, R. E. Slusher, and Z. Bao, Nature 389, 466 (1997).

[45] K. O. Cheon, and J. Shinar, J. Appl. Phys. 81, 1738 (2002).

[46] C. Hosokawa, H. Tokailin, H. Higashi, and T. Kusumoto, J. Appl. Phys. 78, 5831 (1995).

[47] K. Mameno, R. Nishikawa, K. Suzuki, S. Matsumoto, T. Yamaguchi, K. Yoneda, Y. Hamada, H. Kanno, Y. Nishio, H. Matsuoka, Y. Saito, S. Oima, N. Mori, G. Rajeswaran, S. Mizukoshi, and T. K. Hatwar, Proceedings of IDW'02, 235 (2002)/

[48] J. Y. Lee, J. H. Kwon, and H. K. Chung, Org. Electron 4, 143 (2003).

[49] Z. Shen, P. E. Burrows, V. Bulovic, S. R. Forrest, and M. E. Thompson, Science 276, 2009 (1997).

[50] G. Gu, G. Parthasarathy, P. Tian, P. E. Burrows, and S. R. Forrest, J. Appl. Phys. 86, 4076 (1999).

[51] P. E. Burrows, S. R. Forrest, U.S. Patent No. 6,274,980 B1 (Aug. 14. 2001).

[52] T. Matsumoto, T. Nakada, J. Endo, K. Mori, N. Kavamura, A. Yokoi, and J. Kido, SID 03 Digest, 979 (2003).

[53] L. S. Liao, K. P. Klubek, and C. W. Tang, Appl. Phys. Lett. 84, 167 (2004).

[54] N. Miyata, T. Suzuki, and R. Ohyama, Thin Solid Films 282, 218 (1996).

[55] S. A. Aly, S. A. Mahmoud, N. Z. El-Sayed, M. A. Kaid, Vacuum 55, 159 (1999).

[56] T. Tsutsui, and M. Terai n, Appl. Phys. Lett. 84, 440 (2003).

[57] J. Noolandi, and K. Hong, J. Chem. Phys. 70, 3230 (1979).

[58] V. Bulovic, V. B. Khalfin, G. Gu, P. E. Burrows, D. Z. Garbuzov, and S. R. Forrest, Phys. Rev. B 58 , 3730 (1998).

[59] L. A. A. Pettersson, L. S. Roman, and O. Inganas, J. Appl. Phys. 86, 487 (1999).

[60] H. Benisty, R. Stanley, and M. Mayer, J. Opt. Soc. Am. A 15, 1192 (1998).

[61] A. A. Dodabalapur, L. J. Rothberg, R. H. Jordan, T. M. Miller, R. E. Slusher, and J. M. Phillips, J. Appl. Phys. 80, 6954 (1996).

[62] Z. Knittl, Optics of Thin Films (Wiley, London, 1976).

[63] R. M. A. Azzam and N. M. Bashara, Ellipsometry and Polarized Light (North-Holland, Amsterdam, 1977).

[64] Y. Fukuda, T. Watanabe, T. Wakimoto, S. Miyaguchi, and M. Tsuchida, Synth. Met. 111, 1 (2000).

[65] T. Sajoto, P. I. Djurovich, A. Tamayo, M. Yousufuddin, R. Bau, M. E. Thompson, R. J. Holmes and S. R. Forrest, Inorg. Chem. 44, 7992 (2005).

[66] R. J. Holmes, S. R. Forrest, Y.-J. Tung, R. C. Kwong, J. J. Brown, S. Garon and M. E. Thompson, Appl. Phys. Lett. 82, 2422 (2002).

[67] M.-H. Lu and J. C. Sturm, J. Appl. Phys. 2002, 91, 595.

[68] C.-C. Chang, S.-W. Hwang, C. H. Chen, and J.-F. Chen, Jpn. J. Appl. Phys. 43, 6418 (2004).

[69] J. X. Sun, X. L. Zhu, H. J. Peng, M. Wong, and H. S. Kwok, Appl. Phys. Lett. 87, 093504 (2005).

[70] C. W. Law, K. M. Lau, M. K. Fung, M. Y. Chan, F. L. Wong, C. S. Lee, and S. T. Lee, Appl. Phys. Lett. 89, 133511 (2006)

Chapter 5.

Application for Full-Color Displays

5.1 Improving Device Stability

5.1.1 Tom Emission Structure

OLEDs came into practical use in a decade after C. W. Tang first reported the OLED comprised of thin organic layers. The quick transition from research to the commercial production does not mean that little technical challenges are remained to overcome for researches. The market size of OLED displays reached approximately 7 hundred million yen in 2005 whereas that of competing small-sized LCD displays is 2 trillion 5 hundred billion yen. At present, the major applications for OLEDs are sub-displays for cell phones, displays for MP3 players and car stereos. Although an OLED exhibits ideal features for a display such as self-emission, fast-response and wide viewing angle, the adoption of OLEDs for high-quality displays is not much promoted due to the rapid technological progress in the competing LCDs. For a practical use, the following items as well as above mentioned high efficiencies are essential for dominating the LCDs. Or it would be very difficult to win a primary position in the market since the production cost for a LCD is reduced applying large scale production.

Under the circumstances, it is significant to develop the high-efficiency technologies proposed in the previous Chapters in a prototype with a TFT active-matrix backplane. For a practical use, the following items are required.

(1) Low power consumption（a low driving voltage and a high efficiency under high brightness condition）

(2) Long lifetime（over 3000 hours of T50 and over 500 hours of T95 from an initial luminance of white emission : 5000 cd/m^2）

(3) Operational stability of a driving voltage (under 0.5V- rise at 1000 hours), an emission spectrum over a wide range of environmental change.

(4) Color stability over a wide range of currents

The power consumption shown in (1) is most significant characteristic for applying OLEDs in potable electric devices such as cell phones, digital cameras. For lowering a power consumption, the development of device structure is very important in addition to the development of materials mentioned previously. In this chapter, I describe the low-power consumption technology from a view point of modifying the

design of a low temperature polysilicon TFT backplane, especially focusing on the pixel format.

(2) - (4) relate to stability of an OLED. In this chapter, the improved stability is described from an aspect of developing a device structure. Finally, the prospect for the roadmap of OLED power consumption will be described.

Interest in next-generation displays and lighting technologies has stimulated research on organic light-emitting devices (OLEDs). Especially, WOLEDs employing phosphorescent materials have led to significant improvements in efficiency (see Chap. 4) targeting backlights for full color active-matrix displays combined with color filters. [1] However, a disadvantage of conventional bottom-emissive OLEDs when used in a full-color display is that the pixel aperture ratio is diminished by the accompanying backplane electronics circuitry. The displays require an increased current density to accommodate the lower aperture ratio, which leads to a significant reduction in operational lifetime. The relationship between a half luminance lifetime (T) and a current density (J) (T_o and J_o are the control data for projecting lifetime) is estimated as follows.

$$T = T_o \left(\frac{J_o}{J} \right)^{1.5 \sim 1.7}$$

Accordingly, top-emissive OLEDs (see Fig. 5-1) are a desirable means for resolving this problem since all electronic circuitry can be placed on the substrate beneath the light emitter. [2-12] Typically, transparent and efficiently carrier injecting cathodes [13,14] employ sputtered indium tin oxide (ITO) on a thin metal layer such as Mg:Ag. However, the metal layer reduces the transparency to ~60% [6] and can produce microcavity effects[13,16,17] that lead to a directional dependence on the emission output and wavelength as shown in Fig. 5-2, which is reported by Hsu et al. [18]

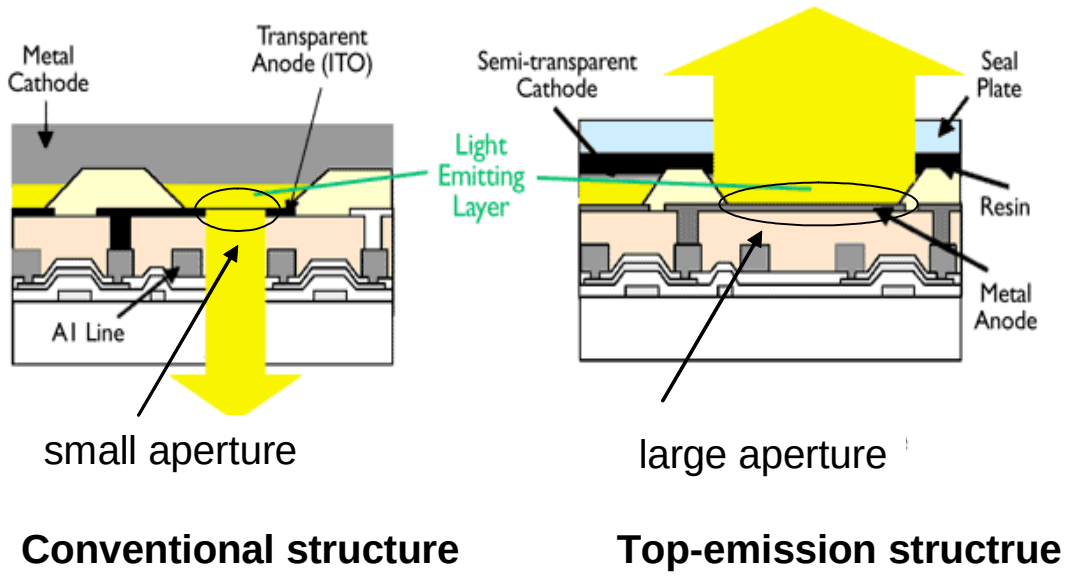

Figure 5-1. Left: The conventional bottom-emissive device structure in a TFT backplane. Right: The top-emissive structure.

A microcavity structure in a top-emitting device is formed between a reflective anode and a semitransparent cathode, and the microcavity effect can be realized as one kind of Fabry–Perot filter which should satisfy the following equation:

$$\frac{2L}{\lambda_{max}} + \frac{\Phi}{2\pi} = \text{m} \quad \text{(m: integer)} \qquad (1)$$

where L is the optical length between the two mirrors, and Φ is the sum of the phase shift from anode and cathode. [13]

The full width at half maximum (FWHM) (Refs. 19,20) can be estimated by

$$\text{FWHM} = \frac{\lambda^2}{2L} \times \frac{1-\sqrt{R_1 R_2}}{\pi (R_1 R_2)^{1/4}} \qquad (2)$$

, where R_1 and R_2 are the reflectance of the two mirrors. Spectral narrowing is the most common phenomena caused by a strong microcavity effect. As implied from Eq. (2), a shorter L as well as lower R_1 or R_2 are preferred to alleviate the undesirable microcavity effect and to obtain wider FWHM emission. Thus, reducing the reflectance of mirrors is key to ease microcavity effects. Wide viewing angle is most attractive features in an OLED display since a competing LCD has the narrower viewing angle. Thus, simultaneous pursuit of a wide aperture in a pixel and a wide viewing angle must be realized for an OLED display.

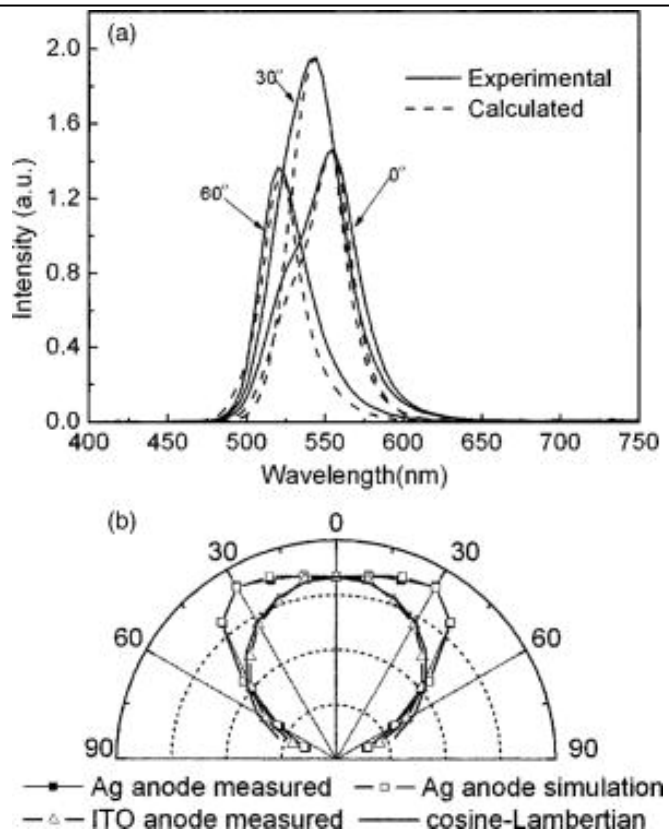

Figure 5-2. (a) shows the electroluminescence (EL) spectra of the device, Ag/NPD/Alq:C545T/Alq/LiF/Al, measured under a current of 20 mA/cm^2 at viewing angles of 0°, 30°, and 60° off the normal direction for the Ag anode. The corresponding angular distributions are compared in (b). It is clear that while the angular dependence of the ITO anode device is well fitted by a Lambertian distribution, the same is not true for the Ag anode device. In fact, the highest luminance was measured at ~30° from the normal. The strong microcavity effects in the Ag anode device can also be quantified using a classical model which calculates the spontaneous radiation of dipoles in thin film microcavities. [21,22] After Hsu et al (2005).

On the other hand, top emissive OLEDs have demonstrated less efficiencies than their bottom emissive counterparts so that to justify using top emissive OLEDs in an active-matrix OLED displays, the gain in aperture ratio must be large enough to offset any efficiency loss. A large fraction of the generated optical power is lost due to total internal reflection and waveguiding. The ratio of optical energy transmitted into material 1 to 2 (B) is expressed in the following equation. And including Fresnel reflections at the the glass-air interface along with the angular distribution of optical energy in the glass substrate [23], only ~17.5% (for a small molecular weight OLED) of the generated optical power is coupled out of the substrate into free-space. [24]

$$B = \left[1 - \left\{ 1 - \left(\frac{n_2}{n_1} \right)^2 \right\}^{1/2} \right] / 2$$

Several methods have been developed that increase the outcoupling efficiency. [25-27] One way to increase the outcoupling efficiencies to insert a low index-of-refraction material between the ITO and the glass substrate. [28] In a conventional OLED, there is a high density of waveguiding modes in the glass substrate due to its thickness (see Fig 5-3). An increase in external quantum emission by a factor of 1.8 from insertion of the aerogel layer was reported. [28] The optical microcavity structure (as manifested in the refractive indices) of the OLED terminates in the aerogel layer due to its thickness and porosity. We find that the structure can be replicated in the top emissive structure by eliminating the metal layer with a high refractive index. Therefore, it is expected that the same suppression of the waveguide modes in the top emissive devices, so that top emissive OLEDs can be more efficient than the equivalent bottom emissive OLEDs on glass substrate.

In order to verify these theoretical predictions in the white-light top-emitting device are designed and analyzed in the next section.

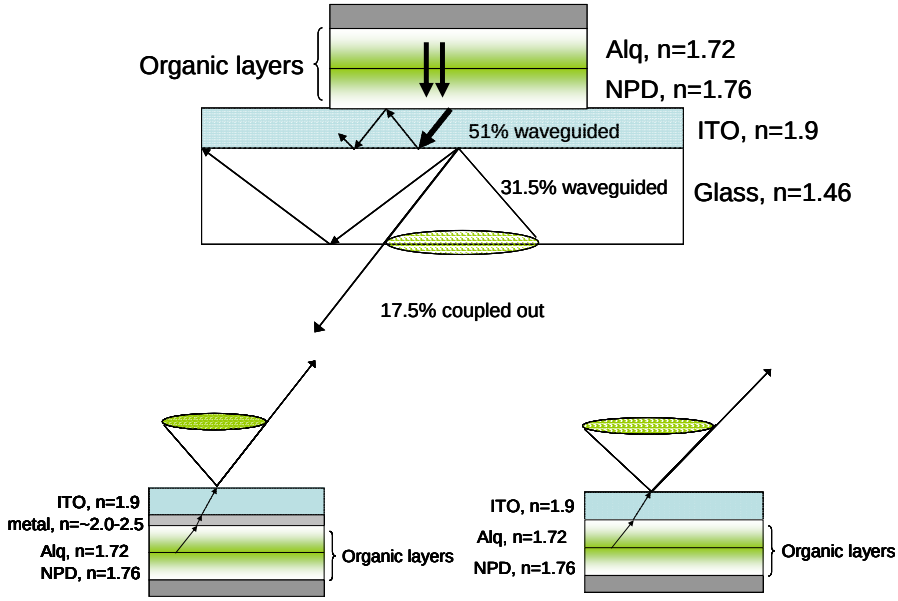

Figure 5-3. Top: Light emission of a conventional OLED. Bottm: (Left) Outcoupling of a top emissive OLED with thin metal layer. (Right) Outcoupleing of the proposed metal-layer –free top emissive OLED.

5.1.2 Wide Viewing Angle with Tom Emission Structure

It is a matter of significance to educe optical losses and microcavity effects by replacing the metal with an organic layer consisting of, for example, copper phthalocyanine [29,30]. However, such "metal-free" transparent cathodes often have an increased operating voltage, reduced electron injection efficiency, and quantum and luminous power efficiencies when compared to conventional OLEDs. [31] Recently, however, reports have shown that efficient electron injection from an ITO cathode on a Li doped 4,7-diphenyl-1,10-phenanthroline (BPhen) layer can be achieved at low contact voltages. [32-34] Here, we demonstrate a high-efficiency, white and top-emitting phosphorescent OLED (WOLED) with a metal-free cathode consisting of Li-doped BPhen followed by a sputtered layer of ITO.

Only a blue and red phosphor are required to obtain chromaticity coordinates near to the ideal white point of (0.33, 0.33), leading to a simple device architecture. Hence, the device in Fig. 5-4 employs two emissive layers (EML) sandwiched between the blocking materials, tris(phenypyrazole)iridium ($Ir(ppz)_3$) and BPhen, that effectively

confine carriers and excitons in their respective EMLs while reducing the density of excitons by separating them into different layers to avoid triplet-triplet annihiliation. [35] The excitons are formed predominantly on the blue phosphor, Ir(46dfppy)3, [36] by charge trapping without forming on the wide energy gap host, UGH2. [37] Similarly, red emission is generated on PQIr doped in 4.4'-N,N'-dicarbazole-biphenyl (CBP). The exciton formation mechanism via trapping is energetically favored, as is inferred from the relative positions of the energies of HOMO and LUMO obtained by ultraviolet photoelectron spectroscopy (UPS) measurements, and shown in Fig. 5-5.

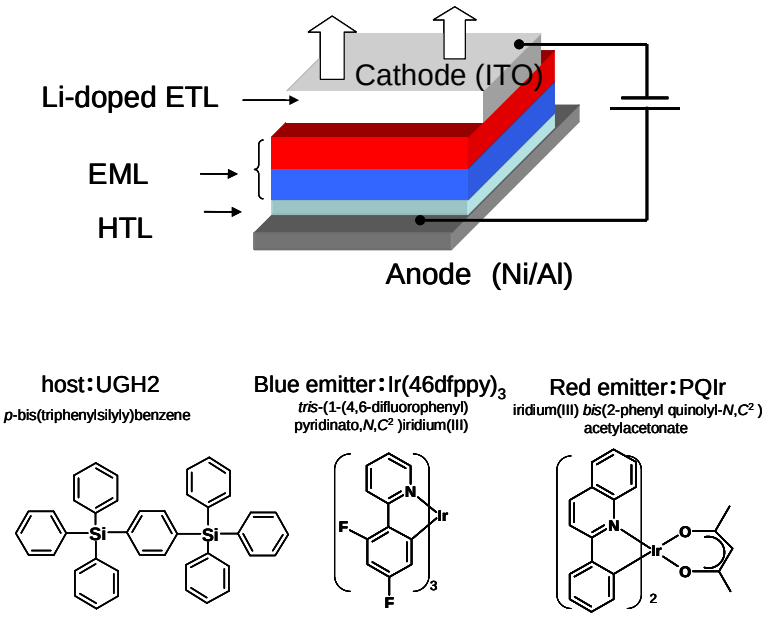

Figure 5-4. Schematics of the top-emissive device structure and the chemical structures of the employed materials.

To investigate the energy levels of the materials, we carried out *in situ* ultraviolet photoemission spectroscopy measurements on organic thin films in a custom-designed UHV chamber. A 400 Å thick Ag layer was first deposited onto a n+-Si(001) substrate via vacuum thermal evaporation in another interconnected UHV chamber. A 200 Å thick organic films were then grown on the substrate. HeI emission ($h\gamma$ = 21.22 eV) from a VG UPS/2 lamp was used as the photon source, and the UPS spectra were recorded with a multichannel hemispherical electron energy analyzer with a pass energy of 2.5 eV. The sample was biased at –3 V to distinguish between the analyzer and

sample cutoffs. The spectral resolution of the UPS measurements is approximately 0.1 eV, determined from the Fermi level width in the UPS spectrum of the Ag layer.

Figure 5-5 shows the UPS spectrum of organic films grown at a rate of 1 Å/s at room temperature. The Fermi level E_F, obtained from the UPS spectrum of the underlying Ag layer, is used as the reference for the binding energy E_B. The HOMO position of e.g., $Ir(46dfppy)_3$, conventionally taken as the intercept between the tangent of the leading edge of the lowest binding energy feature and the background level is located at 2.9 eV below E_F. The low kinetic energy (or high binding energy) cutoff of the UPS spectrum corresponds to the onset of photoemission, from which the vacuum level position can be determined. Thus, the ionization potential (IP) of the $Ir(46dfppy)_3$ film is $IP = h\gamma - (E_{B,\,\mathrm{cutoff}} - E_{B,\,\mathrm{HOMO}})$. 5.6 eV, where $E_{B,\,\mathrm{cutoff}}$ and $E_{B,\,\mathrm{HOMO}}$ are the binding energies corresponding to the photoemission onset and the $Ir(46dfppy)_3$ HOMO level, respectively. Other organic energy levels are taken in the same way.

Figure 5-6 shows the reflection spectra of sputtered Al/Ni anodes employed in Devices 1 and 3, and a thermally evaporated Al cathode in Device 2, where Device 1, 2 and 3 have the structures as shown in Fig. 5-5. Al/Ni retains a reflectivity of >80 % over the EL emission range (with peaks at wavelengths of λ=470 nm and 590 nm) even after oxidization by UV-ozone, which is slightly lower than an as-sputtered Al/Ni layer, but is comparable to that of a simple Al cathode. From UPS measurements of the Ni surface, the work function of Ni is increased by ~0.3 eV, from 4.9±0.1 eV to 5.2±0.1 eV following UV-ozone treatment, due to reaction of Ni with oxygen. This forms a conducting nickel oxide that promotes hole injection into the HOMO of the hole transport layer.[38]

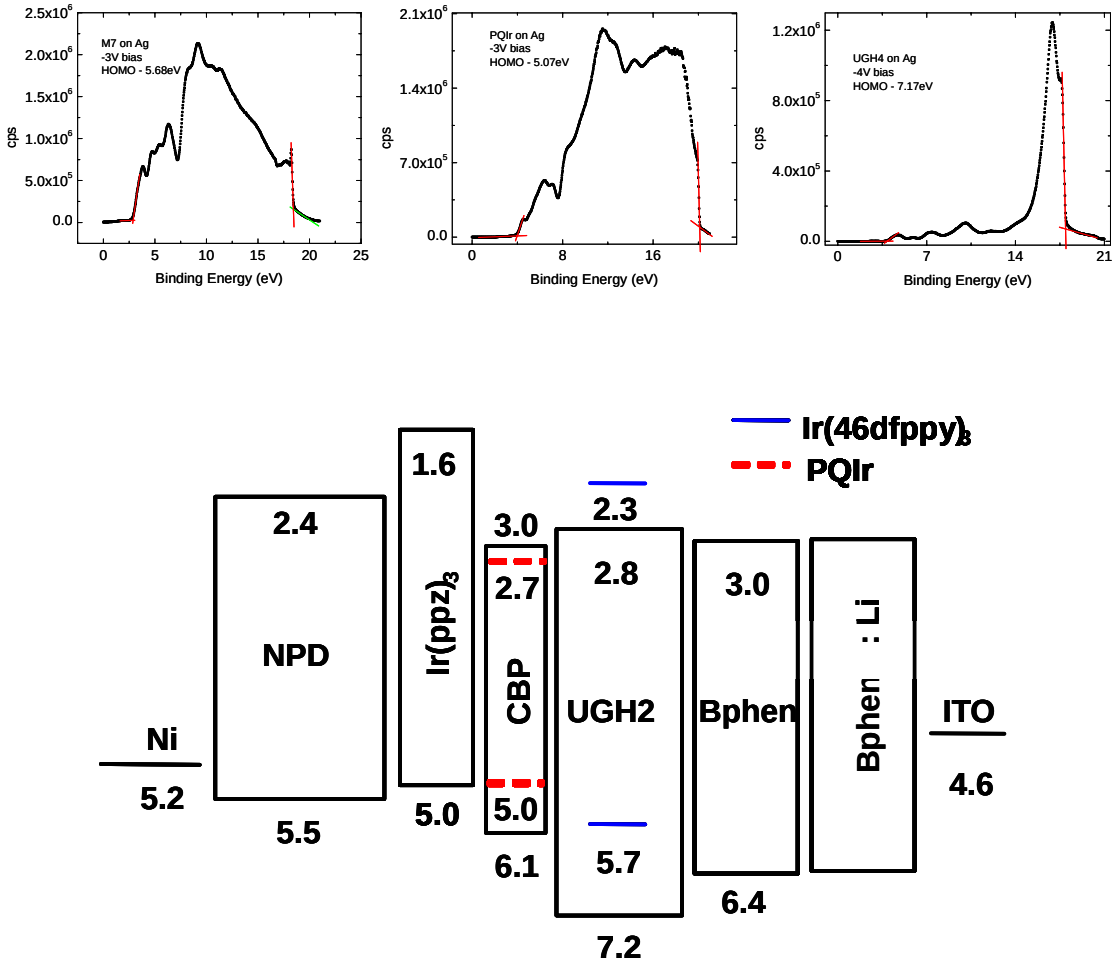

Figure 5-5. Top: Ultraviolet photoemission spectrum of a 200 Å thick employed organic film. The thin solid lines illustrate the method used to determine the HOMO level position and the photoemission onset. The Fermi level E_F is used as the reference for the binding energy. Bottom: The energy diagram of the proposed top-emissive device based on the ultraviolet photoemission measurement.

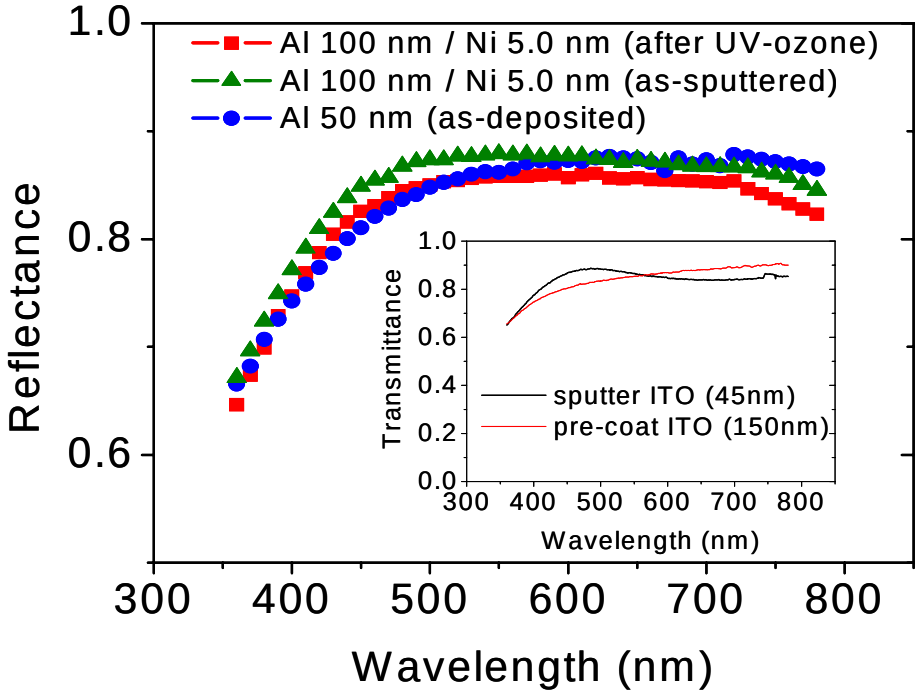

Figure 5-6. Reflection spectra of various cathodes employed. Squares: Al (1000 Å) / Ni (50 Å) after UV-ozone treatment (Devices 1 and 3). Open circles: a similar cathode to Device 1, but with an untreated surface (Device 2). Open squares: as-deposited Al (500 Å). Inset: Transmission spectra of sputtered ITO used in the cathodes of Devices 1 and 3, and glass pre-coated with commercial ITO used as the anode in Device 2.

The transient PL decay for single-doped phosphor and co-doped phosphor are compared. The change in the lifetimes for a blue and a red phosphors between a co-doped film and a single doped film is not significant, signifying the cascade triplet energy transfer is limited even in a co-doped EML system. Moreover, PL emission from each phosphor doesn't change between co-doped film and single-doped film. The proposed device is comprised of two separate EMLs, resulting in the energy transfer across the EMLs is unlikely to be dominant compared to direct excitation of triplet energies on molecules.

Transient PL decay shows single exponential. Both phosphors have relatively short lifetimes (blue phosphor : τ = 1.0ms, red phosphor : τ = 0.7ms).

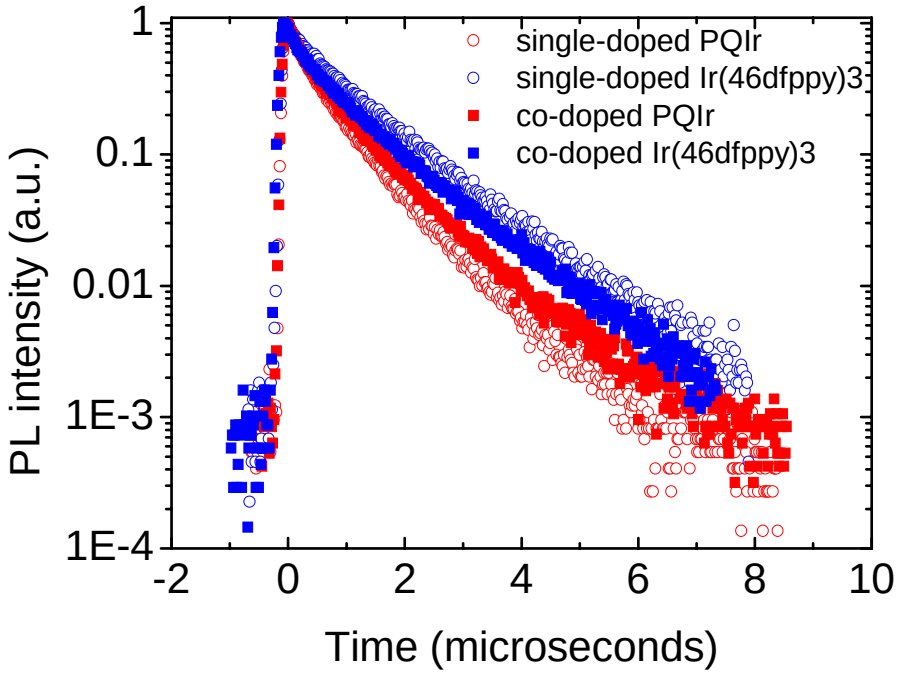

Figure 5-7. PL transient decay of PQIr doped-CBP, $Ir(46dfppy)_3$ doped-UGH2 and double doped film.

The 450 Å thickness of the sputtered ITO is optimized for maximizing outcoupling efficiency. The transmission spectra of both the sputtered ITO cathode and the commercially pre-coated ITO anode show high transmittance over the visible spectral range, achieving transparencies of 83% and 88% at λ=470nm and 590nm, respectively (inset, Fig. 5-6).

In Fig. 5-8, the *J-V* characteristics of Devices 1-3 and Device 4 are shown. Here, Device 4 is otherwise the same as Device 2, but it employs an Al/Ni anode instead of ITO. The operating voltages of Devices 1 and 2 with Li-doped BPhen are significantly lower as compared to Device 3 with undoped BPhen. On the other hand, Devices 1 and 2 behave similarly except at low voltage where no emission is observed. Furthermore, the *J-V* characteristics of Device 2 and Device 4 are nearly identical, indicating that electron injection from LiF/Al into doped BPhen is somewhat more efficient than

injection from sputtered ITO, while efficient hole injection is achieved for both pre-coated ITO and Al/Ni anodes. The slightly higher operating voltage (+0.6 V at J=10 mA/cm^2) for Device 1 compared with Device 2 is due to the higher electron injection barrier from sputtered ITO (4.6 eV) compared with LiF/Al (4.1 eV).

Figure 5-9 shows the EL spectrum of Device 1 at viewing angles of 0°, 30° and 60°. There is only a weak angular dependence in the spectra, and the emission profile is approximately Lambertian distribution pattern in this angular range, indicating only weak or no microcavity effects.

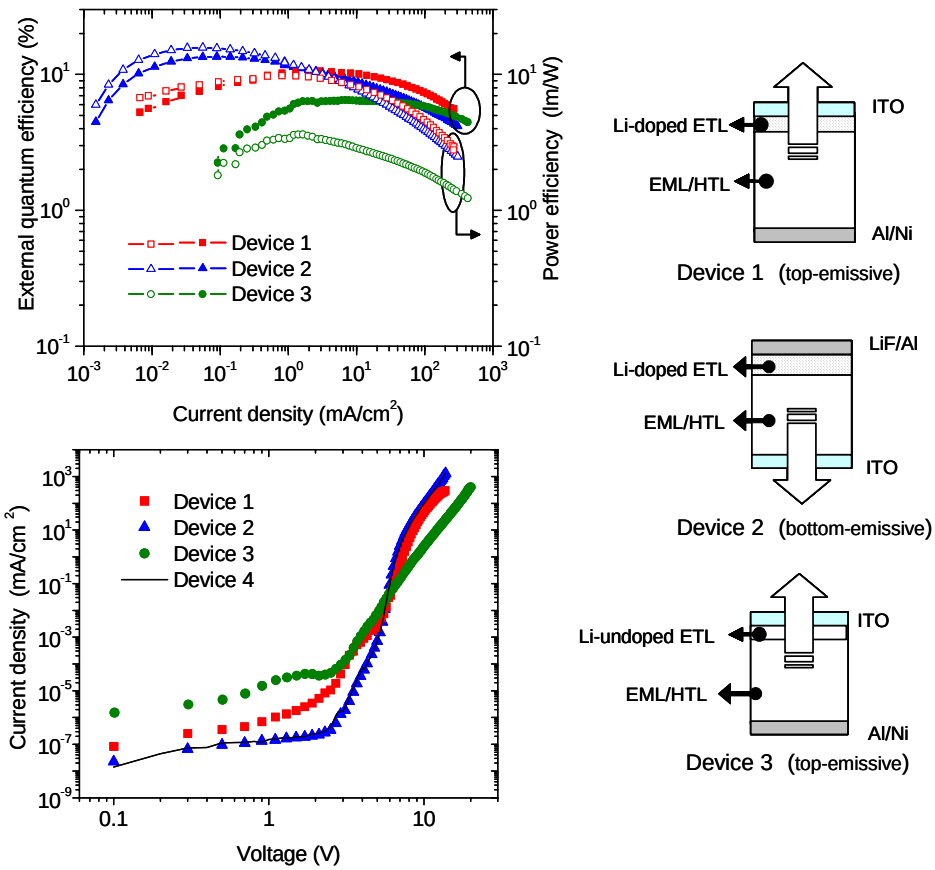

Figure 5-8. Top: The external quantum and luminous power efficiencies of all devices studied as functions of current density. Bottom: Current density vs. voltage characteristics of devices in (a), including Device 4 with a structure similar to Device 2 (see text), except with an Al (1000 Å)/Ni (50 Å) instead of ITO.

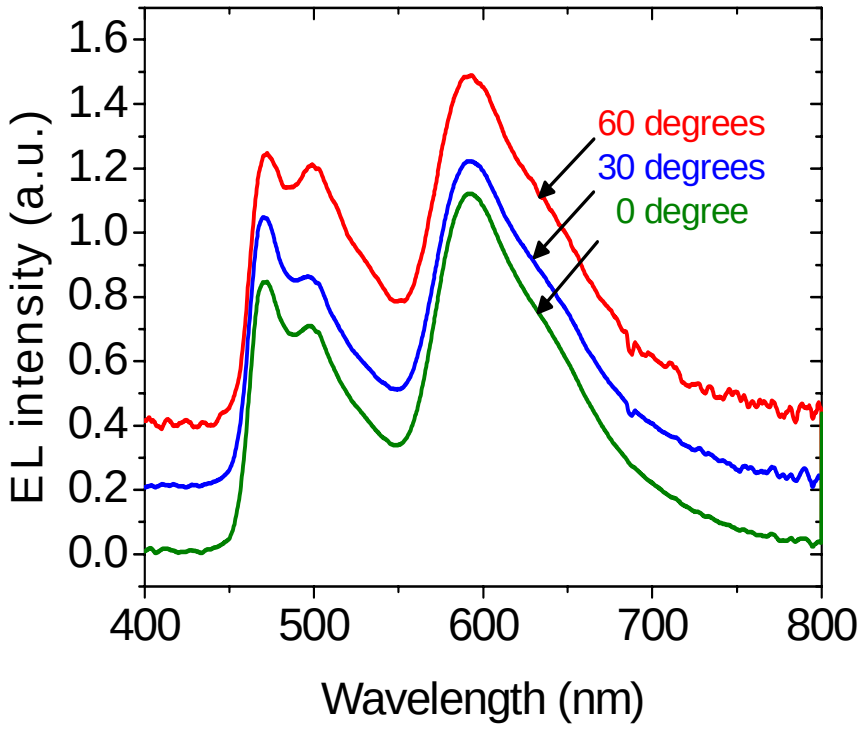

Figure 5-9. Angular dependence of EL spectra of a top-emitting WOLED, Device 1, at a current density of J=10mA/cm2. The CIE co-ordinates are (x=0.42, y=0.39), (x=0.43, y=0.41) and (x=0.44, y=0.40) at 0°, 30° and 60°, respectively. The curves are vertically offset for clarity. Similar results are obtained for the bottom-emitting Device 2.

In summary, we have demonstrated a top emitting electrophosphorescent WOLED employing a metal-free transparent cathode for use in active-matrix displays and back light applications. The devices exhibit operating voltages and external quantum efficiencies (EQEs) comparable to those obtained using a conventional bottom emissive electrophosphorescent OLED. No pronounced microcavity effects were observed for these devices. These results suggest that electrophosphorescent WOLEDs are promising for use in top emitting displays employing non-transmissive silicon-based drive circuitry on the display backplane.

5.1.2 Stacked Structure for a Full-Color Display

High efficiency white organic light emitting diodes (OLEDs)[Chap.4,1,39,40] are of interest due to their potential use in full-color displays coupled with thin film transistors. A stacked OLED [42,43] consisting of multiple electroluminescent (EL) units connected in series has been developed. In the stacked OLED structure, the luminance at a fixed current density increases linearly with the number of stacked and independent EL units. This can lead to a significant improvement in lifetime as well as external efficiency by reducing degradation that accompanies high drive currents required to achieve similarly high brightness in a single unit OLED. More recently, high efficiency stacked OLEDs have been demonstrated that use a transparent charge generating interlayer consisted of metal oxides such as indium tin oxide (ITO), V_2O_5, MoO_3, WO_3 or an organic p-n junction (see Chap.4, Table4-2) where the hole transporting (HTL) and electron transporting (ETL) layers are doped with an metal, such as Li, Cs, or Mg. As is mentioned in the previous section, metal oxides with high refractive indices are not favorable for high outcoupling efficiencies. Furthermore, the alkali metal doping is not desirable since the handling of alkali metal, which is reactive and corrusive, is not good in terms of safety and manageability of production. In addition, the use of alkali metal may influence the performance of TFTs. Therefore, for a practical use, it is also required to develop a charge generation layer which can be coated just like coating of organic layaers.

Here, we demonstrate the green and white stacked OLEDs with new connecting layers without alkali metal doped-ETLs. Furthermore, the devices exhibit high power efficiencies, leading to the low power efficiency, and a long lifetime. Connecting layers are required to have the following properties, (i) high transmittance over the wavelength range from 400 nm to 800 nm to minimize the absorbtion loss, (ii) the comparable reflactive indices to those of organic layers to reduce the microcavity effects for a wide viewing angle, and (iii) the easy fabrication process. However, the previously reported metal oxide interlayers and $FeCl_3$ doped hole transport layer have either severe absorption in the visible range or high reflactive indices. [41 -44] Furtheremore, it is not easy to handle the corrosive and optically absorbing $FeCl_3$. In this papar, we propose the connecting layers which filfills the above mentioned requirements and exnhibits the

efficiency which is increased proportionally to the numbr of the stacked units. It is important to evaluate the proposed stacked OLED technology for a full-color display in terms of a practical use since there is very little reports on this.

It is important to study the performance of the stacked OLEDs with the connecting layers consisted of LiO_2, TR-E314 and LG-101. Here, we demonstrate the high efficiency green-emitting stacked OLED employing the new charge genertaion layers. TPD with higher triplet energy compared to NPD is used for an HTL to prevent the triplet energy from diffusing to the adjacent HTL and being non-radiatively lost. The host material, EMM-004 with the lowest unoccupied molecular orbital (LUMO) energies of 2.8 eV promotes electrons injected from TR-E314 with 2.6 eV LOMO energy since the injection is energetically favorable. Furthermore, the highest occupied molecular orbital (HOMO) energies of TMM-004 is 6.2 eV, which creates the hole blocking interface with TPD with HOMO energy of 5.4 eV. Therefore, it is inferred that the exciton formation primarily occurs in the interface between TPD and TMM-004.

The exceedingly high peak current efficiency 235 cd/A (see Fig. 5-10) is achieved at a current density of 0.5 mA/cm^2. The power efficiencies are roughly 50 lm/W for 1-6 stacked OLEDs and the external efficiencies are proportionally increased with the number of the units. The fact pronouncedly indicates that every connecting layers functions well and each EL unit contributes equally to the external efficiency.

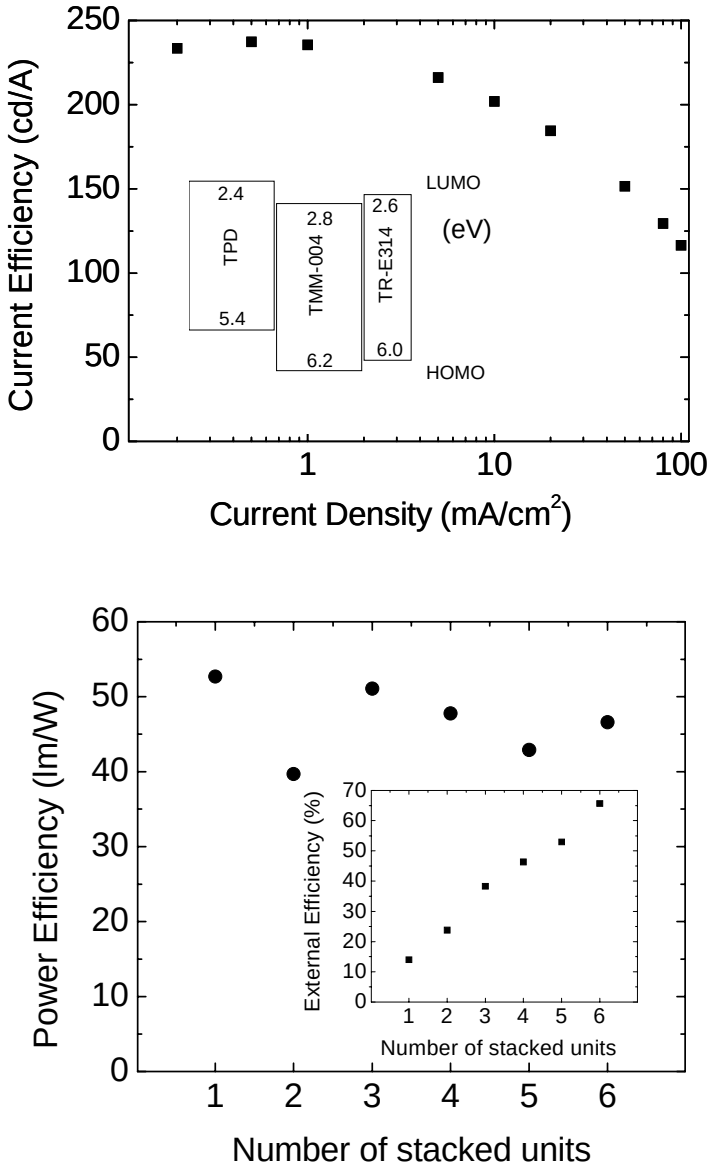

Figure 5-10. Top: Current efficiency of the phosphorescent green oled with six stacked units of LG-101 (20nm) / TPD (60nm) / 20% $Ir(ppy)_3$ doped in TMM-004 (60nm) / TR-E314 (20nm) / Li_2O (2.5nm) / TR- E314 (5nm). Inset: HOMO and LUMO energies of employed HTL, EML and ETL materials. Bottom: Power efficiencies at 0.5 $mA/cm^2$of the same devices as functions of the number of stacked units. Inset: External quantum efficiencies at 0.5 mA/cm^2 of the same devices.

Intensive research on active matrix displays using OLED and low temperature polysilicon thin film transistor (LTPS) has being actively in progress [45-46] since a full color active matrix OLED (AMOLED) is considered to be well-suited for a display of mobile devices, having such outstanding features as a wide viewing angle, vivid picture, and quick response time compared with an active matrix liquid crystal display (AMLCD). The major shortcoming of a AMOLED for mobile device displays compared with a counterpart of AMLCD is a low power consumption and a short lifetime. We have demonstrate a AMOLED with reduced power consumption. [45-46] Here, we describe a full color AMOLED employing LTPS backplane based on a white stacked OLED combined with color filter array.

A drive voltage of 7.1V, current efficiency of 31.9 cd/A, power efficiency of 14.2 lm/W, and CIE coordinates (x=0.29, y= 0.39) are obtained at a current of 20 mA/cm^2 in the white 2- stacked OLED. High current efficiency and low drive voltage are obtained and the performance meets the requirements of practical applications. The properties of the white 1- stacked OLED are drive voltage of 4.7V, current efficiency of 14.4 cd/A, and power efficiency of 9.6 lm/W at a current density of 20 mA/cm^2. In the white 2-stacked OLED, the current efficiency of 2- stacked OLED is more than doubled and the power efficiency is even higher compared to the white 1-stacked OLED.

The lifetimes of the white 1- stacked OLEDs are measured. T95, which is the time for luminance decay by 5% from an initial luminance, is evaluated. Lifetime measurement is done under an acceleration condition, starting from a high initial luminance of 12,000 cd/m^2. It turns out that T95 for the white 2- stacked OLED is 110 hours and that for the white 1- stacked OLED is 20 hours as shown Fig. 5-9. With the reduced initial luminance drop, the burn-in on a display, which is a critical problem, is expected to be greatly improved. The luminance half-decay lifetime (T50) is estimated to be 4,000-6000 hours. The method of the lifetime projection as a function of a current density follows the previous report [47]. The lifetime of the white stacked OLED is significantly improved due to the high current efficiency.

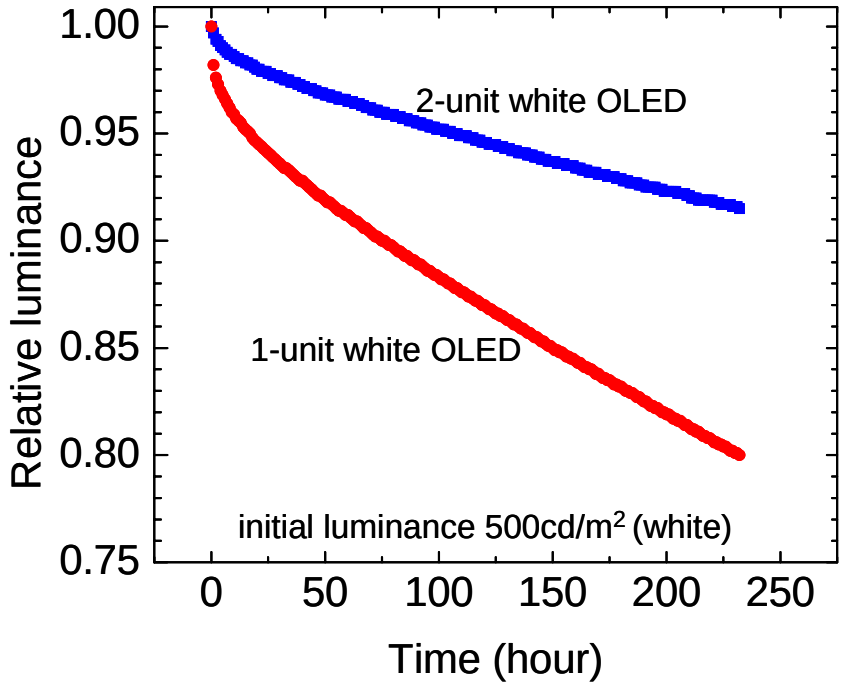

Figure 5-11. Luminance decay of the 1- and 2-unit white OLEDs from an initial luminance of 500 cd/m^2. The white OLED consists of orange and blue EMLs in a white EL unit. The structure of the white stacked OLED is as follows: [ITO / CFx / LG-101 (10 nm) / orange EML (60 nm) / blue EML (50 nm) / TR-E314 (12 nm) / Li (0.6 nm) / LG-101 (10 nm) / orange EML (60 nm) / blue EML (50 nm) / Alq (5 nm) / TR-E314 (7 nm) / LiF (1 nm) / Al (200 nm)]. The orange EML is [NPB (host) : 30% BH-140 (assist dopant) : 3% RD-001 (orange dopant)] and the blue EML is [BH-140 (host) : 16%NPB (assist dopant) : 2.5% BD-102 (blue dopant)] [48,49].

The full-color AMOLED has the arrangement of the color filter is an RGBW format which will be described in the next section. The specifications of this display are as follows: size; 2.2 inch, dot number; 862 x 240 dots, average dot pitch; 0.051mm x 0.137mm, and luminance; 230 cd/m^2. Power consumption is defined to be 30% of the value to make the entire display at 230 cd/m^2 with all the pixels on. The power consumption of an AMOLED with the white 1- stacked OLED is 210mW. On the other hand, the power consumption with the white 2- stacked OLED is 120mW, which is

approximately reduced by 40% from that of the white 1- stacked OLED.

The stacked OLEDs with the new connecting layers are demonstrated. The green 6-stacked OLED exhibit 235cd/A and the current efficiencies are increased proportionally to the number of the stacked units with the power efficiencies remain unchanged. The full color AMOLED having the stacking architecture has been also demonstrated. The power consumption and lifetime are significantly improved. The proposed stacked OLEDs are expected to be applied for a practical use.

5.2 Reduction of Power Consumption

5.2.1 Technology Reviewed

The milestones of the technologies for reduced power consumption after Tang:s classical report are dye doped emitting layer [50], enhanced out-coupling efficiency [24-27,51], phosphorescent OLED with 100% IQE [52]. Most of the efforts have been made to develop organic materials and the optimal device structures, which have been tested using testing devices. However, it is important to consider the device architecture including a TFT design aiming for low power consumption not with a test device but with a full-color OLED display.

One of the approaches for achieving a low power consumption by development of device architecture is improvement of outcoupling efficiency as shown in the previous section and Table 5-1. However, from a macroscopic viewpoint, we have considered the TFT layout design. For example, the aperture size of each RGB pixel must be optimized to minimize power consumption since power efficiency differs from each other.

Table 5-1 Selected outcoupling schemes and factor (F) of outcoupling efficiency improvement over conventional WOLED.

Outcoupling scheme	F	Refs.
Top emitting.	1.2	14
Nanopatterning of glass subtrate.	1.5	27
Microlens array.	1.5	25
Silica aerogels.	1.8	26
Shaped substrates	1.9	24

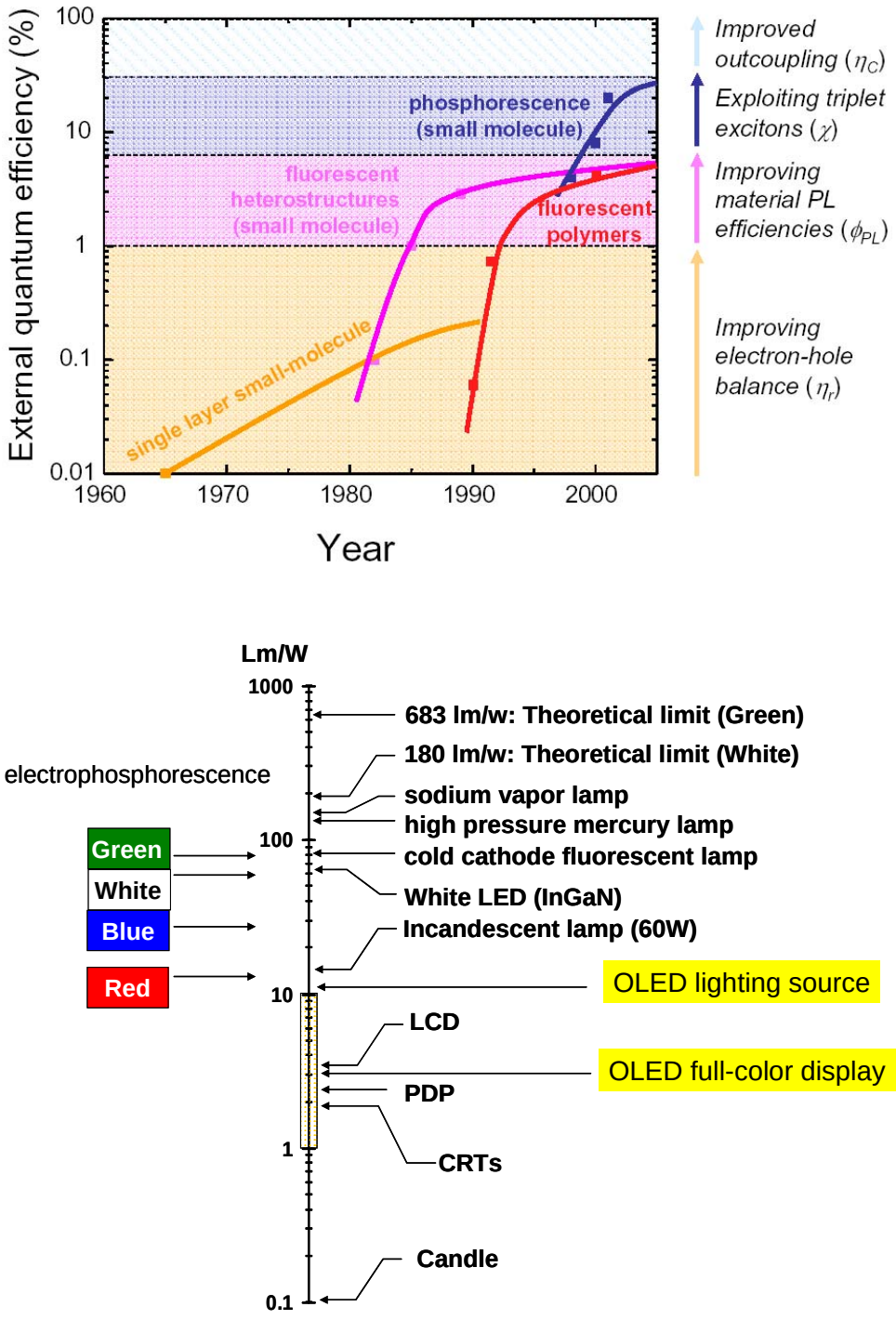

Figure 5-12. Top: Milestone of the improvement of external quantum efficiency. Bottom: Power efficiency of each lighting source and display.

5.2.2 RGBW Pixel Format

An AMOLED employing a low-temperature polysilicon (LTPS) thin-film transistor backplane has been actively developed [45]. Since an AMOLED offers the advantages such as high resolution, high brightness, quick response, a full-color AMOLED is considered to be well suited for a display in mobile devices, which enjoy a large market scale. In terms of production yield and cost, the use of a white emitting OLED combined with red (R), green (G) and blue (B) color filters is much encouraged. The major shortcoming, however, compared to a liquid crystal display (LCD) is higher power consumption, which is significantly important for a battery-powered potable device such as a cell phone and a digital camera. Recently we have demonstrated that the RGBW pixel pattern based on a white emitting OLED and color filters provide a significant reduction in power consumption. [53] In an RGBW AMOLED, the unfiltered white pixel is highly efficient, enabling the large reduction in power consumption. Therefore, key to what makes the power consumption much reduced is a high-efficiency white emitting OLED (see Fig. 5-13).

Here, we discuss the method for a reduction in power consumption of full-color AMOLED in detail as well as a high-efficiency white OLED. The power consumption is compared to a conventional pixel format of an analogous filtered RGB and an unfiltered RGB with pixelated RGB emitters.

For a low power consumption, it is essential to decrease a drive voltage of a white emitting OLED. We have developed a stable and high-efficiency white OLED with double EMLs. [45] The power efficiency, however, needs to be much improved for a practical use. Consequently, we focus on lowering the drive voltage and then adjust the carrier balance in the EMLs for a high efficiency and white emission. The device architecture is designed for the injected electrons and holes to be transferred over a low energy barrier to the recombination zone in EMLs.

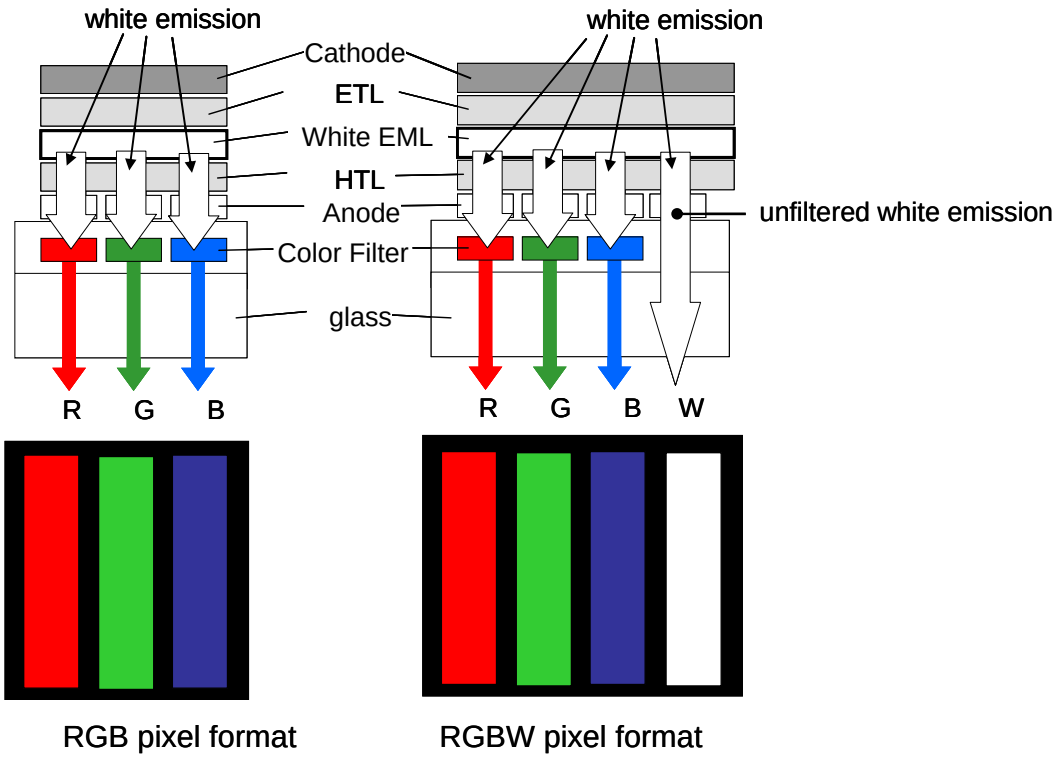

Figure 5-13. Schematic of the pixel array of (left) RGB and (right) RGBW formats.

There are two major full-color formats: (i) an unfiltered RGB pixel pattern where individual RGB OLEDs are formed and (ii) an RGB pixel pattern based on a filtered white OLED combined with color filters, as shown in Fig. 1-12. The advantages of the unfiltered RGB are its high NTSC color reproduction and a high efficiency. However, the production process of an unfiltered RGB format is complicated due to a precision shadow mask process for pixelation of RGB EMLs. This process suffers a low yield and throughput since the display quality is significantly influenced by the dimensional accuracy of a shadow mask and mask alignment. Therefore, the filtered RGB format provides an advantage for manufacturing large area or high resolution AMOLEDs.

In this method, all of the white OLED layers are deposited without a precision shadow mask. This manufacturing process is much easier than the pixelation of the unfiltered RGB pattern.

The main technical challenge for the filtered RGB format is its high power consumption since approximately 70 percents of white emission is absorbed by each of the RGB color filter as shown in Fig. 5-14. Therefore, in order to compensate for this

loss, high currents must be required to obtain high brightness of white emission. This results in high power consumption.

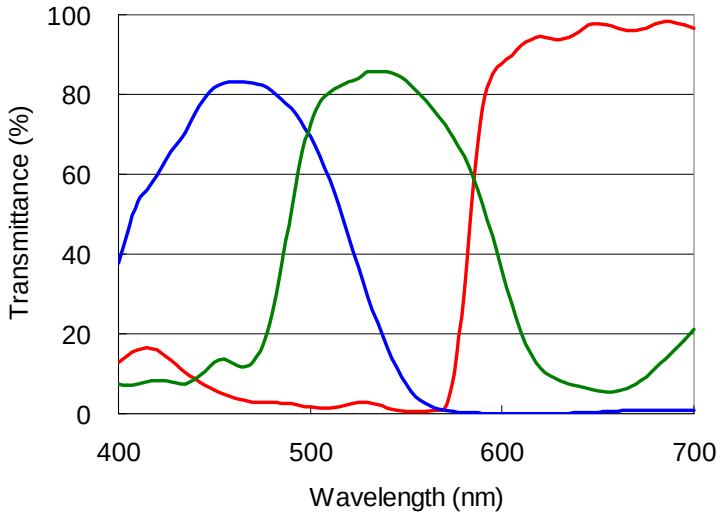

Figure 5-14. Transmittance of typical RGB color filters used for a full-color OLED display

Although a conventional color filter array is consisted of red, green and blue color filters, an additional white-emitting pixel of W is introduced.[53] An RGBW format is a new pixel format in which a color filter-free white pixel is added, as shown in Fig. 5-13. Therefore, there is no dissipation of light and the high-efficiency white emission is directly coupled out from the W pixels.

The RGBW format is also favorable when making neutral colors. For example, a simulation is performed to compare the power consumptions relative to the RGB format when making neutral colors between red and white.

Based on the above mentioned technologies, a full-color AMOLED with a high-efficiency white OLED and an RGBW format is fabricated. The specifications of the display are size: 2.2 inches, resolution: 862x240 dots, average dot pitch: 0.051 mm x 0.137 mm, and maximum luminance: 230 cd/m^2. The fill factor of the high-efficiency W pixel is designed to be relatively larger relative to those of RGB pixels in order to reduce the power consumption. Since the current density of the W pixel is reduced by enlarging the area of a W pixel, the degradation of the W material could be suppressed and the lifetime of the AMOLED is improved. An average aperture ratio of 42.5% is

obtained by optimizing the layout design. The power consumptions of various images relative to all white display (Image 4) in both the RGB and the RGBW formats are shown in Fig. 5-15. It is clearly shown that the power consumption of all white in the RGBW format is much reduced. In Image 4, the reduction rate is largest, 39%. Also in the text image (Image 3), the power consumption of the RGBW format is less than half compared to that of the RGB format. The RGBW format becomes advantageous when the W pixels are more primarily emitted than other pixels. The RGBW format requires approximately one-half the power of the RGB format. When the power consumption of the statistically-averaged image of many photographs in the AMOLED panel is actually measured, it turns out to be 270 mW. The power consumption of the AMOLED is almost equal to that of a liquid crystal display (LCD) with the same panel size and brightness. It is believed that the RGBW format is an effective method for reducing power consumption.

We have developed a full-color AMOLED with an RGBW format and a high-efficiency white OLED. The full-color AMOLED has exhibited the significant low power consumption compared to analogous RGB display. The proposed low-consumption methods are important for a practical use of full-color displays.

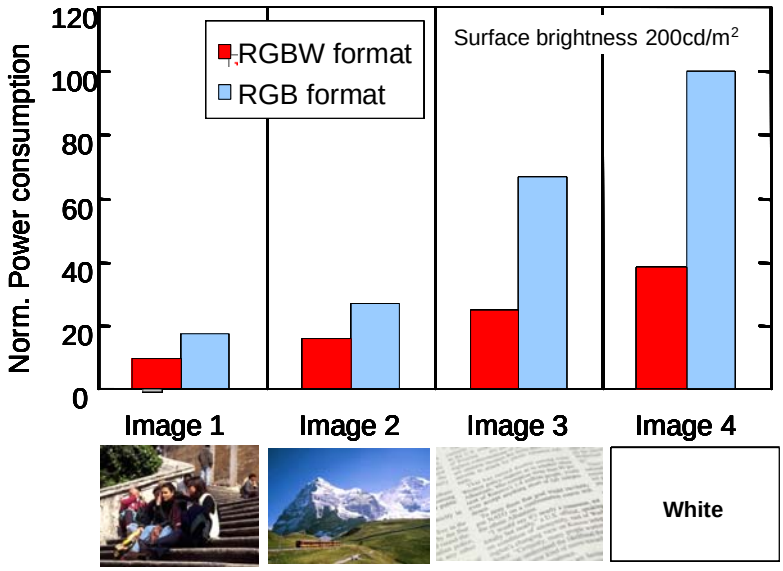

Figure 5-15. Comparison of power consumption between RGB and RGBW formats in various images. The device structure of the white OLED is the same as described in Fig. 5-11.

5.3 Summary

In this chapter, improving lifetime and low power consumption are focused for targeting a practical use of OLED for a full-color display.

In the first section, We have demonstrated a top-emitting WOLED employing a metal free transparent cathode. The devices exhibit operating voltages and external quantum efficiencies comparable to those obtained using a conventional bottom-emitting OLED using a thin film of UV-ozone-treated nickel treated. The WOLEDs reached η_{ext} = 10.5±1% at current densities of J = 1.6 mA/cm2, with a power efficiency of hp = 9.8±1 lm/W at J = 1.0 mA/cm^2. No pronounced microcavity effects are observed for these devices by introducing alkali metal-doped ETL for the first time. These results suggest that the top-emissive white-OLEDs are promising for use in full-color displays for a long lifetime without suffering the feature of wide viewing angle. The stacked white OLED are fabricated on a low-temperature polysilicon TFT backplane. The connecting layer is newly developed for the use in TFT substrate for reducing the microcavity effects and potential defects caused by alkali metal doping. It is proved that the stacked white OLED shows the improved lifetime compared to the conventional OLED with single EL unit.

In the second section, For reduceing the power consumption, a red, green, blue and white (RGBW) pixel format combined with an RGB color filter array (RGBW format) with a common white emission layer (EML) has been developed. We find that the RGBW format can successfully reduce the power consumption of a full-color active-matrix OLED by nearly half that of a conventionally filtered RGB pixel format. This improved power consumption is almost equal to the power consumption of a same-sized LCD. The RGBW format is found to be a promising technique for the further reduction of the power consumption of a full-color AMOLED.

Chapter 5. References

[1] K. Mameno, R. Nishikawa, K. Suzuki, and S. Matsumoto, T. Yamaguchi, K. Yoneda, Y. Hamada, H. Kanno, Y. Nishio, H. Matsuoka, Y. Saito, S. Oima, N. Mori, G. Rajeswaran, S. Mizukoshi, and T. K. Hatwar, IDW'02 Proceedings p. 235 (2002).

[2] T. Guo, F. Yang, Z. Tsai, G. Feng, T. Wen, S. Hsieh, C. Chung, and C. Wu, Appl. Phys. Lett. 89, 051103 (2006)

[3] T. Cho, C. Lin, and C. Wu, Appl. Phys. Lett. 88, 111106 (2006)

[4] H. Peng, J. Sun, X. Zhu, X. Yu, M. Wong, and H. Kwok, Appl. Phys. Lett. 88, 073517 (2006)

[5] L. Hou, Q. Hou, Y. Mo, J. Peng, and Y. Cao, Appl. Phys. Lett. 87, 243504 (2005)

[6] H. Peng, X. Zhu, J.Sun, Z. Xie, S. Xie, M. Wong, and H. Kwok, Appl. Phys. Lett. 87, 173505 (2005)

[7] C. Yang, C. Lin, C. Wu, Y. Yeh, C. Cheng, Y. Kuo, and T. Chen, Appl. Phys. Lett. 87, 143507 (2005)

[8] C.Lin, H. Lin, and C. Wu, Appl. Phys. Lett. 87, 021101 (2005)

[9] C. Wu, C. Lin, P. Hsieh, and H. Chiang, Appl. Phys. Lett. 84, 3966 (2004)

[10] F. Jean, J. Mulot, B. Geffroy, C. Denis, and P. Cambon, Appl. Phys. Lett. 81, 1717 (2002)

[11] H. Cao, D. B. Hall, J. M. Torkelson, and C.-Q. Cao, Appl. Phys. Lett. 76, 538 (2000)

[12] G. Gu, G. Parthasarathy, and S. R. Forrest, ,Appl. Phys. Lett. 74, 305 (1999)

[13] H. Riel, S. Karg, T. Beierlein, B. Ruhstaller, and W. Rieß, Appl. Phys. Lett. 82, 466 (2003).

[14] M.-H. Lu, M. S. Weaver, T. X. Zhou, M. Rothman, R. C. Kwong, M. Hack, and J. J. Brown, Appl. Phys. Lett. 81, 3921,(2002).

[15] G. Gu, V. Bulovic, P. E. Burrows, S. R. Forrest, and M. E. Thompson, Appl. Phys. Lett. 68, 2606 (1996).

[16] H. Riel, S. Karg, T. Beierlein, W. Rieß, and K. Neyts, J. Appl. Phys. 84, 5290 (2003).

[17] C.-W. Chen, P.-Y. Hsieh, H.-H. Chiang, C.-L. Lin, H.-M. Wu, and C.-C. Wu, Appl.

Phys. Lett. 83, 5127 (2003).

[18] Shih-Feng Hsu, Chung-Chun Lee, Shiao-Wen Hwang, and Chin H. Chen, Appl. Phys. Lett. 86, 253508 (2005)

[19] J. Szczyrbowski, A. Dietrich, and H. Hoffmann, Phys. Status Solidi A 78, 243 (1983).

[20] M.-H. Lu and J. C. Sturm, J. Appl. Phys. 92, 595 (2002).

[21] W. Lukosz and R. E. Kunz, J. Opt. Soc. Am. 67, 1607 (1977).

[22] H. J. Peng, Y. L. Ho, X. J. Yu, and H. S. Kwok, J. Appl. Phys. 96, 1649 (2004).

[23] N. C. Greenham, R. H. Friend, and D. D. C. Bradley, Adv. Mater., 6, 491 (1994)

[24] G. Gu, D. Z. Garbuzov, P. E. Burrows, S. Venkatesh, S. R. Forrest, and M. E. Thompson, Opt. Lett., 22, 396 (1997)

[25] S. Moller and S. R. Forrest, J. Appl. Phys. 91, 3324 (2002).

[26] T. Tsutsui, M. Yahiro, H. Yokogawa and K. Kawano, Adv. Mate. 13, 1149 (2001).

[27] Y. J. Lee, S. H. Kim, J. Huh, G. H. Kim and Y. H. Lee, Appl. Phys. Lett. 82, 3779 (2003).

[28] T. Tsutsui, M. Yahiro, H. Yokogawa, K. Kuwano, and M. Yokoyama, Adv. Mater., 13, 1141 (2001)

[29] L. S. Hung, and C. W. Tang, Appl. Phys. Lett. 74, 3209 (1999).

[30] G. Parthasarathy, P. E. Burrows, V. Khalfin, V. G. Kozlov, and S. R. Forrest, Appl. Phys. Lett. 72, 2138 (1998).

[31] V. Bulovic, P. Tian, P. E. Burrows, M. R. Gokhale, and S. R. Forrest, Appl. Phys. Lett. 70, 2954 (1997).

[32] J. Huang, M. Pfeiffer, A. Werner, J. Blochwitz, S. Liu, and K. Leo, Appl. Phys. Lett. 80, 139 (2002).

[33] M. Pfeiffer, S. R. Forrest, K. Leo, and M. E. Thompson, Adv. Mater. (Weinheim, Ger.) 14, 1633 (2002).

[34] G. Parthasarathy, C. Shen, A. Kahn, and S. R. Forrest, J. Appl. Phys. 89 4986 (2001).

[35] M. A. Baldo, C. Adachi, and S. R. Forrest, Phys. Rev. B 62, 10967 (2000).

[36] A. B. Tamayo, B. D. Alleyne, P. I. Djurovich, S.Lamansky, I. Tsyba, N. N. Ho, R. Bau, and M. E. Thompson, J.Am.Chem.Soc. 125, 7377 (2003).

[37] R. J. Holmes, B. W. D'Andrade, X.Ren, M. E. Thompson, and S. R. Forrest, Appl. Phys. Lett. 83, 3818 (2003).

[38] I-Min Chan, and F. C. Hong, Thin Solid Films 450, 304 (2004).

[39] B. W. D'Andrade, R. J. Holmes and S. R. Forrest: Adv. Mater. 16 (2004) 624.

[40] S. Tokito, T. Iijima, T. Tsuzuki and F. Sato: Appl. Phys. Lett. 83 (2003) 2459.

[41] J. X. Sun, X. L. Zhu, H. J. Peng, M. Wong and H. S. Kwok: Appl. Phys. Lett. 87 (2005) 093504.

[42] C.-C. Chang, S.-W. Hwang, C. H. Chen and J.-F. Chen: Jpn. J. Appl. Phys. 43 (2004) 6418.

[43] T. Matsumoto, T. Nakada, J. Endo, K. Mori, N. Kavamura, A. Yokoi and J. Kido: SID Int. Symp. Dig. Tech. Pap. 34 (2003) 979.

[44] L. S. Liao, K. P. Klubek and C. W. Tang: Appl. Phys. Lett. 84 (2004) 167.

[45] G. Rajeswaran, M. Itoh, M. Boroson, S. Barry, T. K. Hatwar, K. B. Kahen, K. Yoneda, R. Yokoyama, T. Yamada, N. Komiya, H. Kanno and H. Takahashi: SID Int. Symp. Dig. Tech. Pap. 31 (2000) 974.

[46] N.Komiya, R. Nishikawa, Y. Saito, S. Oima, K. Yoneda, H. Kanno and H. Takahashi: presented at OLED2000, Hamamatsu, Japan, 2000.

[47] C. Féry, B. Racine, D. Vaufrey, H. Doyeux and S. Cinà: Appl. Phys. Lett. 87 (2005) 213502.

[48] C. Hosokawa, S. Toshio, K. Fukuoka, H. Tokailin, Y. Hironaka, H. Ikeda M. Funahashi, and T. Kusumoto: SID Int. Symp. Dig. Tech. Pap. 32 (2001) 522.

[49] T. Iwakuma, T. Aragane, Y. Hironaka, K. Fukuoka, H. Ikeda, M. Funahashi, C. Hosokawa and T. Kusumoto: SID Int. Symp. Dig. Tech. Pap. 33 (2002) 598.

[50] C. W. Tang and S. A VanSlyke, Appl. Phys. Lett. 51, 913 (1987).

[51] M. Agrawal and P. Peumans, MRS Fall Meeting 2005, Boston, MA.

[52] C. Adachi, M. A. Baldo, M. E. Thompson and S. R. Forrest, J. Appl. Phys. 90, 5048 (2001)

[53] J. P. Spindler, T. K. Hatwar, M. E. Miller, A. D. Arnold, M. J. Murdoch, P. J. Kane, J. E. Lundwicki, and S. A. Van Slyke: SID 06 Digest (2006) 36.

Chapter 6.

Conclusion

In this thesis, the high-efficiency OLEDs and their mechanisms are investigated. The primary focus of the studies is to pursue the high efficiency from improving energy transfer efficiency and a development of organic materials. Furthermore, the feasibilities of the techniques have been evidenced using a low temperature active-matrix TFT backplane.

In Chapter 3, I have developed high-efficiency red emitting OLEDs, which are a matter of importance to reduce power consumption of OLED full-color displays.

Firstly, the new doping method facilitating the energy transfer has been investigated in Chap. 3-1. I have successfully improved the energy transfer efficiency by introducing a dye sensitizer into the conventional EML system comprised of DCJTB doped Alq. I have proved that the fluorescent dye sensitizer has improved the energy transfer from the host material (Alq) to the emitting dopant (DCJTB). Especially, the original idea that rubrene intermediates fluorescent energy transfer has proved to be a promising method in terms of high efficiency, color stability, low voltage, and long lifetime. The current efficiency of the fluorescent dye sensitized red OLED is 4.4 cd/A at 500 cd/m^2, which is over 2-fold increase compared to the conventional red OLED without fluorescent dye sensitizer. The energy transfer mechanism in the device has been studied with the HOMO and LUMO energies and the energy diagram of the employed materials. In addition, I have applied the same concept to phosphor-based red OLEDs successfully. Though there are few robust emitting materials which shows high stability, the sensitization can totally enhance the device performance without suffering anything. The new doping method has been widely used in the industries already.

Secondly, I have developed new classes of materials for red OLEDs in Chap. 3-2. Materials for a red EML, an ETL, and an HTL have been studied respectively. By investigating the functionalities of the materials, the high-efficiency red fluorescent OLEDs have been obtained. The carrier injection and transportation properties for the materials have been studied to maximize the exciton forming possibility in the EML. Especially, the EML comprised of rubrene as a host material and DBP as a red emitter has been proposed for the first time. Furthermore, DBzA as a new electron transporting material can be successfully applied with combination of NPD as a hole transporter,

which gives an excellent balance of carriers injected into the EML. The development of the new class of materials for high efficiency OLEDs has been systematically shown. This work has clearly demonstrate the designing high-efficiency OLEDs focusing on the functionality of each layer such as a HTL, EML, and ETL, respectively. The current, power and external quantum efficiencies at 20 mA/cm^2 are 5.4 cd/A, 5.3 lm/W, and 4.7%, respectively. Those values exceed those of fluorescent dye sensitized red OLED. This work riches in originality in the use of new classes of materials for achieving the high efficiency red OLED.

In Chapter 4, high-efficiency WOLEDs based primarily on phosphorescent emitter are presented, which allows for 100% IQE. The sections cover the most promising technologies for achieving the high efficiencies. Approaches for high efficiency WOLEDs are proposed in terms of improving the efficiency of energy transfer and the device architecture and the necessary conditions are also discussed. Especially, the formation process of excitons is carefully examined in each device considering the energy diagrams. The results can be widely applied for application of full-color displays and lighting sources.

In Chap.4-1, high-efficiency WOLED without ISC energy loss is proposed. The highly efficient WOLED, with a color rendition that is unusually independent of current density, has potential for use in the next generation of sources for solid-state indoor lighting. The total exciton trapping fraction and the exciton diffusion length are analyzed based on the experimental results. The model of exciton transport indicates that the dominant mechanism contributing to the total phosphor emission of the WOLED, although charge trapping is also an important factor in obtaining optimum performance and color balance. The analysis suggests that this particular device architecture can yield a total external quantum efficiency of 31 % using optimized dopants in a CBP host.

In Chap. 4-2, the WOLEDs have an extended carrier recombination zone, which leads to high external efficiencies at high brightness. The devices reach a maximum forward viewing external efficiency of η_{ext} = 8.5±0.3 % for the WSOLED with 8% Ir(ppy)$_3$, and a total efficiency of $\eta_{ext,tot}$ = 13.1±0.5 % at a luminance of 800 cd/m^2. This corresponds to a total power efficiency of $\eta_{p,tot}$ = 20.2±0.7 lm/W with a CRI of 79.

In Chap. 4-3, I have demonstrated the WOLED with the stacked structure. The new charge generation layer is developed, which has is highly transparent in the visible area. The carrier injection properties from the charge generation layer in the device are studied in detail by transient EL decay. The white emission is obtained by tuning the hole and electron carrier injection and adjusting optical length. The devices reach a maximum forward viewing external efficiency of η_{ext} = 33±3 % for a 3-WSOLED, and a total efficiency of $\eta_{ext,tot}$ = 57±6 % at a luminance of 1000 cd/m^2, representing a 25% increase relative previously reported all-phosphor doped WSOLEDs. The result thus far is one of the highest among what have been ever reported. The stacked structure of F/P WOLED is also demonstrated and high efficiencies at high currents have been achieved.

In Chapter 5, improving lifetime and low power consumption are focused for targeting a practical use of OLED for a full-color display.

In Chap. 5-1 section, We have demonstrated a top-emitting WOLED employing a metal free transparent cathode. The devices exhibit operating voltages and external quantum efficiencies comparable to those obtained using a conventional bottom-emitting OLED using a thin film of UV-ozone-treated nickel treated. The WOLEDs reached η_{ext} = 10.5±1% at current densities of J = 1.6 mA/cm2, with a power efficiency of hp = 9.8±1 lm/W at J = 1.0 mA/cm^2. No pronounced microcavity effects are observed for these devices by introducing alkali metal-doped ETL for the first time. These results suggest that the top-emissive white-OLEDs are promising for use in full-color displays for a long lifetime without suffering the feature of wide viewing angle. The stacked white OLED are fabricated on a low-temperature polysilicon TFT backplane. The connecting layer is newly developed for the use in TFT substrate for reducing the microcavity effects and potential defects caused by alkali metal doping. It is proved that the stacked white OLED shows the improved lifetime compared to the conventional OLED with single EL unit.

In Chap. 5-2, for reduceing the power consumption, a red, green, blue and white (RGBW) pixel format combined with an RGB color filter array (RGBW format) with a common white emission layer (EML) has been developed. We find that the RGBW format can successfully reduce the power consumption of a full-color active-matrix OLED by nearly half that of a conventionally filtered RGB pixel format. This improved

power consumption is almost equal to the power consumption of a same-sized LCD. The RGBW format is found to be a promising technique for the further reduction of the power consumption of a full-color AMOLED.

Future Prospective

The researchers working on OLEDs have pioneered new technologies which make OLEDs practically available in the market. Unlike inorganic-based emitting devices, OLEDs include over ten organic materials, especially white OLEDs have complicated device architectures. Due to the complexity and the diversity of an organic compound itself, there have not yet been comprehensive theories for an OLED's performance such as current-voltage characteristics, exciton diffusion and formation, luminance decay and emission outcoupling.

In addition to these basic problems, the remaining challenges for preventing the widespread manufacturing and use of the OLED are (i) production cost, (ii) power efficiency, and (iii) operational stability.

In terms of cost, OLEDs need to be at least equally cheap as competing LCDs, and fabrication technologies need to solve this issue. Previously, we had developed the most efficient production system of OLEDs grown in high vacuum systems using a thermal evaporation source called a linear source as shown in Fig. 6-1.[1] Alternatively, low-pressure organic vapor phase deposition (LP-OVPD), which is similar to hybrid vapor phase epitaxy used in III-V semiconductors, has been shown to have improved control over doping, and is adaptable to rapid, particle free, uniform deposition of organics on large-area substrates [2]. This novel organic deposition technique has recently been commercialized and promises to revolutionize the organic electronics fabrication industry.

However, this is ultimately not the cheapest fabrication route. We expect roll-to-roll manufacturing technique with an analogy of printing technology for mass production of cheap OLEDs, and these processes may eventually make the cost of producing OLEDs competitive. For a full-color display, the precision mask alignment processing is a matter of significance. The alignment accuracy only allows +/- 5 μm for patterning RGB EMLs. It extremely limits the productivity since the maximum size of a

precision mask, or mother glass, is limited and the process causes defects. Consequently, white OLEDs combined with RGB color filters are a promising solution to increase productivity though the loss caused by the color filters must be overcome by high efficiency.

Ultimately, the organic display comprises of OLEDs and organic TFTs on a plastic substrate will make a paradigm shift to organic electronics.

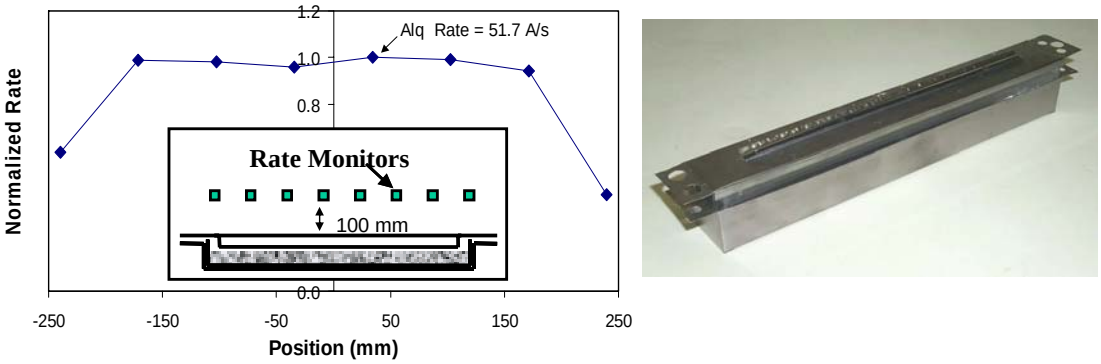

Figure 6-1. The uniformity along the linear source and its whole image.

OLEDs with high efficiencies of ~60 lm/W at 1000 cd/m^2, which are comparable to those of fluorescent lamps and makes huge advantage in power consumption against LCDs, seem to be around the corner, as shown in Chap. 4. Actually the research group in Konica Minolta announced that a stable white OLED with 64 lm/W at 1000 cd/m^2 had been achieved using new materials though the technical details are unknown. It is plain fact that efficiency depends heavily on organic materials. High efficiency blue and red phosphorescent materials still need to be developed.

On the other hand, common commercially available materials have purities of ~99.95% whereas materials with very high purities are used throughout the inorganic field. For emissive devices, impurities may cause quenching and hence decrease the emission efficiency and reproducibility. This reduction in efficiency is in addition to other deleterious effects on charge transport and operational stability. It is required to provide high-purity materials for organic electronics. Thus, the design and optimization of an OLED should be based on analytical models, but lacking these, engineers continue to rely on combinatorial processes that are slow and costly.

The current OLED architecture is limited by a ~20% outcoupling efficiency in the forward viewing direction, which constrains the maximum power efficiency of OLEDs to ~70 lm/W. New outcoupling schemes need to be developed to move beyond this limit to least 80 lm/W. Increased outcoupling efficiency by introducing non-periodic dielectric photonic structures was recently reported by Stanford group.[3] I express an optimistic prospect as shown in Fig. 6-2 introducing the technologies which are mentioned in the previous chapters. The period of application of the technologies is a matter of significance.

Presently, the largest hurdle is operational stability of OLEDs. To be useful for displays, the operational lifetime of an OLED running at 5000 cd/m^2 must exceed 3,000 hrs. The lifetimes of the best green and red electrophosphorescent devices are only 40,000 hrs at 1000 cd/m^2 and 300,000 hrs at 500 cd/m^2 respectively, which barely meet the stability requirement at room temperature. However, blue devices have lifetimes of only ~3,000 hrs at 500 cd/m^2.[4] At present, therefore, the improvement of blue phosphors are considered as an immediate priority. For the development of materials, the analytical and physically theoretical approaches are important as a combinatorial method may accelerate the development speed.

Although these challenges outlined above may not be unconquerable in a couple of years, there is great hope that this technology will meet practical goals and expectations in the future. There are numerous researchers and engineers around the world that are interested in organic devices, because they see potential for new products and discoveries. Indeed, research in organic electronics is vibrant and expanding, and the future of OLEDs is very bright and will illuminate the world.

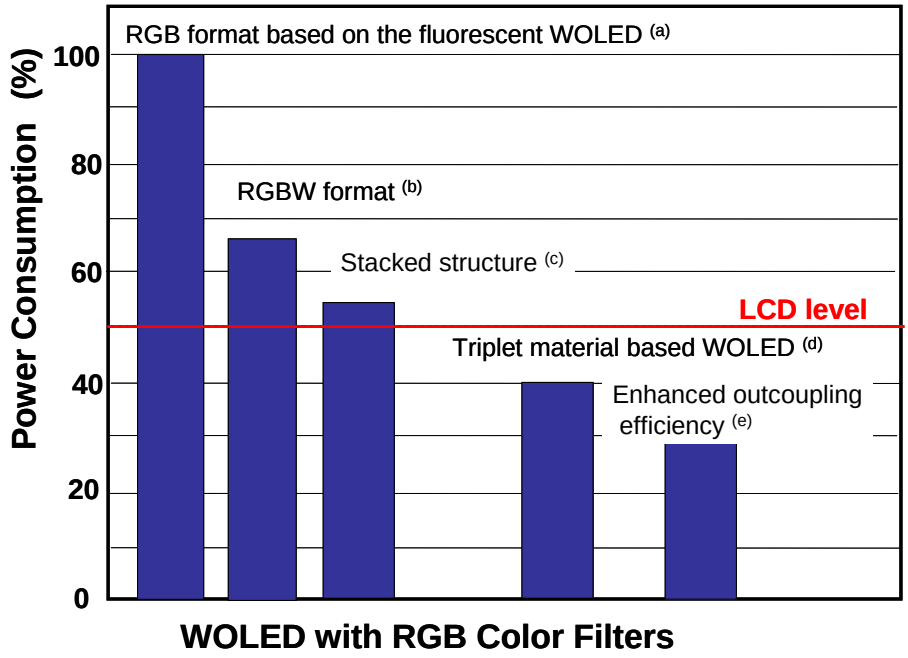

(a) The present status of WOLED shown in Chap. 5.2 with the high efficiency and stability, which is commercially available.

(b), (c) The condition is described in Chap. 5.2.

(d) Prediction according to improvement of blue phosphorescent emitter by Universal Display Corp.

(e) Based on the presentation (Ref XX).

Figure 6-2. Prospects of reduction in power consumption with various technologies.

Chapter 6. References

[1] S. Van Slyke, D. Freeman, N. Redden, H. Kanno, Y. Nishio, D. Waters, H. Kikuchi, and T. Negishi, SID2002 Digest, pp.886 (2002)

[2] M. Shtein, H. F. Gossenberger, J. B. Benziger and S. R. Forrest, Journal of Applied Physics, 89, 1470 (2001).

[3] M. Agrawal and P. Peumans, MRS Fall Meeting 2005, Boston, MA.

[4] A. Chwang, R. Hewitt, K. Urbanik, J. Slivernail, K. Rajan, M. Hack, J. Brown, J. Lu, C. Shih, J. Ho, R. Street, T. Ramos, L. Moro, N. Rutherford, K. Tognoni, B. Anderson, and D. Huffman, SID2006 Digest, 64-2 (2006)

List of Publications

(1) Hiroyuki Fujii, Hiroshi Kanno, Takeshi Sano, Yoshitaka Nishio, Yuji Hamada, Hisakazu Takahashi, Tatsuo Usuki, and Kenichi Shibata:
Durable molecular organic electroluminescent devices and their frequency responses to a new accurate driving method.
IEICE Trans Electron., **E81-C**, 7, 1034-1040(1998).

(2) Yuji Hamada, Hiroshi Kanno, Hisakazu Takahashi:
Organic light-emitting diodes using a gallium complex.
Appl. Phys. Lett., **72**, 1939-1942 (1998).

(3) Yuji Hamada, Hiroshi Kanno, Tsuyoshi Tsujioka, Hisakazu Takahashi, and Tatsuro Usuki:
Red organic light-emitting diodes using an emitting assist dopant.
Appl. Phys. Lett., **75**, 1682-1684 (1999).

(4) Yuji Hamada, Hiroshi Kanno, Hisakazu Takahashi:
Improved luminous efficiency of organic light-emitting diodes by carrier trapping dopants.
Jpn. J. Appl. Phys., **40**, L753-L755 (2001).

(5) Kaori Saito, Noriyuki Matsusue, Hiroshi Kanno, Yuji Hamada, Hisakazu Takahashi and Takeko Matsumura:
Microwave Synthesis of Iridium(III) Complexes: Synthesis of Highly Efficient Orange Emitters in Organic Light-Emitting Devices.
Jpn. J. Appl. Phys., **43**, 2733-2734 (2004).

(6) Hiroshi Kanno, Yuji Hamada, Hisakazu Takahashi (Invited):
Development of OLED with high stability and luminance efficiency by co-doping methods for full color displays.
IEEE J. Sel. Top. Quant. Elec. **10**, 30-36 (2004).

(7) Hiroshi Kanno, Yiru Sun, and Stephen Forrest:
High-efficiency top-emissive white-light-emitting organic electrophosphorescent devices.
Appl. Phys. Lett., **86**, 263502-1~3 (2005)

(8) Hiroshi Kanno, Russell Holmes, Yiru Sun, and Stephen Forrest:
High-efficiency stacked white-light-emitting organic electrophosphorescent devices.
Adv. Mater., **18**, 339-342 (2006)

(9) Yiru Sun, N.Giebink, Hiroshi Kanno, Biwu Ma, Mark E. Thompson, and Stephen R. Forrest:
Management of singlet and triplet excitons for efficient white organic light emitting devices.
Nature, **440**, 908-912 (2006).

(10) Hiroshi Kanno, Noel. C. Giebink, Yiru Sun, and Stephen Forrest:
Stacked white organic light-emitting devices based on a combination of fluorescent and phosphorescent emitters.
Appl. Phys. Lett., **89**, 023503-1~3 (2006).

(11) Kenji Okumoto, Hiroshi Kanno, Yuji Hamada, Hisakazu Takahashi and Kenichi Shibata:
Highly efficient green fluorescent organic light-emitting device with external quantum efficiency of nearly 10%.
Appl. Phys. Lett., **89**, 063504-1~3. (2006).

(12) Kenji Okumoto, Hiroshi Kanno, Yuji Hamada, Hisakazu Takahashi and Kenichi Shibata:
High efficiency red organic light-emitting devices using tetraphenyldibenzoperiflanthene doped rubrene as an emitting layer.
Appl. Phys. Lett., **89**, 013502-1~3 (2006).

(13) Kenji Okumoto, Hiroshi Kanno, Yuji Hamada, Hisakazu Takahashi and Kenichi Shibata:
Organic light-emitting devices using polyacene derivatives as a hole-transporting layer.
J. Appl. Phys., **100**, 044507 (2006)

(14) Hiroshi Kanno, Yiru Sun, and Stephen Forrest:
White organic light-emitting device based on a phosphor sensitized emission layer.
Appl. Phys. Lett., **89**, 143516-1~3 (2006)

(15) Hiroshi Kanno, Yuji Hamada, Kazuki Nishimura, Kenji Okumoto, Nobuo Saito, Hiroki Ishida, Hisakazu Takahashi, Kenichi Shibata, and Kazunobu Mameno:
High efficiency stacked organic light-emitting diodes employing Li_2O as a connecting layer
Jpn. J. Appl. Phys., **45**, **in press**. (2006).

(16) Hiroshi Kanno, Yuji Hamada, Kazuki Nishimura, Kenji Okumoto, Nobuo Saito, Kazunobu Mameno, Kenichi Shibata:
Reduction in power consumption for a full-color active matrix organic light-emitting devices
Jpn. J. Appl. Phys., **45**, L947 (2006).

(17) Hiroshi Kanno, Kaori Ishikawa, Yoshitaka Nishio and Kenichi Shibata:
Highly efficient and stable red phosphorescent organic light-emitting device using bis[2-(2-benzothiazoyl)phenolato]zinc(II) as host material.
Accepted for publication in *Appl. Phys. Lett.*(2007).

Acknowledgments

I have started my research on organic electroluminescence since 1997 in the corporate R&D of Sanyo Electric Co., Ltd. I have been engaged in a lot of activities ranging from basic material developments to productivity improvements in the manufacturing. With help from many collaborators, I have compiled this thesis while working on the practical developments of OLEDs. My enthusiasm for the OLED research is created and elevated by active discussion and mutual encouragement with the collaborators.

First of all, Dr. Kenichi Shibata, Hisakazu Takahashi, Dr. Yuji Hamada, as my closest and reliable collaborators, at Sanyo R&D have continuously encouraged and facilitated the research. I am greatly indebpted to them for the enormous support. Also, I thank Kazuki Nishimura and Dr. Kenji Okumoto for helping daily experiments.

Professor Tadashi Watanabe at the University of Tokyo, he is the advisor for this doctorial thesis as well as the master's thesis. His direct guidance and insights over the master's program of two years were essential to my development as an experimentalist and led to this doctorial thesis. Thank you for your patience, time and enthusiasm.

While in Princeton University for two years, I had been guided by Professor Stephen R. Forrest, who is, presently in University of Michigan, an admirable scientist and notable editor. The prolonged and intense discussions had enhanced my awareness as a self-supporting researcher. Thank you for your wise generosity for giving me the wonderful research environment.

Additionally, I thank the gradutate students in the laboratory who shared long time helping my projects and discussing organic electronics. Especially, I thank Yiru Sun, Russell J. Holmes, Noel. C. Giebink, Stephane Kena-Cohen.

I thank Prof. Mark E. Thompson at University of Southern California for providing me phosphorescent materials and advice about organic

material. Dr. Julie Brown and Dr. Brian D'Andrade at Universal Display Corporation kindly helped my projects with valuable advice.

I thank Professor Tetsuo Tsutsui at Kyushu University and Professor Junji Kido at Yamagata University for helping me realizing my intensive research on OLEDs. Dr. Tukaram K. Hatwar and Dr. Steve Van Slyke had informative discussion and gave me insights for applied technologies.

Finally, I sincerely thank my parents and wife, Keiji Kanno, Sachiko Kanno, and Shima Kanno for all the support. To them I dedicate this thesis.